A STUDY OF MGO-Y_2O_3 BASED NANOPHOSPHORS FOR LUMINESCENCE-BASED APPLICATIONS

A Thesis submitted to the

UPES

For the Award of

Doctor of Philosophy

in

Physics

By

Priyanka Bishnoi

September 2025

Supervisor

Prof. Ranjeet Kumar Brajpuriya

External Supervisor

Prof. Ankush Vij

Department of Physics

Applied Science Cluster

School of Advance Engineering (SOAE)

UPES

Dehradun- 248007: Uttarakhand, INDIA

A STUDY OF MGO-Y_2O_3 BASED NANOPHOSPHORS FOR LUMINESCENCE-BASED APPLICATIONS

A Thesis submitted to the

UPES

For the Award of

Doctor of Philosophy

in

Physics

By

Priyanka Bishnoi

(SAP ID: 500099823)

September 2025

Supervisor
Prof. Ranjeet Kumar Brajpuriya
Head, Applied Science Cluster
UPES, Dehradun

External Supervisor
Prof. Ankush Vij
Dept. Of Physics and Astrophysics
Central University of Haryana, Mahendergarh

Department of Physics,
Applied Science Cluster
School of Advance Engineering (SOAE)
UPES,
Dehradun- 248007: Uttarakhand, INDIA

DECLARATION

I declare that the thesis entitled **"A Study of MgO-Y_2O_3 based Nanophosphors for Luminescence Based Applications"** has been prepared by me under the guidance of Prof. Ranjeet Kumar Brajpuriya, UPES, Dehradun and Prof. Ankush Vij, CUH, Mahendergarh. No part of this thesis has formed the basis for the award of any degree or fellowship previously.

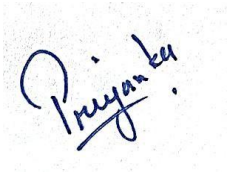

Priyanka Bishnoi
Department of Physics,
UPES, Bidholi, Dehradun.
DATE: 15-09-2025

CERTIFICATE

I certify that Priyanka Bishnoi has prepared her thesis entitled **"A Study of MgO-Y_2O_3 based Nanophosphors for Luminescence-Based Applications",** for the award of PhD degree of the UPES, under my guidance. She has carried out the work at the Department of Physics, UPES.

Internal Supervisor

Prof. Ranjeet Kumar Brajpuriya

Department of Physics,

UPES, Bidholi, Dehradun.

Date: 15-09-2025

Department of Physics & Astrophysics
Central University of Haryana

CERTIFICATE

I certify that Priyanka Bishnoi has prepared her thesis entitled **"A Study of MgO-Y_2O_3 based Nanophosphors for Luminescence-Based Applications",** for the award of PhD degree of the UPES, under my guidance. She has carried out the work at the Department of Physics, UPES.

External Supervisor

Prof. Ankush Vij

Department of Physics and Astrophysics,

Central University of Haryana, Mahendergarh

Date: 15-09-2025

ABSTRACT

The luminescence field has captivated scientific interest for centuries, evolving from ancient observations to advanced cutting-edge lighting, and photonic technologies. With rising demands for nanophosphors that are not only efficient, but also stable, and environment-friendly, oxide-based phosphors have emerged as a promising alternative to traditional halides and sulfides. This study explores the MgO-Y_2O_3 nanophosphors, emphasizing their luminescence, defect alterations with doping of rare earth ions, and capability for industrial applications in lighting, security ink, and radiation dosimetry. MgO is wide band gap oxide with a simple cubic structure, and exhibits native F center-related luminescence, while Y_2O_3 is an inorganic oxide with a bixbyite cubic structure, offers low phonon energy and rare earth solubility but suffers thermal quenching in high power applications. The combination of these two oxides into a composite MgO-Y_2O_3 matrix overcomes individual limitations and enhances overall optical performance.

The MgO and MgO-Y_2O_3 nanophosphors were synthesized by the solution combustion method. Defect modification and luminescence behavior of MgO is investigated with single doping of Bi^{3+}, and Li^{+} ions. XRD and XANES confirmed the single cubic structure of MgO throughout doping at different concentrations with the formation of O, and V(Mg vacancy) defects and interstitial defects. In pure MgO, photoluminescence is observed in blue and red regions due to different F centers and interstitial O present in the lattice, while with Bi^{3+} doping introduced new defect levels and emission is observed due to Bi ion p→s transitions centered at 387nm. Consequently, Li^{+} doping causes the quenching in PL emission suggesting monovalent ions do not have radiative transitions and creating vacancy-related recombination losses. Thermoluminescence studies provide insight into complex defect modulations indicating Li-related shallow traps and Bi^{3+} ions doping enables the charge transfer to deeper levels. Further, MgO is doped with rare earth ions (Sm^{3+}, Ce^{3+}) and co-doped with monovalent Li^{+} ions to investigate

the luminescence mechanism. Sm^{3+} doped MgO demonstrated enhanced red emission due to the f-f transition of Sm^{3+} and color shifting from blue to red on changing the excitation source from UV to blue Li co-doping improved the crystallinity which further increased the luminescence behavior. Ce^{3+} doping, however, introduced secondary phase of CeO_2 confirmed by the XRD and the coexistence of Ce in +3 and +4 states revealed by the XANES. Characteristics emission by the Ce^{3+} is observed, centered at 570 nm and 610 nm, and decreased with an increase in Ce^{4+} concentration. Co-doping Li^{+} again improved the crystallinity and emission, although the solubility remained the limiting factor.

The most comprehensive approach is the emission tunability of MgO-Y_2O_3 with different doping concentrations of rare earth and different excitation sources and exploring the energy transfer mechanism in upconversion and downconversion properties Er^{3+}, $Ho^{3+,}$ and Yb^{3+} pairs. Rietveld refinement of XRD patterns suggested the incorporation of Er^{3+}, Ho^{3+}, and Yb^{3+} at the Y^{3+} position in the lattice. Under UV excitation and 980 nm excitation green, red, and NIR emissions observed from Ho^{3+} and Er^{3+} when co-doped with Yb^{3+} ions, conveyed Yb^{3+} as the efficient sensitizers. The multi-photon process involved in energy transfer from sensitizers to activators for different emission. Successful synthesis of ink and long- term stability of prepared samples over time successfully translating the fundamental findings into practical applications. Ecofriendly synthesis, high- temperature stability, and tunable luminescence properties make MgO-Y_2O_3 a promising candidate in generation of lighting and security devices.

ACKNOWLEDGEMENT

The successful completion of this research journey marks a deeply fulfilling and transformative chapter of my life. It has been a path filled with rigorous research, intellectual work, moments of doubt, and many milestones—none of which would have been possible without the constant support, guidance, and encouragement of eminent professionals. This thesis stands not only as a testament to years of dedicated work but also as a reflection of collective contributions from those who stood beside me in this pursuit.

First and foremost, I express my sincere and heartfelt gratitude to my supervisors, ***Prof. Ranjeet Kumar Brajpuriya***, UPES, Dehradun, and ***Prof. Ankush Vij***, Central University of Haryana, Mahendergarh. Their unwavering guidance, insightful feedback, mentorship, and continued support have been instrumental in shaping and direction and depth of my research. Their constant patience and encouragement – both professionally and personally provided strong foundation I needed to persevere through the challenging phase of this journey. I consider it a great privilege to have worked under their supervision.

My special thanks to ***Dr. Ram Sharma,*** Vice Chancellor, UPES ***and Prof. Ashwin Nangia***, Dean R&D UPES for their support and encouragement throughout this journey. I am also grateful to my supervisory team of professionals, ***Prof. Shalender Kumar***, ***Dr. Aditya Sharma***, ***Dr. Kanak Pal Singh Parmar***, UPES, Dehradun, ***Dr. Ashish Sharma***, Associate Professor, Central University of Jammu, Jammu. Their consistent encouragement and timely support enabled me to navigate academic milestones smoothly. I would like to thank UPES for fellowship and financial assistance, Central Instrumentation Center (CIC), Department of Chemistry, Lab Block (UPES), for providing lab facilities for my research work. I am thankful to ***Dr. Charu Chandra Pant, Dr. Devender Singh Rawat, Tijendra Kumar, and Neeta Rawat***, for providing technical support in using lab facilities at UPES for my research work.

I also particularly grateful to ***Dr. Kaushal Kumar*** and ***Dr. Madaan M. Upadhyay***, IIT, Dhanbad for providing temperature-based upconversion experimental facilities. My special thanks to ***Mr. Abhishek Sharma***, Sr. Scientist, Solid State Physics Laboratory (SSPL), New Delhi, and the Material Science group, IUAC for the TEM facility, ***Mr. Vinod Kumar***, Sr. Scientist, Instrumentation Research & Development Establishment (IRDE), for providing NIR measurements. I would like to thank ***Dr. K.H. Chae*** and ***Dr. S.O. Won***, Advance Analysis Centre, Korea Insititute of Science and Technology, South Korea for X-Ray Absroption Spectroscopic experiments. I owe my thanks to ***Dr. D. Sen*** and ***Mr. Birendra Singh***, Health Physics, IUAC, New Delhi, for conducting the Thermoluminescence experiments. Furthermore, I am deeply thankful to ***Dr Savita***, ***Mr. Maneshwar Thakur,*** whose experiences and guidance offered valuable insights in my early phase of my research. I cordially thank my lab mates, ***Ms. Vaishali Rathi***, ***Ms. Gargi Dhiman***, ***Mr. Kamal Singh, Mr. Manas Nasit, Mr. Nitin Gautam*** for their teamwork and joyful moments we shared in the last few years.

The acknowledgment would be incomplete without appreciating the consistent support and encouragement from my beloved husband, ***Mr. Vinod Kumar***. His faith in my abilities has uplifted me during the most challenging times. His steadfast presence and unspoken contribution have made it possible for me to focus on my research goals. A very special place is reserved for my sons, ***Akshit Bishnoi*** and ***Aayansh Bishnoi***. The fatigue of long days would dissolve in the warmth of their eager welcome, and their presence has been constant source of strength throughout the doctoral journey.

I owe much my resilience to constant love and support from ***my parents, in-laws***. Their blessings provided the strength to persevere through rejections.

Finally, I extend my heartfelt gratitude to the Almighty for his countless blessings and love throughout the journey.

Date:
Pace: Dehradun Priyanka Bishnoi

TABLE OF CONTENTS

TABLE OF FIGURES

LIST OF TABLE

CHAPTER 1

INTRODUCTION

INTRODUCTION

1.1 Luminescence

From ancient times, luminescence has intrigued the world with naturally occurring luminescence such as the glow of fireflies, shimmering aurora borealis, and faint illumination from wood. These mechanism of natural emission from organisms often occurs without heating remained unsolved until 16th century (Armaroli & Bolink, 2016; B., 1926; Kohale et al., 2021; Valeur & Berberan-Santos, 2011). In 1603, an early milestone came when the first phosphorescent material ($BaSO_4$), famously known as the Bolognian stone, was used by Vincenzo Cascariolo to produce the gold. On heating this mineral, he was not able to produce gold, but it was discovered that the residue exhibited persistent luminescence (Armaroli & Bolink, 2016). In the same century concept of phosphorescence, thermoluminescence, and electroluminescence was documented by Robert Boyle while studying diamonds (Virk, 2015). While studying diamonds, it was noticed that this material emits light by absorbing energy from different sources. Mechano-luminescence was also observed while crushing the sugar and salt crystals in a mortar, which produces the flashes, and it was reported in 1684. Throughout the 17th century, several minerals and ceramics were found to exhibit the mechano-luminescence, further expanding this area in research. The luminescence term was scientifically given by Eilhardt Weidemann in 1888 with the explanation of the emission of light without significant heat absorption (Murthy & Virk, 2014; Virk, 2015). The first TL materials (Mn-doped CaF_2 and fluorite) were also reported by Schimdt and Eilhardt in 1895. Additionally, they differentiate the luminescence from incandescence and classify the luminescence into six different types based on excitation energy (Garlick, 1958; Murthy & Virk, 2014).

The study of luminescence increased significantly in the 19th and 20th centuries and attracted the attention of worldwide researchers. Over time, researchers developed different methods to produce luminescence. Photoluminescence, in which light is emitted by absorbing suitable photons mainly

observed in semiconductors and quantum dots (Ermolaev, 2018; Poles et al., 1999). Electroluminescence is another way in which light is generated by applying an electric field, commonly used in LEDs and displays (Tarasov, 1999). Chemi-luminescence is the process in which the emission of light is due to a chemical reaction, widely used in biosciences, pharmaceuticals, and gas analysis (Kricka & Thorpe, 1983). Mechano-luminescence is a process in which light is emitted due to the mechanical stress on materials (Jain & Singh, 2024). Thermoluminescence is the emission of light from the material on heating, while the source of excitation is radiation to which the material is exposed, employed in geology, medicine, and radiation dosimetry. In 2008, the Nobel Prize in chemistry was awarded to Osamu Shimomura, Martin Chalfie, and Roger Y. Tsien for the development of green fluorescent protein which revolutionized bioimaging applications (Craggs, 2009; Zimmer, 2009). In 2014, another Nobel Prize was awarded to Shuji Nakamura, Isamu Akasaki, and Hiroshi Amano for discovering blue LED revolutionized the lighting technology (Akasaki, 2015). The direct conversion from electricity into photons led to new research in luminescent materials, also known as phosphors, which contributes to the savings in energy and earth resources. This discovery of blue LED further opens new paths in the generation of white light, either by combining the blue/ UV LED with suitable phosphors that lead to emission in the visible range and precise color tenability (Akasaki, 2015; Nakamura, 2015).

The luminescence characteristics were significantly modified by shifting the size of phosphors towards the nanoscale as compared to the bulk. The band gap alterations of nanophosphors having a size less than 100 nm lead to controlling the excitation and emission behavior (Aggarwal, 2025; Jaque & Vetrone, 2012; X. Li et al., 2021; X. Shi et al., 2021; J. Yu et al., 2020). The change in intrinsic properties, structure, and surface-to-volume ratio, defect formation, and quantum confinement effect leads to the impact on the emission profile, prolonged emission, spectral intensity, luminous efficiency, and quantum yield of nanophosphors. Thus, nanophosphors research is a key attraction for worldwide researchers in a wide range of other applications such as medical imaging to enhance contrast imaging,

invisible inks, counterfeiting scintillators, solar cells, bio-labeling, etc (Chander, 2005; Kori et al., 2021; Liang et al., 2023). It is critical to understand the emission profile of a phosphor when it is stimulated with a high photon flux, since it is connected to the emission saturation or the emission efficiency of the phosphor. Another challenge in the development of phosphors is the achievement of long-term stability, which is directly connected to the life span of lighting products. On the other hand, chemical stability and degradation of phosphor materials under long-term operation are important aspects of phosphor stability (Cesaria & Di Bartolo, 2019; Kubrin, 2014; Y. Li et al., 2016). The rare earth (RE) doped nanophosphors are nowadays investigated thoroughly because of the sharp and distinct emission of rare earths owing to their shielded f-f transitions (Du et al., 2022; Etafo, 2024; H. Li et al., 2019; Y. Liu et al., 2013; Sharma & Ghosh, 2021; F. Wang & Liu, 2014). Sm^{3+}, Eu^{3+} in $KSrPO_4$ emits red and blue emissions and shows better thermal stability as compared with Ce:YAG (Fujita et al., 2010; Masenelli et al., 2013; Morebodi, 2021; Nishiura et al., 2011; Rahate et al., 2021). Furthermore, Sm^{3+} and Eu^{3+} characteristics emission are in the red range when doped in a suitable host, while Yb^{3+}, Er^{3+} exhibit strong emission in the visible as well as in the NIR region (Chamarro & Cases, 1990; Morebodi, 2021; Pires et al., 2006; Ramasamy et al., 2013; Ramteke et al., 2020). This indicates that doping in a suitable host is another aspect for the stability of phosphor materials. The wide band gap host material, and having low phonon energy, can minimize the quenching due to non-radiative transitions. Multiple combinations of dopants in a single host approach also give broad emission and enhanced quantum efficiency.

1.2 Oxides

Oxides are environmentally compatible, with good thermal and chemical stability, and have a non-toxic nature, making them key materials for optical applications. Oxides are minerals in which oxygen forms a bond with other elements (R. P. Singh et al., 2020). This class of mineral includes perovskites,

spinels, borates, silicates, oxides, etc. Now, sulphides are being replaced by oxides in many fields because of their stable and environmentally friendly advantages (Buissette et al., 2006; Chander, 2005). When lanthanides are doped in oxide-based hosts, the environment around the dopants is distorted and the symmetry is disturbed, causing the forbidden f-f transitions (Hatanaka & Yabushita, 2009; Mason, 1984). The host affects the energy level splitting depending on the site symmetry, which leads to sharp or broad emission. Successful incorporation of rare earth in sufficient quantity depends on the phase stability of the host, which leads to an increase in quantum yield (G. Li et al., 2023; Y. Zhang et al., 2024). Intrinsic defects present in the host again helpful in charge transfer from host to dopant, leading to increase the excitation and emission tenability. The narrow emission of sulphides make them less tunable as compared to oxides (Daksh & Agrawal, 2016; Gupta et al., 2021; Zheng et al., 2022). The low phonon energy of oxides minimizes non-radiative losses which improves the emission characteristics. Although halides also have low phonon energy, suitable for rare earth ions but the complexity and use of corrosive chemicals in their synthesis method make them unsuitable for use as phosphors. The environment-friendly and non-toxic synthesis of oxides makes them better suited as phosphors.

1.3 MgO-Y_2O_3 Nanophosphors

Magnesium oxide is a highly economical, low-cost, and less toxic wide band gap insulating material, highly used in different applications owing to its simple FCC rock salt structure (Kappers et al., 1970). It is a thermally stable oxide and has a melting point of 2850 ºC and a boiling point of 3600 ºC. It has a rock salt FCC structure with space group Fm-3m, in which Mg cations occupy the octahedral sites, lying in a close-packed structure of oxygen ions with a lattice parameter of about 4.202 Å (Uchino et al., 2009). However, MgO is a wide band gap insulator, but owing to the defects present in the lattice make this insulator shows emission in the blue and red regions. Due to these defects present in MgO, it shows

exceptional magnetic and optical properties. Luminescence characteristics are highly governed by the O neutral and charge vacancies known as the F centers,

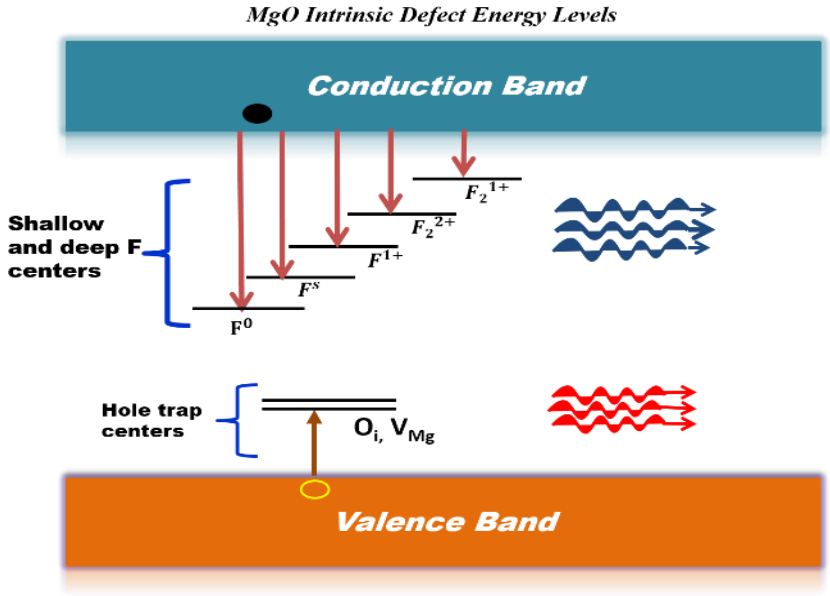

Fig 1.1: Various Intrinsic defects present within the bandgap of MgO

clustering of vacancies, while magnetic properties are controlled by the Mg vacancies present in the oxide (Y. Chen, Kolopus, et al., 1969; Kappers et al., 1970; Uchino & Okutsu, 2008; Uenaka & Uchino, 2011). The different intrinsic defects present in the lattice facilitate the luminescence behavior of this oxide. Additionally other charges defects also exists such as F^{2+} or the pair of neutral F center with F^+, cluster of charged anion vacancies lying adjacent to each other (F^+ and F^+), interstitial neutral or charged O (O^{-1} and O^{-2} defects) lying near the valance band, hole trapped at the place Mg ion vacancy, Schottky defects which collectively are responsible for different optical properties of MgO. The neutral defects are the most stable and lie in the center of bandgap of MgO, while charged F centers (F^+, F^{2+}, F_2^{2+}) lie near the conduction band and form the shallow traps acting as shallow and deep traps depending on their energy position. The different intrinsic defects present in MgO are shown in Fig 1.1.

(Bos et al., 2006), first studied the TL behavior of MgO with rare earth doping of Tb ions. The native defects of MgO have also been studied by using

thermoluminescence and optical stimulated luminescence with doping of different rare earth ions. (Oliveira et al., 2016) fabricated the dosimeter device with Ce, Li, and Sm doping in MgO and studied the stability of the device performance over a period of two months. (Devaraja et al., 2016a) doped the Cr^{3+} and Fe^{3+} in MgO, and red characteristic emission of Cr ions was reported. However, saturation was observed at very low concentrations of Cr ions. Besides various advantages of MgO, the construction of luminescent materials based on rare earth-doped MgO faces substantial challenges due to the low solubility limit of RE ions in the host material. Similar to MgO, Y_2O_3 is one of the sesquioxide materials have excellent thermal and chemical stability (Xu et al., 1997). It has a relatively lower maximum phonon energy (590 cm^{-1}) as compared to other sesquioxides, which helps to reduce the multi-phonon relaxation and further enhances the radiative transitions by minimizing the non-radiative losses. Though Y_2O_3 exhibits stable structural properties, RE-doped Y_2O_3 undergoes thermal and mechanical stresses and has

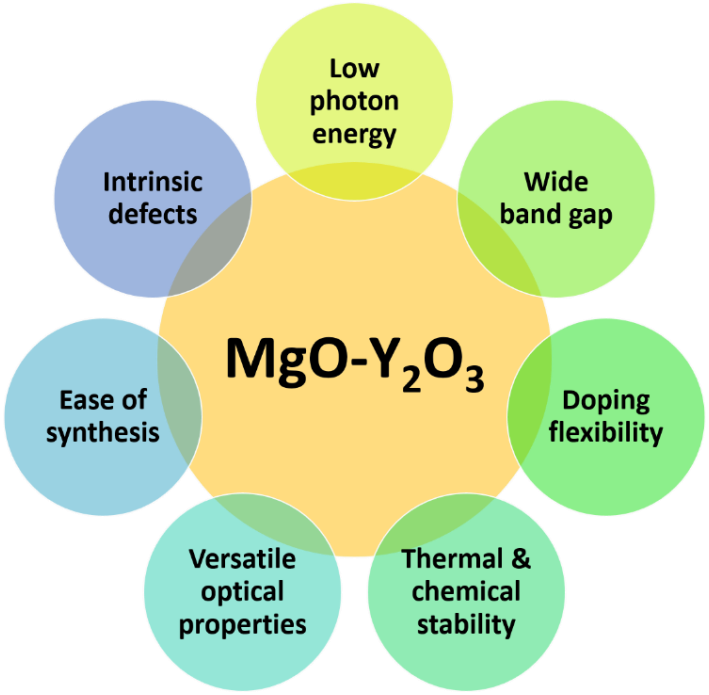

Fig 1.2: Properties of MgO-Y_2O_3

been reported to have inferior luminescence efficiency and luminous flux (An et al., 2019; Pandey et al., 2013; Rai et al., 2012). In a recent study, (S. Chen et al., 2023a) reported that the thermal conductivity of Y_2O_3 decreases from 14W/m/K to 5.9W/m/K with the doping of Eu ions. Likewise, Ho^{3+} doped Y_2O_3 has been reported for lower thermal conductivity (Safronova et al., 2021a). This thermal quenching, indeed, affects the stability of color quality and lowers the luminescence efficiency, specifically, if used in a field of high-power lighting applications. An efficient heat dissipation rate in the host is required to circumvent this thermal quenching behavior. To overcome this drawback in such a host material, a contemporary strategy is the introduction of a second stable phase with excellent thermal conductivity, making the phosphor effective and thermally robust for enhancing optical performance (Balabanov et al., 2025; L. Liu et al., 2020; Permin et al., 2022; Readey et al., 1990; Xiao-Jing et al., 2025).

MgO-Y_2O_3 is a new class of composite that has been reported with improved thermal conductivity thereby helps to improve the performance of Y_2O_3 in NIR range emissions. The various properties of MgO-Y_2O_3 are illustrated in Fig 1.2. MgO, which has been introduced as a second phase with Y_2O_3, is a stable, has wide bandgap with superior thermal conductivity at room temperature. Also, it does not make a mixed phase with the Y_2O_3 because of its high eutectic point (Moshtaghioun et al., 2021). It is used in radiation detectors due to its high resistance for the damage from radiations. It is used in high-power lasers, high temperature applications and shows efficient light emission without degradation. It is widely used in optical window because of its high IR transparency. The spectroscopic characteristics of RE ions in Y_2O_3 do not experience any change with the incorporation in MgO. Ho Jim et al. reported that not only were the photoluminescence and absorption properties of MgO-Y_2O_3, doped with a high concentration of Er^{3+}, improved, but also the beam quality, mechanical, and thermal properties were enhanced (Ma et al., 2018b). Similarly, in Eu^{3+} doped MgO-Y_2O_3, when the ceramics were sintered up to 1800 ºC, a quantum yield of ~ 80 % was achieved from the prepared ceramics

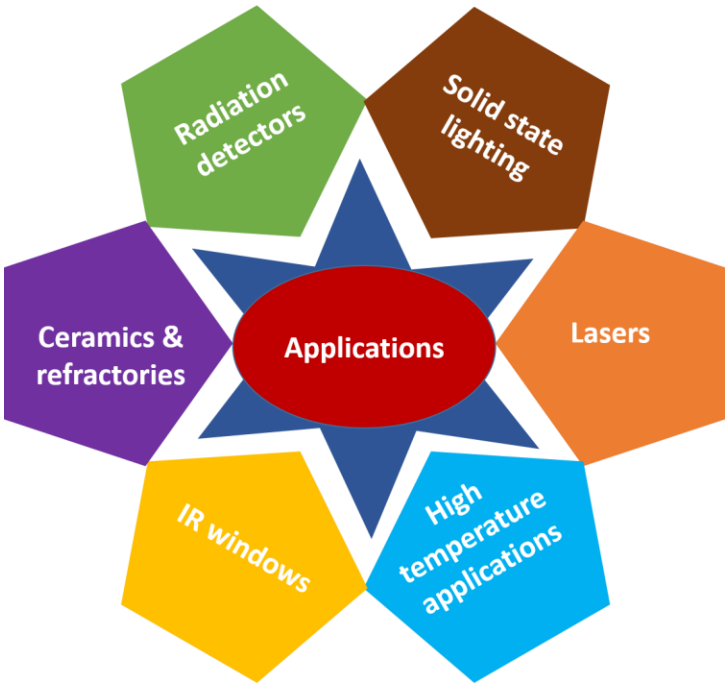

Fig 1.3: Applications of MgO-Y_2O_3

(S. Chen et al., 2023a). Owing to the remarkable properties of MgO-Y_2O_3, this material has been widely used in different fields which are shown in Fig 1.3. Thus, the combination of these oxides is an ideal model for nanophosphors properties. Here, in this context, the present study aims to explore the undoped and doped MgO, MgO-Y_2O_3 with non-rare earth and rare earth ions doping to understand the luminescence behavior.

CHAPTER 2

LITERATURE REVIEW

LITERATURE REVIEW

2.1 Undoped and doped MgO

In its pristine form, MgO exhibits various defects in the matrix, resulting in intriguing properties. These intrinsic defects render this nanomaterial a versatile ceramic, recognized by its exceptional thermal, chemical, and mechanical stability, making it suitable for different applications in industrial, environmental, optoelectronics, and biomedical domains. Undoped MgO is extensively studied by numerous researchers; a few studies are discussed below:

(Y. Chen, Williams, et al., 1969) studied the optical properties of single-crystal MgO irradiated with neutron and electron beams. At lower temperatures, five different bands appeared from the UV to the NIR regions. In neutron-irradiated crystals, the absorption band is attributed to the F centers present in the lattice. However, the mobility of F centers is observed above 900 ºC. The stability of bands in electron-irradiated crystals is greater than that of the neutron-irradiated crystals, predicting the aggregation of F centers in the former crystals.

(Ziniker et al., 1972) reported the thermal luminescence and thermally stimulated luminescence in UV-excited pristine single crystal and Fe-doped MgO. Various glow curve peaks at 375 K and 470 K in pure MgO and additional peaks at 425 K in Fe-doped MgO were observed—red and orange emissions were reported in TSL and fluorescence in undoped MgO. The orange and red emission is attributed to the V centres and inherent Cr as well as Mn impurities in the host, while the blue emission in Fe-doped MgO is due to the F centres.

(Sathyamoorthy & Luthra, 1978) examined the influence of transition metal doping on the thermoluminescence properties of MgO. In pure MgO, Glow curves were observed at five different temperatures and enhanced with doping of Mn, Ni, and Cr along with their characteristic emissions, while quenching was observed with doping of Fe, Cu, and Co. ESR analysis indicated the involvement of V-type defects in MgO specifically at lower temperatures. In case of Cr doped MgO, the

dopant traps the electron carriers while V-type defects of the host matrix behave as the hole trap, and doping of Mn, Cr, and Ni increases the recombination centers within the band gap, enhancing the TL emission.

(Rosenblatt et al., n.d.) analyzed the temperature-dependent decay behavior of F and F+ defects of pristine MgO nanocrystals from 90 K to 573 K. MgO crystals were synthesized by the arc fusion method, in which the H ions were trapped at F-defect states in the lattice. On excitation with 248 nm laser, two bands at 390 nm and 530 nm were observed, attributed to the F^+ and F bands, respectively, confirmed by theoretical models. It was observed that emission around 390 nm shows slower decay compared to the band near 530 nm. Additionally, the decay kinetics from both defect states are modified by the charge carriers trapped at different active sites in the lattice. The ratio of F to F^+ emission increased with the input laser power.

(Aritani et al., 2000) examined the modification in defect sites with Li doping in MgO. From XRD patterns of pure MgO and Li doped MgO single phase of rock salt structure of MgO was observed. At lower concentrations of Li, the diffraction peak intensity increased up to 0.5 mol%, while it decreased afterwards. From XANES of Mg K-edge and XPS conveyed the formation of defect sites near the surface edge was observed at lower concentrations Li ions, while at higher concentrations, bulk defect sites were also formed. These new defects further enhance the oxidative coupling of methane.

(Kawaguchi, 2000) studied the fracto-luminescence in MgO to understand its origin of emission of electrons by the bending fracture of the surface of a single crystal. Time decay studies revealed that blue-green emission decays faster than red emission. The red emission is attributed to the inherent Cr ions impurities in MgO.

(A. Kumar & Kumar, 2008) prepared the MgO nanopowder by using the sol-gel method, and optical studies were analyzed at different temperatures ranging from 500 ºC to 1000 ºC. From TGA analysis, weight loss was observed in two stages; first between 201 to 282 ºC, and second, weight loss between a range of 416

to 564 ºC. From XRD patterns, peaks sharpened with an increase in temperature predicted an increase in crystallite size. From FTIR experiments, the absorption near 3700 cm^{-1} is attributed to the hydroxyl groups present at defect sites in the lattice, which decreased with an increase in deposition temperature. However, red shifting and suppression in peaks from 3432 cm^{-1} to 3419 cm^{-1} were observed, attributed to the reduction in H_2O defects at low coordinated sites and the surface. Based on different optical absorptions observed, it was assumed that the creation of different oxygen defects occurred at the surface as well as in the bulk.

(Martínez-Boubeta et al., 2011) examined the magnetic and photoluminescent properties of MgO thin films prepared via the RF-sputtering method on two different substrates of STO and glass. The observed luminescent characteristics highly depended on the temperature and atmosphere in which the substrates were kept and the input power. The cation-to-anion ratio was altered in an oxygen atmosphere and an Ar^+ ion atmosphere. The O vacancies were controlled by increasing the growth rate. Further, the PL peaks observed were not symmetrical at different temperatures due to the variation in the Mg to O ratio. The blue emission was dependent on of input laser power. Saturation in PL intensity and rapid decay near 460 nm were presumed to be associated with the localized V vacancies functioning as the acceptors.

(H. Li et al., 2013) studied the optical properties of MgO nanobelts prepared by CVD techniques. The structural analysis suggested that at 0.5 min of reaction, the catalyst particles appeared at the tips of nanobelts, while these nanostructures grew longer and became wider. At 5 min reaction time, the isolated and complex nanobelts lengthened up to 100 nm. At a lesser reaction time, the dual phase of Mo and MgO was observed in XRD, while at higher reaction times, the grain boundaries elongated, attributed to the formation of defect sites, further ruling out the PL characteristics. The PL emission observed in the UV and blue region is associated with the O^{2-} at low coordinated sites and electron-trapped F centers, respectively.

(Devaraja, Avadhani, Prashantha, Nagabhushana, Sharma, Nagabhushana, & Nagaswarupa, 2014) examined the effect of the method of synthesis on the formation of defects and variation in PL emission. The MgO nanopowder was synthesized using solution combustion as well as hydrothermal technique. High porosity in SCS-synthesized MgO was observed, while the other MgO powder was fluffy. In the case of SCS-synthesized MgO powder, a broad emission in the blue-violet region centered at 390 nm was observed, while in the case of hydrothermally synthesized MgO, two discrete peaks in the same region were observed, centered at 390 nm and 425 nm. The asymmetry in the emission profile observed in both methods was attributed to the quantum confinement effects and variations in surface and bulk (F and V) defects.

(Choudhury & Choudhury, 2014) monitored the different neutral and charged F centers at different excitation energies in the UV region. The MgO nanocrystals were prepared by using the precipitation method and annealed at two different temperatures of 600 ºC and 800 ºC. At 206 nm excitation, the dominant emission is attributed to the singly charged F centers, while at excitation of 270 nm and 330 nm, clustered F^{2+} and F centers are both responsible for PL emission. At 800 ºC, the quenching in emission due to F^{+} centers was observed, and aggregation of charged defects decreased the ratio of $F^{+}/F_2^{2+,}$ which further accentuates the increment in ratio of F/F_2^{2+}.

(Devaraja et al., 2015a) examined the structural and luminescent properties of MgO doped with the different concentrations of Fe^{3+} ions. After synthesis using the solution combustion method, the structural studies predicts a decrease in crystallite size with an increase in doping of cations. Absorption band between 300 nm and 450 nm attributed to the O vacancies created due to the synthesis method, as UV-Vis studies. With excitation using 378 nm, PL peaks at 513 nm and 720 nm were observed. The green emission is due to the host intrinsic defects, while the red emission is attributed to the charge transfer from O to Fe.

(Pathak et al., 2016a) conducted a comprehensive investigation of experimental studies and theoretical models using DFT for pure MgO. MgO nanocrystals were synthesized using the sol-gel method. The distinct contribution of intrinsic defects of MgO is characterized by using time-resolved spectroscopy, absorption spectroscopy, and time decay studies. Emission was observed from 390 nm to 490 nm with different peaks and from 540 nm to 680 nm with three distinct peaks. The UV-blue emission was attributed to the different charge anion defects, and pair vacancies of $V\text{-}O^{-}$ with $V\text{-}Mg^{0}$. Emission at higher wavelengths is mainly attributed to the shallower defects and interstitial defects present within the band gap of MgO. The transition of charge carriers in these levels enables the range of emission in the visible region. Further, the DFT model studied the nature of different levels, which closely matched the experimental data. The theoretical data was again validated using different excitation wavelengths.

(Oliveira et al., 2016) investigated luminescent characteristics and associated dosimetric properties of triply doped MgO with Ce, Sm, and Li. In undoped MgO, where the TL signal was negligible, co-doping of Ce and Sm ions produced glow curves at 180 ºC. This glow curve is attributed to the unique trapping center generated by the co-dopants. Li doping enhanced the TL intensity up to 30 times compared to the singly doped MgO. It was predicted that the monovalent ions create radiatively favorable defects within the band gap. Furthermore, radio-luminescence spectra again confirmed the enhancement of the intensity with the addition of Li to with Ce^{3+} and Sm co-doped MgO. For applicability in dosimetry, the TL signal of the prepared phosphor was compared with commercial TLD-100 and 80 time more intense signal was observed, indicating the capability of the material for industrial use.

(J. P. Singh et al., 2017) examined the optical properties of undoped MgO synthesized by the sol-gel method, emphasizing the behavior of nanoparticles under diffuse reflectance and XANES. Prepared nanoparticles annealed at 350 ºC for a duration ranging from 0.5 to 12 hours, exhibit the crystallite size of 7 to 11 nm

embedded in carbonaceous matrix, attributed to the low temperature annealing. TEM and SEM revealed the formation of small grains within the matrix. From UV-Vis spectra of bulk and nano MgO, a reduction in reflectance up to 20 % was observed. Additionally, the reduction in band gap of nano MgO is observed as compared to bulk MgO. XANES spectra of Mg and O K-edge predicted the presence of organic impurities in the lattice, which caused the alteration in optical properties of nanoparticles.

(Oliveira et al., 2019a) studied the luminescent characteristics by combined doping of different lanthanides in MgO. All the lanthanides were kept constant at 0.3 mol% and synthesized by using the solution combustion method, while the Li doping was at 3 mol%. The dopants used in this study were Sm, Dy, Eu, Nd, Tm, Yb, and Li. From XRD patterns of all nanocrystals, it was observed that the Ce dopant made a dual phase at 0.3 mol% showed saturation due to the large size of cations compared to the host. In case of doubly and triply doped MgO with Ce, Yb, and Li, the new TL peak at 460 ºC was observed. Additionally, the TL signal was observed only in Sm, Tb, and Ce doping. The doping of Li enhanced the TL intensity due to the neutralization of charge disturbance. The activation energy calculation was carried out by using Dorenbo's model, in which the activation energy was estimated of 1.3 eV. From TL response and radio-luminescence spectra, it was confirmed that Terbium and Cerium dopants behaved as the hole trapping centers, and the other lanthanides, Samarium, Terbium, and Ytterbium, served as the electron trapping centers.

(Balakrishnan et al., 2020) prepared the pure MgO nanoparticles via solution combustion synthesis using urea as a fuel. XRD peaks confirmed the FCC phase with a crystallite size of 27 nm. SEM images revealed the formation of porous, spherical particles with agglomeration, and FTIR spectra predicted the presence of hydroxyl groups at the surface and edges. PL emission showed the defect-related radiative transitions within the band gap. Catalytic activity of MgO

nanoparticles was evaluated by studying the degradation of methane dye under UV radiation, achieving a 75% efficiency in 120 minutes.

(Guckan et al., 2021a) synthesized the Ce, Li doped MgO using the solid state reaction method, and analyzed structural and luminescence characteristics as a function of doping. From XRD patterns polycrystalline cubic phase was confirmed, and grains ranging from 70-200 nm were confirmed by SEM images. Photoluminescence and radioluminescence measurements conveyed the enhancement in emission with Ce doping, and Li ions improved the intensity of two bands around 580 nm and 620 nm which are characteristic emissions of Ce ions. The TL emission was studied after exposing the 10 Gy dose of β radiation, and five different peaks appeared after raising the temperature from room temperature to 400 ºC. Fading of prepared phosphors was observed after four weeks, indicating the stability of the materials. The activation energies ranging from 0.56 eV to 1.53 eV were calculated by different methods.

2.2 Undoped and Doped MgO-Y_2O_3

(J. Wang et al., 2010) examined the infrared transmittance behavior of MgO-Y_2O_3 nanocomposites synthesized by the sol-gel method. The obtained product was confirmed to have a dual phase of MgO-Y_2O_3. Obtained powders were calcinated at high temperature for 2 hours and compressed to convert into disks, followed by pressureless sintering and pressing. SEM analysis revealed the average domain size of 310 nm for both phases. The stability of dual-phase and fine-grain structure and minimum light scattering improved the optical and mechanical characteristics of nano-composites. The nano-composites exhibited the IR transmittance up to 80% in 3-7 μm wavelength and showed the Vickers hardness of 10.6 GPa.

(H. Sun et al., 2014) examined the densification of MgO-Y_2O_3 via microwave sintering and its effect on the optical characteristics for Infrared applications. Nano-composites were prepared using the sol-gel method. The microwave sintering is

compared with the conventional sintering method. Sintering kinetics revealed that while using the microwave sintering technique, the grain boundary diffusion dominated, but volume diffusion dominated in the case of conventional sintering. Activation energy of the conventional sintering method is higher than that of microwave sintering. However, the dense nanocomposites with a grain size of 300 nm, obtained after optimization of dual-step sintering and a Vickers hardness of 11.2 GPa, were achieved.

(Blair et al., 2017) examined the optical performance of Er-doped MgO-Y_2O_3 in the IR region for infrared laser applications. The nanocomposites were prepared by using the co-precipitation method, followed by calcination at 1200 ºC and sintering to convert into pellets for further characterization. Stable dual phase was confirmed by XRD, indicating the uniform doping of Er in Y_2O_3. Sem images revealed porosity in both grains, while the MgO grains were larger and Y_2O_3 remained as dispersed grains. Y_2O_3 grains were located at the boundaries of MgO grains, showing the segregation of both phases. From spectroscopic performance, it was found that 1.5 μm radiative transitions ($^4I_{13/2} \rightarrow {}^4I_{15/2}$) of Er closely matched the commercial Er-doped Y_2O_3 emission confirmed. Minimal quenching at 2% of Er ions was observed in doped nanocomposites with a lifetime of 8.4 ms. The optimized nanocomposite exhibited a balance between thermal conductivity and optical performance, which was critical for mid-IR laser applications.

(Ma et al., 2018a) investigated the optical, thermal, and mechanical performance of Er: MgO-Y_2O_3 ceramics for high-energy laser applications. The nanocomposites were prepared using glycine-nitrate techniques and further sintered at 1500 ºC. For structural analysis, XRD and TEM were used. XRD confirmed the cubic phase of Y_2O_3 and MgO with uniform doping of Er in the lattice of Y_2O_3. The decrease in lattice constant of Y_2O_3 confirmed the substitutional doping of the dopant. Furthermore, a particle size of 20 nm was calculated using TEM images, with well-dispersed Er: Y_2O_3 and MgO phases. From TGA analysis, weight loss of 17.8% was confirmed during calcination, attributed to the dehydration, while the

crystallization occurred at 278 ºC, consistent with an exothermic peak in DSC. From SEM images, dense and pore-free ceramics were confirmed with a grain size of 120 nm. This density increased with the doping from 4.2 to 4.4 g/cm^3. From UV-Vis-NIR spectroscopy, 80% transmittance was observed in the IR range, which was much higher than commercially available Er: Y_2O_3 ceramic. PL spectra exhibited the strong emission of Er at 1535 nm up to 5% doping, and quenching was observed afterwards. The positive grain cross-section above 0.5 inversion threshold indicated the suitability of the material for low-threshold lasing applications. The stability of Vickers hardness at 10 GPa in all the doped ceramics is attributed to the grain boundary strengthening. The thermal conductivity in all doped nanocomposites was two times higher than ER-doped Y_2O_3 due to the better heat dissipation provided by the MgO phase present in the host.

(Safronova et al., 2021b) synthesized the Ho-doped MgO-Y_2O_3 using the sol-gel method, followed by the hot-pressing sintering at various temperatures ranging from 1200-1450 ºC. A Binary phase without any impurity was confirmed by XRD peaks with slight shifting at higher doping and contraction in MgO lattice attributed to the formation of F centers due to the strain at boundaries. SEM and EDS confirmed the even dispersion of Ho, Y, and Mg, suggesting the successful doping incorporation in the Y_2O_3 lattice. Agglomeration was also observed at higher concentrations of dopants, affecting the transparency. From UV-Vis spectra, the highest transmittance of 85% was observed at 3 % of Ho ions, while afterward the transmittance decreased due to the scattering. The emission band observed around 2 μm showed the characteristic emission of Ho ions. The thermal conductivity decreased due to higher doping but remained higher than that of pure Ho: Y_2O_3 ceramics, attaining the value of 9.8 W/m.K at 15 mol%. The induction of the MgO phase improved the thermal behavior by heat dissipation provided by MgO.

(S. Chen et al., 2023b) prepared the MgO-Y_2O_3 nanocomposite doped with Eu ions by using vacuum sintering at 1300-1800 ºC. XRD patterns revealed a double phase of MgO and Y_2O_3, nullifying the impure phase of Eu in the lattices.

From SEM and EDS, the EU ions were found exclusively dispersed in the Y_2O_3 matrix. The encapsulation of MgO grains within the Y_2O_3 showed strong resistance to moisture-induced degradation. On UV excitation at a wavelength of 394 nm, strong red emission centered at 611 nm was observed, achieving the highest intensity at 15 mol% of Eu. The quantum yield was obtained at 80.3% for 15 mol% doping. The time decay study revealed a maximum of 983 μs, and the thermal activation energy of 0.163 eV remained stable across all the compositions. The thermal conductivity measured in nanocomposites was 17.5 W/m·K, whereas that of pure Eu-doped Y_2O_3 was 5.9 W/m·K, significantly lower than the former. The better performance of nanocomposites makes this material ideal for high-power solid-state light and display applications.

The reviewed literature indicates that while there are numerous reports on pure MgO and pure Y_2O_3 nanomaterials, only limited studies have thoroughly investigated the luminescence mechanism within the MgO-Y_2O_3 nanocomposite. In pure MgO, where doping saturates at a very low concentration, it causes a hindrance in luminescence performance due to the smaller size of Mg ions (Oliveira et al., 2019b). On the other side where Y_2O_3 is one of the sesquioxide materials that shows bixbyite cubic structure. As reported in the literature study, the thermal conductivity of Y_2O_3 decreases, and this thermal quenching indeed affects the stability of color quality and lowers the luminescence efficiency, specifically, when used in a field of high-power lighting. An efficient heat dissipation rate in the host is required to circumvent this thermal quenching behavior. To overcome this drawback from such a host material, a contemporary strategy is the introduction of a second stable phase with excellent thermal conductivity, making the phosphor effective and thermally robust for enhancing optical performance. MgO-Y_2O_3 is a new class of composite that has been reported for improved thermal conductivity, which helps to improve the performance of Y_2O_3. MgO, which has been introduced as a second phase with Y_2O_3, is a stable, wide-bandgap material with superior thermal conductivity at room temperature. Also, it does not make a mixed phase with the Y_2O_3 because of its high eutectic point. In literature, doping of Er^{3+}, Eu^{3+},

and Ho^{3+} has been investigated in MgO-Y_2O_3 nanophosphors for different applications (Balabanov et al., 2025; Ma et al., 2018a). From previous studies, it was observed that, with the addition of a secondary phase in pure Y_2O_3, not only were the photoluminescence and absorption properties improved, but also the beam quality, mechanical, and thermal properties were enhanced. Although there have been reports on enhanced NIR emissions of MgO-Y_2O_3 ceramic composition investigations on the upconversion luminescence are lacking, specifically doped with upconverting ion pairs such as Er, Yb, Ho, etc.

Concluding from these research gaps in the literature, the present study focused on exploring the tuning of luminescence properties of MgO-Y_2O_3 nanocomposites doped with selective rare earth ions. This study aims to bridge that gap through a systematic optimization of the synthesis parameters and evaluating the effects of Er, Yb, Ho, and Sm doping on the structural features and their impact on the optical performance of the MgO-Y_2O_3 system. This research focuses on both the downconversion and upconversion luminescence, examining the emission efficiency, energy transfer dynamics within the composite matrix. Additionally, with the detailed analysis of fundamental optical studies, the practical potential for high-security applications is also explored. The detailed findings and insights of the investigation are discussed extensively in the following chapters, offering a valuable contribution to the understanding of scientific and practical applications.

2.3 Aims and objectives

- Synthesis of pure and doped MgO, MgO-Y_2O_3 nanophosphors by solution combustion method
- Elemental and Structural Characterization of the nanophosphors using XPS, XRD, TEM, and XAS.
- Optical characterization of nanophosphors using various spectroscopic techniques.

- Analysis of the obtained results for solid-state light, anti-counterfeiting, and security ink applications.

.

CHAPTER 3

EXPERIMENTAL DETAILS

EXPERIMENTAL DETAILS

3.1 Overview

In recent years, nanomaterials have attracted researchers due to their excellent intrinsic properties as compared to bulk materials (Chinthala et al., 2021). The enhancement in structural and associated domains of nanomaterials is attributed to the quantum confinement effects and high surface-to-volume ratio that exist at the nanoscale. These features cause major alterations in electronic band structures, playing a critical role in the overall performance of materials (Brumfiel, 2003; Hulla et al., 2015). At this scale, various other factors are also crucial in modifying the properties for a specific application area. The synthesis route and incorporation of dopants are crucial factors to meet the particular requirements. Experimental research depends on the carefully chosen synthesis route for the preparation of the target material, which is then examined by using suitable characterization techniques (Mourdikoudis et al., 2018; Rizvi et al., 2022). In the present chapter, the synthesis method and various characterization techniques employed for this research work are discussed in detail.

3.2 Synthesis

3.2.1 Solution Combustion Synthesis

MgO, MgO-Y_2O_3 nanophosphors have been synthesized by using the solution combustion method due to its advantages over other techniques such as the sol-gel method (Livage et al., 1998), solid state reaction method (A. Kumar et al., 2022), hydrothermal method (Gan et al., 2020), etc. This method is environment-friendly, low-cost, and the heat produced by precursors is greater than the heat required for chemical reaction, making the reaction self-propagating, further making it a quick reaction. Due to its self-propagating nature, a low-temperature furnace is sufficient for reaction. Its cost-effectiveness, non-toxic, stable phase formation of products, less equipment requirement, and low temperature and time

reaction make it more advantageous over other methods (Kiminami, 2001; Park & Lee, n.d.; A. K. Tyagi, 2007). This is basically a single-step rapid technique in which oxidizers which are particularly nitrates of salts, are mixed with fuel such as glycine, urea, etc., in a stoichiometric ratio and heated to particular temperature causes the formation of gel and combustion (Amit Sharma, 2015; Khaliullin et al., 2016). Upon heating, an exothermic redox reaction occurred, and a large amount of H_2O, NO_2, and CO_2 was released during the combustion process, leading to the formation of fluffy, foamy crystalline powder.

Here, in the present work, pure MgO and MgO-Y_2O_3 were synthesized by using MgO $(NO_3)_2.6H_2O$ and $Y(NO_3)_3.6H_2O$ as the oxidizers, and urea $CO(NH_2)_2$ as the fuel. The balanced reaction for the synthesis of MgO and MgO-Y_2O_3 is given below:

$$6Mg(NO_3)_3.6H_2O + 10CO(NH_2)_2 \rightarrow 6MgO + 10CO_2 + 56H_2 + 6N_2 \qquad \text{Eq. 3.1}$$

$$3[Mg(NO_3)_2.6H_2O + 2Y(NO_3)_3.6H_2O] + 20CO(NH_2)_2 \rightarrow 3(MgO - Y_2O_3) + 40H_2O + 32N_2 + 20CO_2 \qquad \text{Eq. 3.2}$$

According to the above chemical reaction, all precursors were taken in a stoichiometric ratio, and oxidizers were dissolved in 20 mL of de-ionised water for 20 minutes, and then fuel was added to the mixture and stirred for half an hour to make a homogeneous solution. After that, the solution was placed in a furnace and the temperature was raised to 550 ºC from room temperature. Initially the mixture was transparent. Upon heating, the bubbling of the solution started, and water began to evaporate, and the solution went into rigorous combustion with the evolution of CO_2, N_2 gases. As the reaction progressed, the mixture expanded and developed a frothy texture, which burst into flames. The whole reaction, completed in five to six minutes with the flames visible for around three minutes, leaving the product fluffy and foamy. After cooling down of residue to room temperature, it was crushed into powder by using a pestle and mortar for 20 minutes. Further, for the

removal of impurities and to enhance the crystallization of the material, it was annealed to 800 ºC for 3 hours. A similar procedure of synthesis was followed for the synthesis of singly doped MgO, with Bi, Sm^{3+}, Ce^{3+}, Li, and doubly doped MgO with Sm^{3+}, Li,and for single and double doped MgO-Y_2O_3 with Ho^{3+}, Er^{3+}, Yb^{3+}. In similar way, all the samples were annealed for 800 ºC for 3 hours before further characterization. Fig 3.1 illustrates the process of synthesis through a snapshot taken during the process of synthesis of MgO, MgO-Y_2O_3 samples.

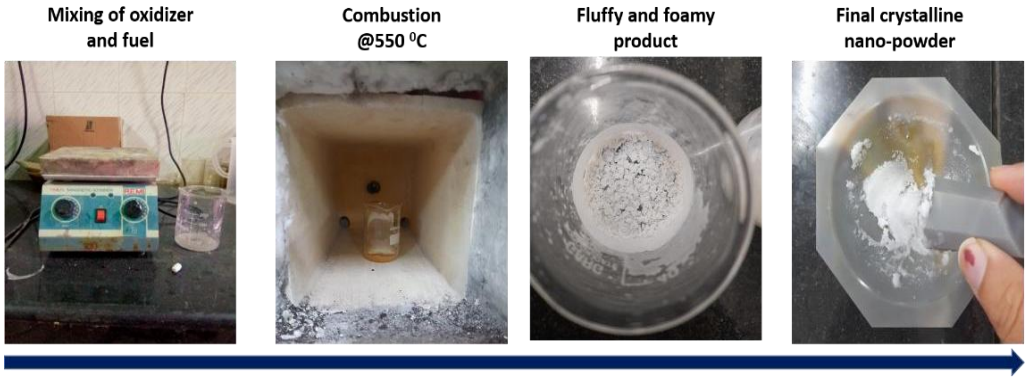

Fig 3.1: Synthesis of samples by solution combustion method

3.3 Characterization techniques

Advancements in the manufacturing of nanomaterials have greatly enhanced their role in different fields of applications. Understanding the chemical composition, size-dependent behavior, charge distribution, and morphological characteristics is crucial for the use of nanomaterials. A thorough and methodical assessment of synthesized nanomaterials is essential to grasp their structural and associated properties utilizing a range of characterization techniques. Various techniques are crucial in the validation of the synthesis of the required phase, examining the structural, morphological properties, and investigating optical, thermal, and elemental characteristics of materials (Leng, 2013; Robertson et al., 2011). In the present study, various characterization techniques have been utilized to analyze the structural and luminescence behavior of MgO-Y_2O_3 nanophosphors. For structural studies, X-ray diffraction (XRD) and refinement of structural

parameters by using Rietveld refinement via FULLPROF software were used, while for analysis of morphological analysis, transmission electron microscopy (TEM), X-ray absorption spectroscopy (XAS) were used. For optical characteristics, UV-Visible-NIR spectroscopy (UV-Vis), photoluminescence spectroscopy (PL), thermoluminescence (TL), temperature-dependent photoluminescence spectroscopy were used.

3.3.1 X-Ray Diffraction

X-rays typically ranging between gamma rays and UV rays having energy between 10 pm and 10 nm was discovered in 1895 by Wilhelm Rontgen. The ability of X-rays for investigating the crystal structure was discovered by Max Von Laue, who illustrated that long-ordered atoms of a crystal could diffract X-rays, confirming the wavelike nature of X-rays (Leng, 2013; Robertson et al., 2011).

This discovery laid the foundation of X-ray crystallography. Later, William Henry Bragg and his son William Lawrence Bragg formulated Bragg's law and used it as a scientific tool in the determination of the atomic structure of crystals (L. Bragg, 1968; W. L. Bragg, 1926). This pioneering work earned them the 1915 Nobel Prize in physics. Bragg's law explains the constructive interference of monochromatic X-rays diffracted by a crystalline sample, where the diffracted rays satisfy Bragg's law

$$n\lambda = 2d\sin\theta \qquad \text{Eq. 3.3}$$

Here, λ is the wavelength of the incident X-ray beam, d is the spacing between atomic planes of the crystals, n is an integer representing the order in which the diffraction occurs, and θ is the angle of incidence. When the monochromatic X-ray beam strikes the crystalline material, the atoms behave like a three-dimensional diffraction grating, and X-rays are scattered in all directions. Bragg's law states that the X-ray diffraction peaks will be observed at specific angles when the diffracted

beams from different planes of crystals are in phase and interfere constructively (Stanjek & Häusler, 2004). The Fig 3.2 illustrates the X-ray diffraction by the different planes of the crystal. In an X-ray diffraction experiment, for the generation of X-rays, Cu (1.5406 Å), Mo (0.7093 Å), and Cr (2.2289 Å) are most commonly used materials (Bhattacharya & Acharya, 2020; Ermrich & Opper, 2011; X-Ray Diffraction - an Overview | ScienceDirect Topics, n.d.). The experimental setup includes an X-ray source, a sample holder, and a detector that captures the diffracted beam by the crystal planes. In powder X-ray diffraction set-up, the most commonly employed configuration has a stationary sample holder, with a rotating source and detector. A collimated X-ray beam is incident on the powder sample, in which every particle consists of randomly oriented crystals.

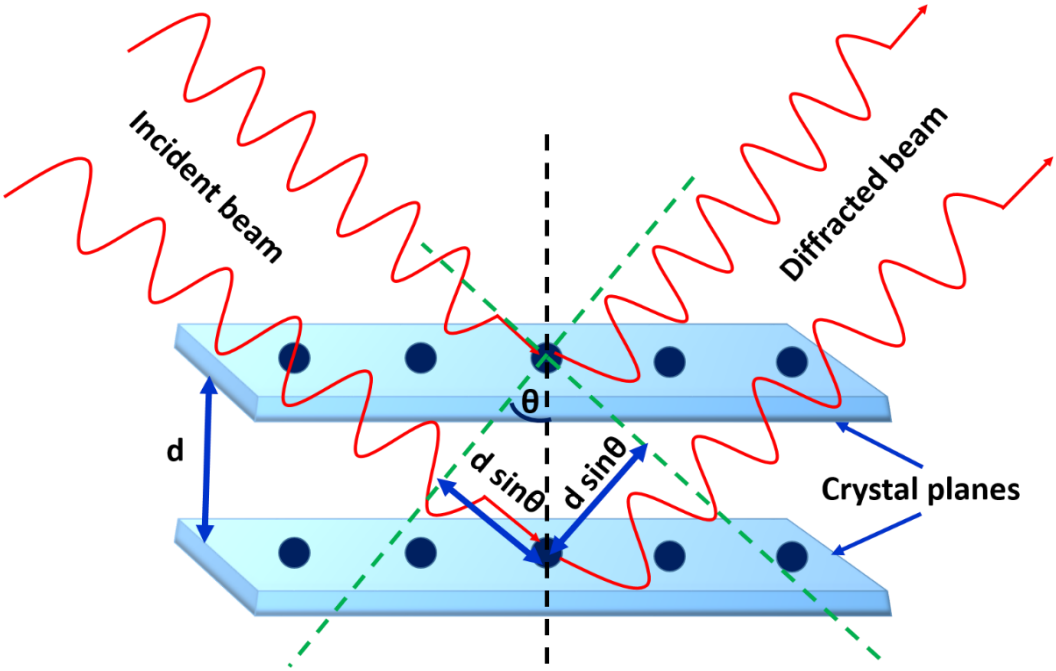

Fig 3.2: Diffraction of X-rays from crystal planes

The X-ray source rotates at different angles of incidence, and the detector moves simultaneously to attain the 2θ angle with the incident beam. The detector records the intensity at 2θ angle, producing the diffraction pattern. The obtained pattern have the peaks corresponding to different crystallographic planes, which is further

used to identify the phase and determine structural parameters such as crystallite size of samples by using Scherer formula (Patterson, 1939);

$$d = \frac{k*\lambda}{\beta*\cos\theta} \qquad \text{Eq. 3.4}$$

where d denotes the crystallite size, k is constant (0.9), β is average FWHM of obtained XRD peaks, λ is the incident X-ray wavelength, θ is the diffraction angle.

.

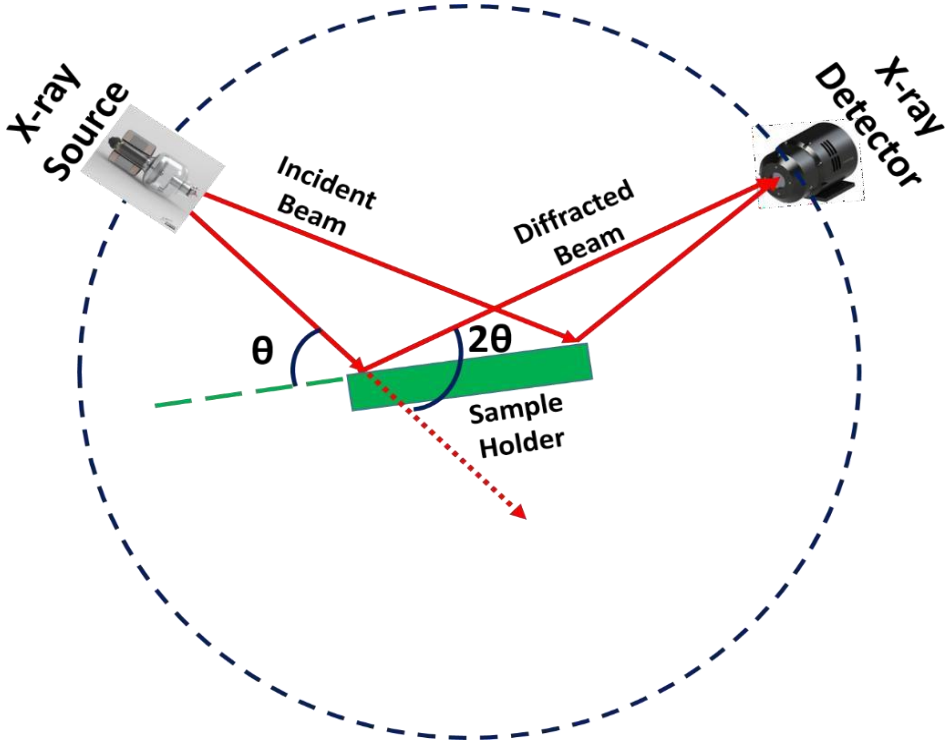

Fig 3.3: Set-up for X-ray diffraction

Fig 3.3 shows the experimental setup of the X-ray diffraction. In the present work, Cu-Kα was used as the X-ray source, and diffraction peaks were recorded at 2θ

angle ranging from 20-80º. Obtained peaks were compared with the JCPDS card to analyze the phase of the synthesized powder samples.

3.3.2 Transmission Electron Microscopy

Transmission electron microscopy (TEM) is a highly sophisticated imaging technique that has revolutionized the analysis of materials at the nanoscale. With the capability to discern features at the atomic scale, TEM is crucial in the realm of nanotechnology and a wide array of scientific disciplines. In material science, TEM is indispensable for the study of crystal defect formation, dislocation of atoms in the lattice, and many other characteristics at the atomic level (Egerton, 2016; Thust, 2009). In TEM, direct images are obtained by the reciprocal lattice. Due to the wave-like nature of electrons, they undergo diffraction by the crystals, enabling the study of their internal arrangements and defects at the atomic scale. TEM operates on the principle that the sample must be thin such that the electron beam can transmit through it rather than be absorbed or scattered away. The sample thickness must be less than 150 nm to minimize the interaction between electrons and sample atoms, specifically elastic and inelastic scattering, which further reduces the clarity of images and information. Fig 3.4 illustrates the typical setup of components used in imaging with TEM. It mainly consists of three components: electron generation material, electron beam control and fluorescent screen to detect electrons(Kannan, 2018). The source material used in the electron gun depends on the type of emission system used. Generally three types of electron guns depending on the required brightness is used to generating the electron beam. After the generation of electrons, the beam is passed through various lenses, including electromagnetic lenses, objective lenses, to control the area and intensity. After interaction of the beam with the specimen, the transmitted beam is directed through projector lenses and projected on a fluorescent screen, and it produces photons, and an image is collected by the camera. Additionally, the TEM technique is used to obtain the selected area electron diffraction (SAED) patterns of the prepared samples. In SAED mode, a

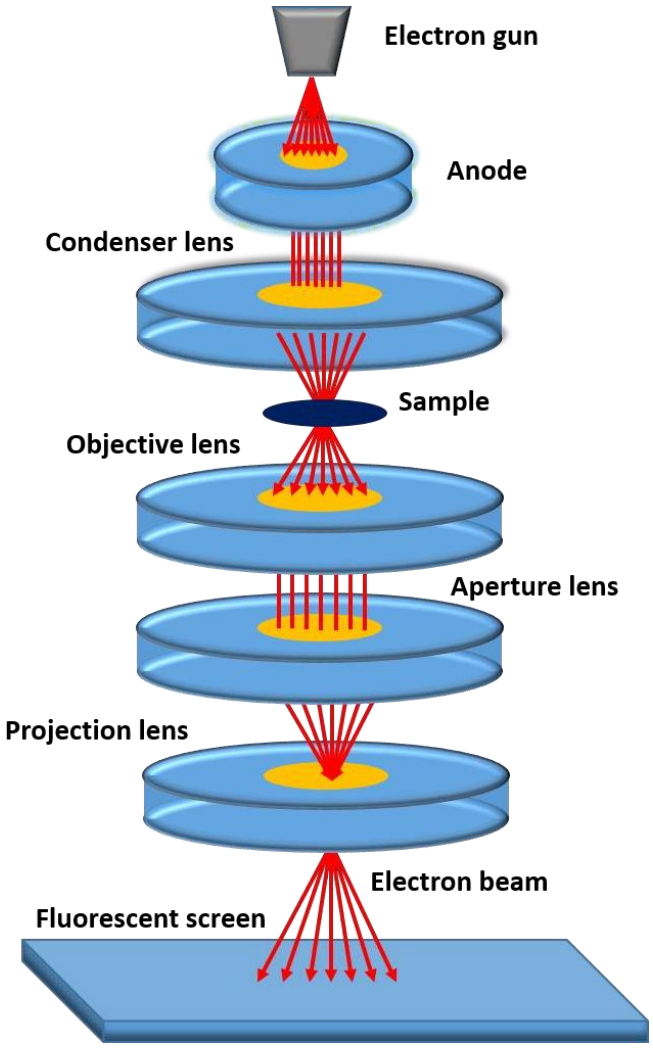

Fig 3.4: Principle of transmission electron microscopy (TEM)

specific part of the sample is chosen where the electron beam interacts and undergoes elastic scattering and formation of the diffraction patterns. The resulting diffraction pattern is a two-dimensional projection of the reciprocal lattice consisting of ring patterns for polycrystalline samples (Fultz & Howe, 2023).

3.3.3 X-ray Absorption Spectroscopy

X-ray absorption spectroscopy is a scientific tool employed to investigate the changes in local environment of a single element because of its inherent capability of measuring electronic structure properties that single atom within a complicated matrix. This technique is bulk and surface sensitive and provides information, such as symmetry around atoms, valence state of elements present within the compound, interatomic interactions, defect formations, etc (Natoli et al., 2003; Yano & Yachandra, 2009). It works on the principle that the quantity of absorption of X-rays depends on the energy of X-ray radiation. The X-ray coefficient measures the quantity of absorbed X-ray radiation (de Groot, 2001; Penner-Hahn, 1999; Yano & Yachandra, 2009). The spectrum of XAS is divided into two regions. The first one is near-edge energy X-ray absorption spectra XANES, which covers the energy range of 10-50 eV and the pre-edge region where the energy is less than the absorption edge. The other is extended X-ray absorption fine structure EXAFS, where the energy range goes up to 1000 eV. Here in the

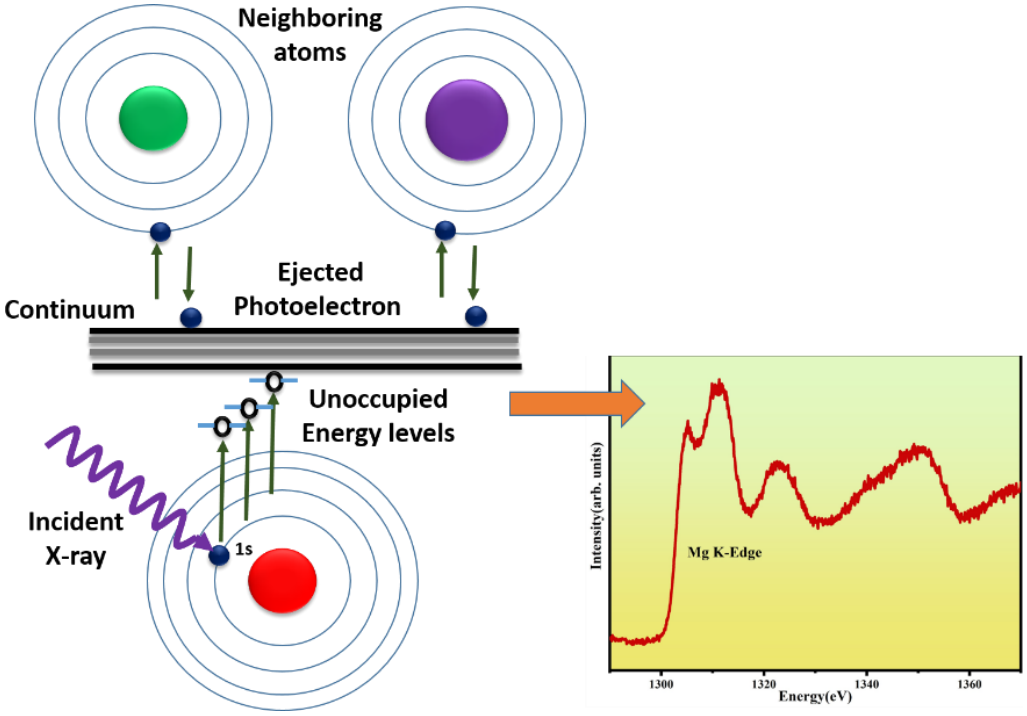

Fig 3.5: X-Ray absorption spectroscopy- depiction of local interactions

present study, we focused on XANES spectra of all the samples. XANES spectra are sensitive to the coordination geometry of native as all as the dopant, oxidation state of cations present in the compound (Behrens, 1992; Henderson et al., 2014; Natoli et al., 2003; Parsons et al., 2002). XANES spectra is also strongly affected by the scattering effects of the neighbor atoms in lattice, further depending on the crystal structure, defects and oxidation state of ions present within the lattice. As shown in Fig 3.5, when the X-ray photon absorbed matches the binding energy of the core shell electron of the respective element, then a core electron is excited to the unoccupied states (known as the photoelectric effect) (Iglesias-Juez et al., 2022; Yano & Yachandra, 2009). At this transition, the absorption coefficient increases abruptly, and a step has been observed in the spectrum. The absorption edge is associated with the core-shell electron energy, unique to each element, thereby allowing for element-specific XANES analysis. Different nomenclature of edges corresponds to the transitions from occur from respective edges. In spectra before this absorption edge, the small peaks are observed named as the pre-edge region, which arises due to the transition of core electron to the one of the bound states, i.e lower energy of empty orbitals or the new degenerated states or mixed states created due to interaction of different atoms present in compound. The intensity and energy of peaks are highly dependent on the oxidation state and symmetry of the ions present in the compound, specifically on the covalency and empty orbitals. The oscillations slightly after the edge are also observed in XANES, indicating the density of unoccupied states and variation of these states of the element in the matrix (Achkar et al., 2011; Asakura et al., 2019; Nakai et al., 1987).

3.3.4 UV-Vis-NIR Absorption Spectroscopy

Light interacts with material differently at the nanoscale depending on the size of the nanomaterials. The various methodologies are usually based on the absorption, scattering, or emission of light, which provides information about the band structure properties of nanomaterials. UV-Vis absorption spectroscopy is a

non-destructive technique and is widely applied to assess the electronic absorption spectrum, providing insights into the optical behavior of different solid-state materials (Khalid et al., 2024; Mäntele & Deniz, 2017; Ricciardi, 2021; Shahab et al., 2017). This technique helps in understanding the defects, molecular orbitals, charge transfer, and information about the band gap and structure alteration with changing the different parameters during synthesis, doping, etc. The principle of absorption spectroscopy is based on Beer's law (Mäntele & Deniz, 2017), when the light propagate through any medium, them some part of light is absorbed by the medium and is defined in terms of the absorption coefficient: $I(x) = I_0 e^{\alpha x}$; where I(x) is the intensity in direction x when moving in medium. I_0 is the intensity of light at the surface, and α is the absorption coefficient, which depends on the wavelength. The spectrum shows absorption as a function of wavelength which provides the information of electronic characteristics of the specimen. The Fig 3.6 shows the schematic set-up of a UV-Vis spectrometer, where the deuterium halogen lamp is used as the source of light, and a CCD detector, the sample and reference are placed between source and detector. The reference sample used in the present work is Teflon, which reflects 99.99% of light. When the sample absorbed the radiation at a particular wavelength, the intensity of transmitted radiation was reduced and plotted in the graph as a function of wavelength.

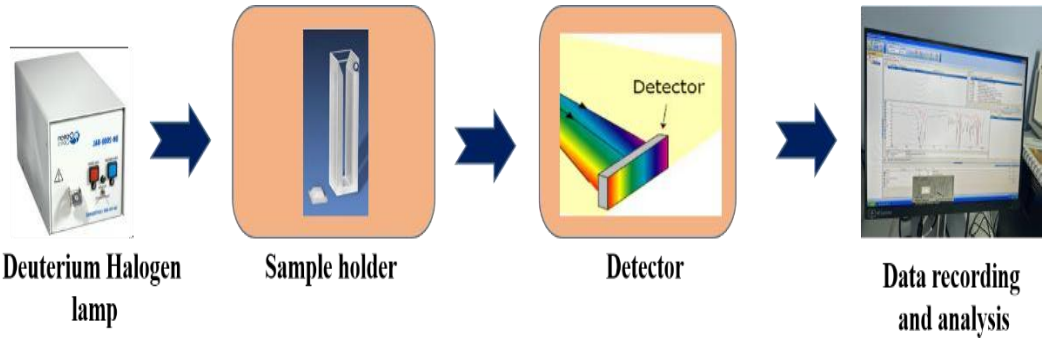

Fig 3.6: UV-Vis spectroscopy set-up

3.3.5 Photoluminescence Spectroscopy

When an atom absorb energy from any external source other than heating and get excited to higher state, it has tendency to get stabilized by releasing the excess energy through various transitions. When this released energy lies in visible region, then it is known as luminescence and if the excitation source is light then the process is defined as photoluminescence. Photoluminescence is another non-destructive spectroscopic technique in which the spontaneous emission of light by the de-excitation of electrons from higher energy levels is measured (Aoki, 2012; Fox, 1997; Schmidt et al., 1992; Shahab et al., 2017). It is one of the essential characterizations that helps in understanding the nature of intrinsic defect states, band-to-band transitions, and the mechanism of electronic transitions between the defects present within the band gap of nanomaterials (Abdi-Jalebi et al., 2020; Aoki, 2012). The process of the excitation and decaying path of electrons through different routes was explained by the polish physicist named Alexander Jablonski in 1930, famously known as the Jablonski energy level diagram(Jablonski, 1933). This diagram widely used in spectroscopy and photochemistry, in which it helps to understand the mechanism of absorption and emission of light by different molecules or compounds specifically fluorescence and phosphorescence mechanism. Furthermore, this graphical representation led to foundation of time resolve spectroscopy, fluorescence spectroscopy, and molecular sensor development. Fig 3.7 depicts the Jablonski diagram showing graphical representation of various routes of excitation from ground state and radiative and non- radiative de-excitation from higher singlet and triplet excited states. After absorbing energy from an external source, the electrons in the singlet ground state S_g is excited to the higher singlet states S_{e1} or S_{e2}. While de-excitation from higher levels, there are multiple possible radiative and non-radiative transitions. The electron can relax non-radiatively via vibrational relaxation (typical lifetime of 10^{-12} to 10^{-10} sec), or internal conversion occurs between the vibrational levels of higher excited state (S_{e2}) and lower excited states S_{e1} and then radiatively decay to the ground state known as fluorescence (typical lifetime $\leq 10^{-8}$ sec). Apart from it,

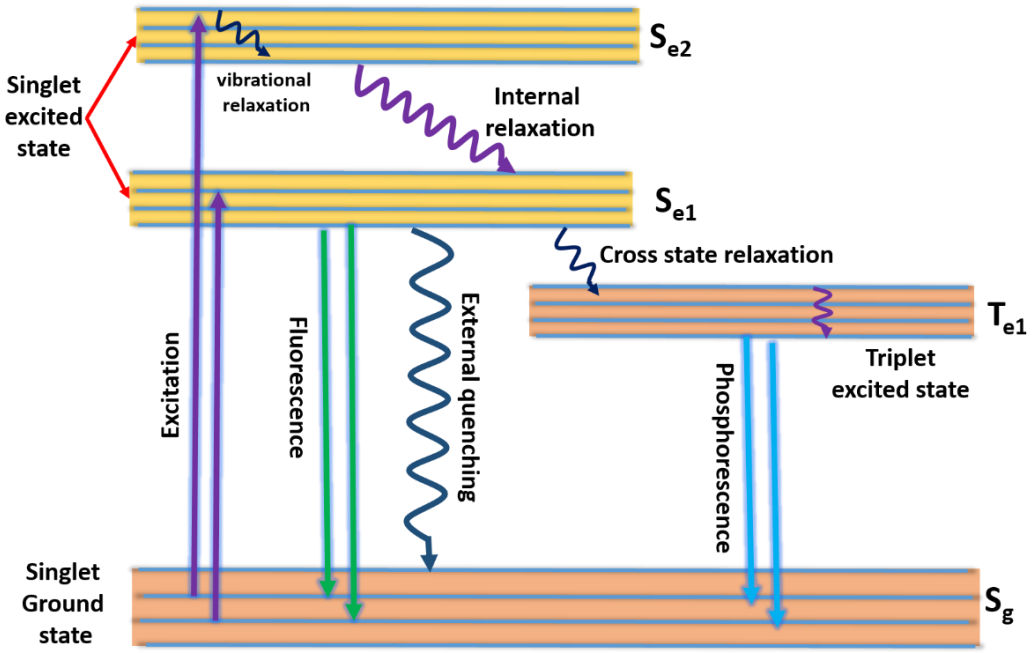

Fig 3.7: Jablonski diagram showing different absorption and emission pathways

the other possible path is intersystem conversion. This forbidden transition occurs between the excited singlet state (S_{e1} or S_{e2}) to the triplet state T_{e1} overlapping each other and then radiatively decaying to the ground state causes the delayed emission typically of 10^{-3} sec to 10^{3} sec time. This delayed emission is known as phosphorescence (Aoki, 2012; Chopra et al., 2022; Gilliland, 1997; Lakowicz, 1999; B. Yan, 2022). Generally, Stoke's shift in emitted wavelength is observed as the radiative transitions accompanied by the non-radiative transitions. However, there is a non-linear process of emission in which two or more low-energy photons are absorbed by the intermediate states and combine to emit a high-energy photon known as the upconversion luminescence (J. Chen & Zhao, 2012). This kind of emission is also known as the anti-Stokes shift. Both the downconversion and upconversion process is shown in Fig 3.8(a, b). The non-linear process can occur in various ways. In Fig 3.9(a) second harmonic generation is shown where the incident photons must be coherent and the emitted photon has double frequency of the absorbed photon. Another way of the non-linear process of emitting high-

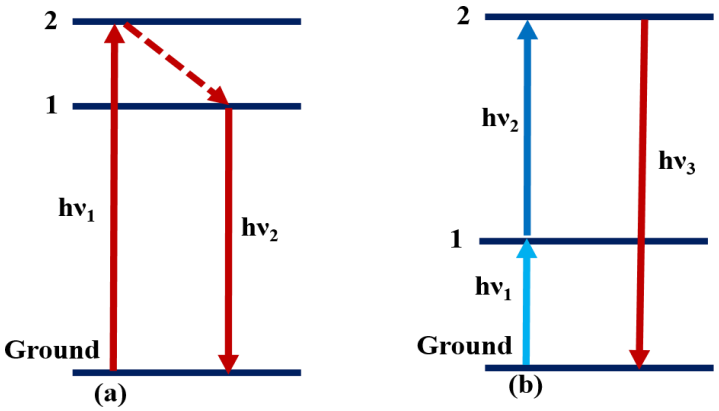

Fig 3.8: (a) Downconversion and (b) upconversion process

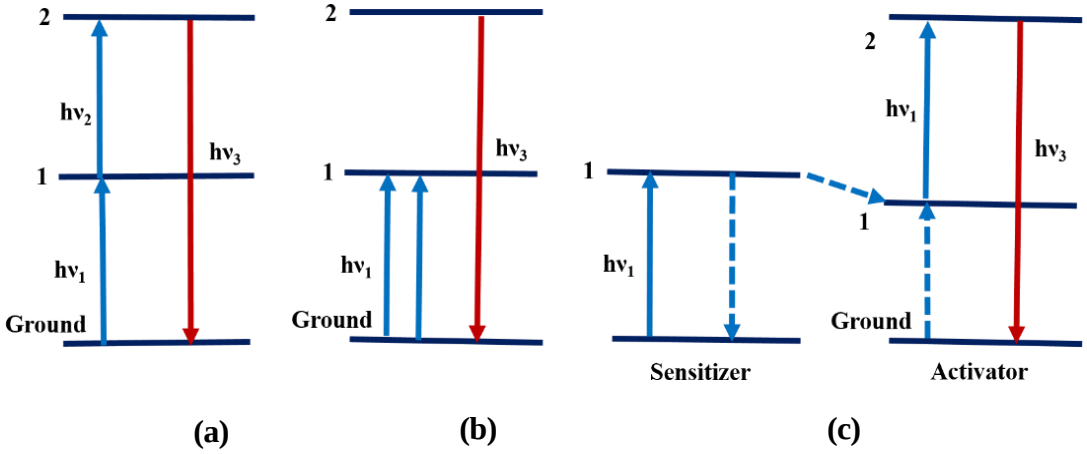

Fig 3.9: Different non-linear processes (a) SHG (b) STPA (c) upconversion mechanism

energy photons by absorbing two low-energy photons simultaneously is called simultaneous two-photon absorption (STPA) (Fig 3.9(b)) (Dubey & Chandra, 2022; Nadort et al., 2016). The third process is upconversion, in which intermediate levels are present where the low-energy photon is accommodated before absorbing

another photon and being excited to a higher level. This process is more efficient than STPA because of the presence of intermediate energy levels. The upconversion process include different type of absorption such as excited state absorption in which single activator ion exist and its energy levels has ladder like structure and has sufficient absorption cross-section in the region which enable the electron from ground state to absorb the photon and excited to successive higher energy levels before decaying back to the ground level (Dubey & Chandra, 2022; Patel et al., 2022; Zhou et al., 2015). When there is a sensitizer ion present along with the activator ions, the process of exciting an electron to higher states is carried out by energy transfer from the sensitizer ion to the activator after absorbing the input photon and excite it to the higher excited states from where it decays back to ground state after emitting the high energy photon (Etchart & Cheetham, 2007). In Energy transfer upconversion (ETU) process, the concentration and distance etween sensitizers and activator ion govern the emission (Collins, n.d.; Etchart & Cheetham, 2007). All different non-linear processes are shown in Fig 3.9(a-c). In the present work, along with the downconversion, upconversion by using NIR radiation has also been studied. In a typical PL spectrometer, there is a light source (Xenon lamp) with an excitation monochromator, and a grating on the source side is placed, and the sample holder is placed at a 30º angle with respect to the excitation assembly to avoid the reflection of light (Lakowicz, 2006; M., 1980). On the other side of the sample holder PMT detector with grating and mirrors is placed to receive the signal, which is further connected to the computer system. High-pass filters were placed on the detector side to block the unwanted signal from the excitation assembly. The data recorded is the luminescence intensity as a function of wavelength. For excitation spectra collection, the monochromator on the detector side was used to fix the emission wavelength at which the excitation graph was plotted (Marzouk et al., 2020). In the case of upconversion luminescence, a diode laser of fixed wavelength of 980 nm with variable input power from 0.5 mW to 2.5 mW has been used to excite the sample, which is further attached to the detector and computer.

3.3.6 Thermoluminescence Study

Thermoluminescence (TL) is a tool to understand the nature of intrinsic defects present within the lattice and modifications in them due to changing parameters such as the addition of dopants, annealing, etc. It is a process in which heating of material causes the emission, but the initial source of energy is not the temperature (Bos, 2017; Christy & Mayhugh, 1972; Marczewska et al., 2021). The material is exposed to radiation or charged particles initially, which is also known as thermally stimulated luminescence. Thermoluminescence is widely used in the application of dosimetry, geology for age information, identifying minerals, forensic sciences, and mineralogy etc (Abdurabu Thabit et al., 2024; Nieto, 2018). In this technique, first the sample is heated to a certain temperature to remove the defects generated due to the environment, and then it is exposed to radiation such as UV-radiation, γ-rays, and other ionizing radiations. Due to irradiation, the defect states were created, and electron-hole pairs were generated within the bandgap (Salah et al., 2023; Tamrakar et al., 2014). Electrons trap states often lying near the conduction band (CB) or electrons move in CB, while the hole trap centers are created near the valence band (VB) or lie in VB. When the temperature is raised, either of the charge carriers (electron or hole) from the traps recombines with the other, which behaves as the recombination centers and emits a photon (R. Chen et al., 2018; Vedda et al., 2009). When the charge carriers are thermally released, the probability of release from the trap per unit time (p) is given by $p = s$. Here, s is the frequency of attempt to release, E is the activation energy, k is the Boltzmann constant, and T is the temperature. The TL peak intensity is plotted as a function of temperature. The either of the charge carriers (electron or hole) from the traps recombines with the other, which behaves as the recombination centers and emits a photon (R. Chen et al., 2018; Vedda et al., 2009). The radiative relaxation process of charge carriers by different recombination paths is shown in Fig 3.10. When the charge carriers are thermally released, the probability of release from its state when the temperature is raised, trap per unit time (p) is given by $p = s$. Here, s is the frequency of attempt to release, E is the activation energy, k is the Boltzmann

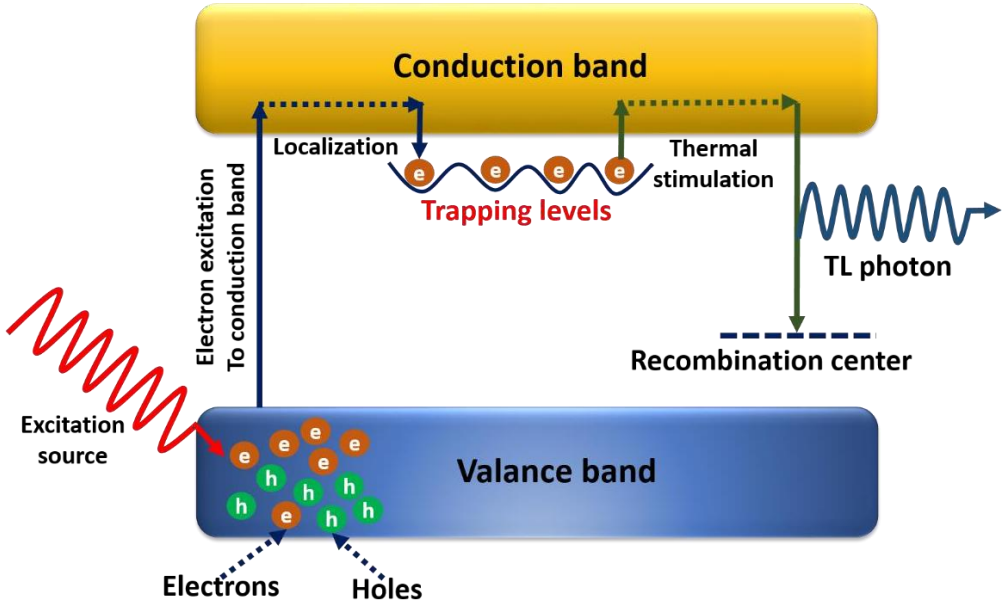

Fig 3.10: Schematic of Thermoluminescence process

constant, and T is the temperature. The TL peak intensity is plotted as a function of temperature. The shape of TL glow curves depends on the nature of trapping and retrapping behavior of charge carriers in the material. There are various approaches to analyze the nature of glow curves and their dependence on different kinetic parameters. The first and simplest model was proposed by Randel and Wilkins, considered the first-order kinetic, where the number of trapped electrons is proportional to the recombination centers, nullifying the retrapping behaviors (Uzun, 2021). The other model was given by Garlick and Gibson, in which the probability of retrapping is proportional to the recombination and was named as second-order kinetics (Bos, 2001; Meno et al., 2012; Prakash, 1993). After these two models, the general order kinetics model was given by May & Partridge (Kitis et al., 2025; Sunta et al., 1997; Vejnović et al., 1998), which came out most suitable model for practical problems. In the present work, experimentally obtained glow curves were further simulated by using a theoretical model by using TLANAL software to analyze the behavior of trapping and retrapping of charge carriers by using kinetics parameters (Kitis et al., 2008; Meno et al., 2012).

CHAPTER 4

STRUCTURAL, MORPHOLOGICAL, AND LUMINESCENCE STUDIES OF PURE MgO AND Bi^{3+}, Li^{+} DOPED MgO NANOPHOSPHORS

STRUCTURAL, MORPHOLOGICAL, AND LUMINESCENCE STUDIES OF PURE MgO AND Bi^{3+}, Li^{+} DOPED MgO NANOPHOSPHORS

4.1 Introduction

Many oxide materials exhibit luminescent characteristics and are being investigated for various applications such as solid-state light, radiation dosimetry, and pharmaceuticals (Guckan et al., 2021b). Among the other oxides, MgO stands out as a promising member of the family, displaying luminescence and boasting an abundance of commercial applications in the fields such as liquid crystal displays, electronics, pharmaceuticals, and ceramics. (Guckan et al., 2021b)(Devaraja, Avadhani, Prashantha, Nagabhushana, Sharma, Nagabhushana, Nagaswarupa, et al., 2014)(W. Wang et al., 2009). This inorganic metal oxide is an insulator with a band gap of 7.8 eV and a face-centred cubic (FCC) crystal structure (space group *Fm-3m*) in which oxygen occupies corners and magnesium occupies octahedral sites in the lattice. MgO exhibits luminescence properties due to the presence of oxygen and magnesium-related defects (vacancies and/or interstitials) namely, F centers (F, F^{+}, F^{2+}) and V centres (V, V^{-}, V^{2-}) (Choudhury et al., 2014). The energy of these defect states lies in the band gap of MgO. These F and/or V centres show luminescence after being excited by external energy sources. Besides the native defects in MgO, the foreign element doping has also been reported for tailoring the optical, magnetic, and microstructural properties (Orante-Barrón et al., 2011). In the present work, we have extended research to investigate the native defects of MgO and the correlation between Bi^{3+} and Li ions concentration and luminescence properties of MgO nanocrystals by applying a method which offers a high yield of nanocrystals synthesis and cost-effectiveness. This study explores the effect of non rareearth ions Bi^{3+} and Li^{+} ions doping at the sites of Mg^{2+} ions in MgO lattice and its consequences on the lattice distortion. Charge and ionic radii imbalance can offer intriguing defect states of oxygen and/or magnesium in the MgO host which, in turn, may facilitate diversifying and obscured luminescence properties.

Moreover, by analyzing the distribution of traps, it is also possible to comprehend the function of Li^{+} and Bi^{3+} ions in the thermoluminescence (TL) mechanism of magnesium oxide (MgO). For application purposes, the colorimetric parameters and luminous efficacy of prepared phosphors need to be explored.

4.2 Experimental details

Synthesis and Characterization

Pure, Lithium and Bismuth-doped MgO nanocrystals were prepared by solution combustion methods using magnesium nitrate hexahydrate $Mg(NO_3)_2.6H_2O$ (Merck, 99%), bismuth nitrate pentahydrate ($Bi(NO_3)_2.5H_2O$) (Merck, 99%) and Lithium nitrate $Li(NO)_3$ as an oxidizer, and urea ($CO(NH_2)_2$) (CDH, 99%) as fuel. The sample thus prepared was annealed at 1173 K for 3 hours. The samples with x = 0.00 mol%, 0.01 mol%, 0.05 mol%, 0.1 mol%, 0.3 mol%, 0.5 mol % are named as: B0, B1, B2, B3, B4 and B5, respectively.

X-ray diffraction (XRD) measurement were performed using Bruker-D8 Advance EcoPro diffractometer, radiated with Cu K_α radiation (λ=1.54056 Å). Transmission electron microscope (TEM) images are studied with the JOEL-2100 instrument, which operates at a voltage of 200 kV. The X-ray absorption near edge spectroscopy (XANES) spectra at O K- edge and Mg K-edge were collected in total electron yield mode at the soft X-ray beam line (10D XAS KIST-PAL) and Bi L_3-edge XANES data was collected at 1D X-ray scattering beam line of Pohang Accelerator Laboratory, South Korea. UV-visible absorption spectroscopy measurements were performed in diffuse reflectance mode using RIMS UV/Vis spectrometer at room temperature. Photoluminescence experiments are carried out with Fluromax+ spectrometer using a Xenon lamp. Samples were pre-annealed at 723 K for an hour for TL measurements. Subsequently, the samples were gamma irradiated at the dose of 500 Gy utilising a ^{60}Co source in gamma chamber 1200. The Harshaw TL Analyzer Model-3500 was used to record the glow curves within a temperature range of 325 K to 660 K, with a heating rate of 5 K/s.

4.3 Results and discussion of Bi^{3+} doped MgO

4.3.1 X-ray Diffraction Study

Fig 4.1 shows the XRD patterns of pure and $Mg_{1-x}O:Bi_x$ (x= 0.00 mol%, 0.01 mol%, 0.05 mol%, 0.1 mol%, 0.3 mol%, 0.5 mol %) samples namely; B0, B1, B2, B3, B4 and B5, respectively. All of the diffraction peaks are well match with card

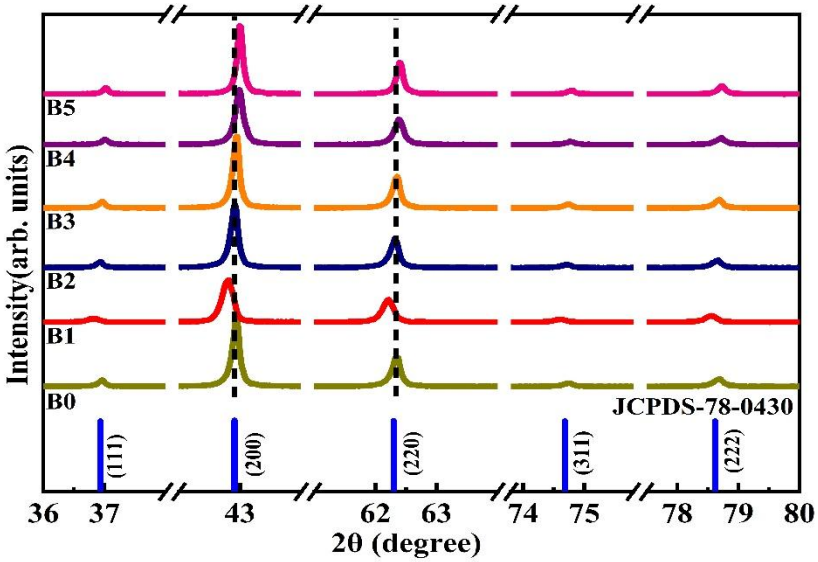

Fig 4.1: XRD patterns of pure and Bi doped MgO

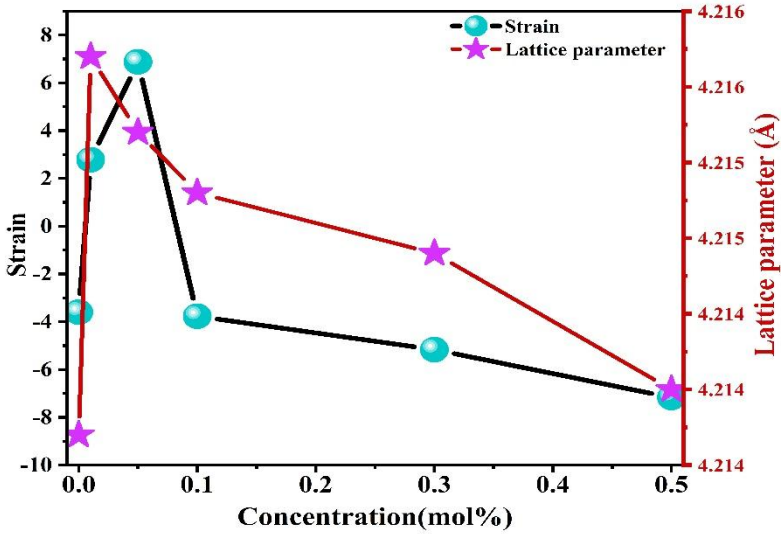

Fig 4.2: Strain and lattice parameter as a function of Bi^{3+} ion doping

JCPDS no. 78-0430 of cubic MgO with space group; *Fm-3m* (Halder & Bandyopadhyay, 2017). There is no diffraction peak related to other secondary phases of Mg, Bi and/or binary oxides and, therefore, confirming the single phase nature of as prepared samples with varying Bi concentrations in MgO. It is noticeable that XRD peak position shows uneven shifting upon increasing the Bi doping concentrations. For the first two concentrations (i.e., x = 0.01 and 0.05 mol %) the XRD peaks show shifting towards lower diffraction angles. However, at higher doping concentrations (x = 0.1 to 0.5 mol %) a marginal shifting towards the higher diffraction angles is observed. This kind of peak position shifting may give intriguing structural parameters of MgO and, therefore, have been examined by Rietveld refinement of the XRD patterns. Rietveld refinement was performed by utilizing the Fullprof software suite .The various refined parameters are also enlisted in Table 4-1. From the Table, it is observed that incorporation of Bi has an effect on lattice parameters, unit cell volume and Mg – O bond distance. The lattice parameters, unit cell volume and bond Mg – O bond distance first increases for the two doping concentrations (x = 0.01 and 0.05 mol %) and then marginally decreased for the higher Bi doping concentrations (x = 0.1 to 0.5 mol %). Lattice parameter variation and Mg – O bond length alteration could be due to the strain produced in the MgO lattice upon incorporation of Bi^{3+} ions. The lattice micro-strain is evaluated using the Williamson's-Hall (W-H) method; $\beta\cos\theta = \frac{k\lambda}{D} + 4\varepsilon\sin\theta$ where k=0.9, D is the crystallite size, β is the FWHM of the diffraction peaks, ε is strain, and λ is the wavelength of the used X-rays (Williamson & Hall, 1953) . Fig 4.2 shows the micro-strain and lattice parameter variation in different samples as a function of Bi^{3+} ions doping concentration. The tensile strain in these two compounds suggests that the MgO lattice is offering substitutional doping to the larger sized Bi^{3+} ions (0.103 nm) at the sites of smaller sized Mg^{2+} ions (0.072 nm) (Devaraja et al., 2016b). Therefore, an increase in the lattice parameter values has been observed in Fig 4.2 which indicates the compressive strain in the higher concentration (x= 0.1 mol% to 0.5 mol%) Bi^{3+} ions doped

samples. This could be due to the interstitial mi gration of Bi^{3+} ions in the MgO lattice and, thus, resulting shrinkage of Mg–O bonds and lattice parameters and the refined patterns are shown in the Fig 4.3.

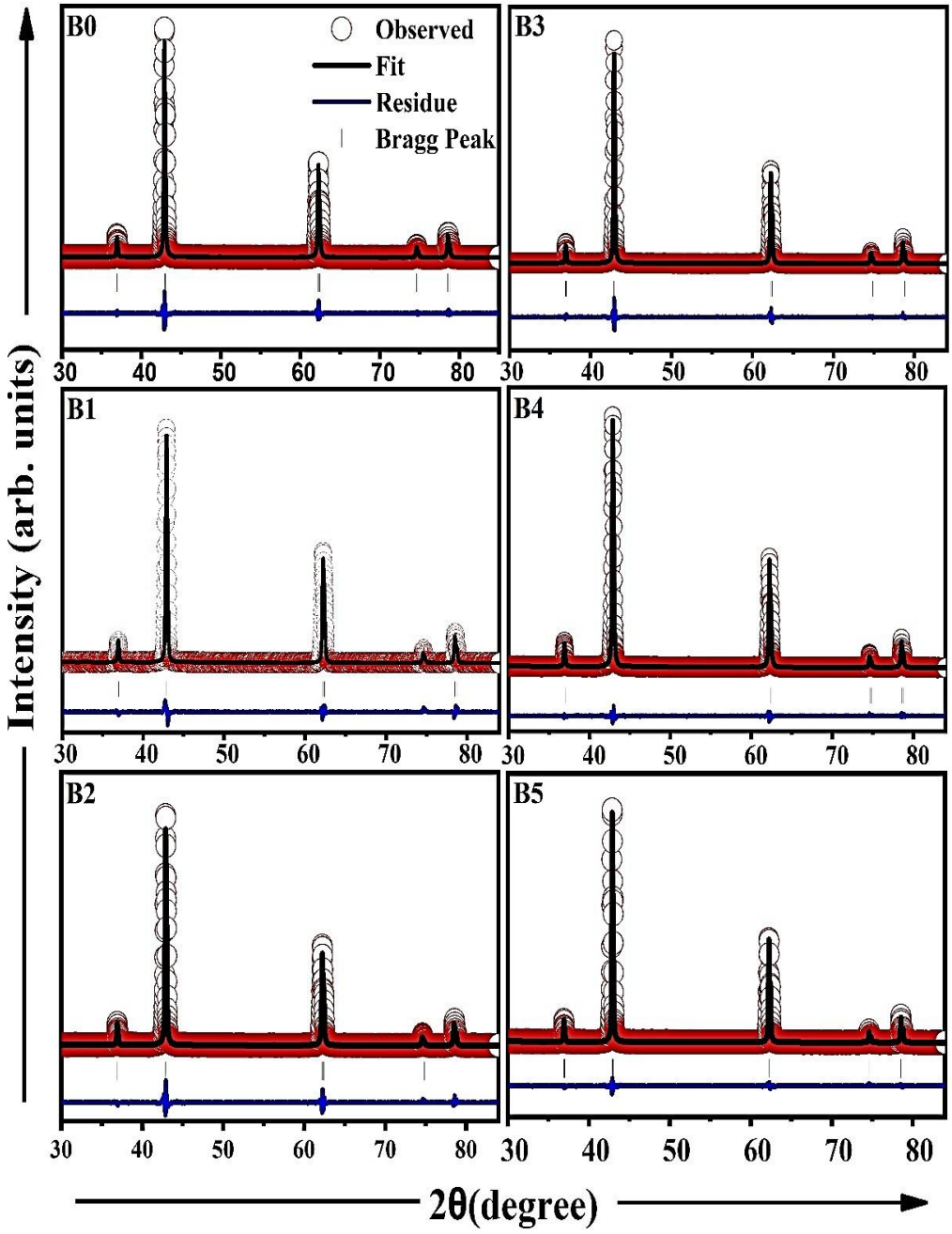

Fig 4.3: Rietveld Refined pattern of pure and Bi doped MgO

Table 4-1: Crystal parameters of MgO unit cell calculated by XRD patterns and Rietveld refinement of XRD patterns

Sample	B0	B1	B2	B3	B4	B5
Lattice parameter Å	4.213(7)	4.216(2)	4.215(6)	4.215(3)	4.214(9)	4.214(8)
Occupancy Oxygen Magnesium	 0.999 0.9471	 0.8871 0.8391	 0.8802 0.7048	 0.9951 0.9540	 0.9991 0.8980	 1 0.8995
Bond length (Mg-O) Å	2.107(2)	2.108(1)	2.107(8)	2.107(0)	2.107(6)	2.107(0)
Quality of fit						
R_f	9.11	9.44	10.2	9.01	7.18	6.97
R_{wp}	11.8	13	12.9	11.7	10.1	9.85
R_{exp}	9.40	9.82	9.15	9.10	9.04	9.06
$\chi 2$	1.6	1.7	1.9	1.6	1.2	1.1
GOF	1.1	1.3	1.4	1.3	1.1	1.1

4.3.2 Transmission Electron Microscopy Study

Fig 4.4(a, b) shows the TEM images of the pure and B2 samples. It is noticed that nearly the spherical morphology of nanoparticles is formed along with agglomeration of particles. This agglomeration is possible due to annealing-induced diffusion of particles. The SAED images shown in Fig 4.4(c, d) reflect

typical ring patterns and confirm the polycrystalline nature of the prepared samples. In the ring patterns, the crystallographic planes: (111), (200), (220), (311), and

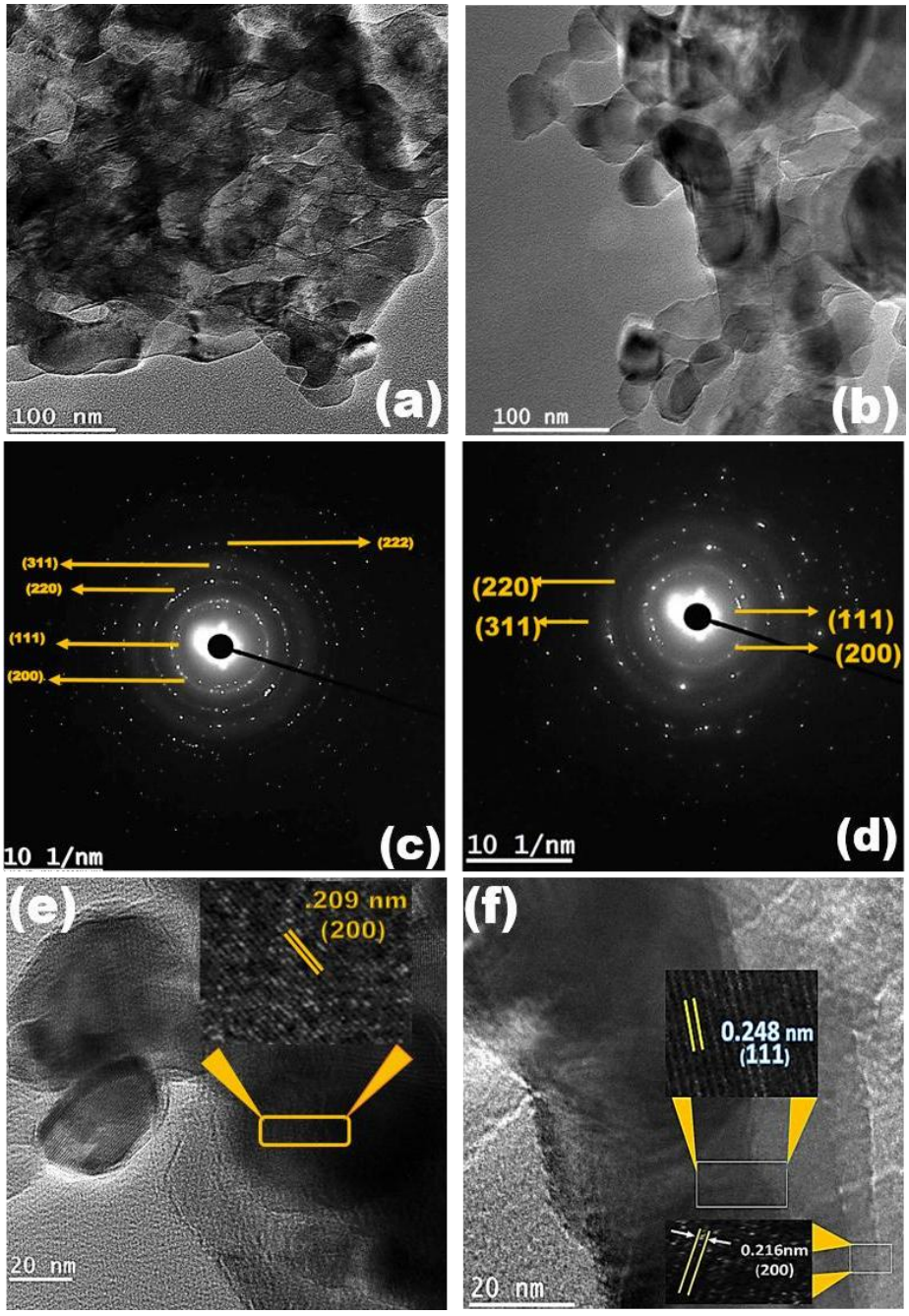

Fig 4.4: (a, b) TEM image of pure and B2 (c, d) SAED pattern analysis (e, f) Lattice fringes of sample

(222) of the MgO phase are apparent, and no other plane of any secondary phase could be detected and confirming the absence of trivial phases in pure, and doped MgO samples. Fig 4.4(e, f) shows the magnified view of nanoparticles with apparent lattice fringes. The crystal planes in TEM images show that a more inter-planar distance of 0.209 nm is observed in the pure MgO sample for the (200) crystal plane. Inter-planar spacing values are evaluated in doped MgO to 0.248 nm, which corresponds to MgO crystal planes (111). Such values are fairly matching with the values obtained from XRD data.

4.3.3 X-ray Absorption Spectroscopy Study

Fig 4.5(a) depicts the XANES spectra of O K edge for pure and Bi doped samples. Sharp spectral features are observed at 532 eV, 538 eV, 544 eV, and 555 eV, marked as **a, b, c, d** respectively. All the features observed in spectra are very consistent with the O K-edge spectra of pure MgO reported elsewhere (Th. Lindner, H. Sauer, W. Engel, 1986). The eV), having **c** and **d** features. Transitions between O-1s orbitals and empty mixed O-2p states with Mg-3s cations are responsible for the post-edge features **a**, **b**, and **c** (Frati et al., 2020). Feature at **d** is due to the multiple resonances scattering from neighboring atoms associated with XAFS oscillations. Pre-edge feature of O K edge observed in pure MgO, which is sensitive to the localized bound states and defects, (J. P. Singh, Lim, et al., 2018) is absent in all doped sample. It is observed that the peak intensity of **a** and **b** features is enhanced in Bi^{3+} doped samples. It could be due to the availability of unoccupied states formed via hybridization of Bi states with O states. The shoulder at **b'** is well resolved in B3, B4, and B5 indicates the increase in oxygen defects in the MgO lattice upon increasing the Bi doping concentrations (Th. Lindner, H. Sauer, W. Engel, 1986)(Mizoguchi & Tanaka, 2000). Fig 4.5(b) depicts the Mg K- edge XANES spectra from pure and Bi doped samples. Spectral features **a** at 1305.2 eV, **b** at 1311.8 eV**, c** at 1322.9 eV, and **d** at 1351.2 eV are observed. All these features have similarity with the Mg K edge XANES observed for MgO (i.e., Mg in 2+ valence state) by Th. Lindner et.al., (Th. Lindner, H. Sauer, W. Engel, 1986).

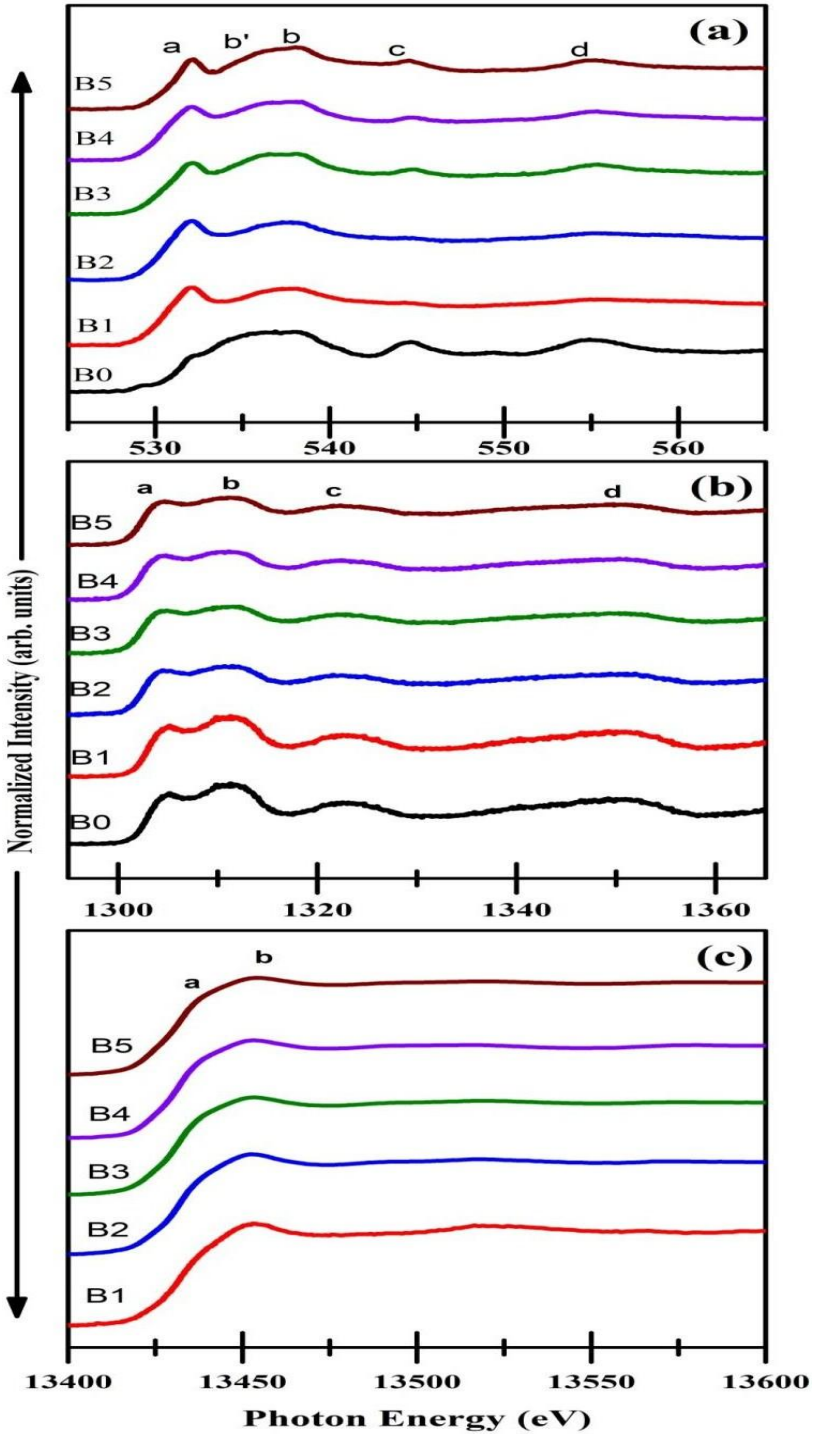

Fig 4.5: (a) O K-edge XANES spectra (b) Mg K-edge spectra and (c) Bi L_3-edge XANES spectra

Post edge features are associated with the transition between Mg-1s orbitals and degenerated 3p orbitals and mixed states of Mg-3p and O-2p [18, 19, 20] In literature, it was reported through experimental and theoretical calculations that Mg K-post edge feature at 1310 eV is sharp due to the lowering of degeneracy in 3p orbitals and this feature shifts to lower energies in cationic disorder in lattice in various minerals (Farangis et al., 2003; Ildefonse et al., 1995). There is no edge-energy or white line peak position shift observed for the Bi doped samples. This suggests, no significant changes in the oxidation state and local coordination chemistry of Mg^{2+} ions as a function of Bi concentrations. There is slight decrease in the intensity of **b** feature upon Bi doping. This indicates marginal migration of Mg^{2+} ions from the proper lattice sites towards the interstitial sites in MgO (i.e., formation of F centers) which is possible due to the significant difference in the ionic radii and charge of Bi^{3+} ions and Mg^{2+} ions. Feature **d** is attributed to multiple scattering by neighboring atoms producing peak at 1350 eV (Jain et al., 2021). The Mg K-edge spectra exhibit distinct resolution of all four features, and no merging/broadening of spectral peaks is observed across all doping concentrations of Bi. This indicates that the augmentation of Bi^{3+} ions concentration does not create significant distortion in the crystalline lattice or amorphization of the MgO.

Fig 4.5(c) shows the Bi L_3-edge XANES spectra of all of the Bi-doped samples. The energies of the features (**a** and **b**) lie between 13425 eV and 13500 eV. The transitions between $2p_{3/2}$ and empty 7s and 6d orbitals of Bi cause such spectral features in the Bi L_3-edge XANES spectra. The transition from $2p_{3/2}$ to 6d orbitals causes the shoulder at **a.** Feature **a** become more significant upon increasing in the Bi concentration. It shows an increase in Bi related unoccupied 6d levels in the system. These features match well with the Bi L_3-edge XANES spectra of Bi_2O_3 (i.e., Bi in 3+ valence state) observed by (Gholam et al., 2019) . There is no spectral shifting upon increase in the Bi concentrations and, thus, ruled out the formation of other phases of Bi with other oxidation states.

4.3.4 UV-Vis Absorption and Photoluminescence Spectroscopy Study

Fig 4.6 shows the UV-vis absorption spectra of pure and Bi doped MgO samples. In pure MgO sample, the absorption is mainly observed at 220 nm with two weak bands at 250 nm and 300 nm. The main absorption peak gives band gap energy ~ 4.7eV which is close to reported values. As reported in previous study (Hao et al., 2017)(Pathak et al., 2016b), two absorption peaks (250 nm and 300 nm) can be assigned to the color centers in the sample or low coordinated sites (i.e., F and/or V centers) in the MgO. Moreover, the absorption spectra in Bi doped samples (between 250 to 350 nm) are showing much enhancement in the intensity. This could be due to Bi doping induced formation of shallow levels in the band gap of MgO and, additionally, formation of vivid F and/or V centers.

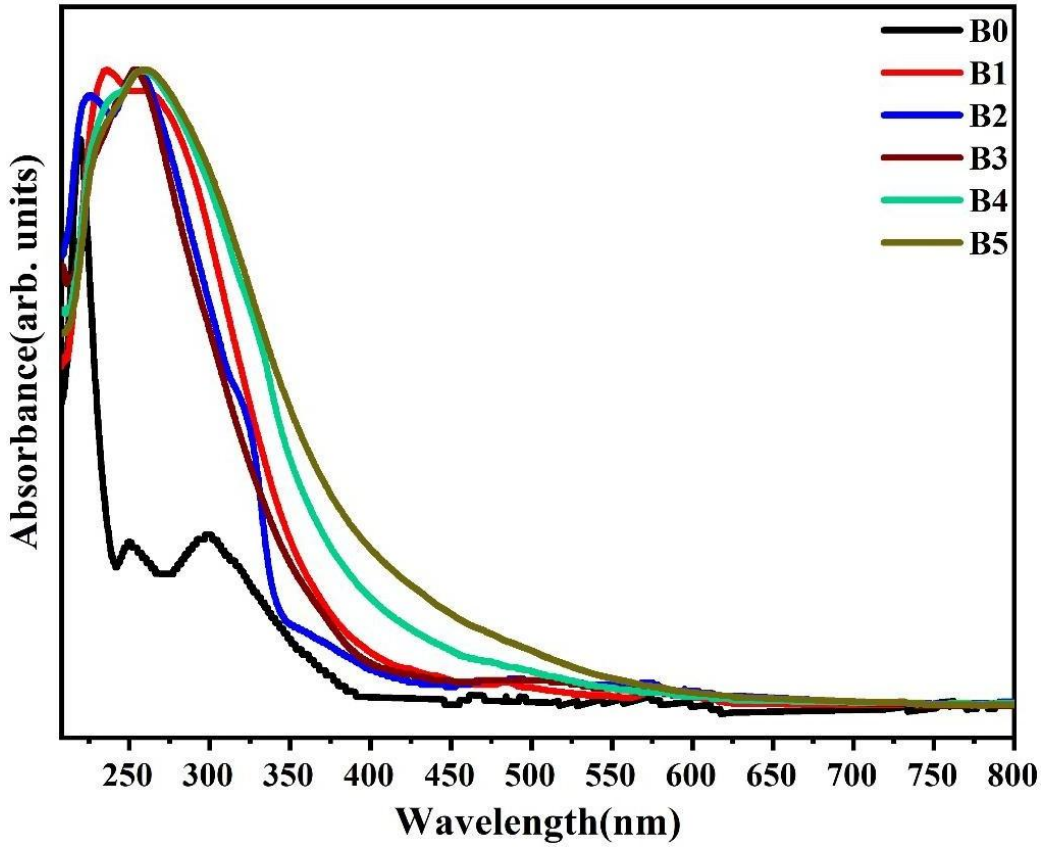

Fig 4.6: UV-Vis absorption spectra of pure and Bi doped MgO samples

The observed luminescence spectrum under UV (275 nm) excitation in host is composed of different emission peaks marked as A, B, C, D, E shown in Fig 4.7 Broad luminescence spectrum in blue region consists of peak centered at 427 nm with shoulders at 386 nm and 405 nm and a wide hump around 445 nm. The emission in red region is centered at 690 nm. The shoulder at 386 nm is observed due to surface defects (F_s) having a singlet to singlet transition between $^1A_{1g} \rightarrow {}^1A_{1g}$ $[(^2p_z) \rightarrow (^1S)_2]$ (Gibson et al., 1994; Illas & Pacchioni, 1998; Rinke et al., 2012; Shvets et al., 1985).

Photoluminescence in Pure MgO

Fig 4.7 shows the PL spectra of pristine MgO. F is a vacancy of oxygen in MgO occupied by two electrons to maintain the charge neutrality and strain in lattice. In case of F_0 vacancy, only nearest neighboring atoms gets affected. Vacancy will

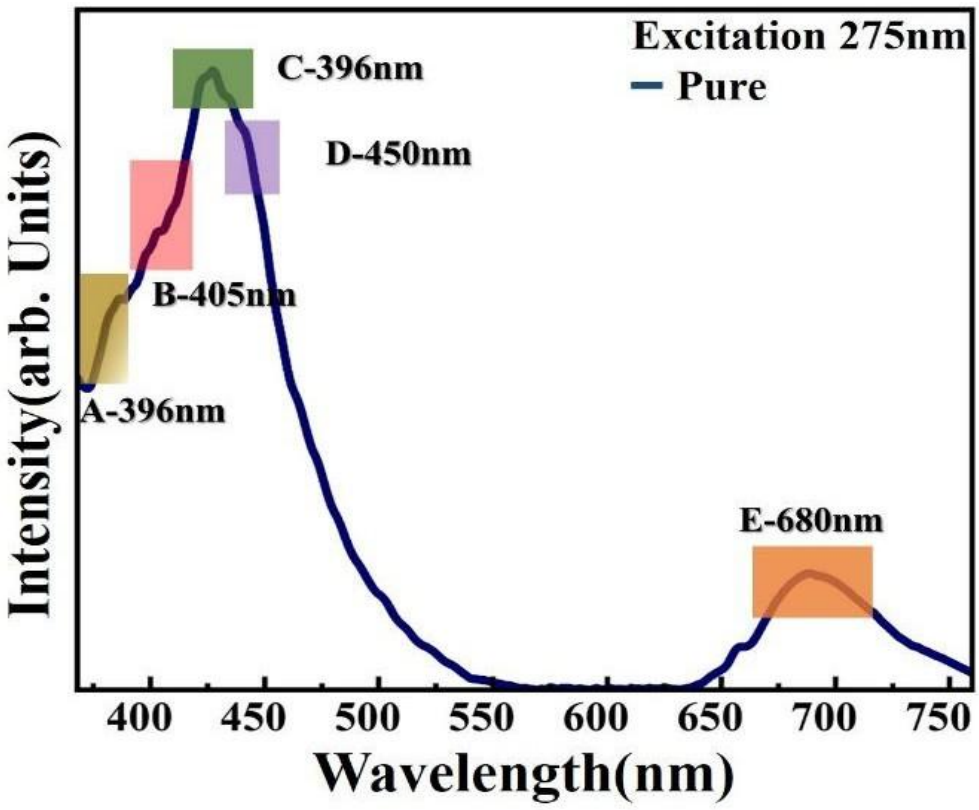

Fig 4.7: Pl emission of pure MgO under 275 nm excitation

get charged when one or two electrons is removed from neutral defect centre, then atoms next to nearest neighbour atoms shift inwards and nearest atoms are repelled outward. However, the symmetry around vacancy in lattice is not broken in any of defects created in bulk or at surfaces. The transition between $^2T_{1u} \rightarrow {}^2A_{1g}$ at bulk F^+ centre is an allowed transition according to dipole selection rule which is observed at shoulder around 395 nm which is similar to the 390 nm observed by G H Rosenblatt et. al. and A. Kumar et. al. Feature at C and D indicates the presence of cluster of charged $F2^{2+}$centres in bulk (Busker et al., 2000; Coudray et al., 2000; Richter et al., 2013). The broad feature at E is due to the emission from cluster of singly charged vacancies within the band gap.

Photoluminescence in Bi Doped MgO

Fig 4.8(a-c) displays the emission and excitation spectra of all the doped samples. Upon excitation with a Xenon lamp with 275 nm wavelength, an intense blue region (300-480 nm) is observed in the visible band. The electronic configuration of Bi^{3+} is Xe $4f^{14}5d^{10}6s^26p^0$, but only excitation of 6s to 6p state is involved in the optical emission. Emission from Bi^{3+} ions is highly dependent on its surrounding environment in lattice. As an activator, Bi^{3+} emits from blue to green emission depend on the host material in which it is doped (Scarangella et al., 2017) (H. T. Sun et al., 2014). In MgO lattice, Mg^{2+} ions occupy the octahedral sites in closed packed structure of oxygen anions and possess inversion symmetry. If Bi^{3+} ions are doped in MgO, they occupy the cation sites in lattice. However, interstitial oxygen will be introduced, in order to compensate the charge, and one Mg vacancy will be created for two trivalent ions incorporations thus favors the formation of F and V centers in the MgO lattice (Devaraja et al., 2015b). Due to the crystal field effects, the energy levels of Bi^{3+} ions split into the triplet $^3P_0$, $^3P_1$, $^3P_2$ and singlet $^1P_1$ excited states in a sequence of increasing energy. The electric dipole transition between $^1S_0$ to $^1P_1$ is allowed, but $^1S_0$ to $^3P_0$ and $^1S_0$ to $^3P_2$ are spin

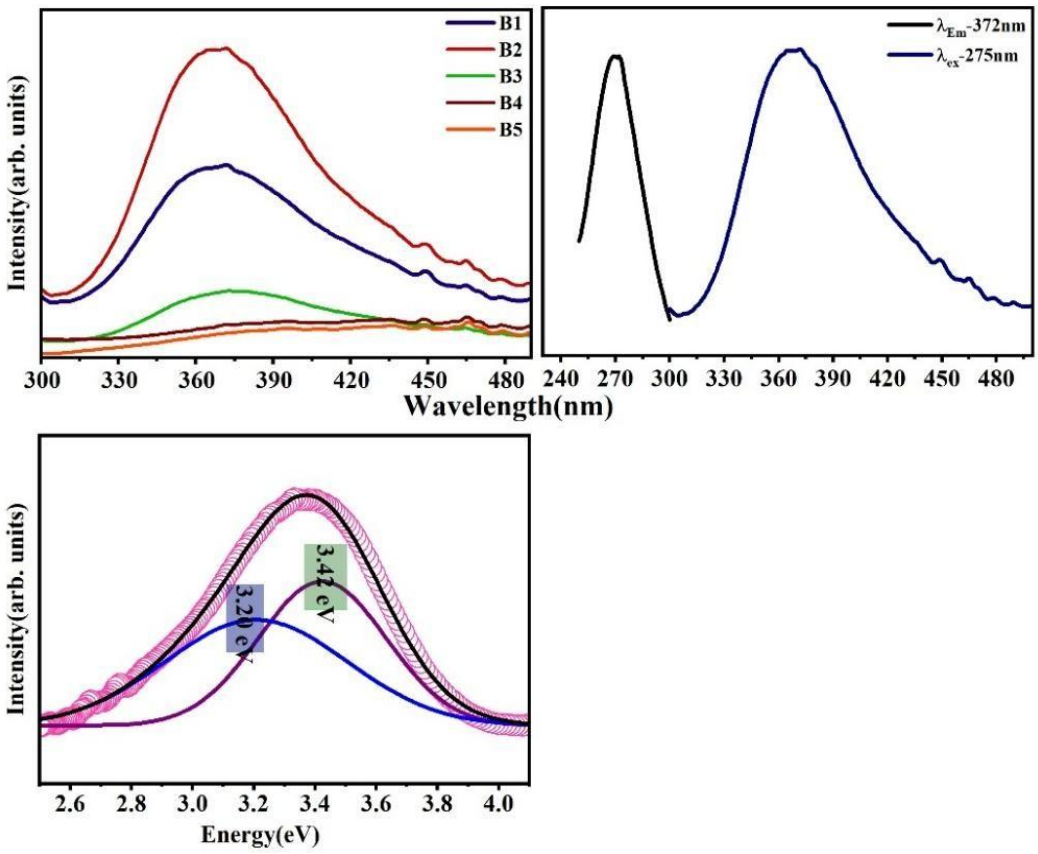

Fig 4.8: (a) PL emission of all Bi doped samples at excitation wavelength of 275 nm, (b) Excitation and emission spectra of B2, (c) Deconvoluted PL emission spectra of B2

forbidden according to the LS coupling scheme (H. T. Sun et al., 2014). Due to spin orbit interaction and asymmetrical lattice vibration between the $^1P_1$ and $^3P_1$ of Bi ions, mixed states are generated, and the transition between $^1S_0$ to $^3P_1$, $^3P_0$ becomes possible in these states (Ellervee, 1977)(L. Chen et al., 2008). Broad band absorption between 250 nm and 300 nm observed in the excitation spectra in Fig 4.8(b). It is consistent with the $^1S_0$ to $^1P_1$ transitions observed at 260 nm by Abdelrehman et.al., for Bi doped SrO (M. H. M. Abdelrehman et al., 2019). Deconvolution of broad spectra is performed using the Gaussian peak shape function to locate the defect centers within the band gap after the converting the

data from wavelength into energy scale using the Jacobian transformation. The formula for conversion is; $f(\lambda) = f(E)\frac{hc}{E^2}$ The de-convoluted peaks are shown in Fig 4.8(c) which exhibits two peaks at 362 nm and at 387 nm which are attributed to the transition between $^3P_1$ to $^1S_0$ and $^3P_0$ to $^1S_0$. Similar optical bands of Bi^{3+} ions transition are observed by (L. Chen et al., 2008)(Yamashita et al., 1987) in the photoluminescence studies. The schematic diagram of possible radiative and non-radiative paths is shown in Fig 4.9. Electrons stimulated to $^1P_1$ level, then non-radiatively relaxed to $^3P_1$ and $^3P_0$ levels due to reduced energy difference. Subsequently the transitions from $^3P_1$ and $^3P_0$ to $^1S_0$ gives emission peaks shown in Fig 4.8(c) also depicted in Fig 4.9.

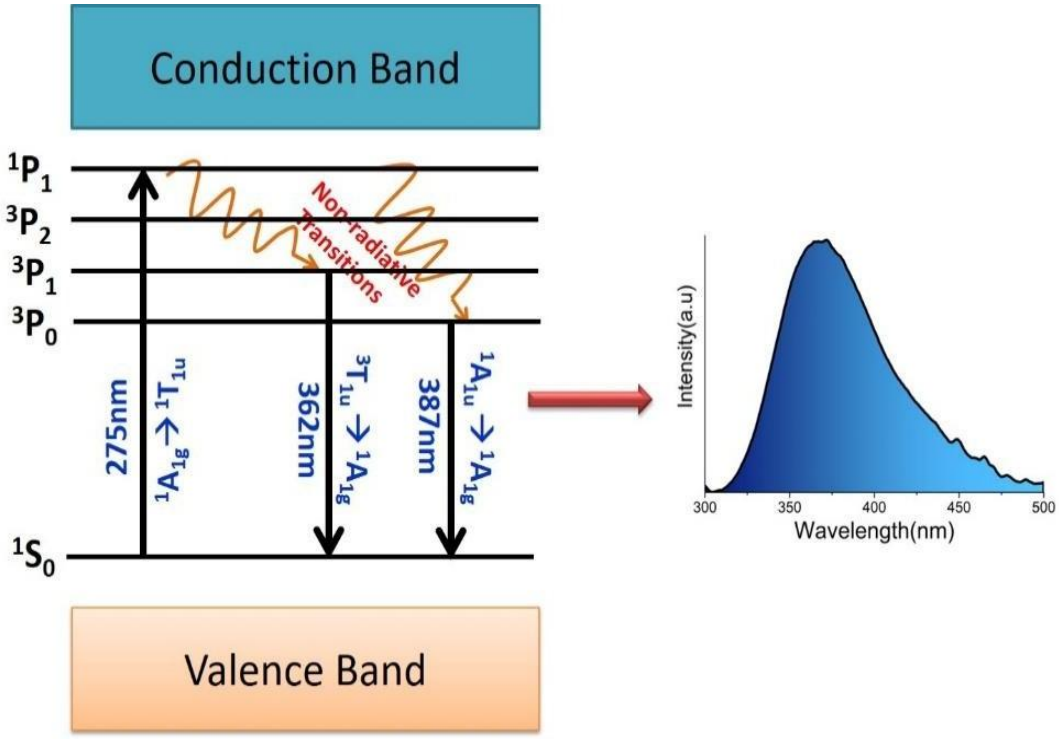

Fig 4.9: Schematic band model depicting the emission mechanism

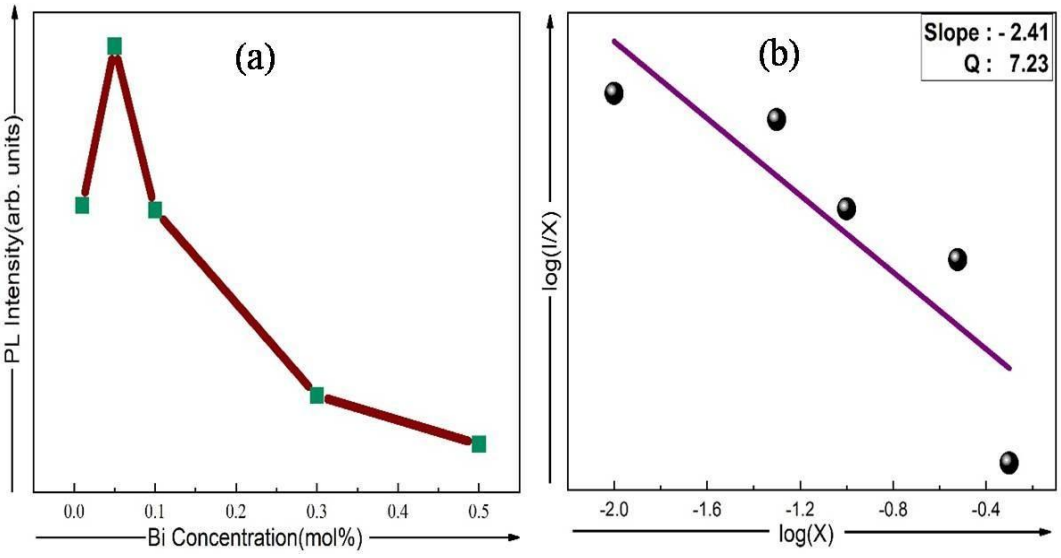

Fig 4.10: (a) PL intensity variation with Bi^{3+} concentration; (b) Log (I/X) vs log(X) in Bi^{3+} doped MgO

The variation of PL emission intensity with dopant concentration is shown in Fig 4.10(a). It is observed that critical concentration of Bi^{3+} ions for MgO host is 0.05 mol%. The PL intensity increases as the Bi concentration increases up to 0.05 mol%. After this concentration, it is decreasing due to concentration quenching, and the highest intensity is observed at 0.05 mol%. The reduction in PL emission due to the variation of concentration is attributed to the change in local field around the Bi^{3+} ions. The quenching in luminescence is observed with an increase in the concentration of doped ions because of energy transfer between the activators which occurs until energy is lost non-radiatively in the lattice. When Bi^{3+} concentration increased in MgO, the distance among the Bi^{3+} ions decreased leading to the strong interaction between the ions and making non-radiative energy transfer process dominating during the emission process. There are three important factors affecting the non-radiative transitions which are; (a) Multipole–Multipole interaction, (b) Exchange interaction between ions; and (c) re-absorption of energy (Blasse, 1968).

The exchange interaction factor plays an important role in quenching mechanism if the separation between the activators is less than 5 Å. However, in the present samples, calculated distance between the activator ions is 41.32 Å using the relation:

$$R = 2\left(\frac{3V}{4\pi N X}\right)^{1/3} \qquad \text{Eq. 4.1}$$

where V=73.9166 $Å^3$ is volume of unit cell, X = 0.0005 is Bi^{3+}concentration, and N = 4 is cations per unit cell. It means exchange interaction is negligible in this case and quenching is occurring due to the multipole-multipole interaction between the activators' ion. According to (Dexter, 1953), multipole–multipole interaction between the activator ions can occur by different ways, such as quadrupole-quadrupole, dipole-dipole, and dipole-quadrupole interactions. Energy transfer process between activators ions of host is theoretically studied by (Van Uitert, 1967). If the dopant concentration is greater than the critical one, the correlation of the emission intensity and dopant concentration is given by;

$$I/X = k[1 + \beta(X)^{Q/3}]^{-1} \qquad \text{Eq. 4.2}$$

where X is dopant concentration greater than the critical concentration, for the same excitation condition of host, k and β are constants, I is emission intensity of emission spectra. According to above (3), if Q = 3 energy is transferred between nearest neighbors and for dipole –dipole, dipole- quadruple, and quadruple-quadruple interactions Q is 6, 8, 10 respectively. Above equation can be written as for $\beta(X)^{Q/3} \gg 1$ and the X has relation with Q:

$$\log(I/X) = K' - (Q/3)\log(X) \qquad \text{Eq. 4.3}$$

To calculate the value of Q, graph is plotted for log (I/X) as a function of log (X) shown in Fig 4.10(b).The value of slope for linear line is -2.41 and Q is 7.23 which are very close to Dexter's theoretical value of 8 for dipole-quadruple interaction. This suggests that the concentration quenching in $MgO_{(1-x)}:Bi_x$ nanophosphors is caused by dipole-quadruple interaction.

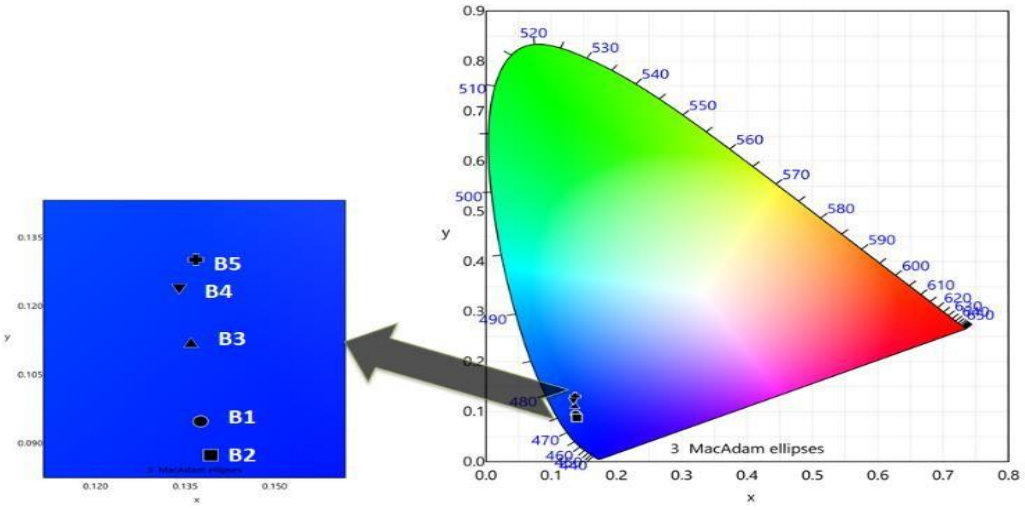

Fig 4.11: CIE chromaticity diagram of all prepared sample for excitation wavelength of 275 nm

Colorimetric properties are studied to evaluate the nanophosphors performance by calculating the CIE coordinates using a color calculator by using OSRAM software, Fig 4.11 shows the color region of emitted light by all samples with different (x, y) coordinate, which shows that the emission of all samples lies in the blue region. All the color parameters are shown in Table 4-2. It is noticed that purity is highest in B2, indicating that this concentration has the greatest color richness with CCT 2609K. The materials used for color conversion for LED displays are highly in demand especially in context of augmented reality and virtual reality. The advancements in digital processing, display technologies have opened up new possibilities for the widespread use of augmented reality (AR) and virtual reality (VR) applications (Hsiang et al., 2021). The present phosphors are very

efficient in producing blue light, which can be efficiently used as color conversion materials for LEDs. Colorimetric properties of prepared nanophosphors can be enhanced by further co-doping of rare earth elements and by optimizing the dopants concentration in host.

Table 4-2: Colorimetric parameters of samples reported by various authors

Samples	Coordinates (x, y)	Color Purity (%)	CCT(K)
B1	(0.1376,0.0984)	90.7	3163
B2	(0.1393,0.0874)	91.3	2609
B3	(0.1368,0.0130)	86.1	1732
B4	(0.1360,0.1118)	88.8	4487
B5	(0.1340,0.1243)	87.7	6170

4.3.5 Thermoluminescence Study

The observation of visible emission in bismuth-doped MgO nanophosphors suggests the possible existence of deep and shallow levels within the forbidden band gap. Fig 4.12 shows the results of gamma irradiation dose (500 Gy) on TL glow curve, which helps to identify the presence of trapping state in the band gap. This information will be useful in further research for dosimetric applications. In all of the samples, two regions are observed in the glow curves: 350 K-500 K and 525 K- 650 K marked as **P** and **Q,** respectively. In pure MgO sample, feature **P** with a broad hump with less intensity is appeared and **Q** is sharp. It is observed that TL emission in region **P** is high as compare to region **Q** in doped sample. However, glow curve analysis shows B1 has the highest TL intensity. The shallow and deep traps in B1 are narrow and intense, but as concentration increases up to B3, the shallow traps become broader. With increase in concentration, redistribution of

traps takes place and deep traps emission is diminished. Upon increasing the concentration to B3, the characteristics **P** and **Q** exhibit a notable amalgamation, which can be attributed to the recapturing of charge carriers from shallow traps to deep traps. No emissions were detected in the B4 and B5 samples within the **P** region, whereas broader curves were observed at elevated temperatures. Additionally, the maxima of shallow traps are exhibiting a shift towards higher temperatures, indicating a transfer of charge carrier density from shallower traps to deeper traps. This similar quenching behaviour of Bi^{3+} ions in different hosts is also (Yousif et al., 2020)(M. Abdelrehman et al., 2020).

Based on the literature regarding the behaviour of Bi^{3+} ions in various hosts, it has been observed that these ions can function as both hole and electron traps (Yousif et al., 2020)(Lyu & Dorenbos, 2018). Here in our samples, the increase in doping results in the restructuring of traps located within the forbidden energy gaps,

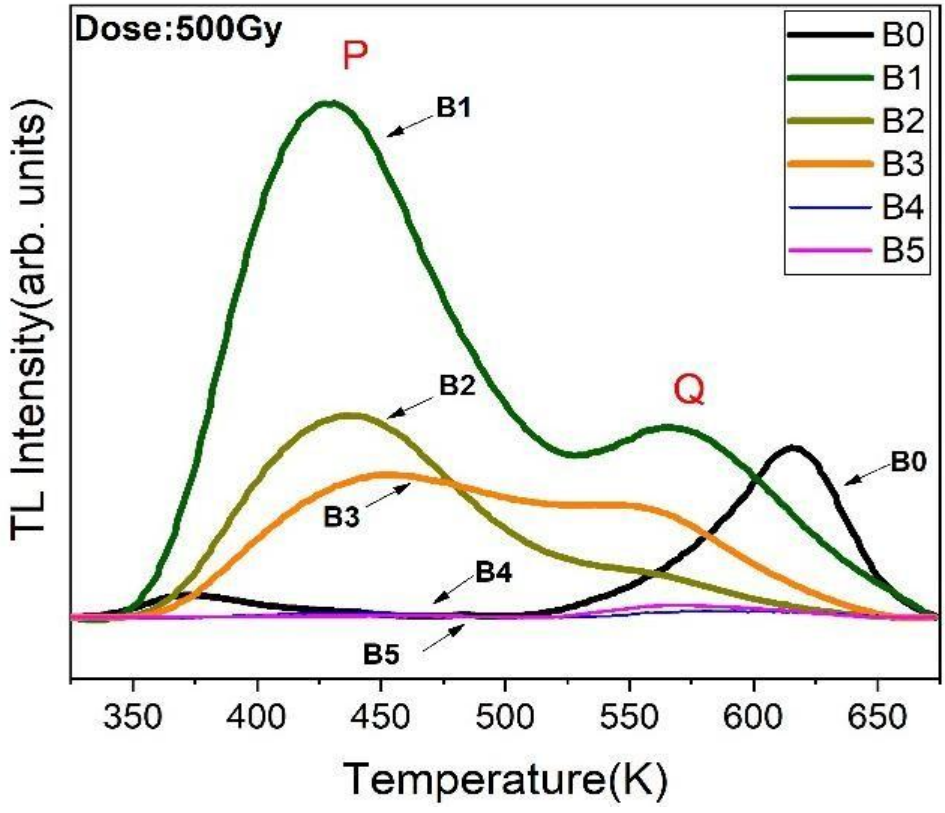

Fig 4.12: Glow curve of pure and Bi doped MgO samples at 500 Gy

thereby leading to the increase in deep traps with increase in concentration. The concentration quenching behaviour may be attributed to either a variation in trap density governed by Bi^{3+} or to the reduction in trapping probability for a given trap, resulting from an increase in the density of the activator ions. Because of the increase in density, the spatial distance between the activator ions and the excitons generated is reduced leading to quenching behaviour.

Glow Curve Analysis and parameters

The glow curves exhibited complex nature, as they represent of several trap centres that can be identified through deconvolution of the curves. To visualize the frequency factor, order of kinetics, number of generated carriers and activation energies, the deconvolution of TL glow curves were performed utilising general order kinetics within the TLANAL software. Fig 4.13(a-c) displays the de-convoluted glow curves of samples B1, B2 and B3 for 500 Gy dose. (Kitis et al., 1998) formula for deconvoluting glow curves with general order kinetics is given by:

$$I(T) = I_m b^{b/(b-1)} \exp\left(\frac{E}{kT} \times \frac{T-T_m}{T_m}\right) \times [(b-1)(1-\Delta)\frac{T^2}{T_m^2} \times \exp\left(\frac{E}{kT}\frac{T-T_m}{T_m}\right) + z_m]^{-b/(b-1)} \quad \text{Eq. 4.4}$$

where, $\Delta = \frac{2kT}{E}$, $Z_m = 1 + (b-1)\Delta_m$, $\Delta_m = {2kT_m}/{E}$, T_m is corresponding TL peak temperature for maximum intensity(I_m), E shows the depth of trap from conduction band, k is Boltzmann constant, b is order of kinetics. The entire glow curves are de-convoluted to four peaks. The figure of merit (FOM) is calculated to check the goodness of fit, $FOM = \frac{\sum|TL_E - TL_F|}{\sum TL_F}$, TL_E and TL_F are experimental and

fitted data of curves obtained by deconvoluting the glow curves. Table 4-3

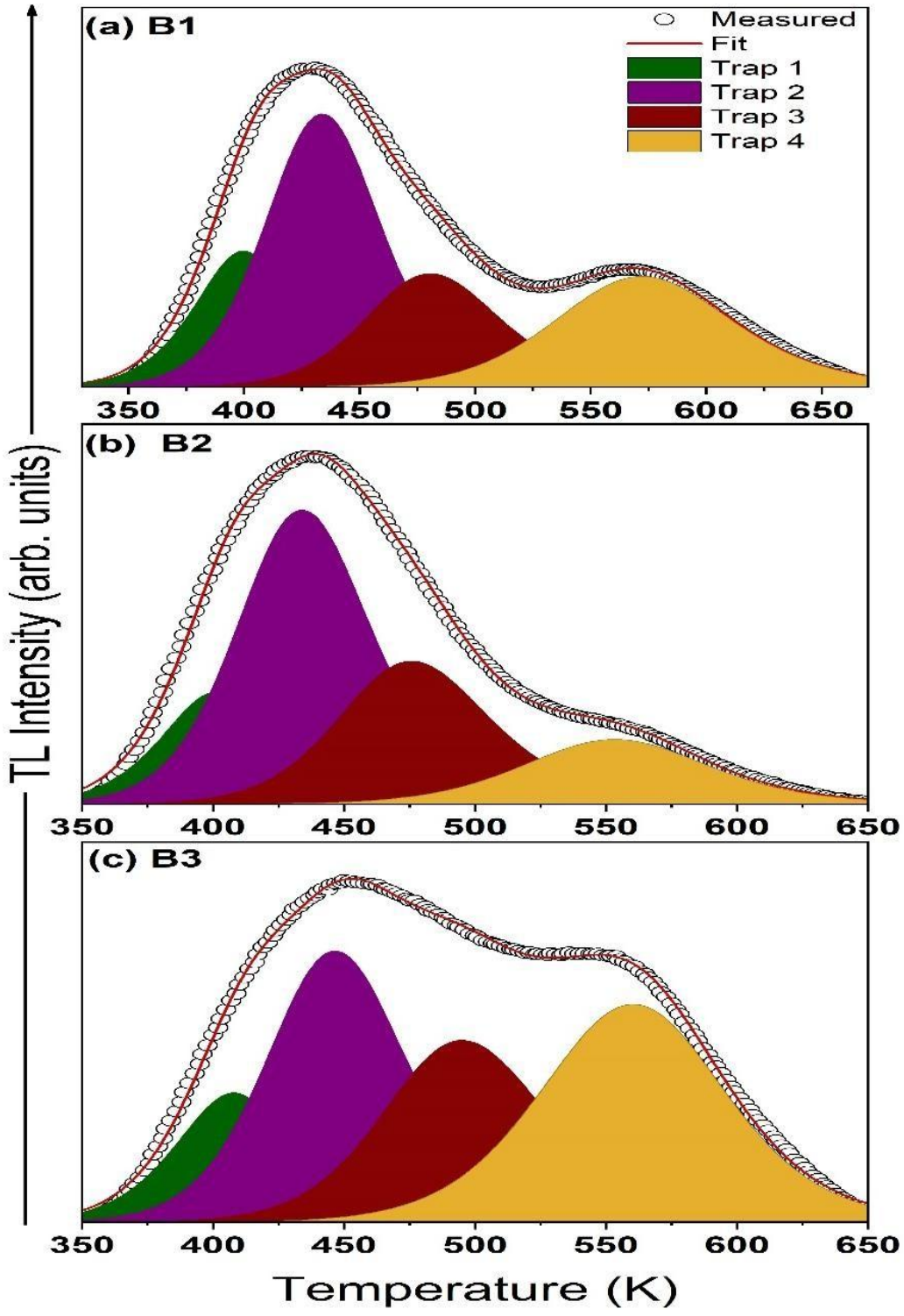

Fig 4.13: De-convoluted TL glow curves at 500 Gy dose for B1, B2 and B3 samples

summarizes the glow curve parameters for B1, B2 and B3 for 500Gy dose. The FOM values across all samples are less than 3% suggesting the good fit. The **b** value represents order of kinetics, exceeds 1.5 for each of the traps except first trap, indicating the presence of re-trapping phenomenon in glow curves. In B1, the estimated T_m of all four traps is at 402 K, 435 K, 480 K and 571 K. It can be visualized in graph that region P is narrow in B1 and merging of P with Q region is observed in B3. In B1, the main contribution in TL intensity is due to trap 2 and 4. The observation of a small shoulder in B2 suggests an increase in the contribution of trap 2 while the peak at higher temperature is suppressed is due to the lesser contribution of trap 3 and trap 4. However, the collectively increased contribution of trap 3 and trap 4 influences the broadness of curve and trap distributions in B3. It is believed that the proximity of traps is a necessary condition for the overlapping of their charge wave functions, which results in the tunneling of carriers and broadens of the overall curve. The discussed mechanism appears to enhance the re-trapping of carriers and allows the transfer of charge from shallow traps to deeper ones, thereby reducing the frequency factors. Incorporation of Bi ions cause the lattice distortion and the restructuring of traps by increasing the concentration of dopant causes the shifting in peaks observed in comparison to the peaks reported in literature (Yousif et al., 2020)(M. Abdelrehman et al., 2020). As we did not find any study of thermoluminescence behaviour of bismuth doped MgO, so we could not confirm the nature of origin of these traps. But our results agree with the results reported by several authors while studying the thermoluminescence behaviour of MgO doped with different impurities. (Luthra et al., 1977; Sathyamoorthy & Luthra, 1978) has studied thermoluminescence in MgO and reported TL peaks at 370 K, 425 K, 470 K and 545 K. In present study the broad peak from 340 K-470 K and from 500 K- 670 K is complementing with the literature. Several other have also reported TL peaks at similar temperatures (Kadari & Kadri, 2010). The observed peak at 402 K can be attributed to the V-centre of the host, (Soliman, 2009) which has been significantly modified by the presence of a nearby bismuth impurity. TL peak behavior is similar to the peak observed by J. Vignolo et. al., at

Table 4-3: Kinetic parameters of TL glow curves of all the traps for B1, B2 and B3 for 500Gy dose

Sample	Trap	T_m (K)	n_0	E (eV)	s (s^{-1})	b	FOM (%)
B1	1	402	8.6×10^7	0.758	9.8×10^8	1.12	2.3
	2	435	2.4×10^8	0.846	1.7×10^9	1.77	
	3	480	1.2×10^8	0.934	1.4×10^9	2	
	4	571	1.5×10^8	0.945	3.3×10^7	1.78	
B2	1	402	2.4×10^7	0.764	1.1×10^9	1	2.3
	2	434	9.5×10^7	0.852	1.9×10^9	1.90	
	3	475	5.3×10^7	0.929	1.52×10^9	2	
	4	554	2.8×10^7	0.951	7.7×10^7	1.71	
B3	1	405	2.3×10^7	0.758	6.0×10^8	1.19	2.2
	2	445	6.6×10^7	0.857	1.1×10^9	1.86	
	3	494	5.3×10^7	0.923	5.0×10^8	2	
	4	559	6.9×10^7	0.951	5.9×10^7	1.63	

430 K. The behavior of this peak is attributed to the cluster of V-type vacancies which recombine with the interstitial defects created by the dopant in host (Soliman, 2009). The peaks at 480 K and 571 K are attributed to the trapped hole during irradiation which released during the TL read out and recombines with electron trapped at the activator ions (Luthra et al., 1977). Here authors assume that there is a possibility that the all peaks are observed due to the recombination of released holes from V centres to the F centers in lattice.

4.4 Results and discussions of Li doped MgO

4.4.1 X-ray Diffraction Study

XRD patterns of pure and doped samples shown in Fig 4.14 are in accordance with the JCPDS card number 78-0430, which corresponds to the cubic structure of MgO with the space group F m -3 m. After doping of Li in MgO, there is no additional peaks observed shows the successful incorporation of monovalent ions in host matrix. However, there is slight shifting of peaks towards higher angle is observed which is due to difference in ionic radii of Li (0.068 nm) and Mg (0.072 nm) cations. Fig 4.14 and Table 4-4 shows the refined patterns and parameters by using Rietveld Fullprof program (Cui et al., 2015). Pseudo-Voigt function has been used to refine the XRD pattern and is consistent with cubic phase of F m -3 m space group. From the refined parameters, the lattice parameter of the doped sample is reduced, which can be attributed to the replacement of larger Mg ions with smaller Li ions at substitutional sites. The reduction in bond length of Mg-O can be attributed to the lattice distortion resulting from the inclusion of monovalent ions. TEM images were shown in Fig 4.15(a, b) with the resolution of 100 nm of pure and doped samples. It is observed from images that particles are of polygon shape. Fig 4.15(c) shows the SAED patterns of doped sample. The rings correspond to plane (111), (002), (022), (222) are consistent with the plane indexed in XRD patterns.

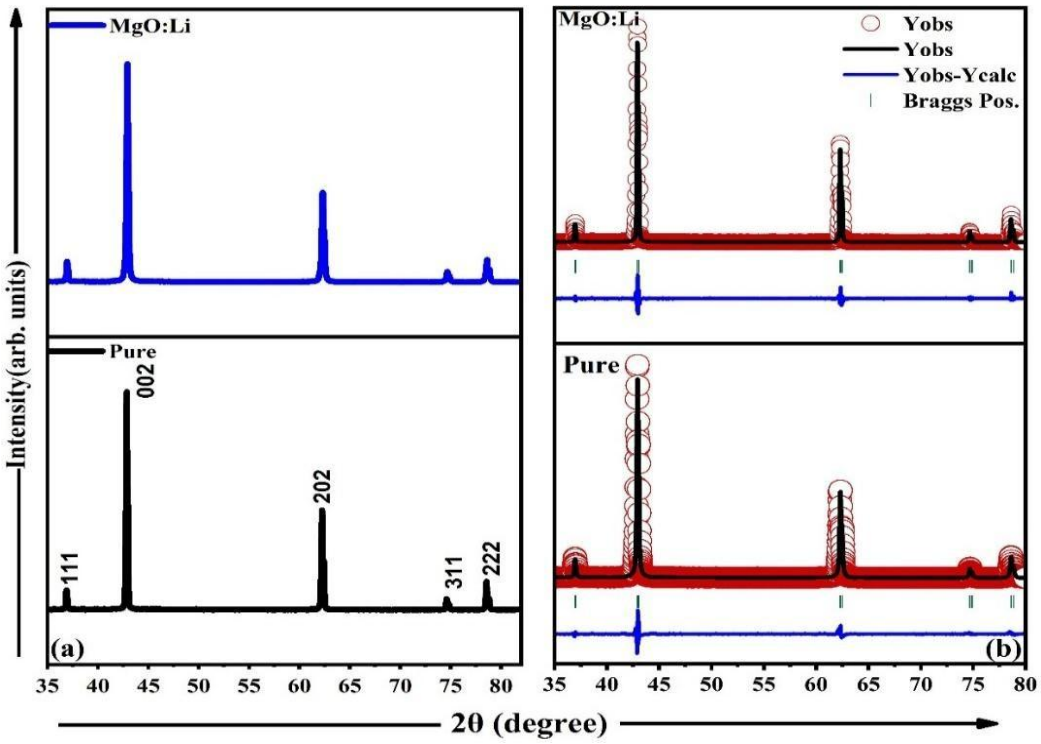

Fig 4.14: XRD pattern and Rietveld refined XRD pattern of pure and doped sample

Table 4-4: Refined parameters obtained from XRD and Rietveld refinement

Sample	Pure	MgO: Li
Lattice constant (a) Å	4.2137	4.2122
Bond length (Mg-O) Å	2.1068	2.1052
Occupancy O Mg Li	1 0.9542 -	1 0.9699 0.0300
GOF	1.3	1.1

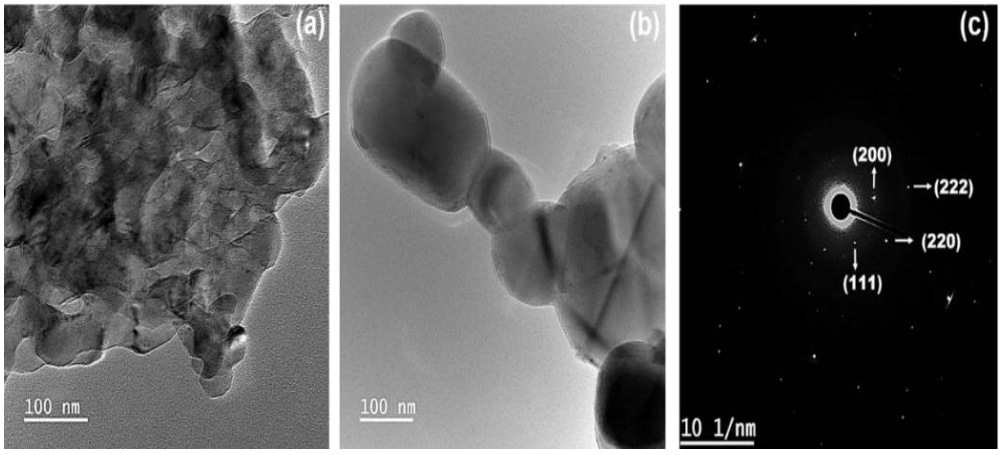

Fig 4.15: TEM images of (a) Pure; (b) MgO:Li ; (c) SAED pattern of MgO:Li.

4.4.2 X-Ray Absorption Spectroscopy Study

Fig 4.16(a) shows the Mg K-edge spectra of doped and pure samples in total fluorescence mode. In both samples, spectral features appear at 1305eV (a), 1310.2eV (b), 1322eV (c), 1351.2eV (d). These spectral features are well matched with those of standard MgO (Fronzoni et al., 2005). The feature **'a'** and '**b'** are attributed to the sharp transition from Mg-1s orbital to degenerated Mg-3p unoccupied orbitals. In doped sample, a minor displacement is observed in feature

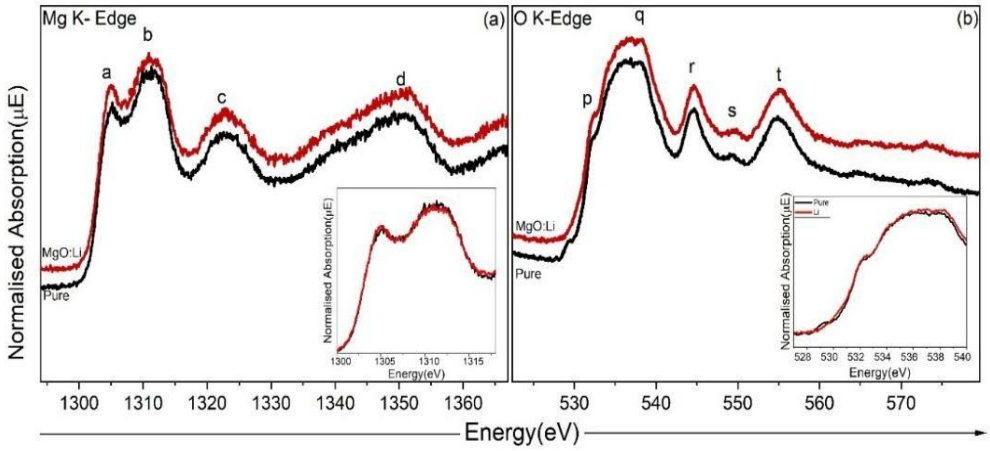

Fig 4.16: (a) Mg K-edge and (b) O K-edge spectra of pure and doped samples in TFY mode

'a' towards lower energy levels as shown in the inset. This displacement can be attributed to the formation of non-saturated host cations in close proximity to oxygen vacancies (Ildefonse et al., 1995). These cations also contribute to the XANES spectra together with the bulk ions of Magnesium. The phenomenon of edge shifting can be ascribed to a decrease in the coordination state of ions with the same valence state (Khamkongkaeo et al., 2018). The feature at 1351.2eV is due to the scattering of nearest neighbors. The overall Mg K-edge spectra do not show any changes which depicts that Mg coordination is not distorted upon doping. Fig 4.16(b) depicts the O K-edge XANES spectral features 532 eV, 535-538 eV, 544.5 eV, 549.6 eV and 555.1 eV marked as p, q, r, s, t. The observed O K-edge spectral characteristics are indicative of MgO and are commonly observed in the O K-edge spectra of MgO. Just like the Mg K-edge spectra, the O K-edge spectra also exhibit no changes upon doping. The feature from p and q arises from the hybridized state of Mg and O sites and O-2p non-bonding states. Pre-edge feature in pure sample is due to bulk Mg vacancies that causes the high density of unoccupied states of O (J. P. Singh et al., 2015a). The absence of pre edge feature in doped sample indicates that the Li is going on substitution sites in lattice and hybridization of Li with O ions causes the reduction in unoccupied states of anions. The substitution replacements of cations is also complementing with the XRD pattern where lattice parameters is decreased after addition of Li in host (Soma & Uchino, 2017). These modification in oxygen vacancies in the lattice also governs the photoluminescence characteristics.

4.4.3 Photoluminescence Spectroscopy Study

The PL spectra of prepared samples is shown in Fig 4.17(a, b). Upon exciting at 275 nm wavelength (Fig 4.16(a)), MgO shows two broad emission bands (i) 350 nm to 500 nm centered at 426 nm and (ii) weak band from 650 nm to 750 nm centered at 680 nm. While, under excitation of 406 nm spectra from 650 nm to 800 nm is observed. The PL characteristics in MgO are due to intrinsic defects

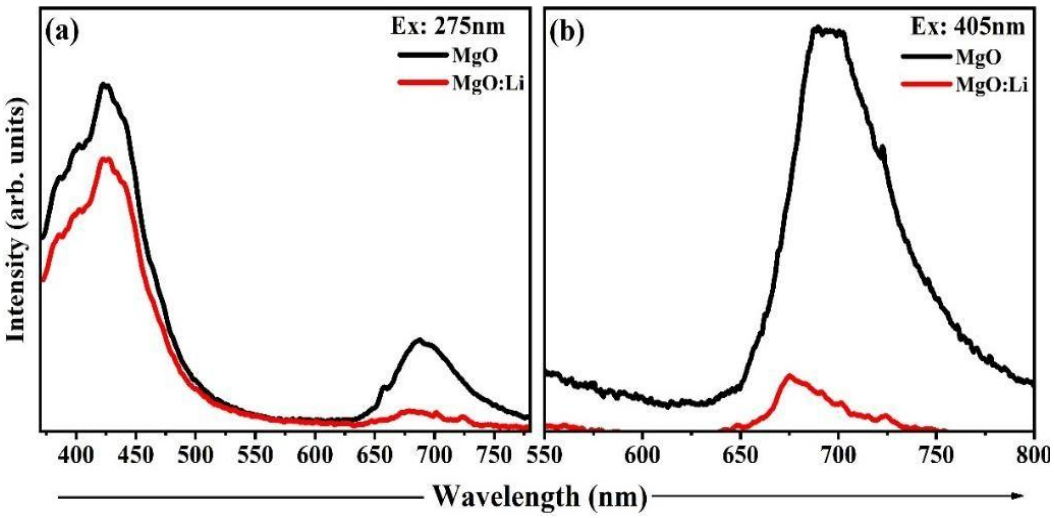

Fig 4.17: Room temperature photoluminescence spectra of pure MgO and MgO: Li under (a) 275nm and (b) 405nm.

present within the band gap and are responsible for emission at different wavelength ranging from UV to red region, as discussed earlier. The addition of lithium in host lattice causes the decrease in overall PL intensity of pure samples. However, the red emission is strongly diminished as compare to the blue emission. The decrease in intensity is due to the additional states created by dopant which attracts the electrons and causes the separation between the electron hole recombination. As reported in literature, addition of lithium enhances the accumulation of electron by creating the defects (Li^+ O^-) and causes the cross relaxation process which occurs when lithium ions adjacent to the hole vacancy (Y. Chen et al., 2020; Uchino & Okutsu, 2008; Yantake et al., 2021). This suggests that monovalent ions function as electron traps, thereby generating novel non-radiative pathways inside the lattice and impeding the radiative recombination of intrinsic defects within the host material. Luminescence behaviour in red region is also observed on excitation of 405nm in pure and doped sample (see Fig 4.17(b). The red emission in pure which is generated due to the recombination of hole (V) from valence band and the interstitial oxygen is completely suppressed with doping. This indicates that the Li^+ does not favour the photo conversion process of V vacancies in lattice. The monovalent ion Li^+ create the charge deficient site at cations sites

which strongly causes decrement in Mg vacancies (Soma & Uchino, 2017), further affects the emission in red-NIR region. Here, we suggest that in Li doped MgO the charge shallow traps are significantly influenced and interact with the hole states generated by the Li defects. The energy level diagram shown in Fig 4.18 depicts the radiative and non-radiative transition in MgO and doped sample.

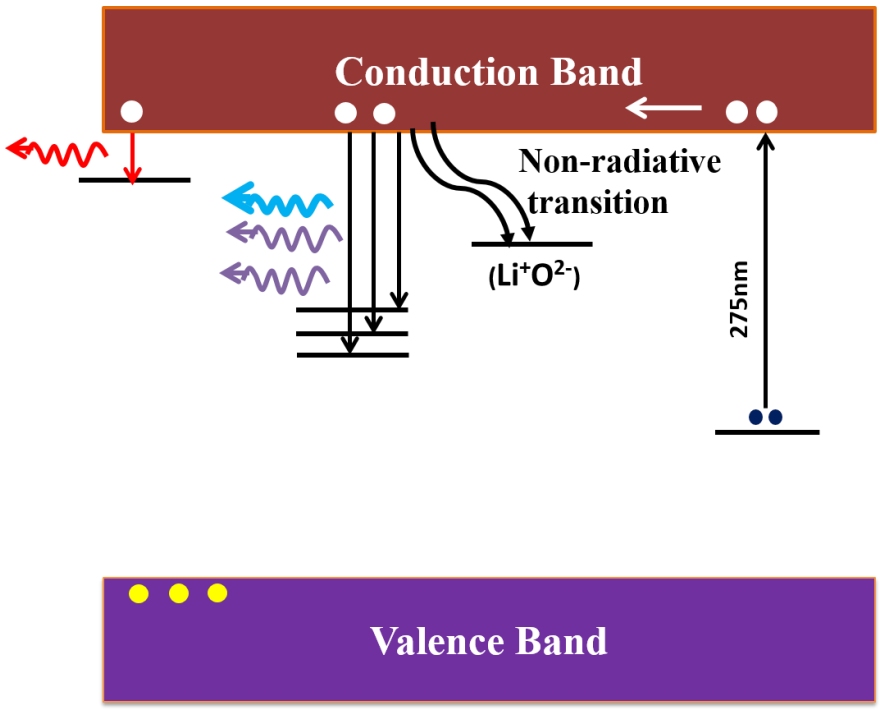

Fig 4.18: Schematic diagram of radiative transition of host defects and new defects created by Li doping. White solid circles shows the electrons in CB and yellow circles are the holes present in VB

4.4.4 Thermoluminescence Study

The photoluminescence response of doped samples discussed above shows that doping affects the multiple traps present in the host by creation of new path. To further evaluate the trap states present in pure and created by Li ions in host, thermo luminescence response were studied after irradiating with gamma radiation

with three different doses (100 Gy, 500 Gy, 1 kGy). Fig 4.19 show the TL glow curves of pure and Li doped MgO. The glow curve peaks in pure sample present in two regions: small and broad peaks from 350 to 450 K and sharp peak from 550 to 675 K centered at 610 K marked as A, B, and C respectively. In pure sample with increase in dose the overall intensity of glow curves decreased in both region. On the other hand, with doping of Li ions the peak at 425 K marked as **B** is increased abruptly while **A** appeared as shoulder of **B** which was prominent in pure sample. The TL intensity increases with dose increment in doped samples specifically at 425 K. Similar results were also reported when Li^+ was doped with other rare earth ions (Y. Chen et al., 2020; Kumawat et al., 2023; Oliveira et al., 2016). It may be assumed that creation of new defects (Li^+ O^-) with addition of Li ions which behaves as electron trap as per previous reports shows the TL peak at 425 K. Apart from new defects, the increase in the number of oxygen vacancies inside the host, as a result of the doping of Li+ ions into the lattice may be responsible for the increased TL signal that was detected for the doped sample. The increment in intensity was attributed to the generation of favorable radiative defects during gamma irradiation. Variation of peak B and C with the doses of doped sample is shown in Fig 4.19(c). The TL intensity of B exhibits a linear increase with dose. This behavior can be explained through track interaction model which suggests that when the sample is exposed to radiation, ionized traps generation depends on cross sectional area and length of tracks within lattice. According to track interaction model, the generation of number of charge carrier concentration depends on the length and cross-section of tracks in matrix. The length of tracks in nanostructures is constrained to a few tens of nanometers, resulting in lesser number of traps at lower dosages. The TL signal is attributed to the longer distance between the activators ions and emission is due to the radiative transitions of charge carriers in respective tracks. When these tracks overlap on higher doses, the TL intensity becomes saturated. While on further increase in dose, the overlapped tracks become more prevalent, allowing electrons to transition between tracks. This collective

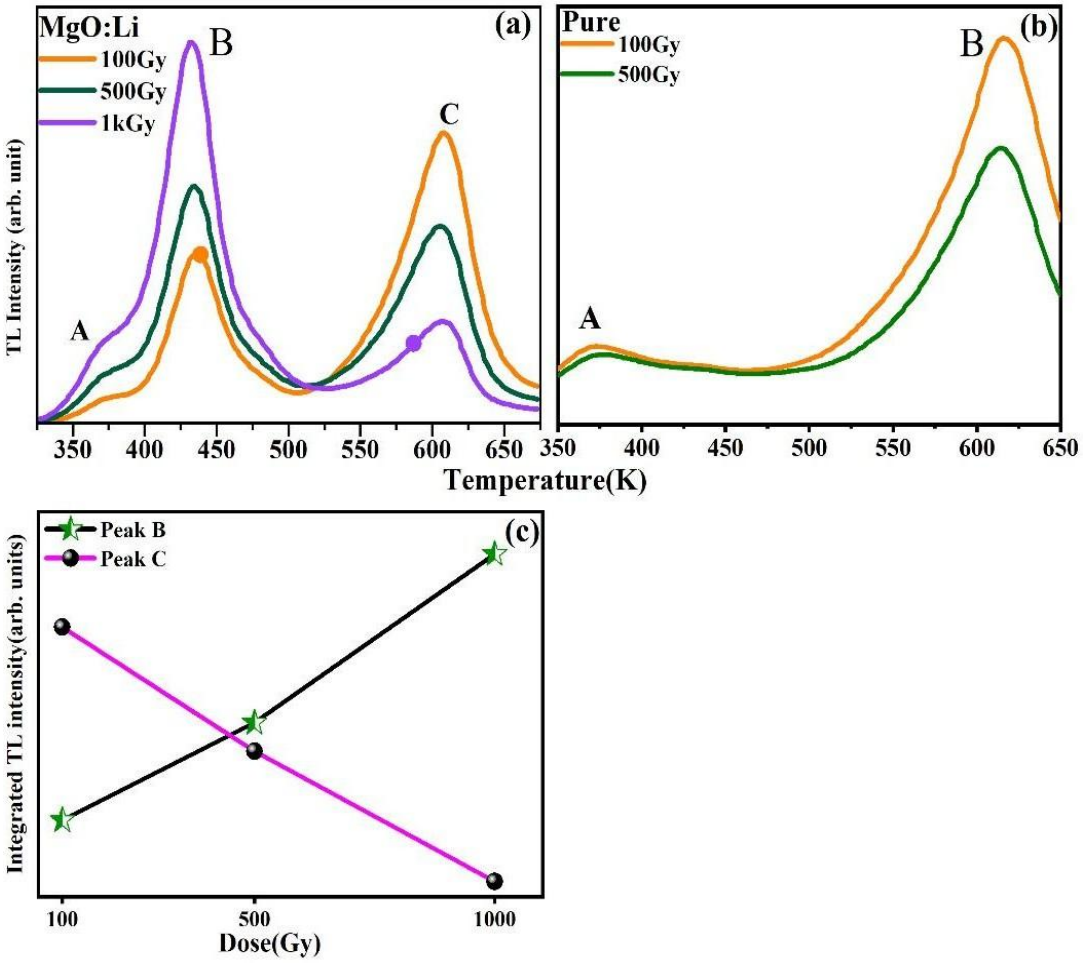

Fig 4.19: TL Glow curves of (a) Pure; (b) Doped sample; (c) Integrated TL intensity of peak B and C of doped sample at all doses.

interaction of the tracks results in a linear correlation between the thermoluminescence (TL) intensity and the dosage (Jain et al., 2020). However, with increase in dose the peak C is decreased shows that addition of Li ions restructuring of traps and make favorable recombination centers to shallow traps as compare to deeper ones. The increase in overall TL intensity with dose and stability of maxima temperature (T_m) of peaks with increase in dose in doped sample indicates the enhancement in the dosimetric characteristics of MgO. To study the behaviors of glow curves of doped sample has been investigated by using TLANAL software. The trap depth, number of charge carriers, frequency factors and order of

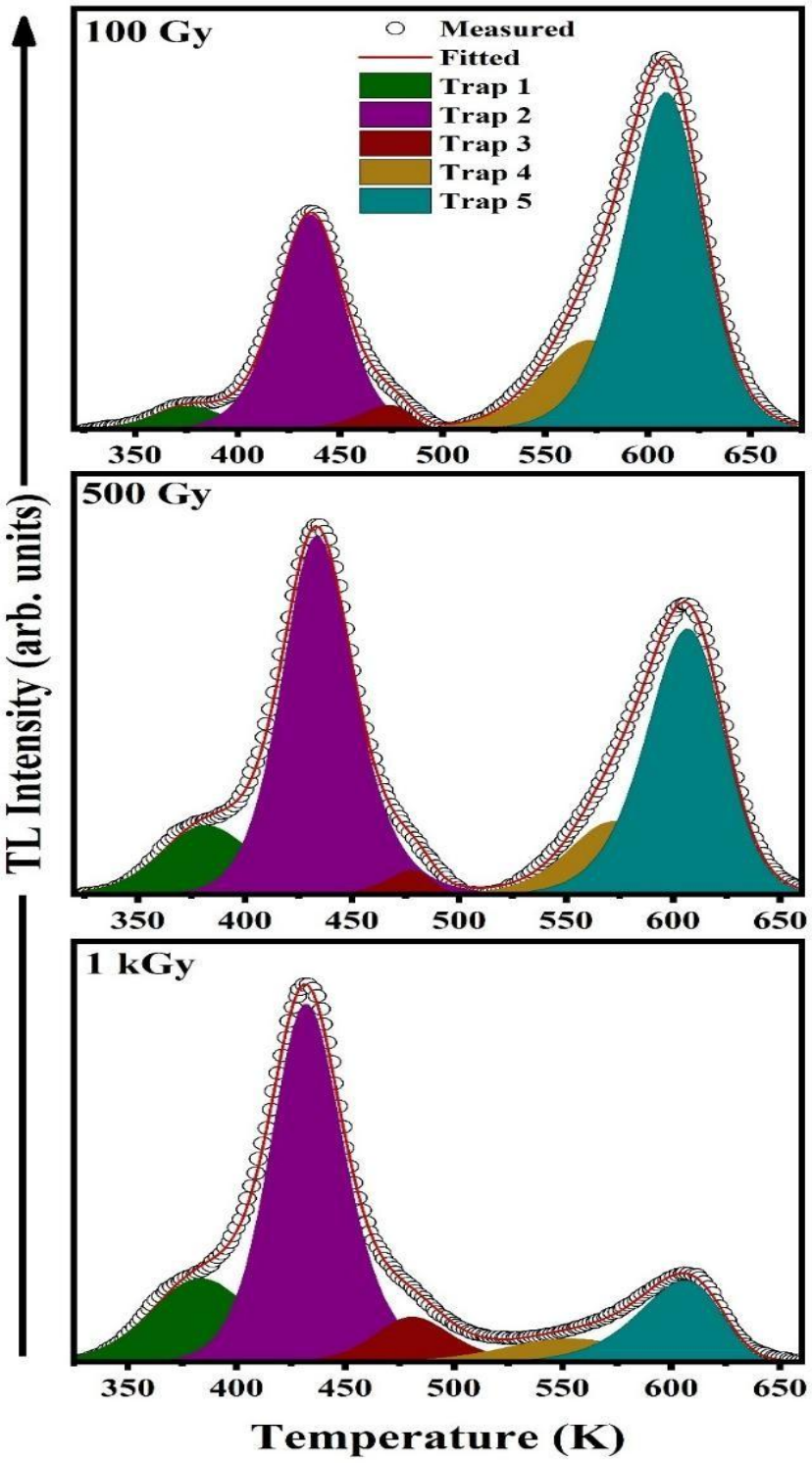

Fig 4.20: Deconvoluted of TL glow curves of doped sample at 100 Gy, 500 Gy, 1 kGy by using TLANAL software

Table 4-5: Kinetics parameters of MgO: Li using TLANAL software

Dose (Gy)	Trap	T (K)	n_0	E (eV)	S (s^{-1})	b	FOM
100	1	375	1.56×10^6	0.923	9.55×10^9	1.21	1.85
	2	437	1.70×10^7	1.143	5.85×10^{10}	1.25	
	3	468	3.42×10^6	1.396	3.99×10^{12}	1.22	
	4	568	8.88×10^6	1.725	6.32×10^{12}	1.82	
	5	608	3.61×10^7	2.022	1.76×10^{12}	1.52	
500	1	376	5.14×10^6	0.940	1.29×10^{10}	2	1.73
	2			1.127	1.47×10^{11}	1.49	
	3	470	3.11×10^6	1.402	3.11×10^{12}	1.15	
	4	570	7.56×10^6	1.739	5.81×10^{12}	2	
	5	608	2.09×10^7	2.075	5.47×10^{12}	1.41	
1000	1	376	1.09×10^7	0.945	1.47×10^{10}	2	2.85
	2	435	4.75×10^7	1.076	1.89×10^{11}	1.61	
	3	475	9.32×10^6	1.412	2.57×10^{12}	2	
	4	559	4.76×10^6	1.720	1.28×10^{12}	2	
	5	605	1.16×10^7	2.094	3.63×10^{12}	1.35	

kinetics of peaks has been analyzed by using the general order kinetics. Fig 4.20 shows the deconvoluted curves of MgO: Li on all the three doses. The graphs show the presence of five traps at 375 K, 437 K, 468 K, 568 K, and 608 K. At 100 Gy dose, the peaks from deeper traps (trap 4 and trap 5) is dominant in the doped samples. It is generally observed that peak at higher temperature in MgO is due to the recombination of hole generated during gamma irradiation with trapped electron during TL readout (Lee & Crawford, 1979; Sathyamoorthy & Luthra, 1978). While with increase in dose at 500 Gy and 1 kGy, the shallow traps contribution is increased while the traps at elevated temperature become broad and weak. The broadening of curves is due to the overlapping of wave function and causes the tunneling of charge carriers. All the kinetics parameters are summarized in Table 4-5. The figure of merit for all deconvoluted peaks is less than 3% showing the good fit. The activation energy of traps lies from 0.92 to 2.02 eV and kinetic order of all traps for 100 Gy is first order kinetics while for higher doses it shows the second order kinetics. The trap depth of trap 5 is increased due to the decrement in population of carriers while the trap depth of trap 2 is decreased due to increase in population as discussed above.

4.5 Conclusions

Undoped, Bi, and Li doped MgO nanophosphors were prepared using the solution combustion method. As-prepared, samples were annealed in air at 1173 K. XRD results and Rietveld refinement have confirmed the single-phase formation of pure, MgO: Li and MgO: Bi with space group *Fm-3m* . MgO lattice offered substitution sites to the Bi^{3+} ions at low doping concentrations (x= 0.01 mol% and 0.05 mol %) which leads to tensile stress and enlargement of the Mg–O bond length. On the other hand Bi^{3+} ions occupy interstitial sites for the higher Bi^{3+} concentrations (x= 0.1 mol% to 0.5 mol%) and, therefore, the MgO lattice experienced compressive strain and a shrinkage of the Mg–O bond length. In case of Li doped MgO, Li doping led to decrease in crystallite size attributed to the

cationic substitution in lattice. UV-visible absorption spectroscopy results convey the Bi^{3+} doping-induced formation of defect centers (F and/or V centers) in the band gap of MgO. TEM images and SAED patterns confirmed the crystalline nature of $Mg_{1-x}O:Bi_x$ samples with an average particle size of ~37.9 nm. XANES investigations at the Mg K-edge and Bi L_3-edge confirms the Mg^{2+} and Bi^{3+} ions in the samples. Bi doping induced modification in the spectral features of the Mg K edge and the O K-edge XANES conveys the Mg and O defects in the $Mg_{1-x}O$: Bi_x samples. While in Li doped MgO, O K-edge revealed that the hybridization of Li ions with oxygen caused a decrease in the unoccupied state of oxygen. PL spectra confirmed blue emission from Bi^{3+} ions, which is attributed to the $^3P_1$ and $^3P_0$ to $^1S_0$ transitions of Bi. The photoluminescence intensity increases up to 0.05 mol% of bismuth, after which it is quenched. Li doping mainly affected the red emission of the host due to the creation of Li+ O- which accumulated the electron and caused the separation between the recombination of the Mg vacancy and the electron. According to the CIE coordinates, the sample with the maximum color purity of 91.3 % was $Mg_{1-x}O$: Bi_x (x = 0.05 mol %). Studies of gamma-irradiated TL properties revealed the presence of distinct band-gap traps. The observed quenching was determined by the concentration of dopants, which alters the density of traps within the band gap. PL and TL properties of $Mg_{1-x}O$: Bi_x nanophosphors may pave the way for applications in solid-state lighting and dosimetry. On the other hand TL results shows that Li ions enhanced the TL intensity with an increase in dose at lower temperatures, which indicates the creation of favorable shallow traps and decrement in deeper traps by affecting the host V vacancies which are complementing the PL results. The stability of peaks in the Li-doped sample with an increase in dose exhibited an improvement in the dosimetric characteristics of MgO, and further optimization in other parameters can improve dosimetry aspects in future endeavors

CHAPTER 5

EFFECT OF RARE EARTH (Sm^{3+}, Ce^{3+}) AND Li^{3+} IONS CO-DOPING ON THE LUMINESCENCE STUDIES OF MgO NANOPHOSPHORS

EFFECT OF RARE EARTH (Sm^{3+}, Ce^{3+}) AND Li^{+} IONS CO-DOPING ON THE LUMINESCENCE STUDIES OF MgO NANOPHOSPHORS

5.1 Introduction

The MgO, a prime member among all the oxides family is still being studied because of its unique characteristics in both bulk and nanoscale forms, and its diverse uses in microelectronics, photocatalysis, plasma display panels, dosimetry, and biomedical applications (Chinthala et al., 2021). Various approaches have been employed to manipulate the characteristics of pure MgO, including varying precursor materials, synthesis methodologies, and annealing temperatures.

MgO was first introduced as a TL phosphor by Thomas et al. (Uenaka & Uchino, 2011). Due to its small effective atomic number (Z-10.8), which is virtually identical to that of human tissue, it has been rigorously studied for dosimetry applications (Oliveira et al., 2016). However, due to the absence of a consistent pattern in the TL properties of this material was initially rejected for dosimetry applications (Soliman, 2009; Yukihara et al., 2013). Several factors lead to inconsistent TL such as; variations in sample sources, pre-exposure annealing, exposure followed by annealing, and thermal behaviour. A consistent TL peak at 300 K, which is prominent for dosimeter detectors, was reported by Bos et al. (Bos et al., 2006). They have investigated stable and broad emission from the Tb^{3+} in MgO which is attributed to the interaction of clustered V vacancies with impurity ions. Enhanced glow curves near 400 K have also been reported with doping of Ce^{3+}, Tb^{3+}, Eu^{3+}, Yb^{3+}, Dy^{3+}, and Nd^{3+} in MgO in different experimental studies (Bishnoi, Dhiman, et al., 2024; Bishnoi, Kumar, et al., 2024; Gu et al., 2008; Guckan et al., 2020, 2021b; Kaur et al., 2021; Oliveira et al., 2019b; Seth et al., 2023; Srisuvetha et al., 2020). Rare earth elements and transition elements have been utilized as dopant phosphors in past years due to their

well-known luminescence properties and lifetime. Lanthanide elements have exceptional characteristics such as forbidden f-f transition due to their potential optical properties which are controlled by host emission is a key factor for luminescence applications. Therefore, doping of RE elements influences the luminescence of MgO which may be due to the modification in density of defects, surface defects, aggregations of intrinsic defects, and recreation of new traps.

It is imperative to investigate and acquire a comprehensive understanding of the alterations that occurs in the band structure of the MgO compound when doping of Sm, Ce, and co-doping with Li ions are modified. The MgO lattice consists of Mg^{2+} ions under the octahedron environment of O ions and the introduction of new defects may lead to the distortion in the Mg-O bonds which, indeed, dictates the modifications in the crystal structure, energy band-structure, and, consequently, the luminescence properties. Substitution of Sm^{3+}, and Ce^{3+} at place Mg^{2+} changes the symmetry around cations and disturbs the cationic distribution. This, in turn, induces phonon-photon interaction within the lattice. This interaction gives rise to the potential occurrence of forbidden transitions during photo-excitation, leading to a finely tuned emission.

5.2 Experimental details

Synthesis and characterization

Pure and doped samples have been prepared by using the solution combustion method. Magnesium nitrate hexahydrate (CDH 99%), Samarium nitrate (CDH 99.9%), Cerium nitrate $Ce(NO_3)_3.H_2O$ and Lithium nitrate (CDH 99 %) are used as oxidizers, and Urea (CH_4N_2O) is used as fuel. All the precursors and fuel were mixed in 100 ml distilled water after being taken according to stoichiometric ratio. The homogenous solution was prepared by stirring for half an hour. The solution was heated in a furnace at a temperature

of 600 ºC. After completion of the combustion process, the obtained white fluffy product was crushed into fine powder. Synthesized samples were annealed to 1173 K for three hours. Undoped MgO is referred to as **Pure** throughout the study. Samples doped with 0.1 mol%, 0.2 mol%, and 0.5 mol% of Sm are referred to as **S1, S2, and S3** in the report, while the sample co-doped with 0.1 mol% of Sm and 3 mol% of Li is named **SL.** Additionally, the other series of samples which Ce and Li are doped with 0.05 mol%, 0.1 mol%, 0.2 mol%, and Ce with 0.1 mol%; Li with 3 mol% is referred as **C0, C1, C2, C3, and CL** for further analysis. To analyze the crystal structure and phase identification of powder samples, X-ray diffraction (XRD) patterns were recorded using an X-ray diffractometer (Bruker, D8 advance EcoPro) irradiated with Cu-K_α radiation (λ = 1.54056 Å). Transmission electron microscope (TEM) images were collected, for morphology analysis, from the JOEL-2100 instrument operated at a voltage of 200KV. The low energy X- ray absorption near-edge structure (XANES) spectra at O K-edge and Mg K- edge are collected in total fluorescence yield mode at the soft X-ray beamline (10D XAS KIST-PAL). Sm L_3-edge, Ce L3-edge XANES spectra are collected in total electron yield (TEY) mode under a vacuum of $1.5x10^{-8}$ Torr at the 1D X-ray scattering beamline of the Pohang. Photoluminescence (PL) experiments were carried out at room temperature using a RIMS spectrometer with two excitation sources: a LED of 275 nm and a laser of 405 nm. Long pass filters of 320 nm and 420 nm were used to deduct the signal of the source spectra. UV-Vis spectra has been recorded at room temperature by RIMS UV spectrometer using deuterium and halogen lamp as source and Teflon as the reference for sepctra. In the context of thermoluminescence (TL) experiments, the samples underwent an initial preheating process at a temperature of 773 K for 1 hour. Subsequently, the samples were exposed to gamma rays at doses of 100 Gy, 500 Gy, and 1 kGy, utilizing a ^{60}Co source within Gamma Chamber 1200. Thermoluminescence

(TL) glow curves were collected with a heating rate of 5 °C per minute within the temperature range of 323 K to 623 K.

5.3 Results and discussion of singly doped Sm^{3+} MgO and co-doped with Sm^{3+}, Li^{+}

5.3.1 X-ray Diffraction Study

Fig 5.1(a) shows the XRD patterns of Pure, S1, S2, S3, and SL samples. The peak position at angles 36.94º (111), 42.91º (020), 62.29º (022), 74.68º (311), and 78.61º (222) were well indexed and matched with the JCPDS card no- 87-0653 with space group *Fm-3m* (225) revealing the formation of single cubic phase of MgO nanocrystals. No XRD peaks from samarium oxide or lithium oxide are detected, under the detection limit of used XRD, thus nullifying the trivial phase formation in the present study. At lower concentrations, the XRD peaks are shifted

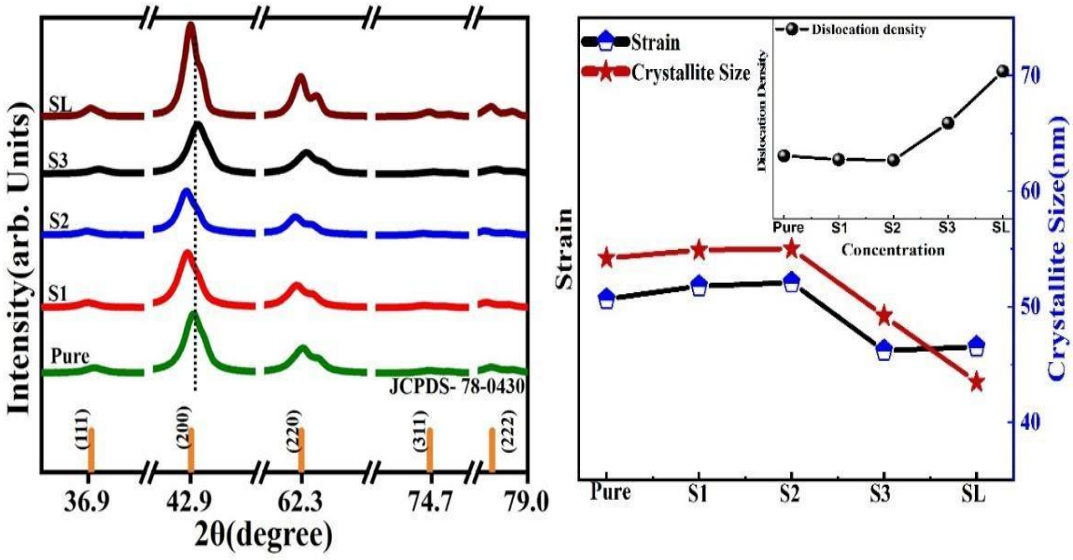

Fig 5.1: (a) XRD patterns of all of the Sm^{3+} and Sm^{3+}, Li^{+} doped MgO nanocrystals (b) Variation of strain and crystallite size with concentration

However, with increasing the Sm^{3+} doping concentrations (sample S3), the XRD peaks shift to higher angles. Similar kinds of competitive behavior of substitution and interstitial doping of rare earth elements have been reported in the literature (Kumawat et al., 2023; Q. Shi et al., 2014). The XRD peak shifting can be understood by considering the ionic radius of host cation and dopant cations (Sm^{3+} = 0.096 nm Mg^{2+} = 0.072 nm). The observed broadening in XRD peaks may be attributed to the strain in the MgO lattice. Likewise, variation in the XRD peak intensity ratio and variation in the FWHM may correlate with the formation of vacancies and other structural perturbations. Dopants may create dislocations/defects by occupying the interstitial or substitutional sites in MgO. The dislocation density is given by $\delta = 1/D^2$ where D is crystallite size (P. Kumar et al., 2023). The calculated dislocation density is higher in doped samples and indicates a significant amount of imperfection in the MgO lattice upon Sm^{3+} doping, which causes the strain in the lattice. The strain in the lattice is calculated using the W-H

Table 5-1: Lattice parameters of pure and doped MgO nanocrystals

Sample	Lattice parameter (Å)	Crystallite size (nm)	FWHM (°)	Strain (10^{-4})	I_{200}/I_{220}	$\delta=1/D^2$
Pure	4.21	54.3	0.21	1.56	2.35	0.000341
S1	4.22	44.1	0.24	2.33	2.20	0.000332
S2	4.21	46.3	0.24	2.53	2.19	0.000332
S3	4.20	49.2	0.23	-1.44	2.26	0.000413
SL	4.18	43.5	0.13	-1.22	2.29	0.000528

plot (Kaur et al., 2021; Kumawat et al., 2023) and strain and crystallite size variation has been shown in Fig 5.1(b). The calculated lattice parameters and W-H strain parameters of all samples are tabulated in Table 5-1. It has been reported that the increased strain, with doping concentrations, can facilitate an increase of non-stoichiometric oxygen and cationic vacancies in the lattice of the host compound (Malleshappa et al., 2014). The shifting of the (200) peak from 42.8˚ to 43.92˚ in the co-doped sample (SL) shows a competing behavior of Li^{+} and Sm^{3+} substitution at Mg^{2+} lattice sites. The substitution of Li^{+} at the Mg^{2+} site is more favorable because of its smaller ionic radii (0.068 nm). Apart from that increase in diffraction intensity and a significant decrease in FWHM (from 0.23º to 0.13º) is also observed in the co-doped sample. It indicates that Li^{+} promotes the crystallinity of the MgO. Moreover, the incorporation of Li^{+} ions may also provide (Li_i) interstitial defects in MgO because of its small size.

5.3.2 Transmission Electron Microscopy Study

Morphological analysis is carried out using TEM images of S3 nanocrystals at a resolution of 100 nm and is presented in Fig 5.2(a). The morphology of samples demonstrates that crystals are polyhedron-shaped. The broad distribution of size is due to the agglomeration of crystals during annealing at 900 °C. Calculated particle sizes from TEM images complement with results of XRD data. The crystal planes in TEM images (see Fig 5.2(b)) shows an interplanar distance of 0.203 nm and 0.148 nm is observed in the S3 sample corresponding to (200) and (220) planes, respectively. Such observations are convincing the interplanar spacing calculated from XRD data; i.e. 0.207 nm and 0.149 nm correspond to (200) and (220) crystal planes, respectively. A particle size distribution is evaluated using ImageJ software and shown in Fig 5.2(c). The size distribution is in the range of ~50 nm for the S3 sample. The SAED images in Fig 5.2(d) reflect typical ring patterns and confirm the polycrystalline nature of the prepared samples. In the ring

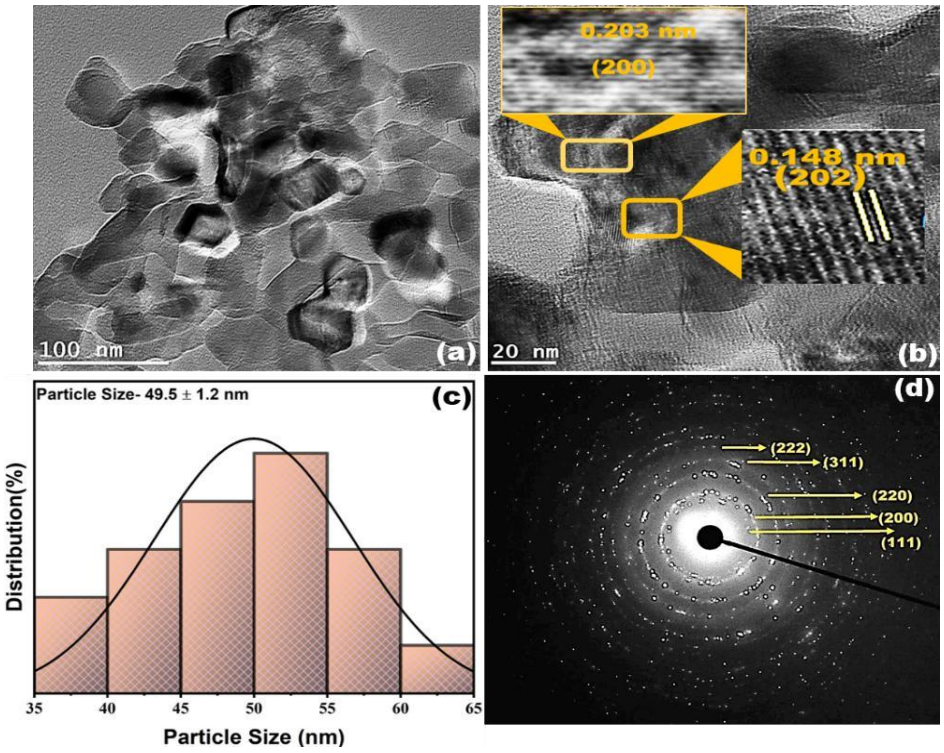

Fig 5.2: (a) TEM images at 100 nm resolution (b) Interplanar spacing of pure and S3 at a resolution of 20 nm (c) Particle size distribution Sm doped MgO (S3) (d) SAED patterns

patterns, the crystallographic planes: (111), (200), (220), (311), and (222) of the MgO phase are apparent and no other plane of the secondary phase could be detected and convincing the absence of trivial phases in pure and doped MgO samples.

5.3.3 X-ray Absorption Spectroscopy Study

Fig 5.3(a) depicts the XANES spectra of Mg K-edge for pure and doped samples. The prominent spectral features at 1304.9 eV, 1310.5 eV, 1322.6 eV, and 1350.9 eV are marked as **B_1, B_2, B_3, and B_4,** respectively. In previous reports, the spectral features of Mg K-edge XANES have been reported for identifying the tetrahedron and/or octahedral site symmetry of Mg ions under the same valence state (Hao et al., 2017). It has been reported

that the white line peak position of Mg K-edge XANES, of $MgAl_2O_4$ compound, appeared at 1294.5 eV for tetrahedrally coordinated Mg ions but the MgO obeys white line peak position at 1304.6 eV for octahedrally coordinated Mg ions (Yoshida et al., 1995). Likewise, for the distorted octahedron, the edge-energy position moves towards the higher energy in the case of Mg(OH) and $Mg_2CO_3(OH)_2$ compounds (Yoshida et al., 1995). In the present study, the maxima of feature **B_1** moves from 1304.9 eV to 1303.6 eV as a function of doping. Trivalent dopants may create unsaturated Mg cations adjacent to anion vacancies in lattice. With the increase of doping concentrations, the δB1B2 (energy difference between peak B1 and B2) decreases from 6.6 ± 0.2 eV to 6.2 ± 0.2 eV. This indicates a net distortion around the geometry of host cations and, seemingly, fractional tetrahedral occupancy of Mg cations in the doped samples (J. P. Singh et al., 2015a). O K-edge spectra are shown in Fig 5. 3(b). Spectral features observed at 529 eV, 532 eV, 536-538 eV, 544 eV, 549 eV, and 555 eV are marked from **p** to
v. Pre-edge feature, **p,** is well resolved in the pure sample which is attributed to the surface defects and or localized bound states (Y. Chen et al., 2024; J. P. Singh et al., 2019, 2021; Zhai et al., 2024)

The intensity of pre-edge feature is diminished with doping and indicating minimal interaction between the Mg-3s and O-2p localized bound states. The intensity of the **q** feature is enhanced (inset of Fig 5.3(b)), with dopant concentrations, indicating the availability of more unoccupied O-2p and Mg-3s hybridized, density of states due to the development of more charged vacancies in the host MgO. This enhancement of charged vacancies can affect the ionicity between Mg-O bonds causing the reduction in feature
r. The feature**s** were merely affected at low doping concentrations but sharpened at higher doping concentrations indicating the increase in interstitial oxygen in lattice. The charge neutrality of the MgO lattice is disturbed because of the different valance states of cations in the doped samples. The charge neutrality can be compensated by forming neutral or

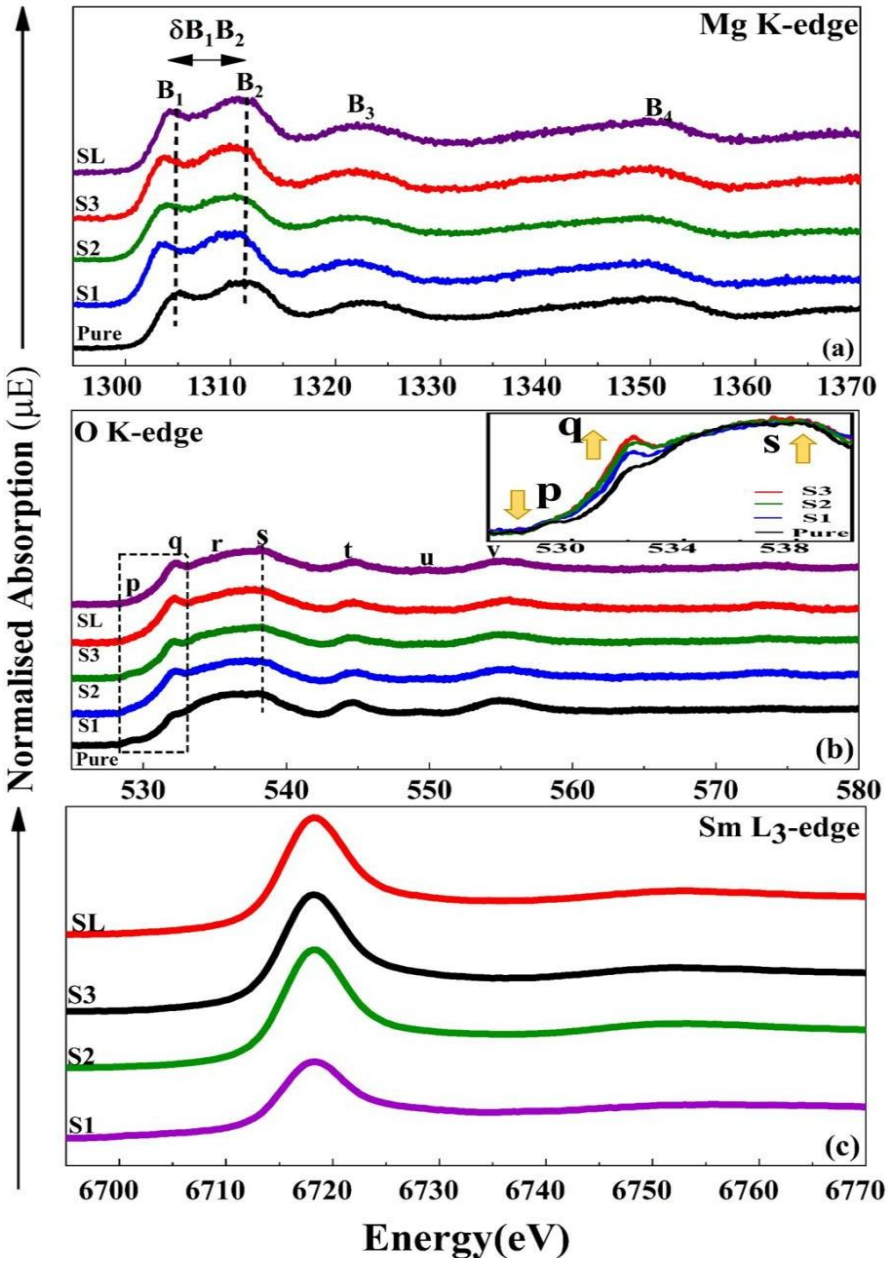

Fig 5.3: XANES spectra of (a) Mg K-edge (b) O K- edge (c) Sm L_3- edge.

charged O defects as a function of doping concentration (Frati et al., 2020). Such defects, indeed, affected the luminescence properties and shall be discussed in the following sections of the article. The Sm^{3+} L_3-edge XANES spectra are shown in Fig 5.3(c). All of the spectra are very similar and reflect

that Sm^{3+} ions are in a +3 oxidation state. The post-edge features in Sm^{3+} L_3-edge are attributed to the 2p to 5d transitions (Nantharak et al., 2017). No additional peaks and observable shifting of peaks are observed which indicates an invariance of the valance state in all of the samples. However, intensity is low at lower Sm^{3+} concentrations and increases at higher doping concentrations. This indicates the existence of more unoccupied 5d orbitals as the Sm^{3+} ions are incorporated into the host.

5.3.4 Photoluminescence Spectroscopy Study

The Room temperature emission spectra of pure and doped MgO are recorded at excitation of 275 nm (UV LED) and 405 nm (blue laser) and presented in Fig 5.4(a,b). The Emission spectra (at $\lambda_{excitation}$ = 275 nm) consist of three features: (i) intense emission centered at 427 nm, (ii) broad emission in the red region centered at 690 nm, and (iii) weak and sharp peaks in the range of 550 to 680 nm. The doping of Sm^{3+} ions in MgO creates various imbalanced charge states in the lattice. Either interstitial oxygen is added to the lattice or one Mg vacancy (V_{Mg}) is introduced for two trivalent impurity ions($2Sm^{3+}$)to balance the charge. The equations for these generated defects are shown below:

$$3Mg^{2+} = 2Sm^{3+}_{Mg} + V_{Mg} \qquad \text{Eq. 5.1}$$

$$3Mg^{2+} = 2Sm^{3+}_{Mg} + Mg^{2+} + O^{2-}(\text{interstitial}) \qquad \text{Eq. 5.2}$$

In the present study, from Fig 5.4(a) it is clear when the dopant is introduced in the host, the emission of the host is suppressed in both regions in S1 in S2, while in S3 the emission in red is enhanced. Dopant emission is visible only at higher concentrations with low intensity due to its low absorption in the UV region also

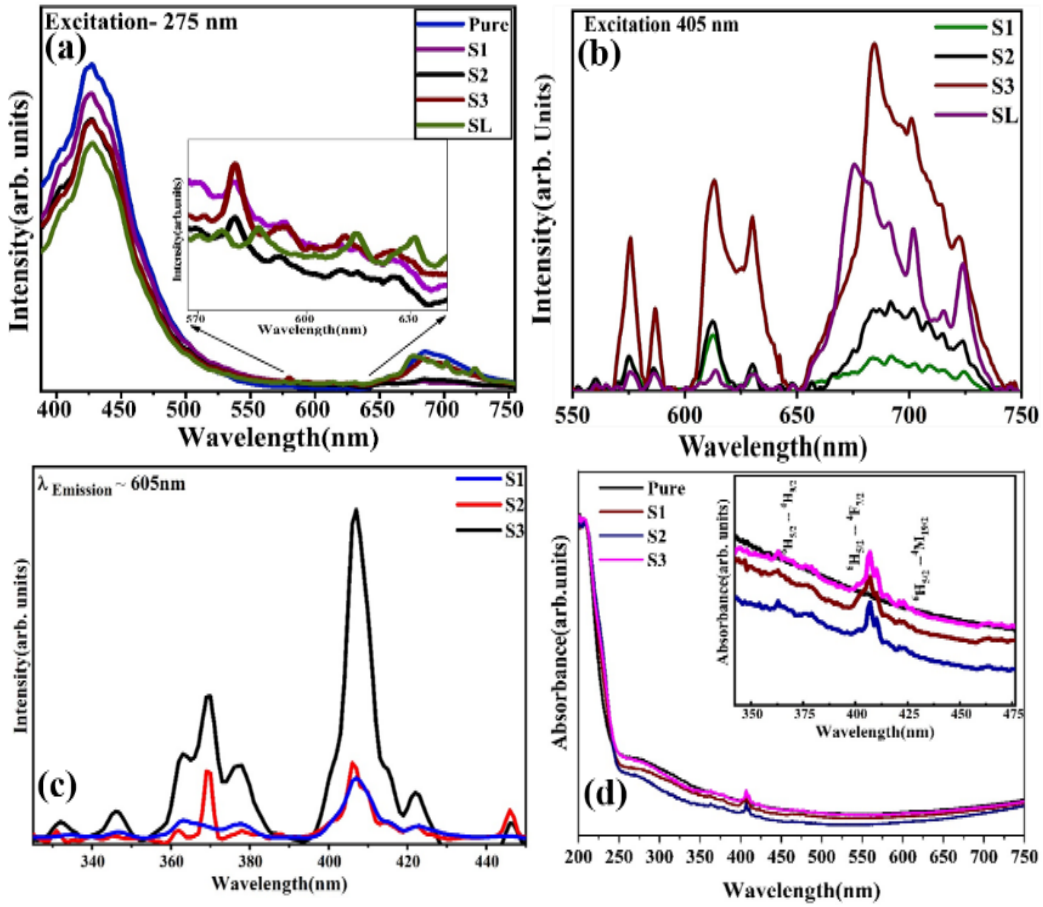

Fig 5.4: (a) PL emission at excitation of 275 nm (b) PL emission of pure and doped samples at excitation of 405 nm (c) Excitation spectra of doped samples recorded at emission wavelength 615 nm (d) UV –Vis absorption spectra of Sm^{3+} doped MgO nanocrystals

confirmed by UV-Vis absorption shown in Fig 5.4(d) (Dillip et al., 2013). Based on the observations of XRD and XANES, it has been determined that the introduction of Sm^{3+} ions has an impact on the Mg coordination and charged vacancies within the host material. This effect is further evidenced by the photoluminescence (PL) behavior, specifically concerning the radiative recombination of single vacancies and F^{+}, F^{2+} charged cluster centers within the host material. Due to this reason, the red region is diminished effectively as

compared to the blue region at low concentrations. Therefore, at low concentrations, Sm^{3+} is not able to act as an efficient luminescent center but it acts as an electron trap contributing to the non-radiative recombination. In S3, a decrease in the blue emission while the increase in characteristics emission of dopant along with the host red emission is observed. Red emission at higher concentrations is due to an increase in interstitial defects as indicated by the O K-edge XANES spectra. It is assumed that increased concentration causes the redistribution of defects in the band gap and increases the probability of charge transfer to the dopant from the host. From Fig 5.4(b), a similar pattern in the emission profile of all samples is observed on exciting with 405 nm wavelength. Characteristic emission of dopants at 405 nm is due to efficient charge transfer from to dopant and its absorption near 400 nm as per recorded excitation spectra on fixed wavelength emission of 615 nm shown in Fig 5.4(c) which is well matched with the absorption spectra shown in Fig 5,4 (d) (Z. Wang et al., 2012). The sharp and distinct peaks, shown in Fig 5.4(b), arise due to the intra-f-f transitions of Sm^{3+} ions. Peaks between 550 nm to 570 nm are due to the magnetic dipole (MD) transitions of $^4G_{5/2}$ to $^4H_{5/2}$. Peaks between 580nm to 615 nm are due to the mix of components of magnetic dipole and electric dipole (ED) transitions from $^4G_{5/2}$ to $^4H_{7/2}$ while peaks in the range of 640 nm to 670 nm are due to an electrical dipole transition from $^4G_{5/2}$ to $^4H_{9/2}$. Peaks at 705 nm and 725 nm imposing with host broadband are due to the transition from $^4G_{5/2}$ to $^4H_{11/2}$ which is again electric dipole transition (Dillip et al., 2013). The electric dipole transitions are extremely sensitive to the crystal field environment because these are forbidden as per Laporte's rule and only occur due to doping which breaks the inversion symmetry of ligands in the crystal. To calculate the symmetric nature of the MgO host matrix, the ratio of the intensity of peaks due to electric dipole transition i.e. $^4G_{5/2}$ to $^4H_{9/2,}$ and due to the magnetic dipole transition i.e. $^4G_{5/2}$ to $^4H_{5/2}$ is measured.

$$\frac{\oint \mathbf{I_1}(\mathbf{4G_{5/2}\rightarrow 4H_{9/2}})\mathbf{d\lambda}}{\oint \mathbf{I_2}(\mathbf{4G_{5/2}\rightarrow 4H_{5/2}})\mathbf{d\lambda}} = \mathbf{S_{12}} \qquad \text{Eq. 5.3}$$

Here S_{12} is a symmetric ratio and I_1 and I_2 are intensities arising from the ED and MD transition. The ratio comes out to 21.02 in all concentrations. In our investigations, the intensity due to ED transitions is more intense than the Intensity due to the MD transition which shows the asymmetric nature of the MgO host matrix. Changes in the local environment of Sm^{3+} ions in the host and reduction in the symmetry strength of MgO are responsible for the intensity reduction and broadening of emission peaks. In the SL sample, dopant characteristics peaks with broadband emission of the host in the red region were enhanced and showed a significant effect of Li ions co-doping in S1. When trivalent ions are introduced in the MgO and occupy the divalent Mg places in the host, due to the difference in charge and radii of dopant and host lattice distortion occurs, and symmetry around dopants changes (Gu et al., 2008; Oliveira et al., 2013). The addition of lithium ions at the site of Mg sites in the lattice created a negative charge defect which acts as an optimal charge compensator that influences the luminescence in the host MgO. In general, high-crystalline phosphors are brighter in emission (Gu et al., 2008). From XRD results it is observed that Li addition improves the crystallinity in MgO which complements our PL results.

To study the efficiency of illumination of prepared samples CIE chromaticity parameters are studied. From Fig 5.5(a, b) it is visualized that by switching the excitation wavelength from UV (275 nm) to blue (405 nm) region the emission of samples is tuned from blue to red region indicating that in the case of 405 nm the dominant emission due shallower cluster defects of the host along with the characteristics peaks of dopant. This behaviour is more prominent in the S3 sample as the coordinates are moving towards the red region, shown in the enlarged image of Fig 5.6(a). All the chromaticity parameters are tabulated in Table 5.2. The color purity of raw phosphors is in the range of 82 to 84% on UV excitation and, the purity is
99.9 and 99% for 403 nm excitation in all samples which is much higher than any other host such as Sm doped in $Sr_{19}Mg_2PO_4$ which has a purity of 96.7% while another phosphors $KNaB_2P_3O_{10}$ when doped with Sm gives purity of

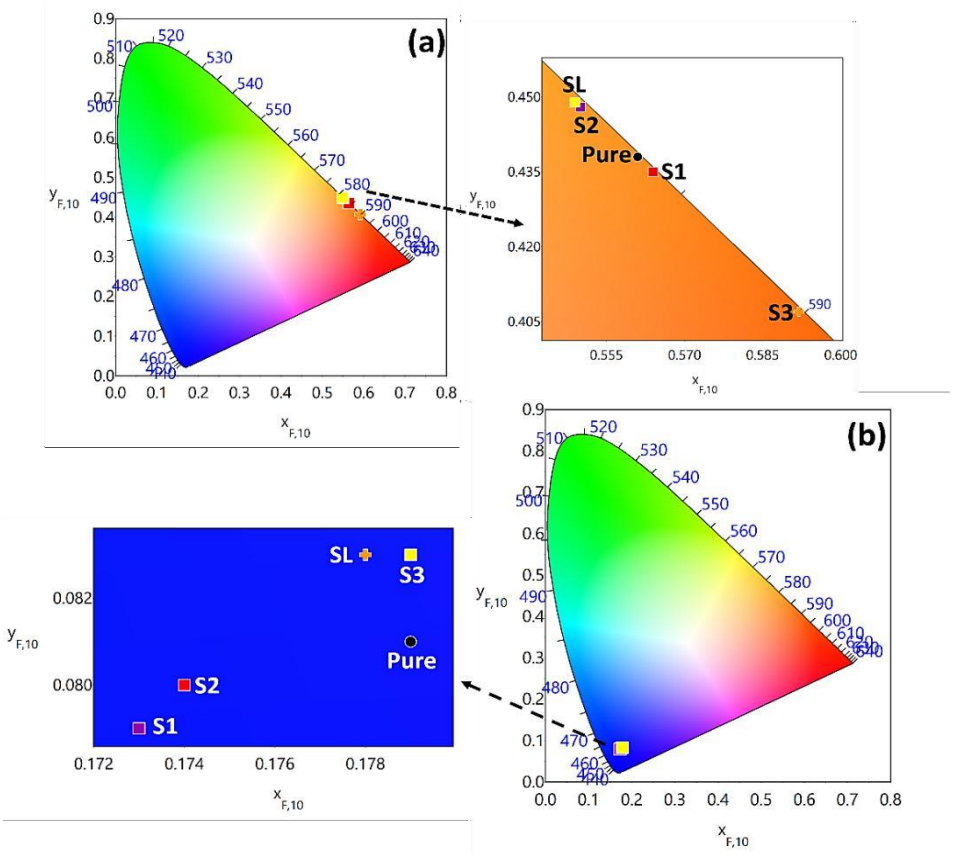

Fig 5.5: CIE diagram for excitation at (a) 405 nm and (b) 275 nm.

Table 5-2: CIE colorimetric parameters

	UV LED (275nm)			Blue Laser(405nm)		
Samples	CIE (x, y)	Purity (%)	CCT (K)	CIE (x, y)	Purity (%)	CCT (K)
Pure	(0.179,0.081)	82.2	1825	(0.561, 0.438)	99.9	1882
S1	(0.174, 0.080)	83.6	1841	(0.564, 0.435)	99	1842
S2	(0.173,0.0791)	84.1	1850	(0.550, 0.448)	99.1	2024
S3	(0.178,0.083)	82	1854	(0.592, 0.407)	99	1933
SL	(0.179,0.083)	82.2	1854	(0.549,0.449)	99	2029

83% (Seth et al., 2023). The observed CCT value on both excitation sources is below 3200 K. The CCT and purity indicate that prepared phosphors are warm emitters and are efficiently used for the respective application of WLEDs.

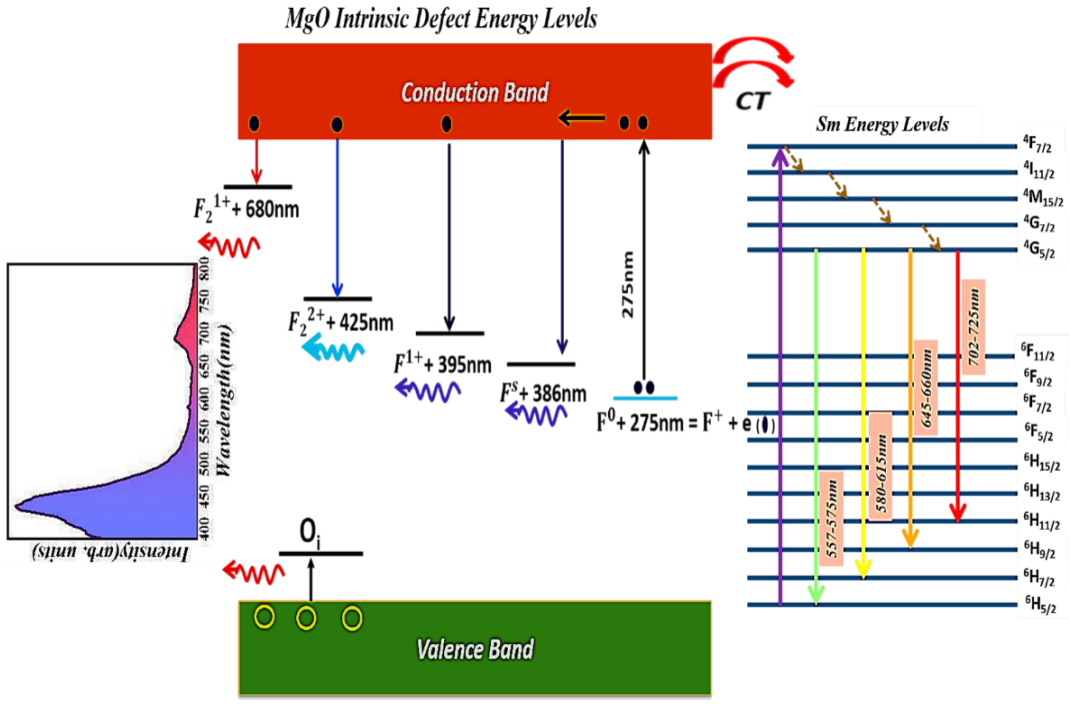

Fig 5.6: Schematic model diagram representing the energy transfer mechanism and PL emission

The mechanism of emission due to host and dopant is explained with the help of a model of the band diagram shown in Fig 5.6. Solid circles are electrons, hollow circles are holes and solid arrows are transitions involved. In the energy level diagram, the solid violet arrow excitation process and brown arrows are the non-radiative transitions of Sm3+ ions solid arrows are radiative transitions of Sm3+ ions. On excitation at 275nm, electrons get excited to CB from a defect present inside the band gap and act like free charge carriers by recombining with different defects emitted at different wavelengths. Emission at 386 nm is the trapping of free electrons at F^+ centers

and photoconversion of F^+ into F by eq. $F^+ + e^- \rightarrow F^0 + h\upsilon$ (386 nm). Similarly, photoconversion of F_2^{3+} in F_2^{2+} by recombination of an electron to the F_2^{3+} and emission designated as F_2^{2+} emission at wavelength 427 nm and 441 nm. Emission at 680 nm is due to F^+ centers attributed to the encounter of e^- on F_2^{2+} centers. The diagram shows the charge transfer between the host and Sm^{3+} energy levels involved in emission.

5.3.5 Thermoluminescence Study

To examine the trap states present in the samples, various doses (100 Gy, 500 Gy, 1 kGy) of gamma rays were utilized to irradiate all of the samples. It is observed that glow curves consist of several peaks and indicate multiple trap participation in thermoluminescence properties. At low- temperature, peaks ranging from 340 K – 470 K are observed in all of the samples; while in higher-temperature regions, peaks are observed ranging from 500 K- 670 K, and 525 K-675 K in Pure, and doped samples, respectively. TL glow curves of all samples at different doses are shown in the Fig 5.7. The lower region has two features marked as **A,** and **B** shows broad and symmetrical behaviour in all samples while an additional feature is observed at the higher temperature region marked as **C**. In the Pure MgO sample, feature **A** and **C** are sharp while a broad hump with less intensity appears at **B**. Peak at 374 K is the signature peak of pure MgO that arises due to the presence of intrinsic V_m (neighbouring defects) vacancies (Luthra et al., 1977). Peak slightly higher than 540 K in pristine MgO is due to the surface defects present in the host reported by several authors (Guckan et al., 2020, 2021b; Oliveira et al., 2019b). No shifting is observed in maxima temperature (T_m) with an increase in dose, indicating that T_m is constant with dose, however, the intensity is decreased with an increase in radiation dose, suggesting that the glow curves follow the first order of kinetics. At the

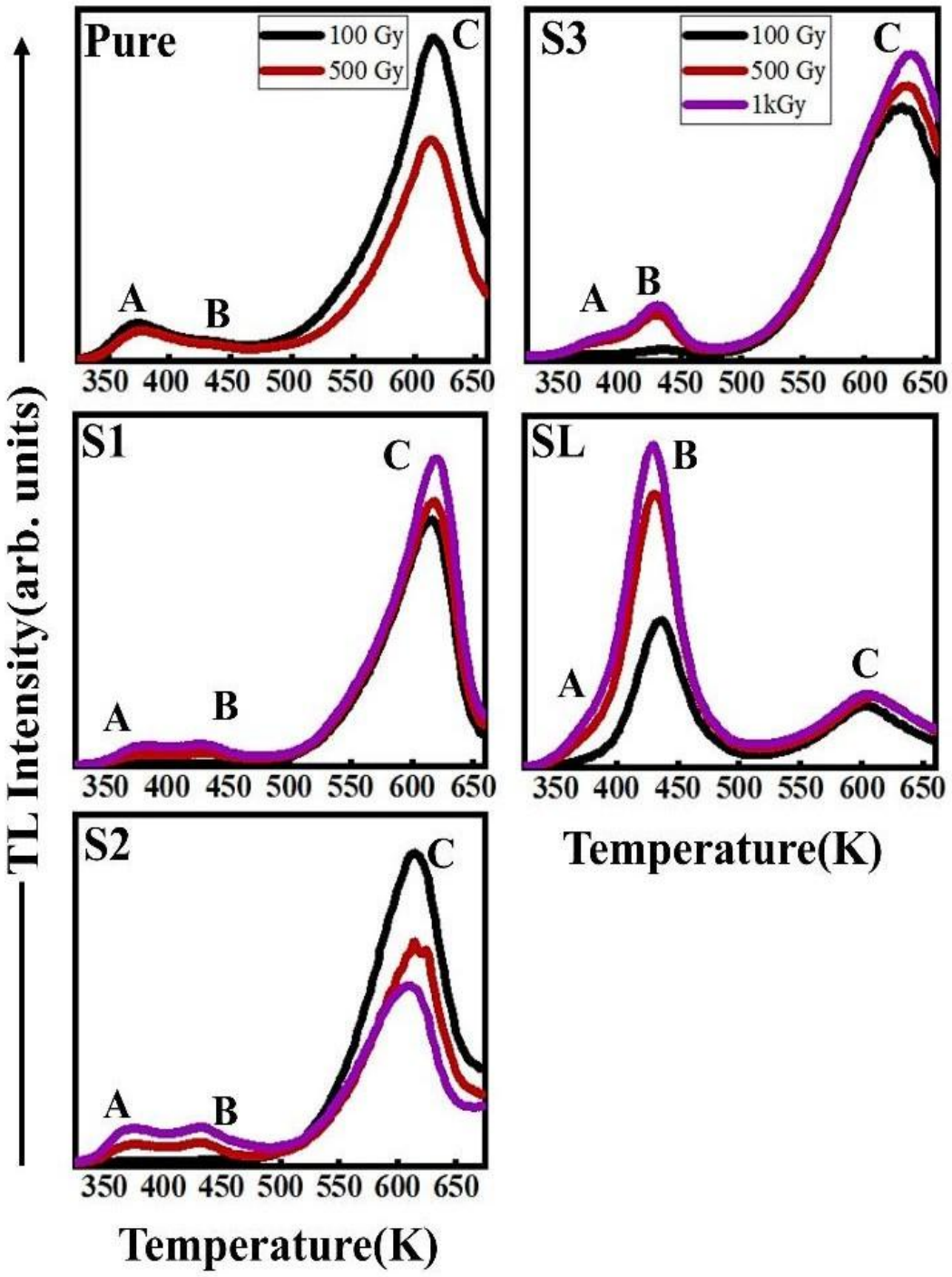

Fig 5.7: Glow Curves of all the samples at various doses.

lowest dose in S1 and S2, the emission of TL is solely detected at 615 K. However, at higher doses, along with feature **C**, feature **B** becomes more apparent and feature **A** becomes broadened in comparison to the **Pure** sample. The observed intensity variation with dose is opposite in both regions. With the increase in dose radiation, the merging of features **A** and **B** is attributed to the charge transfer from shallower traps to the deeper ones. In S3, feature B is enhanced while **A** suppressed and only appears as a shoulder at higher doses. A peak at 437 K is absent in **Pure** that appeared after doping and enhancement in this peak is observed by the increase in concentration and co-doping. The results suggest that the presence of Sm^{3+} ions leads to an increase in radiative recombination compared to the **Pure** sample, indicating that Sm^{3+} ions function as TL activators in the samples. Prior research has reported radiative recombination in MgO at low temperatures after doping. Introducing Ce^{3+}, yielded characteristics of glow curves at 438 K, 501 K, 591 K, and 660 K has been reported. Interestingly, co-doping with Li of 3 mol% intensified glow curves (Oliveira et al., 2019b). This intensification of glow curves is also observed in our co-doped samples. In another study, co-doping of Sm and Li peaks, glow curves at 373 K and 448 K demonstrably enhanced (Oliveira et al., 2016), further complementing with present findings.

In SL, the behavior of glow curves is different from other samples. Apart from the merging of peaks with dose increment, the T_m shifts towards lower temperatures in lower regions while no apparent change in peak maxima is observed at higher temperatures. The data reveals a consistent trend wherein the presence of doping leads to an increment in feature **B** and the opposite in **A** across all dosage levels. Moreover, the transition to higher temperatures is seen in feature **C** at elevated temperatures. Satyamorthy (Luthra et al., 1977) reported that glow curves at higher temperatures are not affected by impurity ions because of the dissociation of host defects from dopants but here we did not observe a similar behaviour of peaks at higher temperatures. This can be attributed to the potential existence of two or more

closely situated traps for radiative recombination at deeper levels, with varying intensities relative to the radiation dose, which may be contributing to the observed shift.

Glow Curve analysis and kinetic parameters

TL glow curve has shown the presence of multiple traps representing complex behavior of curves, so de-convolution was performed using general order kinetics within the TLANAL software to visualize the frequency factor (s), order of kinetics (b), number of charge carriers (n), and activation energies (E) of present trap in the host. The de-convoluted graphs of all of the samples irradiated at 500 Gy dose are displayed in Fig 5.8. It is observed from deconvoluted results that four traps are present with T_m (maxima temperature) at 376 K, 423 K, 586 K, and 618 K. In doped samples, with deeper traps, the T_m shifts towards the higher temperatures and the number of charge carriers (n_o) decreases as compared to **Pure** indicating that increase in non-radiative recombination at these levels. The charge density for the second trap is increased abruptly with the co-doping of Li ions indicating the increase in recombination centres. The activation energy of all traps falls within the range of 0.824 eV to 1.940 eV, indicating the presence of both shallower and deeper traps that overlap. In shallower traps, the order of kinetics (b) lies between 1.5 and 2 which indicates the retrapping of charge carriers before reaching recombination centers, while for deeper traps **b** is shifting towards 1 in singly doped samples. In the doubly doped sample, **s** value of all traps is shifted towards 2 which shows the TL emission is mainly due to the retrapping from the shallower trap to the deeper ones. Nevertheless, the frequency factor of all traps falls within the range of 10^9 to 10^{15}, which is slightly greater than the value (10^9 to 10^{13}) associated with lattice vibrations. Table 5-3 provides a summary of all the parameters. It is found in the literature that the raised value of s from its normal value is due to the overlapping of TL sites, we assume that at deeper levels the TL emission is

due to the overlapping of emission from isolated traps and combined emission centers.

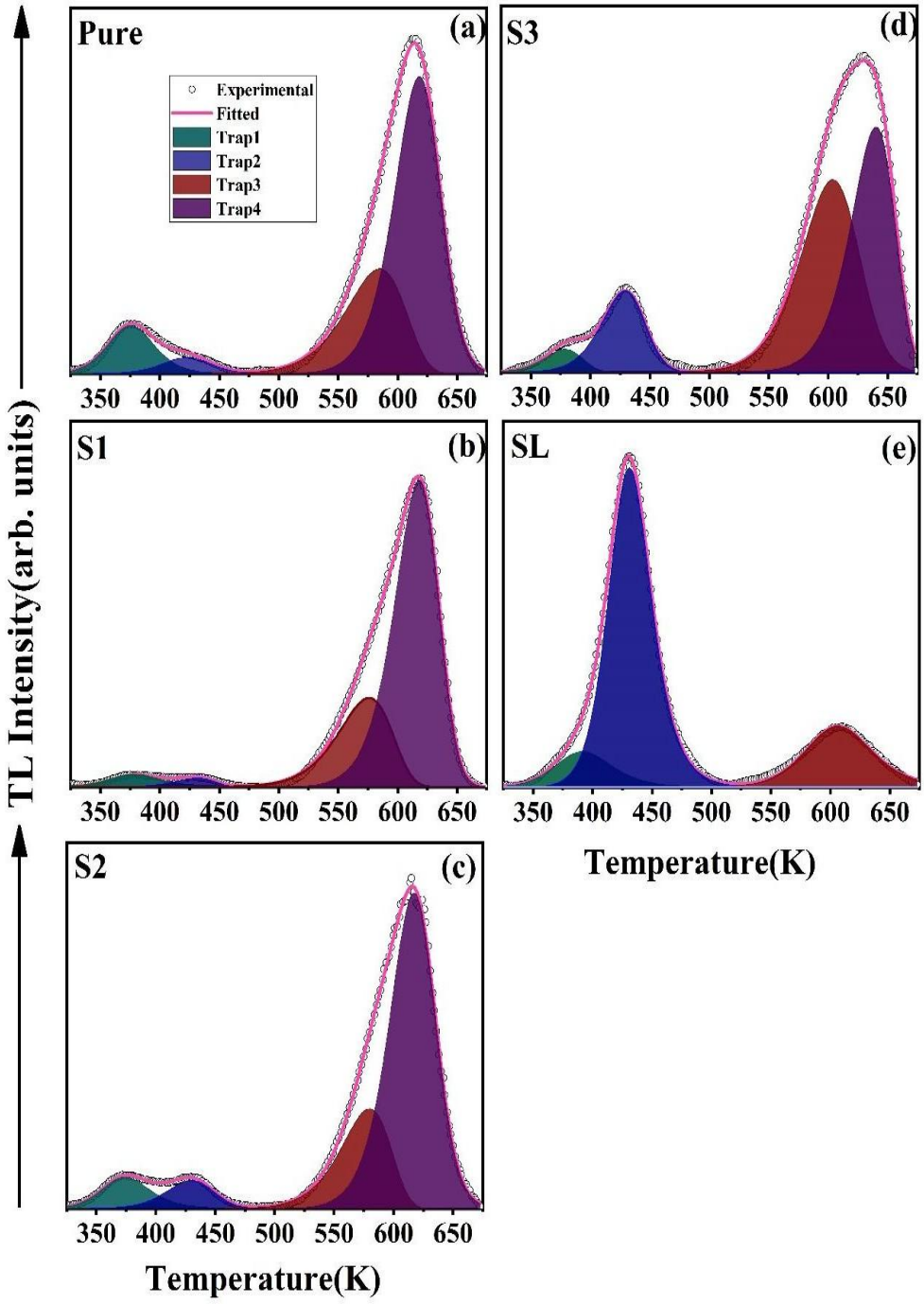

Fig 5.8: De-convoluted Glow Curves of all samples at dose 500 Gy.

Table 5-3: Kinetic parameters of all samples at 500 Gy dose afer de-convoluting

Samples	Trap	T_m (K)	n_0	E (eV)	s (s^{-1})	b
Pure	1	376	7.46×10^6	0.824	3.73×10^{10}	1.81
	2	423	2.73×10^6	0.896	1.31×10^{10}	1.53
	3	586	2.05×10^7	1.144	1.40×10^9	1
	4	618	4.57×10^7	1.940	1.87×10^{15}	1.33
S1	1	374	1.67×10^6	0.829	4.81×10^{10}	2
	2	431	1.45×10^6	0.890	7.37×10^9	1.30
	3	580	5.33×10^6	1.361	1.59×10^{11}	1
	4	617	1.58×10^7	2.000	6.39×10^{15}	1.40
S2	1	379	1.08×10^6	0.830	3.52×10^{10}	2
	2	431	6.55×10^5	0.934	2.34×10^{10}	1.63
	3	575	8.55×10^6	1.236	1.43×10^{10}	1
	4	619	2.45×10^7	1.897	8.29×10^{14}	1.17
S3	1	379	1.80×10^6	0.835	4.33×10^{10}	1.19
	2	430	7.43×10^6	0.951	4.26×10^{10}	1.25
	3	603	2.37×10^7	1.397	1.00×10^{11}	1.25
	4	640	2.27×10^7	1.943	5.35×10^{14}	1.06
SL	1	391	1.89×10^6	0.758	1.55×10^9	2
	2	431	1.27×10^8	1.253	1.67×10^{14}	2
	3	606	3.76×10^7	1.571	2.72×10^{12}	1.95

Role of Dopants in TL

A possible mechanism Sm^{3+} of TL behavior in all doped samples needs to be elucidated that could potentially explain the observed aspects like the appearance of a peak at 437 K with Sm^{3+} doping, enhancement of the same peak with co-doping of Li, and shifting at higher temperatures. Due to the difference in ionic radii and charge difference of the dopant and host, the introduction of Sm^{3+} ions in the host lattice would create defects. When Sm^{3+} substitutes the Mg cations, Sm^{1+} defects will be created and to neutralize the charge difference produced by the dopant, V_x^{2-} defects will be created in a lattice. In this study, it is hypothesized that the thermoluminescence mechanism observed in MgO: Sm, Li may potentially involve multiple types of traps and recombination centers as shown in Fig 5.9 which represents the mechanism of the trapping and ionization process during irradiation and TL readout. It is reported by several authors that Sm efficiently acts as an

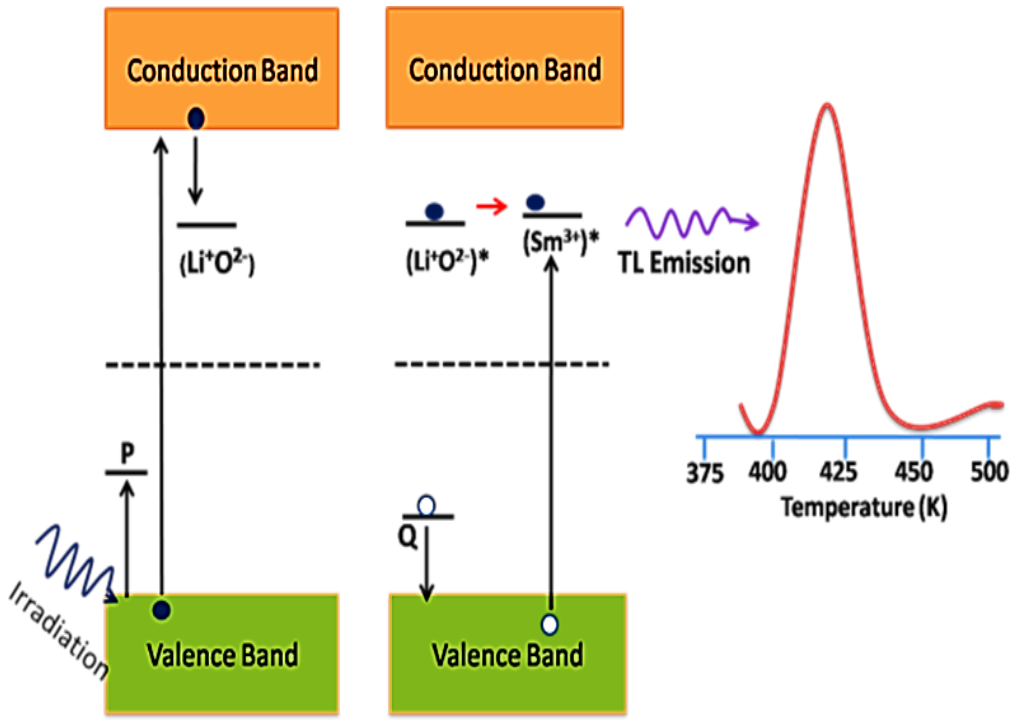

Fig 5.9: Schematic model diagram of the mechanism involved in during irradiation and TL readout.

electron trap (Oliveira et al., 2016, 2019b; Seth et al., 2023). When the sample is irradiated, initially holes and electrons are trapped at different respective defect centers. TL Fig 5.9 (a) represents the process during irradiation of samples and creation of traps within band gap while Fig 5.9 (b) shows the TL emission from different radiative recombination from Sm^{3+} and Li ions. Blue solid circles are electrons, white circles are holes and black arrows are the transition of carriers.

Let's assume a hole is trapped at any defect center **P** and an electron gets trapped at the site of Sm^{3+}, then during TL readout, a trapped hole is released and may recombine with the electron, reverting the Sm^{2+} to Sm^{3+}. The summary of the reaction that occurs during irradiation and thermoluminescence (TL) readout is presented below:

During irradiation:

$$P + h^{+} = Q \qquad \text{Eq. 5.4}$$

$$Sm^{3+} + e^{-} = Sm^{2+} \qquad \text{Eq. 5.5}$$

During TL readout:

$$Q + kT = P + h^{+} \qquad \text{Eq. 5.6}$$

$$Sm^{2+} + h^{+} = Sm^{3+} + h\upsilon \qquad \text{Eq. 5.7}$$

Doping of Li in Sm^{3+} doped host, the intensity at 430 K abruptly increased, and the peak at 370 K present dominantly in pure appeared as a shoulder of 430 K peak. However, glow curves largely remain unchanged and no new peak is observed. The incorporation of lithium as a charge compensator in a lattice serves to relieve the stress generated within the lattice. Similar luminescence behaviour of Li ions is also observed in other hosts (Q. Shi et

al., 2014; Z. Wang et al., 2014; Yantake et al., 2021). When Li^{+} and Sm^{3+} substitute the Mg^{2+} ions, the monovalent ion creates a negative charge defect which compensates for the positive charge defect created by the other trivalent ion, facilitating the addition of more Sm^{3+} ions. The presence of Li ions also generates more defects which facilitates the transfer of charge to recombination centres. This transfer occurs when certain conditions are met, including resonance of energy and distance between the involved centers. By substituting the cations with monovalent ions in the lattice, defect centers (Li^{+} O^{-}) are generated via trapping a hole in adjacent anions. These defect states can trap electrons which relax the excited anions (Y. Chen, 1979). In contrast, the formation of a Li^{1+}charge-deficient site at Mg^{2+} suppresses the cation vacancies because charge compensation by Li^{+} ions does not favor the formation of V-type defects, resulting in the absence of the 370 K peak. Based on the above discussion, the mechanism Li^{+} and Sm^{3+} can be summarised by the following equations:

During irradiation:

$$e^{-} + [Li]^{o} \rightarrow (O^{2-})^{*}(Li^{1+}) \qquad \text{Eq. 5.8}$$

During TL readout:

$$(O^{2-})^{*}(Li^{1+}) + Sm^{3+} \rightarrow (O^{2-})(Li^{1+}) + (Sm^{3+})^{*} \rightarrow (O^{2-})(Li^{1+}) + (Sm^{3+}) + h\nu \qquad \text{Eq. 5.9}$$

5.4 Results and Discussion of Ce^{3+} and Ce^{3+}, Li^{+} Doped MgO

5.4.1 X-ray Diffraction Study

Fig 5.10 illustrates the XRD patterns of all compositions after annealing at 900˚ Celsius for 3 hours. No secondary phase is observed up to Ce^{3+} (0.2 mol %) and in co-doped nanophosphors. In the case of Ce^{3+} 0.2 mol% doping, an impure phase of CeO_2 has been observed as shown in the enlarged image of Fig 5.10. It indicates

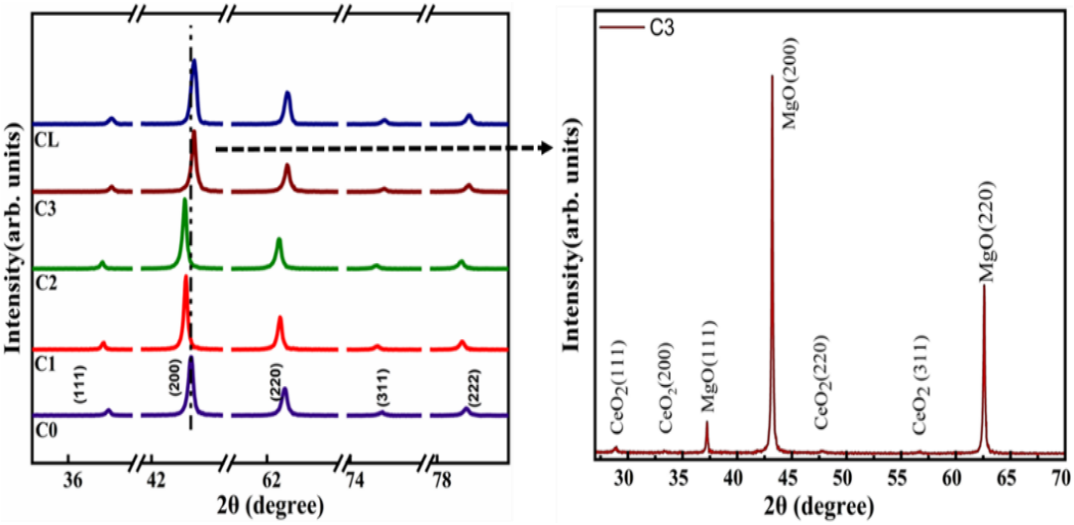

Fig 5.10: XRD of pure and Ce^{3+} doped MgO with an enlarged image of C3 composition

that up to 0.1 mol% of Ce^{3+}, the dopant, is easily incorporated in the host lattice. However, afterward, incorporation became difficult and CeO_2 was formed. In this work, further studies have been carried out up to 0.1 mol% of Ce^{3+} and for co-doped composition. From XRD patterns shown in Fig 5.11, it has also been observed that peaks are shifted towards lower angles as the concentration increases. The change in lattice parameter of doped samples is due to the difference in ionic radii of Ce^{3+} (0.103 nm) and Mg^{2+} (0.072 nm) cations and indicates that Ce^{3+} ions substitute the host cations instead of creating interstitial defects. In a co-doped sample, the incorporation of Li ions causes a decrement in lattice parameters because of the

smaller ionic radii of Li ions than those of the host ions. The shifting in peaks towards a higher angle can be attributed to the substitutional Li ions in the host lattice, which also act as charge compensators by neutralizing the charge disturbance created due to the charge difference between Ce^{3+} dopant and Mg ions which further influences the luminescence properties of MgO.

5.4.2 X-Ray Absorption Spectroscopy Study

From Fig 5.11(a), the features observed at 1305.2 eV, 1311.1 eV, 1322.5 eV, and 1350.6 eV are marked as **u, v, w,** and **x,** respectively. All the features observed in the spectrum are from Mg K-edge confirming the rock salt MgO structure and well matched with the features reported in the literature for MgO XANES (Brow et al., 1996; Farangis et al., 2003). Fig 5.11(b) illustrates the shifting in edge with an increase in doping which shows that there is distortion around Mg ions after doping. It is reported in the literature that the position of the absorption edge of Mg K-edge in tetrahedral Mg sites always lies lower than that of octahedral Mg sites, while the energy value of absorption edge for distorted octahedral will be higher than regular octahedron Mg (Aritani et al., 2000; Jain et al., 2021). Here, in the present study, the shifting indicates the change in local structure around host cations. Doping may cause the co-existence of low co-ordinated Mg ions with the bulk MgO in the structure which also contributes to the spectral features along with the octahedron Mg in lattice. Apart from shifting, the intensity from 1308 eV to 1314 eV is also decreased with doping. This feature is affected by the doping as Ce-host substitution directly affects the Mg–O interaction. In O K-edge spectra, features at 533.1 eV, 542.1 eV, 546.7 eV, 551.2 eV, and 559.1 eV are marked as **p, q, r, s,** and **p**' pre-edge feature at 531.9 eV (Fig 5.11(c-d)). Pre-edge feature in MgO is due to the localized bound states created by Mg 3s and O 2p orbitals (J. P. Singh et al., 2015b, 2016; J. P. Singh, Kim, et al., 2018) which are decreased after doping. The intensity of the **p** feature is enhanced upon doping and indicates the increase in hybridization between Ce 4f and O 2p orbitals as

shown in Fig 5.11(d). The intensity of feature **r** and **s** is significantly reduced. It is assumed that the substitution of Ce is responsible for the alterations in the band structure, which may involve the introduction of modifications associated with

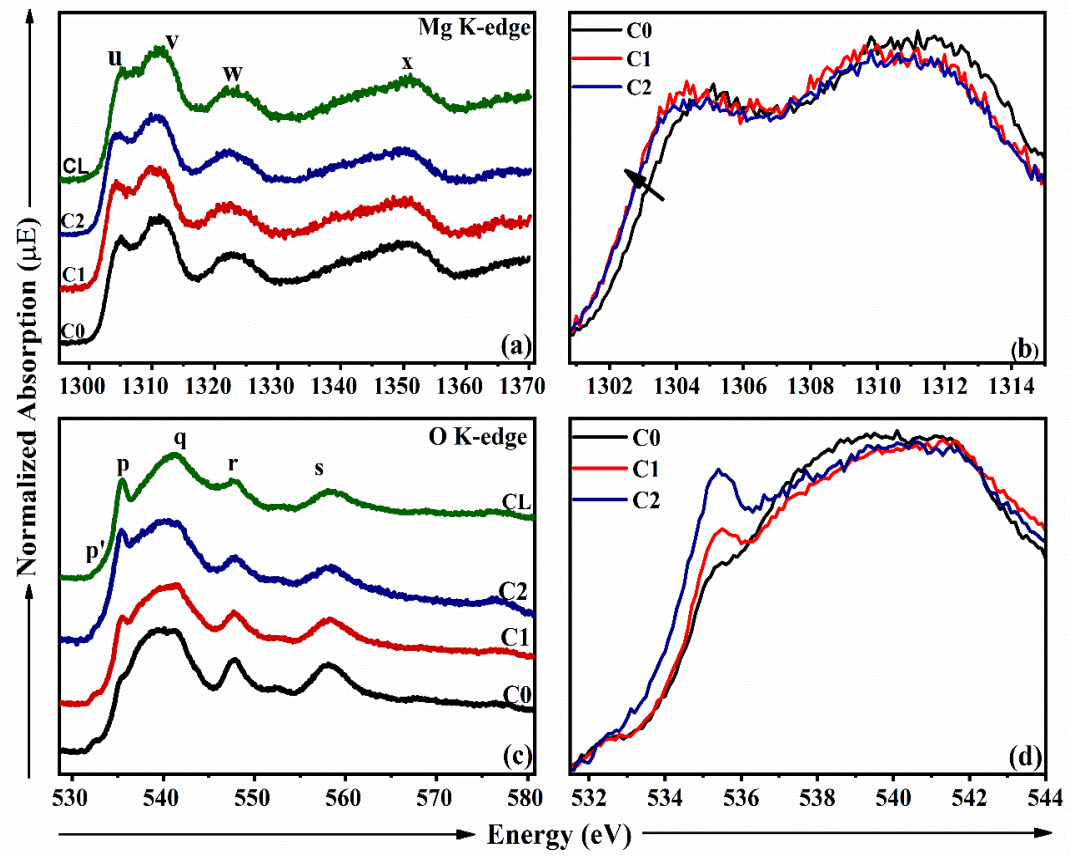

Fig 5.11: (a) Mg K-edge XANES spectra; (b) Enlarged image of Mg K edge; (c) O K-edge XANES spectra; (d) Enlarged image of near edge features of O K-edge.

hybridization. These modifications are responsible for the broadening of spectral characteristics at higher energies and the reduction in their intensity. The change in O K-edge is also supported by the Mg K-edge spectra which reveal the change in environment around Mg ions upon doping. The Ce L-edge XANES spectra of reference CeO_2, C1, C2, and CL samples are examined to get the oxidation state of cerium and to determine their relationship with the associated luminescence properties. The features observed at 5725 eV, 5728 eV, and 5735 eV are marked as

m, n, o shown in Fig 5.12(a). Feature **m** is due to Ce^{3+} (similar to CeF_3 bulk samples) and **n** and **o** are due to Ce^{4+} (Beck et al., 1989; Löble et al., 2015; F. Zhang et al., 2004). Fig 5.12 indicates that the spectral features of C1, C2, and CL samples are partially matching with the spectral features of bulk CeO_2 (Ce^{4+}) and previously reported features of CeF_3 (Ce^{3+}) samples. It conveys that the C1, C2, and CL samples consist of, both, Ce^{4+} and Ce^{3+} ions. The spectral features of C1 samples are less resolved because of the low Ce concentrations. To, quantitatively, evaluation of Ce^{4+} and Ce^{3+} ions, the Ce L-edge XANES spectra have been de-convoluted and presented in the Fig 5.12(b-c). Since the ratio of peak **n** and **o** gives the information for the hybridization of Ce 4f – O 2p orbitals and the probability of

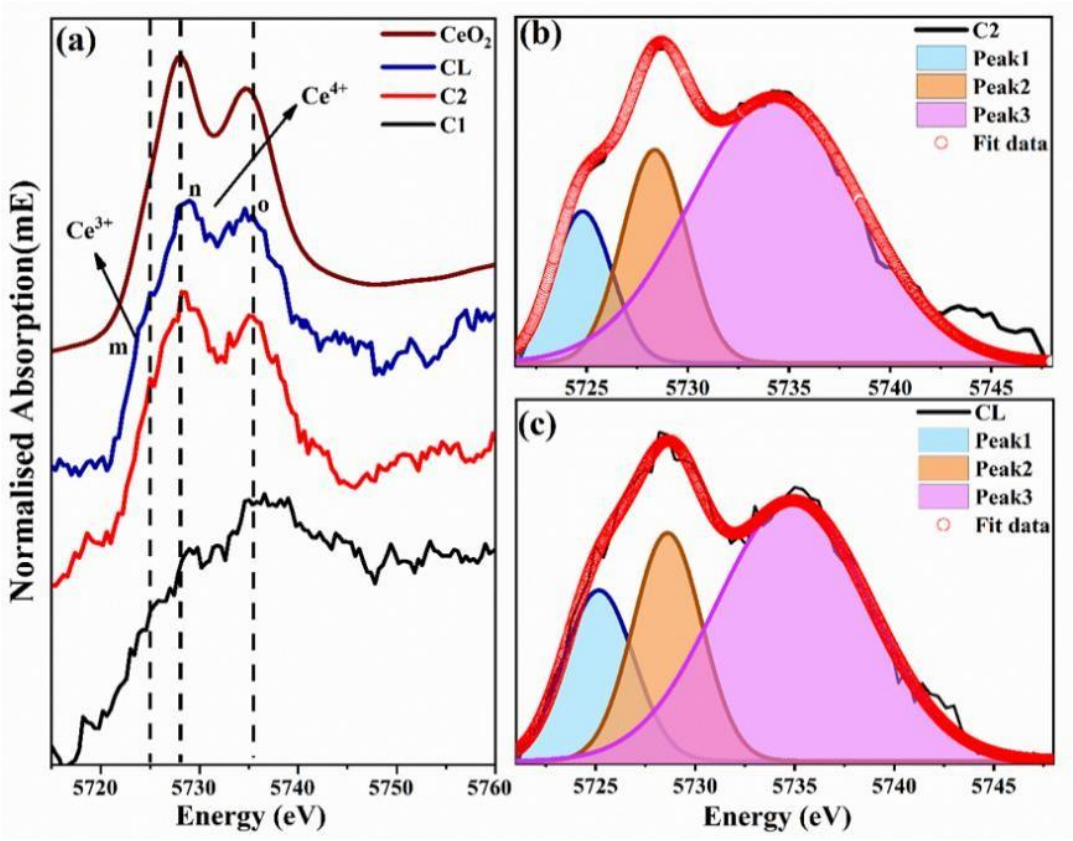

Fig 5.12: (a) XANES spectra of Ce^{3+} L_3-edge at different concentrations of Ce^{3+} ions (b,c) Deconvoluted XANES spectra of C2 and CL sample

hopping electrons at $2p4f^1$ and $2p4f^0$ orbitals (Shirbhate et al., 2016). The Ce-O interaction governs the covalent nature of the bond. At lower concentrations, all the features are merged, indicating the less covalence nature of Ce-O. The features **n** and **o** are visible along with **m** as shoulder in C2 (Ce 0.1 mol%) and the co-doped sample indicates the covalancy of the Ce-O bond due to the presence of Ce^{4+} along with Ce^{3+}. The intensity ratio of m to n + o may give the Ce^{3+}/Ce^{4+} concentration in the respective samples. Therefore, the area under the peak m, n, and o are evaluated (within the given goodness of fitting parameter ~ 0.9 to 1.1). It has been observed that the CL sample exhibits slightly higher Ce^{3+} content (Ce^{3+}/Ce^{4+} = 2.135) as compared to the C2 sample (Ce^{3+}/Ce^{4+} = 1.503) and, thus, conveys less hybridisation of Ce-O in CL sample. This weak hybridization may leads to PL bands alteration and has been discussed in the following sections. Moreover, enhancement in the intensity of spectral features (**n** and **o)** shows the increment in covalancy ascribed to the decrease in interatomic distance between Ce and O due to the difference in ionic radii of Ce^{3+} (0.103 nm)and Ce^{4+} (0.87 nm). From XRD, the slight shift in peaks towards a higher angle and presence of secondary phase at higher concentration also indicates the decrease in crystallite size and complementing with the observed XANES spectra.

5.4.3 Photoluminescence Spectroscopy Study

To probe the intrinsic defects within host materials and modification of defects due to doping is studied by using PL spectroscopy. The pristine as well as doped samples were excited by using UV LED sources of 275 nm and 310 nm. Fig 5.13 shows the PL emission of pure and doped nanophosphors excited at 275 nm and 310 nm. At the excitation of 275 nm, in pure MgO two bands are observed in the blue and red region. The region between 400 nm and 500 nm is due to the relaxation of F^+ centers to F centers which has been discussed in our previous work in detail (Bishnoi, Brajpuriya, et al., 2024; Bishnoi, Dhiman, et al., 2024). The red region is due to the clustered singly charged O^- defects present near the CB (Pathak

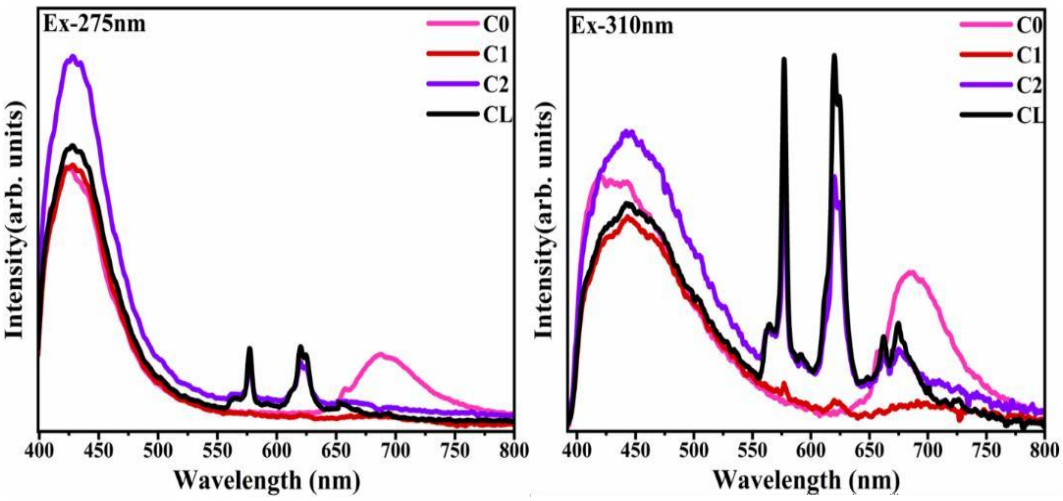

Fig 5.13: PL spectra of all samples on excitation at 275 nm and 310 nm

et al., 2016b) (Pikhitsa et al., 2015). The modification in emission due to doping is observed indicating the modification in defects present in between the band gap of MgO. The dopant diminishes the red region emission while the blue region is enhanced with increasing doping. XANES spectra indicate the strong hybridization between Ce and O orbitals which causes the transfer of electrons from the O to Ce energy levels, further decreasing the intensity of the host in the red region. At higher concentrations, the weak and sharp peaks are also visible ascribed to the 5d to 4f transition of Ce^{3+} ions (Orante-Barrón et al., 2011). In literature, the emission peaks are reported from the UV to red region because the position of the emission band has a strong dependence on the host surrounding. L.G van Uitert (van Uitert, 1984) reported Ce emission in different compounds i.e. in the CaF_2 position the peak of Ce^{3+} is at 314 nm while in the Y_2O_2S peak position is around 670 nm.

Here in the present study, the presence of two bands indicates the splitting of energy levels of Ce ions. At lower concentrations, where the CeO_2 phase was not observed, there is weak hybridization between Ce-O orbitals which preserves the sharpness of emission peaks. Different authors reported the presence of comparable emission bands in Ce^{3+} in different oxides during their respective

studies (Guckan et al., 2021b; Lehmann, 1973; Oliveira et al., 2019b; Orante-Barrón et al., 2011). On excitation by 310 nm, the emission bands of Ce are quite intense along with the blue emission. The increase in PL intensity suggests that Ce^{4+} is functioning as an intermediate state, trapping the excited electrons and leading to the excitation of Ce^{3+} levels. Upon de-excitation, the Ce^{3+} ions emit photons at wavelengths of 570 and 610 nm. The contribution of Ce^{4+} in luminescence has been documented previously in several compounds where Ce^{4+} and Ce^{3+} coexist in a comparable amount (Jia et al., 2018; Lin et al., 2007; M. Tyagi et al., 2021; Wu et al., 2014). In the Ce and Li co-doped sample the host emission was suppressed while the Ce emission was significantly enhanced. Li ions can generate charge-deficient sites when they replace the Mg ions. Multiple authors reported that the newly formed site is capable of forming a bond with a neighboring O^{2-} and trapping a hole that functions as a recombination center for electrons (Boldu et al., 1979; Lee & Crawford, 1979). CIE coordinates for both the excitation wavelength for all samples is shown in Fig 5.14. For excitation at 275 nm, the blue region dominates in all samples while for 310 nm coordinates shifted towards white light.

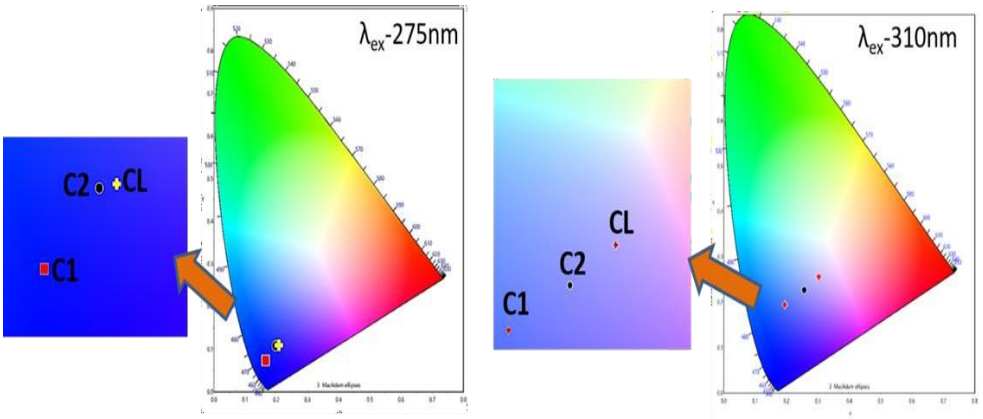

Fig 5.14: CIE coordinates at excitation 275 nm and 310 nm

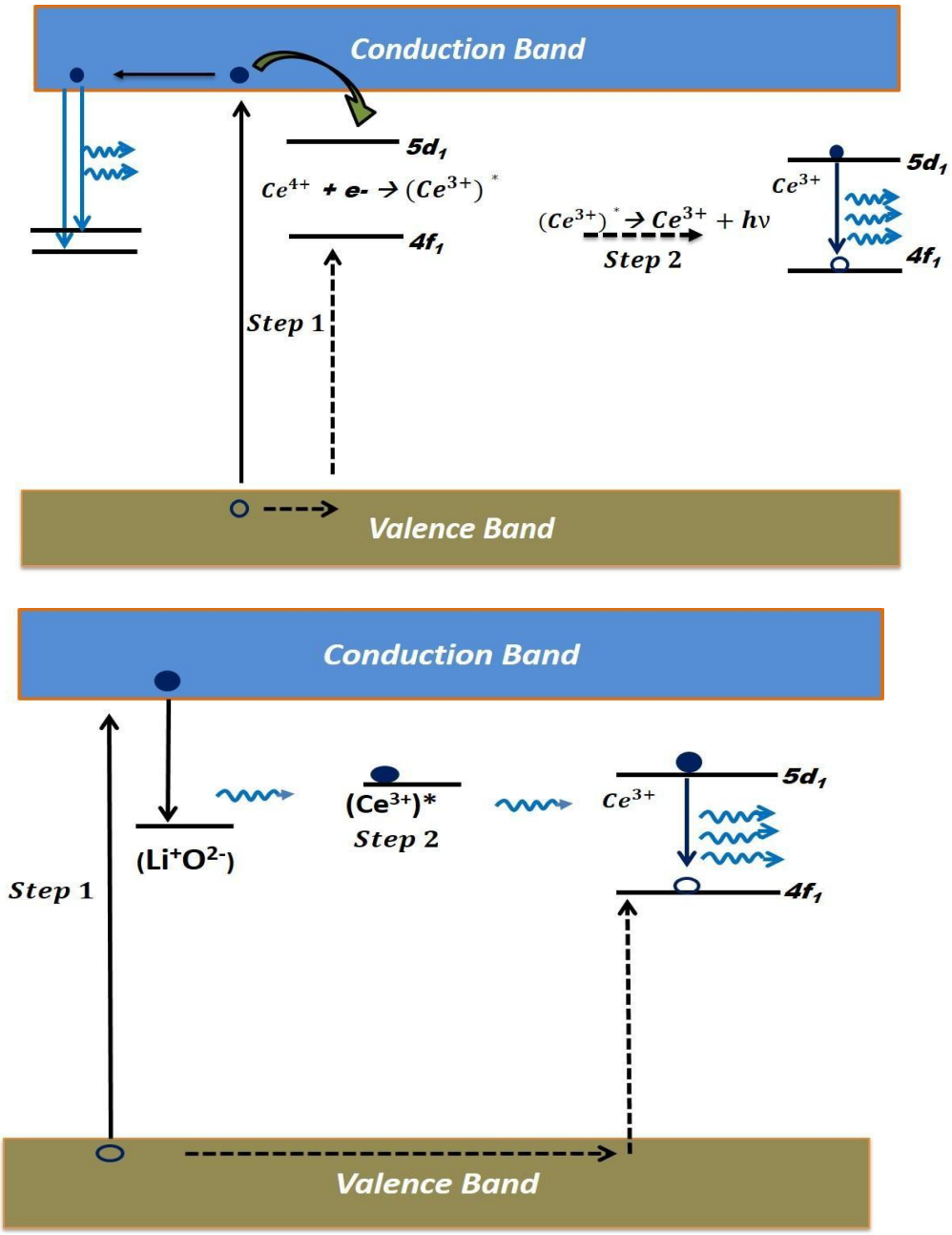

Fig 5.15: . Schematic diagram of luminescence and role of Ce^{4+} and Li^{+} ions in luminescence mechanism. (a) Emission from singly doped MgO; (b) emission scheme with co-doped MgO with Li and Ce ions

To understand the luminescence mechanism of Ce and Li ions in MgO, a schematic diagram is shown in Fig 5.15. In step 1; Ce^{4+} traps the electron from the conduction band and converts into Ce^{3+*} state as shown in step 2. These excited states de-excite

radiatively and give characteristics of emission of Ce^{3+} ions. It shows the mechanism of co-doped samples where Li ions make centers ($Li^{+}O^{-}$) and capture electrons. On relaxation, it excites the Ce^{3+} and creates $Ce^{3+\ *}$ centers which radiatively de-excite and generate the Ce^{3+} emission. The dual contribution from Ce^{4+} and $Li^{+}O^{-}$ increases the intensity observed in Fig 5.15(b).

5.4.4 Thermoluminescence Study

The PL spectra of doped MgO indicate defect levels in between the band gap. Fig 5.16 shows the effect of gamma irradiation doses (100 Gy, 500 Gy, 1 kGy) on the TL glow curve, providing valuable insight into the presence of trapping states within the band gap. The combination of Li and Ce^{3+} ions favors the shallow traps and new peaks appear at 435 K in singly doped and an intense 475 K peak appeared in co-doped MgO. As discussed above, the covalancy of the Ce-O bond increases with the concentration causing the saturation in TL intensity at elevated temperature. These peaks are well-matched with the peaks reported in the literature (Bapat M, 1985; Guckan et al., 2020; Oliveira et al., 2016). The slight variations in the TL peaks observed in different studies are attributed to the different rates and detection windows used by researchers. In doped samples, the TL glow curve intensity increases with dose increment and the stability of traps. Fig 5.17 represents variation in integrated TL intensity of co-doped MgO as a function of dose-response. The overall TL signal is compared with the peak (325 K- 517 K) and peak at 610 K.

Lower temperature peaks show linear behavior with dose but for higher temperature peaks there is saturation at 500 Gy dose afterward it increases again. As discussed earlier the doping does not favor the deeper traps which leads to a decrease in ionized tracks, but on further increase in dose, the overlapped traps are more prevalent, and overall interaction at higher temperatures results in a slight enhancement in TL signal (Vij et al., 2009). Here, we can suggest that the overall

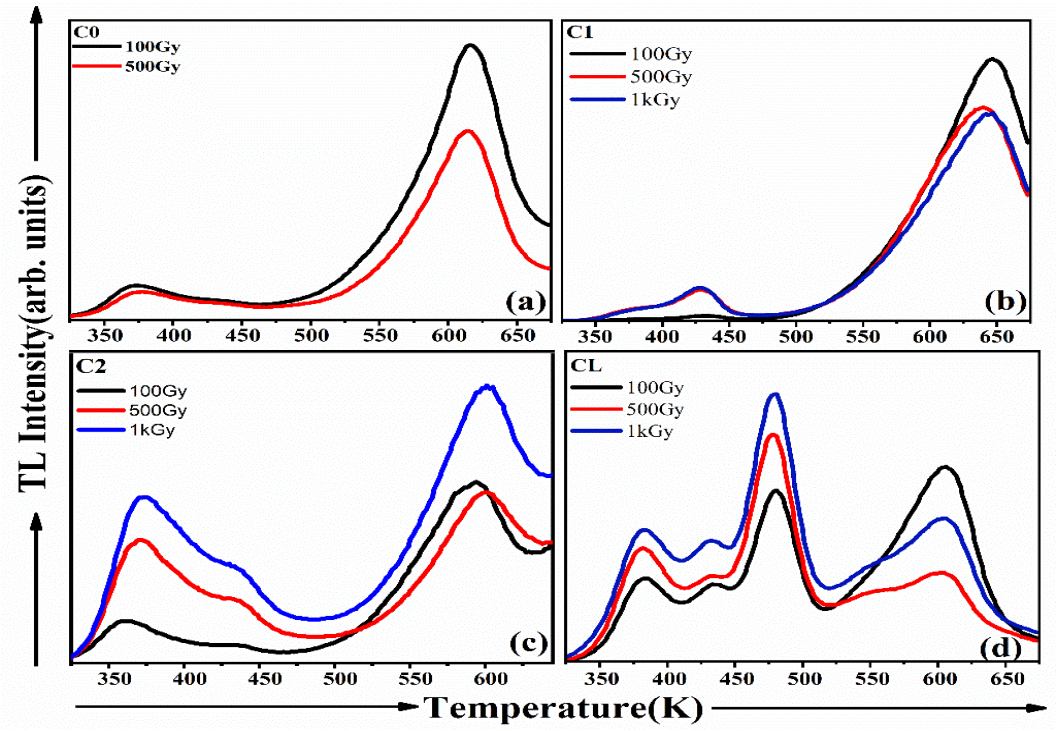

Fig 5.16: TL glow curves of all samples irradiated at doses 100 Gy, 500 Gy, and 1 kGy

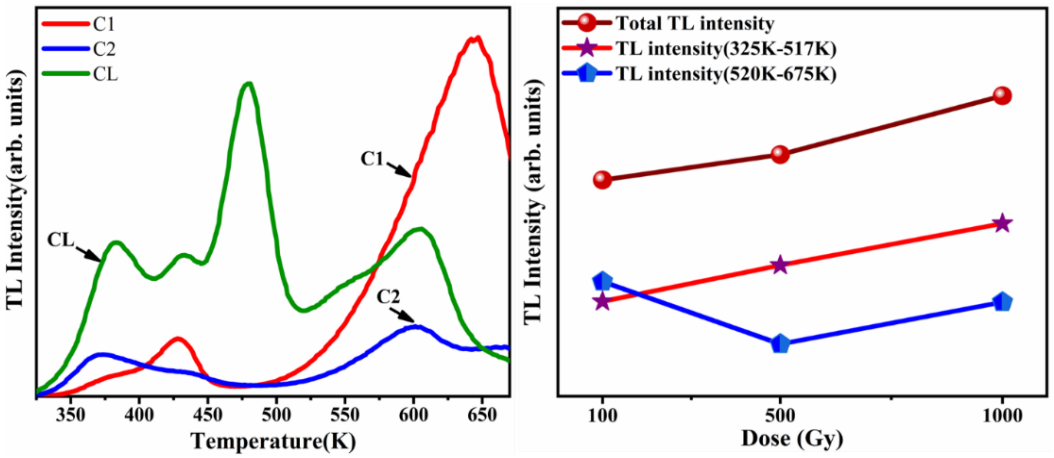

Fig 5.17: (a) Behavior of CL samples at all three doses; (b) Concentration behavior of TL glow curves at 1 kGy Dose

increment in TL signal is mainly due to the contribution of the larger number of traps at lower temperatures. Multiple peaks indicate the presence of more than three traps. Thus to analyze the trap peaks for doped MgO, glow curves has been deconvoluted by using TLANAL software using Kitti's formula as shown in Fig 5.18 and all the parameters calculated are tabulated in Table 5-4. C1 and C2 are concise with four traps, while in CL five traps are present. The kinetic order is greater than unity for all the traps, showing the retrapping behavior of all trap centers before reaching to emission centers. The energy of all traps lies between 0.87 to 1.49 eV. The stability of traps with respect to dose and concentration is promising for the use of Ce^{3+}, and Li-doped MgO in dosimetry applications.

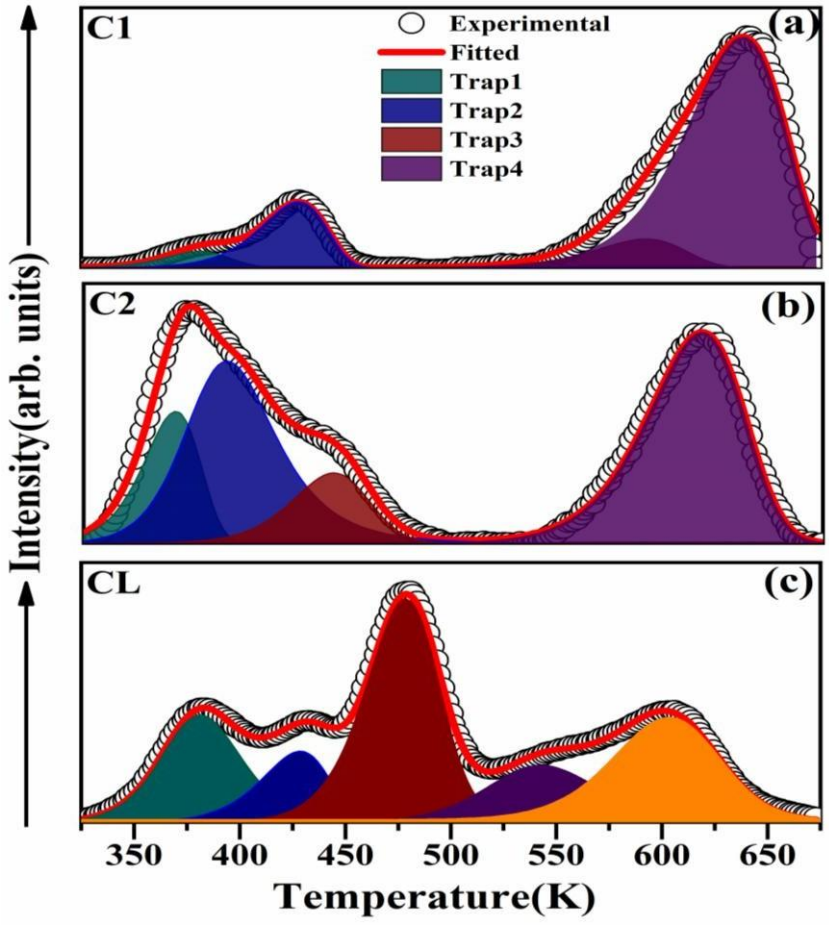

Fig 5.18: Deconvolution of Ce-doped MgO at 1 kGy as a function of concentration

Table 5-4: Trap data of glow curves of double-doped MgO calculated by TLANAL software

Sample	Trap	T_m (K)	n_0	E (eV)	S (s^{-1})	b	FOM (%)
C1	1	377	1.8×10^6	0.890	2.06×10^{11}	1.2	2.63
	2	430	7.6×10^6	0.978	1.03×10^{11}	1	
	3	590	4.5×10^6	1.412	2.40×10^{11}	1	
	4	635	3.4×10^7	1.489	1.21×10^{11}	1	
C2	1	375	2.6×10^6	0.939	3.78×10^{12}	1.1	2.4
	2	389	6.1×10^6	0.978	1.75×10^{12}	2	
	3	437	1.9×10^6	1.071	8.42×10^{11}	1.3	
	4	594	7.1×10^6	1.489	8.98×10^{11}	1.1	
CL	1	382	2.7×10^7	0.893	2.13×10^{11}	1.9	1.8
	2	428	1.4×10^7	0.973	8.33×10^{10}	1	
	3	479	5.1×10^7	1.291	1.27×10^{13}	1.3	
	4	544	2.1×10^7	1.324	4.89×10^{11}	2	
	5	603	3.3×10^7	1.489	3.34×10^{11}	1.4	

5.5 Conclusion

In this study, Sm^{3+}, Ce^{3+} rare earth ions are singly and co-doped into MgO, using the solution combustion method. XRD patterns revealed the formation of single-phase MgO nanocrystals. Sm^{3+} ion doping, at lower concentrations, produces tensile strain and enlarges the unit cell parameters. The co-doping of Li^{+} and Sm^{3+} ions resulted in a competition for substitutional sites, leading to a reduction in the lattice parameter. TEM and SAED analysis indicated a reduction in particle size in doped samples while maintaining a similar crystalline nature to pure samples. XANES results confirmed Mg^{2+} and Sm^{3+} ions in the samples. Mg K edge XANES indicated the creation of unsaturated bonds of Mg–O and distortions in geometry around Mg^{2+} ions. Likewise, O K-edge XANES spectra reveal an increase in F- enters, interstitial defects in the lattice, and a net decrease in the hybridization of Mg 3s - O 2p orbitals. The emission properties of doped and undoped samples were tuned from the blue to red region by changing the excitation wavelength ($\lambda_{excitation}$ = 275 nm and 405 nm), indicating defect-controlled radiative transitions. The optimal doping concentration for enhanced luminescent properties was found to be 0.5 mol% of Sm, with characteristic peaks observed at this level along with enhanced red emission. Thermoluminescence (TL) analysis revealed the creation of multiple levels of radiative traps by doping, enhancing peak intensity at 437 K, and radiation fluence-independent TL characteristics. Additionally, the effect of Ce^{3+} and Ce^{3+}, Li co-doping on the MgO defect structure was examined by using XANES of Mg K-edge, O K-edge, and Ce L_3-edge. XANES spectra of the O K-edge confirmed variations in O vacancies due to dopant introduction. Unsaturated Mg cations in the lattice were confirmed from XANES spectra at the Mg K-edge, also resulting from dopants induced defects in the lattice. Analysis of the Ce L_3-edge revealed the presence of Ce ions in both +3 and +4 oxidation states, suggesting significant Ce-O hybridization increasing with concentration. The incorporation of Ce^{3+} and Li ions significantly affected the local structure of the host, influencing its luminescence properties. PL spectra exhibited two emission bands at 570 nm and 610 nm attributed to 5d-4f transitions. Li co-doping enhanced

characteristic Ce^{3+} emission by acting as a charge compensator. A schematic diagram was proposed for the PL emission mechanism. The presence of Ce^{3+} ions with various valencies led to the formation of new traps within the host material, in addition to inherent defect states. The TL signal stability increased with dose for MgO:Ce^{3+} and MgO:Ce^{3+}, Li^{+}. The introduction of gamma-irradiated nanocrystals in Ce-doped and Ce, Li-doped MgO resulted in TL peaks at temperatures of 435 K and 475 K, respectively. Kinetic parameters of the observed glow peak were calculated using TLANAL software, revealing retrapping and closely spaced traps within the forbidden band gap. The band diagram model, for a mechanistic explanation of TL, suggests the feasibility of improving the radiative pathways and facilitating efficient charge transfer to activators through strategic doping manipulation and potential application in dosimetry.

CHAPTER 6

UPCONVERSION LUMINESCENCE STUDY IN Er^{3+}, Yb^{3+} and Ho^{3+}, Yb^{3+} CO-DOPED $MgO\text{-}Y_2O_3$ NANOPHOSPHORS

UPCONVERSION LUMINESCENCE STUDY IN Er^{3+}, Yb^{3+}, AND Ho^{3+}, Yb^{3+} CO-DOPED $MgO-Y_2O_3$ NANOPHOSPHORS

6.1 Introduction

Upconversion nanophosphors provide a range of distinct advantages compared to downconversion nanophosphors such as negligible noise signal from self-fluorescence, extended decay period, and exceptional upconversion efficiency (Upadhyay & Kumar, 2023). Additionally, in the biomedical field, the NIR radiation used in the upconversion process easily penetrates the biological tissue and gets less scattered as compared to the UV and visible radiation allowing the capture of more in-depth images (Bazhukova et al., 2020). Among various lanthanides, the Ho^{3+} can produce UC emissions in blue, green, and red regions after absorbing NIR radiation due to the presence of ladder-like energy levels (Jiang et al., 2024; Lei et al., 2024; M. Li et al., 2024). The upconversion efficiency from this kind of emission can be remarkably enhanced by co-doping of a sensitizer ion which exhibits a strong absorption cross-section in the NIR region and whose excited level matches well with the activator ion through which it can efficiently transfer energy to the activators. Yb^{3+} is one of the ions that exhibit this behavior by having a large absorption near 980 nm and is used as a sensitizer with different activators as per reported literature (Pandey et al., 2013; Wei et al., 2011; Y. Yu et al., 2011). Various parameters of the host matrix such as phonon frequency of host lattice, and particle size govern the emission characteristics of RE ions. The inorganic oxides are one of the potential members in luminescent materials due to their ability to emit in the UV and visible region and their capacity to be easily doped with RE ions (Cao et al., 2018; Z. Liu et al., 2021). The present work mechanistically investigated the effect of variation of both the dopants independently and the possible population routes involved in the UC and DC such as excited state absorption, ground state absorption, cooperative energy transfer, and back energy transfer. The non-contact thermal approaches have been used to examine the luminescence intensity ratio for thermal sensing characteristics. The

laser-induced thermal experiments has also been carried out to investigate the stability of samples with time up to 60 minutes at intervals of 5 minutes. Moreover, investigations on the efficacy of doped MgO-Y_2O_3 phosphors as security ink for anticounterfeiting applications are attempted in this study for the socio-economic uses of MgO-Y_2O_3 compounds.

6.2 Experimental details

6.2.1 Synthesis and characterization

All the samples were synthesized utilizing the low-temperature solution combustion method. For MgO-Y_2O_3 sample, Magnesium nitrate hexahydrate ($MgO(NO_3)_3.6H_2O$ > 99%, CDH), Yttrium nitrate hexahydrate ($Y_2O_3(NO_3).6H_2O$= 99.99 %, CDH), were used as oxidizer and urea (CDH>99%) were used as a fuel. In doped samples, in addition to the from nitrates of Magnesium and Ytterium, Holmium nitrate pentahydrate ($Ho(NO_3)_3.5H_2O$), Erbium nitrate and Ytterbium nitrate pentahydrate $(NO_3)_3.5H_2O$, all with purity of 99.99 % were used as oxidizers with the same fuel. The prepared samples were annealed up to 1073 K for 2 hours. The two series were prepared by varying the concentration of dopants. The pure samples have been labeled as pure in further analysis in the report. In the first series, in which Er^{3+} is kept constant and Yb concentration varied from 0.1 mol% to 15 mol% and nomenclature was given as EY1, EY2, EY3, EY4, EY5, EY6 . In other series, where Ho^{3+} was varied with 0.1 mol%, 0.5 mol%, and 1 mol% with Yb^{3+} kept constant at 0.5 mol% were labeled as H1, H2, and H3. In separate series, where $Yb^{3+}$was varied with 0 mol%, 5 mol%, 10 mol%, 15 mol%, 20 mol% and 25 mol% were labelled with Y0, Y1, Y2, Y3, Y4, Y5 in throughout the report. Bruker-D8 Advance EcoPro diffractometer, which was irradiated with Cu-Kα radiation (λ = 1.54056 Å) has been used for X-ray diffraction measurements. JEOL/JEM-F200 with Thermal Electron Field Emission Electron Gun (TFEG) and OneView CMOS Camera (4k × 4k pixels) have been used for Transmission electron microscopy (TEM). UV-visible measurements have been carried out by using the Cary 5000

UV-Vis-NIR instrument. Photoluminescence experiments were carried out by two different sources: The downconversion emission was recorded using a Horriba fluromax+ spectrophotometer with a Xenon lamp and the upconversion emission is carried out by using continuous wave NIR diode Laser of 980nm wavelength with varying power upto 2.5 mW power at room temperature. The temperature-dependent upconversion spectra were recorded using the same diode laser, CCD, and optical fiber integrated with a homemade small heater and thermocouple. A potentiometer was used to control the heater temperature.

6.2.2 Synthesis of security ink

The optimized sample Y2 has been used for security ink application due to its favorable results. To achieve better writing or drawing patterns ink's viscosity and dispersion of the sample in solvent without agglomerating are essential. These properties ensures the smooth flow through writing equipments and uniform deposition on the different substrates.

For this experiment commercial available resin binder polyvinylpyrrolidonek-30 manufactured by SRL has been used as stabilizing agent due to its known solubility in ethanol and ability to stabilize dispersions. In the experiment, the Y2 sample was first mixed in 10 ml ethanol in a beaker. A small amount of PVP-30 was added to mixture. The resultant suspension was sonicated for 1 hour until the particles were completely dispersed in the solvent and the transparent solution was obtained. The sonication was crucial to break apart any kind of agglomerates and ensure complete and uniform dispersion of sample within the solvent. This obtained solution was then filled into a standard ink pen. Using this pen test patterns and words were written on the paper and plastic sheet for further experiments. To evaluate the ink's performance, visibility and stability, the prepared samples were tested regularly up to one month under different conditions. The entire synthesis and applications process was shown in Fig 6.1.

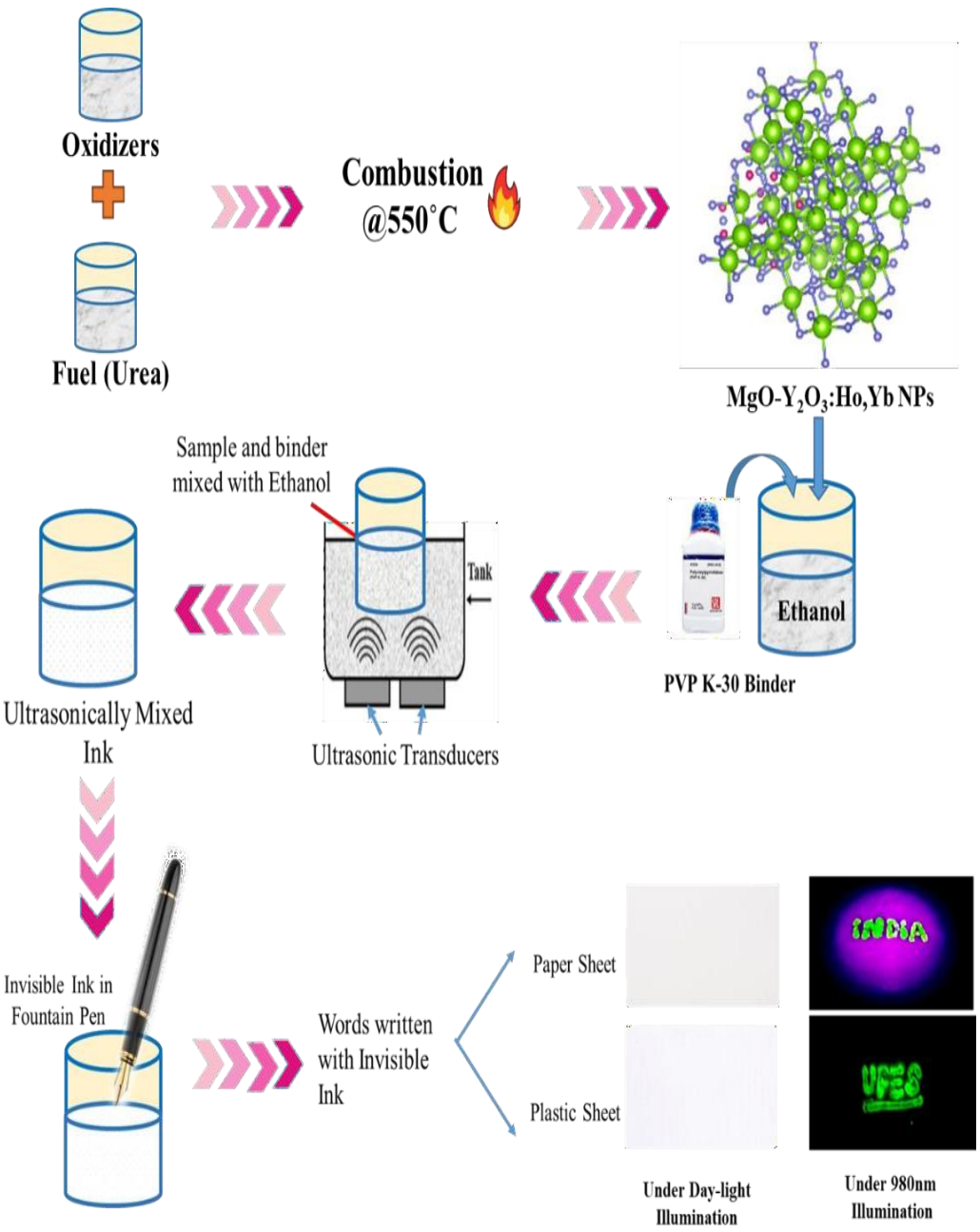

Fig 6.1: Synthesis process of MgO-Y_2O_3 nanocomposites and derived invisible ink for security applications

6.3 Results and Discussion

6.3.1 X-Ray Diffraction Study

Figure 6.2 shows the XRD patterns of Er Yb, co-doped MgO-Y_2O_3 nanophosphors. According to the obtained XRD patterns, it can be verified that the phases match with MgO (JCPDS-74-1225) and Y_2O_3 (JCPDS-43-1036), with the space groups Fm-3m (225) and Ia-3 (206), respectively (Bishnoi, Brajpuriya, et al., 2024; Rai et al., 2012). In all the samples, dual stable phase is observed, nullifying the impure phase formation of dopants. At lower concentrations of Yb ions, less than 1 mol%, no significant shifting in peaks is observed. While at higher concentration, the shifting of peaks towards higher angles reveal a decrease in crystallite size due to the smaller ionic radii of Yb ions than Y ions. For detailed analysis, Rietveld refinement of all the samples was carried out, and refined patterns are also shown in Fig 6.2. The parameters are summarized in Table 6-1. From refined parameters, it was observed that the crystallite size of MgO in the nanocomposite is consistent throughout the doping. It revealed that all dopants are

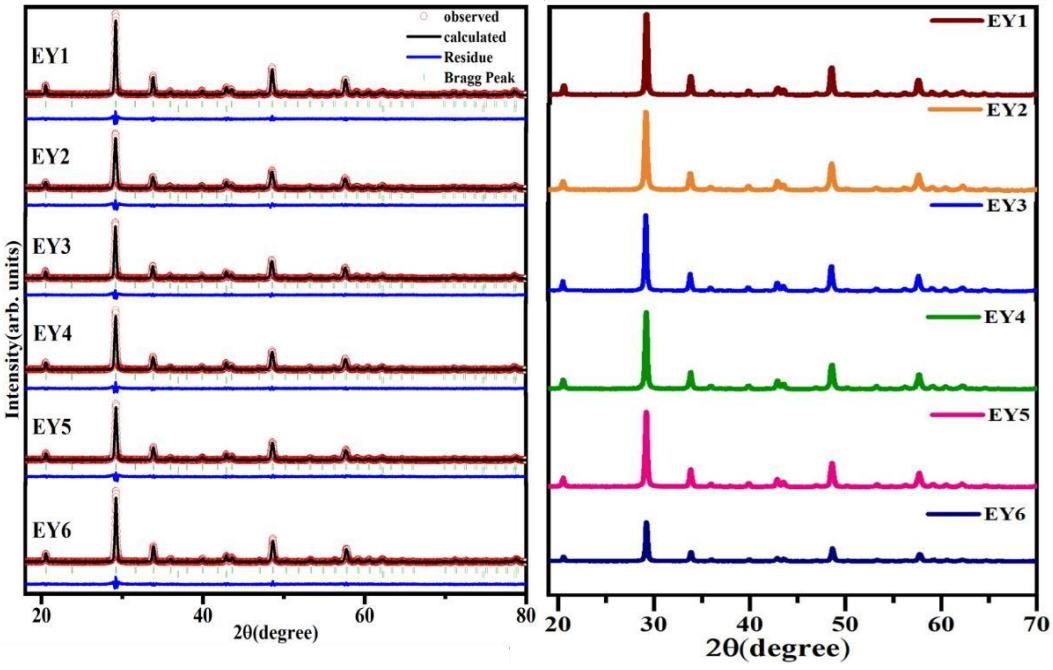

Fig 6.2: XRD patterns of Er, Yb doped MgO-Y_2O_3 and Rietveld refined patterns.

substituting Y sites in the Y_2O_3 lattice. However, some O vacancies were observed with doping. Er ions occupy the random site of Y in lattice, but Yb ions prefer for C2 sites specifically at higher concentrations, which further governs the luminescence behavior in the host.

Table 6 1: Calculated structural parameters for Er, Yb-doped compositions

		EY1	EY2	EY3	EY4	EY5	EY6
Lattice parameter (Å)	Y_2O_3	10.609	10.608	10.608	10.597	10.597	10.586
	MgO	4.217	4.217	4.217	4.216	4.217	4.217
Occupancy	Y_1 (C_{3i})	0.4955	0.4736	0.4465	0.4343	0.4943	0.4207
	Y_2 (C_2)	0.1409	0.1363	0.1355	0.1378	0.1534	0.1344
	O	0.8668	0.9960	0.9931	0.9995	0.9994	0.9998
	Er_1	0.0048	0.0044	0.0049	0.0049	0.0048	0.0046
	Er_2	0.0014	0.0015	0.0016	0.0015	0.0017	0.0014
	Yb_1	0.0006	0.0054	0.0049	0.0276	0.0558	0.0749
	Yb_2	0.0001	0.0046	0.0016	0.0082	0.0181	0.2495
Quality of Fit	GOF	1.5	1.6	1.5	1.5	1.5	1.5

A similar observation was noticed when Ho, and Yb were doped in MgO-Y_2O_3 nanophosphors. The X-ray diffraction peaks of all the samples are shown in Fig 6.3. Notably, no peaks of Yb_2O_3 and Ho_2O_3 were observed in the entire series of samples within the detection range of the employed XRD, ruling out any

presence of impurities. For detailed in-depth structural analysis the intense peak at 29.15˚(222), 33.78˚(040), 48.53˚(044), 57.63˚(262) of Y_2O_3 and 36.89˚(111), 42. 87˚(020), 62.19˚(022) of MgO were used. It is interesting to note here that with the

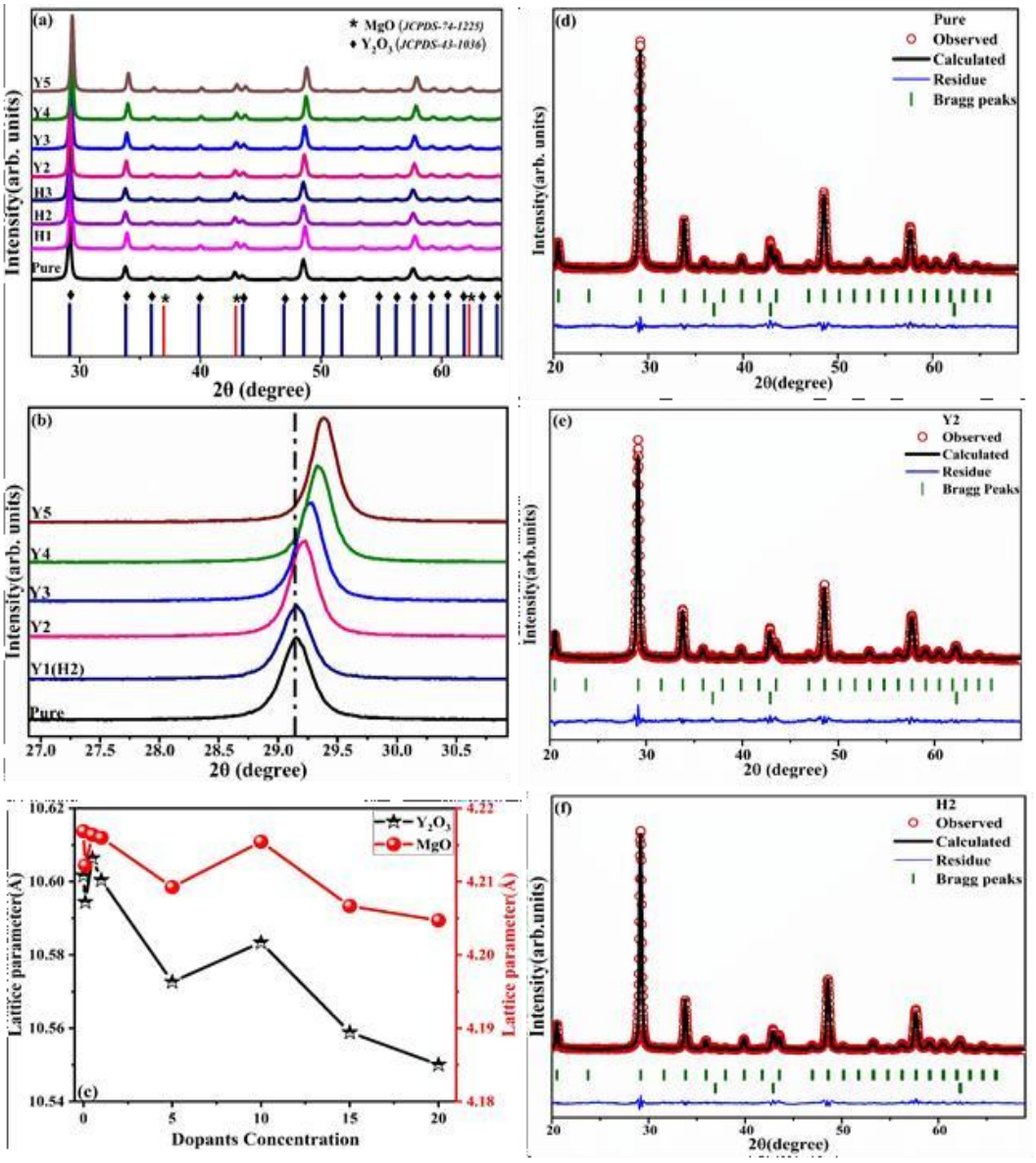

Fig 6.3: (a) XRD pattern of Ho, Yb doped MgO- Y2O3; (b) enlarged image showing shifting of peaks with dopant concentration; (c) Variation of lattice parameter of Y2O3 and MgO with dopant concentration; (d-f) Reitveld refined patterns of pure, Y2, and H2

increase in Ho^{3+} concentration up to 0.5 mol%, the shifting is not observed, whichcan be due to the similar ionic radii of Y^{3+}(1.040 Å) and Ho^{3+}(1.041 Å). However, the decrease in FWHM was noted, exhibiting a better crystallinity in the doped samples. Besides this, at Ho^{3+} (1 mol%) the maxima slightly shifted towards the higher angle, and the FWHM of Y_2O_3 peaks enhanced attributed to the structural perturbations (Mondal & Rai, 2018). The anticipated dislocations, caused by dopants have been evaluated using the formula: $\delta = 1/D^2$, where D is crystallite size which has been calculated using Debye-Scherer formula, $D(crystallite\ size) = \frac{k\lambda}{\beta cos\theta}$, where $\boldsymbol{k}$ is shape factor, $\boldsymbol{\beta}$ represents FWHM, $\boldsymbol{\lambda}$ is source wavelength and $\boldsymbol{\theta}$ represents diffraction angle. It is observed that dislocation density is highest in H3 sample, likely due to the distortion in the crystal structure of host due to the dopant, which further also affects the luminescence properties. Similarly, with Yb^{3+}concentration the peaks prominently shifted towards the higher angles (shown in enlarged Fig 6.3(b)) indicating the shrinkage of crystallite size due to the difference in ionic radii of Y^{3+}(1.040 Å) and Yb^{3+}(1.008 Å) (Y. Wang et al., 2023). The FWHM of peaks first decreases up to Y3 and then again increases which shows the enhancement in crystalline nature. Due to variation in peak broadening, the dislocation density also shows variation with the minimum observed in Y2. As the Yb^{3+} concentration increases in the host, the dislocation density increases, which in turn affects the associated spectroscopic characteristics of the host.

For the detailed analysis of structural perturbations the Rietveld refinement of XRD patterns has been conducted of pure as well as of H2 and Y2 samples using FULLPROF software (Fig 6.3 (d-f)). The formation of both the phases of MgO and Y_2O_3 was confirmed through double-phase fitting of patterns in pure and doped samples. The refined parameters suggest that dopant cations occupy both the Y sites (C_{3i} and C_2) resulting in the contraction of the lattice parameter and reduction in the bond length of Y_2O_3. The bond length of Mg-O is consistent at 2.418 Å, with doping nullifying the insertion of Ho^{3+} and Yb^{3+} in the MgO lattice. Conversely,

the Y_1-O (C_{3i}) decreases from 4.31 Å to 4.30 Å while the bond length of Y_2-O (C_2) decreases from 4.193 Å to 4.190 Å, respectively. At lower concentrations of Yb^{3+} and Ho^{3+} ions, the bond length of both sites of Y experienced a slight reduction, indicating the distribution of dopants in a random way. However, at higher Yb^{3+} concentrations, the Y_1-O bond length shows contraction as compared to the Y_2-O conveying that the Yb^{3+} ions prefer to occupy 8b (C_{3i}) Wyckoff positions in the

Table 6-1: Calculated structural parameters for all the compositions

Samples / Parameters		Pure	H2	Y2
Lattice parameter (Å)	Y2O3 MgO	10.6089 4.2177	10.6026 4.2167	10.5704 4.2082
Crytsallite Size (nm)	Y2O3 MgO	24.67 25.13	23.96 24.41	24.88 21.60
Dislocation Density		0.00164	0.00174	0.00161
Occupancy	Y1(C3i) Y2(C2) O H1 H2 Yb1 Yb2 Mg O	0.4955 0.1409 0.8668 - - - - 1 0.999	0.4429 0.1210 0.9502 0.0015 0.00092 0.0030 0.00076 1 0.9832	0.4465 0.1355 0.8539 0.0009 0.0007 0.0265 0.0083 1 0.9482
Bond Length (Å)	Y1–O(C3i) Y2–O(C2) Mg-O	2.314 2.193 2.418	2.312 2.190 2.418	2.306 2.190 2.418
Quality of Fit	Rwp Rxp GOF	6.9 5.1 1.9	8.2 5.2 2.1	6.5 5.0 1.6

lattice. These site occupancy preferences further affect the luminescence properties. In other studies, the random distribution of lanthanides such as Eu, Gd, and Ho at both the sites of Y has been reported(Antic et al., 1995; Concas et al., 2003; Mitric et al., 1997). Furthermore, the generation of O^{2-} defects in the MgO lattice was also inferred from the occupancy of O. Previous reports, indicated an increase in distortion in the lattice can increase the O and cationic defects in the host compound (Perrella et al., 2023). Here, with the variation of both the dopants, change in the lattice parameter and FWHM of MgO is also observed, showing the creation of different vacancies in the MgO lattice, too. All the refined parameters have been tabulated in Table 6-2.

6.3.2 Transmission Electron Microscopy Study

The morphology of annealed samples was evaluated by using TEM and SAED analysis. Fig 6.4(a-c) shows the TEM images of pure, H2, and Y2 samples at 50nm magnification scale. It is observed that the crystals are polyhedron in shape and agglomerated in all three samples. This high-temperature annealing causes grain growth which reduces the grain boundaries. The particle size of crystals shown in Fig 6.4(d-f) remains consistent with doping concentration and also complements the XRD result. In Fig 6.4(g-i) the planar spacing has been derived by using FFT in ImageJ software. The planes 1.863 Å and 1.506 Å correspond to the (343) and (345) planes of Y_2O_3. In H2 and Y2 planar spacing 1.891 Å and 1.863 Å correspond to the (044) plane of Y_2O_3 while 2.116 Å observed in Y2 corresponds to the (020) plane of MgO confirms the presence of both the lattices and also matches well with the planar of Y_2O_3 and MgO from XRD patterns. Some *moire* fringes were also calculated using the formula shown below which is shown in Fig 6.4(g).

$$d_{moire} = \frac{d_1 d_2}{\sqrt{d_1^2 + d_2^2 - 2 d_1 d_2 \cos \emptyset}} \qquad \text{Eq. 6.1}$$

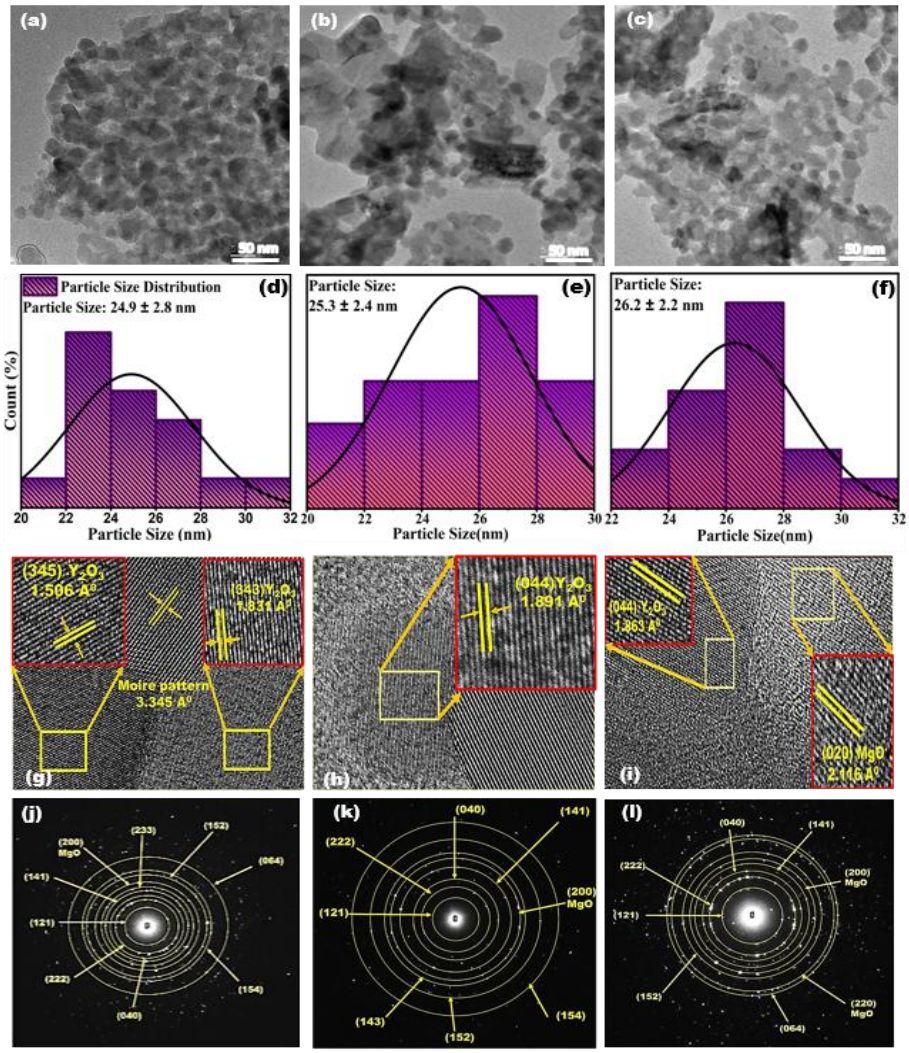

Fig 6.4: (a, b, c) TEM images of pure, H2, Y2 respectively (d, e, f) particle size of pure, H2, Y2 respectively (g, h, i) lattice planes observed in pure, H2, Y2 samples (j, k, l) diffraction patterns of pure, H2, Y2 samples

Here, d_1 and d_2 are the d-spacing of primary lattices in the image and d_{moire} is the spacing for the *moire* fringes. The angle ϕ is the angle at which both the actual lattices were orientated. The ring patterns observed in SAED as shown in Fig 6.4(j-l) confirm the polycrystalline nature. The observed rings exhibit the planes of Y_2O_3 and MgO in pure and doped samples. No additional plane belonging to the other phases could be detected, confirming the absence of secondary phases in all of the samples.

6.3.3 UV-Vis Absorption Spectroscopy Study

Absorption spectra of all phosphors in the range of 220 nm to 1150 nm have been illustrated in Fig 6.5. The absorption in the UV region is attributed to the host. Apart from the host absorption, several other peaks of Ho^{3+} and Yb^{3+} ions have also been observed. The peak near 450 nm is attributed to the absorption from $^5I_8$ to

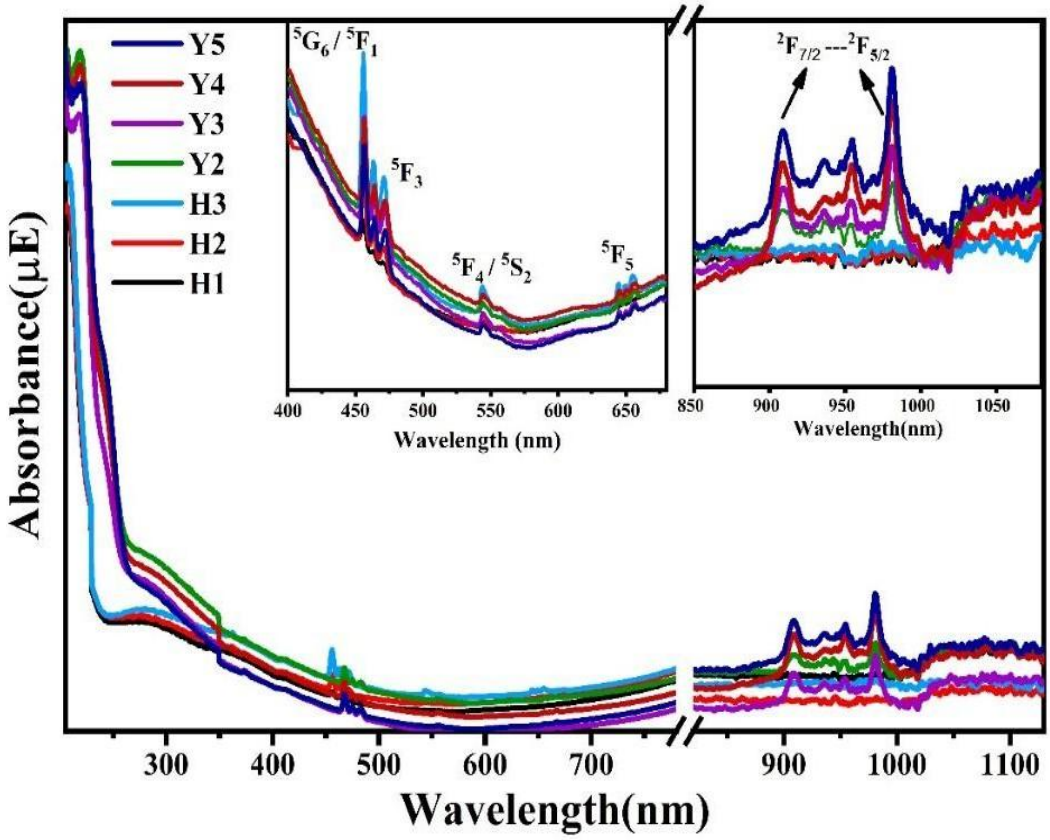

Fig 6.5: UV-Vis spectra of Ho Yb doped MgO-Y2O3 nanocomposites

higher energy levels $^5G_6$/ $^5F_1$, and $^5F_3$, the other peak around 550 nm is due to the transition from $^5I_8$ to $^5F_4$/$^5S_2$, and peaks near 650 nm are contributed by transitions between $^5I_8$ to $^5F_5$ (Pan et al., 2021; H. Wang et al., 2017). Additionally, the increase in Yb^{3+} ions peak near the NIR region from 900 nm to 1000 nm also enhanced attributed to the Yb^{3+} transition from $^2F_{7/2}$ to $^2F_{5/2}$(Xiang et al., 2017). These transitions remarkably increase with the Yb^{3+} concentration suggesting the strong absorption of Yb^{3+} ions in this region, which further governs the upconversion as

well as downconversion mechanism of Ho^{3+} ions.

6.3.4 Photoluminescence Spectroscopy Study

Luminescence mechanism in Er, Yb-doped MgO-Y_2O_3

The DC and UC of the Er, Yb-doped samples, were investigated using excitation at 378 nm and 980 nm. Fig 6.6(a) shows the emission spectra in the range of 500 nm to 700 nm on the excitation of 378 nm at different concentrations of Yb^{3+}. The strong emission is observed in green with weak red emission. The emission in the green region, ranging from 520 nm to 565 nm attributed to the $^2H_{11/2}$, $^4S_{3/2} \rightarrow {}^4I_{15/2}$ transitions, and the red emission is due to the $^4F_{9/2} \rightarrow {}^4I_{15/2}$ transition of Er ions. The emission in the green region increased with increasing concentration of Yb up to 1 mol% and was highest in the EY3 sample. The red

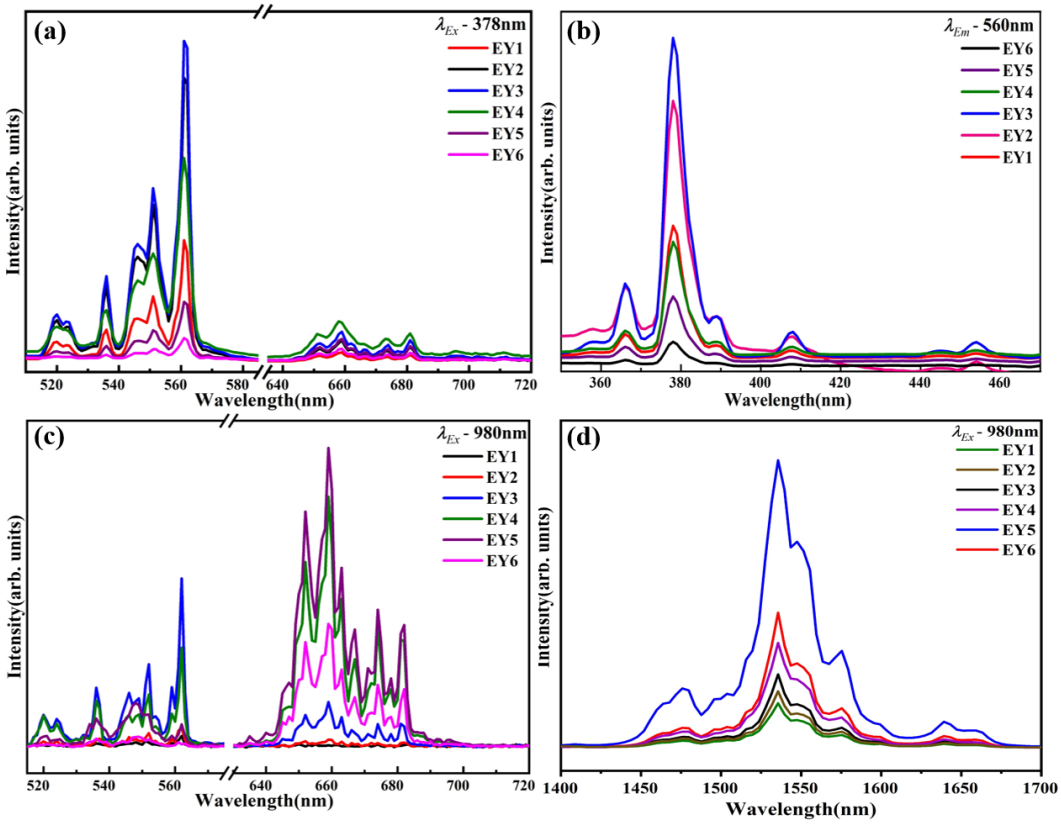

Fig 6.6: (a) DC of Er, Yb doped samples at 378 nm excitation; (b) Excitation spectra of Er, Yb doped samples at 565 nm emission; (c) UC of Er, Yb doped samples at 980 nm excitation; (d) NIE emission of all the samples at 980 nm excitation

region increased up to a Yb concentration of 5 mol% and then saturated. The saturation of intensity indicates the charge transfer from Er to Yb ions due to the resonant energy levels of the two. The Fig 6.6 (b) shows the excitation spectra of all the samples at fixed emission at 565 nm. Different peaks in the UV and blue region were observed centered at 368 nm, 378 nm, 409 nm, and 456 nm. All the peaks attributed to the Er ion transitions from $^4I_{15/2}$ to different levels. $^4I_{15/2} \rightarrow {}^4G_{11/2}$ is the absorption that occurs at 378 nm. While the peak at 409 nm occurs due to the transition between the ground level to $^4H_{9/2}$. Similarly peak at 456 nm arises due to the excitation from ground level to the $^4F_{3/2}$ of Er ions. From refined parameters observed from XRD patterns, it was observed that Er ions occupy random Y sites. In Y_2O_3, C_{3i} sites are favorable for magnetic dipole transitions, and C_2 sites are always favorable for electric dipole transitions. This may be assumed that for lower concentrations of Yb, Er can efficiently occupy the C_2 sites, which favours the radiative transitions, and green and red emission is observed. However, due to the preferred occupation of Y at C_2 sites, the Er are substituting the C_{3i} sites, and quenching is observed in emission.

In the UC mechanism, the emission is investigated on excitation wavelength of 980 nm, again, green and red emission of Er ions is observed (Fig 6.6(c)). In the UC mechanism, the green emission increased up to EY3 and afterwards started decreasing. On the other side, the red emission is stronger than observed in DC and increases up to 10 mol% of Yb ion, and is highest in EY5. This indicates that Yb ions efficiently transfer the energy to the Er ions, which is favorable for the red emission. The C_2 site preference of Yb ions makes favorable radiative transitions for red emission. Apart from this, the NIR emission is also recorded on excitation at 980 nm and shown in Fig 6.6(d). The emission is observed from 1450 nm to 1650 nm. These transitions are attributed to the $I_{13/2} \rightarrow I_{15/2}$ arising due to the Stark splitting. The emission increased up to Yb 10 mol% and afterwards decreased.

Luminescence mechanism in Ho, Yb-doped MgO-Y_2O_3

The impact of Ho^{3+} and Yb^{3+}dopants on DC and UC luminescence in MgO-Y_2O_3 nanocomposite at room temperature was examined by varying both concentrations. Fig 6.7(a) depicts the emission spectra in the range of 500 nm to 800 nm on the excitation of 448 nm at a fixed concentration of Yb^{3+} (0.5 mol %) and different concentrations of Ho^{3+} (0.1, 0.5, and 1 mol %). The spectra consist of three green, red, and NIR emissions ranging from 521 nm to 570 nm, 635 nm to 670 nm, and 735 nm to 775 nm respectively. The green band is attributed to the transitions from $^5F_4$/ $^5S_2$→$^5I_8$, while red and NIR bands are due to the $^5F_5$→$^5I_8$ and $^5F_4$ / $^5S_2$→$^5I_7$transition of Ho^{3+} ions, respectively (Monika et al., 2021; Pan et al., 2021). The PL spectra conveyed the increase in intensity of NIR and green regions with Holmium concentration up to 0.5 mol%, followed by quenching afterward.

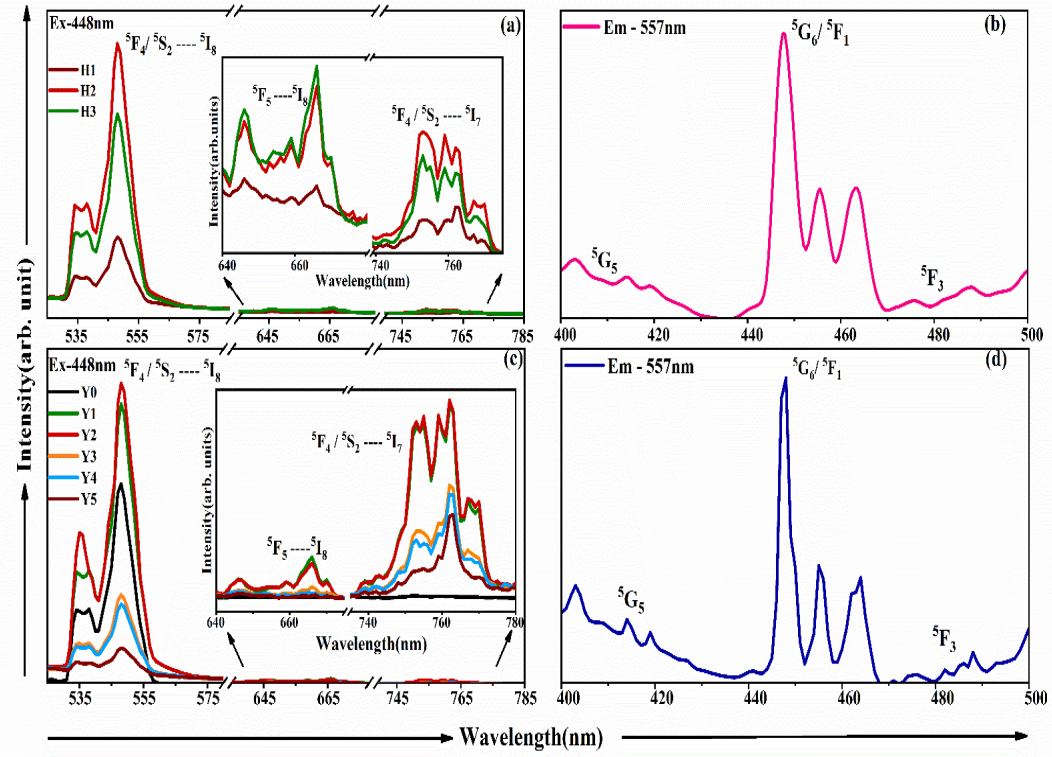

Fig 6.7: (a) Emission spectra of Ho^{3+} concentration on excitation of 448 nm; (b) Excitation spectra of H2 sample; (c) Emission of Yb^{3+} concentration at excitation of 448 nm; (d) Excitation spectra of Y2 sample

However, the intensity in the red region showed constant increment with an increase in the concentration of Ho^{3+} ions, indicating the increase in populations at the $^5F_5$ level. No emission was observed at wavelengths below 500 nm implying that first all populations of electrons non-radiatively decayed at $^5F_4/^5S_2$ and $^5F_5$from upper levels and then exhibited the radiative transitions to various lower levels. To further study the influence of Yb^{3+}concentration on luminescence behavior, the Yb^{3+}concentration was increased from 0 to 20 mol% after optimizing the Ho^{3+}concentration at 0.5 mol%, and spectra were collected at room temperature. Fig 6.7(c) depicts the emission spectra at various Yb^{3+} concentrations, which shows saturation of intensity at Yb^{3+} 5 mol%. It is interesting to note that the red region, which is enhanced as Ho^{3+}concentration increases, behaves oppositely to the Yb^{3+}concentration. It indicates the energy transfer (ET) from Ho^{3+} to Yb^{3+} from $^5F_5$ levels of Ho^{3+}. The various routes have been described later by using the energy level diagram. Fig 6.7(b, d) shows the excitation spectra for emission at 547 nm, 667 nm, and 756 nm. Different excitation peaks were observed near 404 nm, 414 nm, 448 nm, 452 nm, 466 nm, and 487 nm. All the peaks observed belong to the Ho^{3+} transitions. The major contribution is from 448 nm to 466 nm, attributed to the transition ($^5I_8 \rightarrow {}^5G_6$, $^4F_1$). The excitation spectra also complement the UV-Vis spectra which show strong absorption of Ho^{3+}ions near 420 nm, 448 nm, 450 nm, 465 nm, and 480 nm. After absorbing a photon of 448nm wavelength, electrons from $^5I_8$ jump to the $^5G_6/^5F_1$ of Ho^{3+}. After non-radiative relaxations from higher levels, the electrons will be populated to $^5F_3$ and $^5S_2/^5F_4$ before showing radiative transitions. The UC luminescence for various Ho^{3+} and Yb^{3+} concentrations has been recorded on a 980 nm excitation wavelength. Fig 6.8(a,b) shows the emission at fixed Yb^{3+} of 0.5 mol% and different Ho^{3+} concentrations from 0.1 to 1 mol%. Like DC, efficient emission was concentration observed in all three regions attributed to the Ho^{3+} transitions. The emission intensity, in all regions, increased for 0.5 mol% doping and decreased with further increase in concentrations. The intensity ratio of NIR and red with green decreases at 0.5 mol% and slightly increases at 1 mol% shown in Fig 6.8(c) which will be discussed below with the

help of the energy level diagram. Further, the effects of Yb^{3+} concentration on UC luminescence taken on the fixed concentration of Ho^{3+} of 0.5 mol% is shown in Fig 6.8(d,e). The emission in NIR and the green region shows quenching after Yb^{3+} of 5 mol%, but the red region intensity enhanced up to 15 mol% of Yb^{3+}, afterward got saturated at 20 mol%. The intensity ratios of red to green first decrease on the introduction of Yb^{3+} ions and increase after 5 mol% while the intensity ratio of NIR to green constantly decreases after a 5 mol% concentration of Yb^{3+} shown in Fig 6.8(f). This also will be discussed with an energy level diagram. For further analysis of the UC

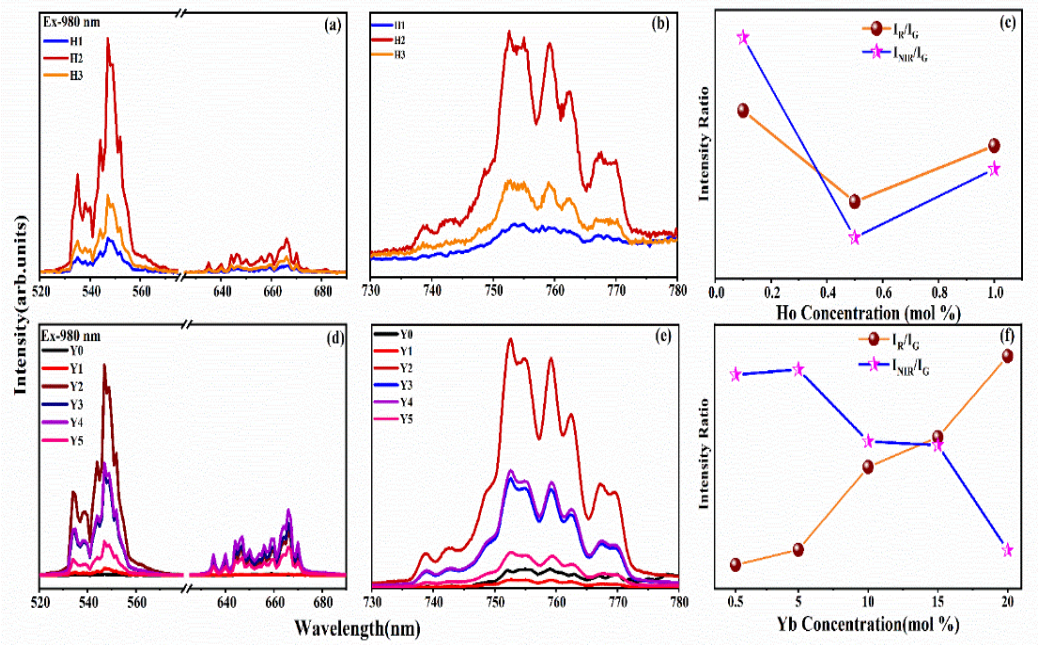

Fig 6.8: (a) Emission spectra of Ho^{3+}series in visible region under excitation of 980 nm; Emission of Ho^{3+} series in NIR region; (c) Intensity ratio of red and NIR with green emission in Ho^{3+} concentration; (d) Emission spectra of Yb^{3+} series in visible region under the excitation of 980nm; (e) emission spectra in NIR region;

mechanism the emission spectra of prepared phosphors have been studied by varying input pump power of 980 nm laser. The non-linear process is involved in the upconversion mechanism where the intensity is proportional to the power of

input radiation represented below $I\alpha\ P^n$ Here, I represents the UC intensity, P represents the pump power density (mW) and n is the number of photons involved in the UC process. Fig 6.9(a, b) illustrates the behavior of spectra of H2 and Y2 with input power as both phosphors exhibited the optimum emission in DC as well as in the UC process in the whole series. The intensity of both phosphors increases as the input power increases indicating the stability of the samples. After evaluating the slope values by taking a logarithmic plot between the integrated intensity and input power number of photons involved in the UC process has been summarized in Table 6-. It is observed that the value of n lies between 3 to 4 for green intensity, while it lies between 2 to 3 for red and NIR. However, at a higher concentration of Yb^{3+}, the value shifted towards 4 for green indicating that more photons are required for the green emission.

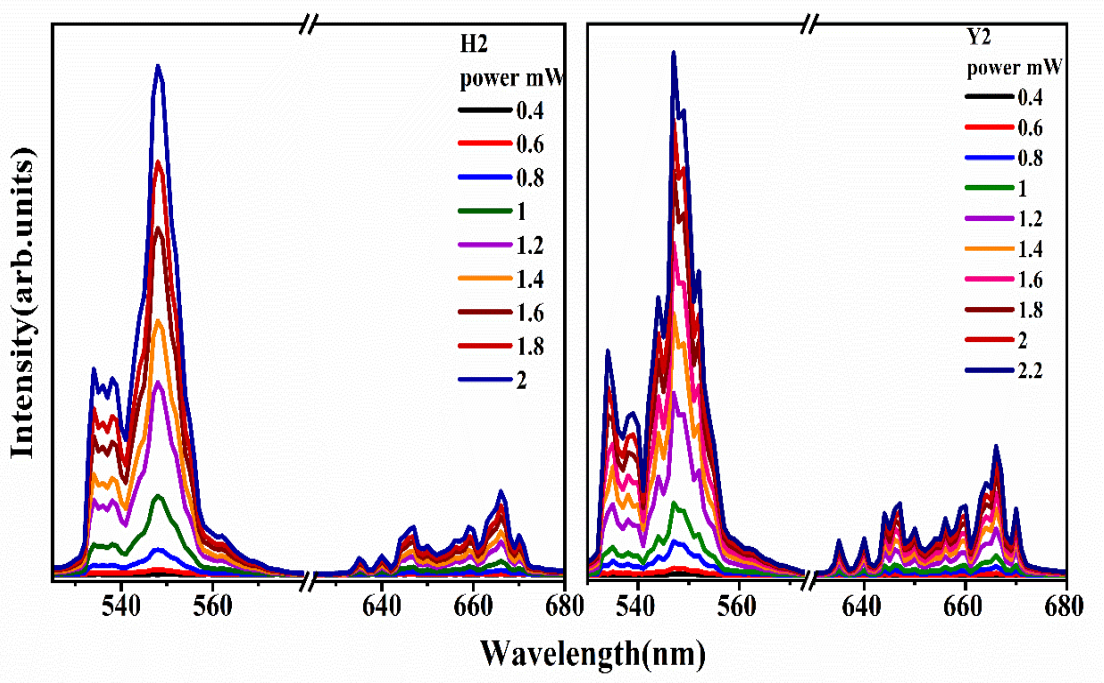

Fig 6.9: (a) Intensity variation with the function of input pump power of sample H2; (b) Intensity variation of Y2 sample with input pump power

Table 6-2: Slope value obtained by fitted experimental data of integrated intensity of green, red, and NIR emission

Sample	g_{reen}	n_{red}	n_{NIR}
Y1	3.1	3.3	2.6
Y2	2.9	2.8	3.2
Y3	3.2	2.7	2.8
Y4	3.4	2.3	2.4
Y5	3.7	2.9	2.4

To gain a deeper understanding of the different processes involved in UC/DC mechanisms, such as ground state absorption (GSA), excited state absorption (ESA), energy transfer (ET), and cross-relaxation (CR), are illustrated in band diagram shown in Fig 6.10. In the case of a single doped Ho^{3+}, the weak green, red, and NIR emission is observed due to weak absorption of Ho^{3+} ions near NIR region. After absorbing the photon of 980 nm Ho^{3+} ions excited to the 5I6 level denoted as GSA in the band diagram shown in Fig 6.10. After absorbing simultaneously another photon the electrons get excited to $^5F_4$, and $^5S_2$ levels denoted as ESA1, and there it decays to the $^5I_8$ and ^5I showing the green and NIR emissions respectively. Apart from these two emissions, the red emission arises by another pathway from $^5I_6$, electrons first non-radiatively decay to $^5I_7$, and from there after absorbing another photon gets excited to $^5F_5$ (denoted as ESA2) and radiatively decays back to $^5I_8$. When Yb^{3+} is introduced along with Ho^{3+} ions in the host the intensity in all regions is enhanced abruptly as Yb^{3+} has a large absorption near 980 nm cross-section and exhibits the transition from $^2F_{7/2}$ to $^2F_{5/2}$ (Upadhyay & Kumar, 2023; D. C. Yu et al., 2014). Then, Yb^{3+}ions transfer their energy to Ho^{3+}ions via ET1 to $^5I_6$ as the energy of $^5I_6$ matches well with the $^2F_{5/2}$ of Yb^{3+} (Bai et al., 2009). Simultaneously Yb^{3+} ions, after absorption of two photons transfer energy (ET2) to Ho^{3+}ions which enhances the population at $^5F_4$, and $^5S_2$ and causes intense green

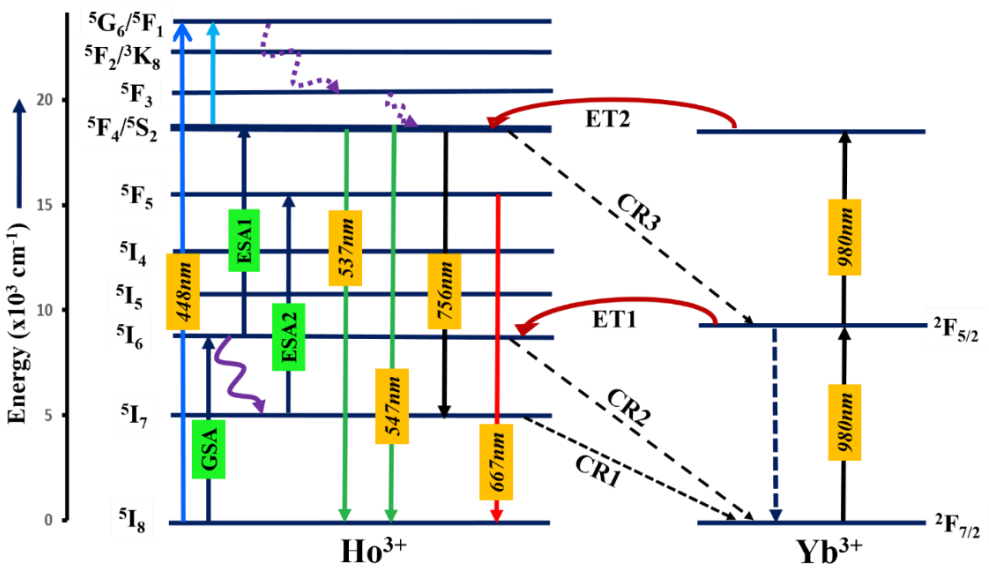

Fig 6.10: Energy level schematic diagram of Ho, Yb doped MgO: Y_2O_3. The solid blue lines represent the absorption at various levels (GSA ground state absorption; ESA- excited state absorption); Curvy dotted lines denoted non-radiative transition involved; Black dashed lines denoted cross-relaxation (CR1, CR2, CR3) while red solid line denoted as (ET)energy transfer between Ho to Yb ions. Green, Red, and Black solid lines represent the various emissions involved in up/down conversion luminescence.

emission. Therefore for green emission, four photons are required which also complements our fitted results, where the derived value of the photon required lies in 3 to 4. As the concentration of Yb^{3+} increases, the green and NIR emission saturation is observed first. BET from Ho^{3+} to Yb^{3+} is possible via $^5F_4/^5S_2 \rightarrow {}^2F_{5/2}$, $^5I_7 \rightarrow {}^2F_{7/2}$, and $^5I_6 \rightarrow {}^2F_{7/2}$ denoted as CR1 CR2 and CR3. The $^5F_4/^5S_2$ and $^5I_7$ populations declined fast through CR1 and CR3 at Yb^{3+} more than 5 mol%. Then, the energy from $^2F_{5/2}$ is again re-transferred to the $^5I_6$ via ET1 due to populations which causes the increase of red emission. Thus the intensity of green decreases while red increases and the ratio I_r/I_g also increases indicating that level $^5F_4/^5S_2$ depopulates faster than $^5F_5$ as the concentration of Yb^{3+} increases (Xiang et al., 2017). Apart from this the increment in concentration of Ho^{3+} ions also causes the

saturation of intensity after 0.5 mol% indicating the concentration quenching caused by the decrease in the inter-ionic distances between Ho^{3+} ions increasing the energy reabsorption. The ratio of red intensity to green first decreased and then increased at 1 mol% showing the parallel cross-relaxation between $^5F_5 \rightarrow {}^5I_7$ and $^5S_2/^5F_4 \rightarrow {}^5I_6$ affects the population at excited levels causing a decrease in intensities as well as the ratio as per earlier reported literature (L. Guo et al., 2012; Mahata et al., 2020; Monika et al., 2021; H. Wang et al., 2017).

Optical Temperature sensing study and laser-induced thermal effect based on Intensity Ratio

Due to the prolonged necessity of luminescence materials, which typically cause an increase in the temperature or operation at elevated temperatures, understanding their temperature-sensing properties becomes increasingly essential. However, the traditional contact measurements are inadequate to monitor the accurate internal temperature of these nanophosphors. Therefore, it is imperative to identify a non-contact technique for measuring the internal temperature. For luminescence materials to be more effectively used in practical situations, it is essential to comprehend the influence of temperature on their associated spectroscopic properties. In this work the upconversion of Ho^{3+} ions in H2, and Y2 across the temperature ranging from 298 K to 683 K is investigated.

The levels $^5F_4$ and $^5S_2$ of Ho^{3+} ions, which lie with a separation of 305 cm^{-1} (Cheng et al., 2023; Hou et al., 2024), follow the Boltzmann distribution in the thermal equilibrium state. This temperature-dependent behavior of the green emission can be further analyzed for exploring the temperature sensing study by probing the intensity ratio between the upper level ($^5F_4$) and lower level ($^5S_2$) at different temperatures. The relationship between two intensities is described by Eqn 6.1 (Monika et al., 2021; Tiwari et al., 2015):

$$LIR(T) = \frac{I_u}{I_l} = B\ exp\left(-\frac{\Delta E}{kT}\right) \qquad \text{Eq. 6.2}$$

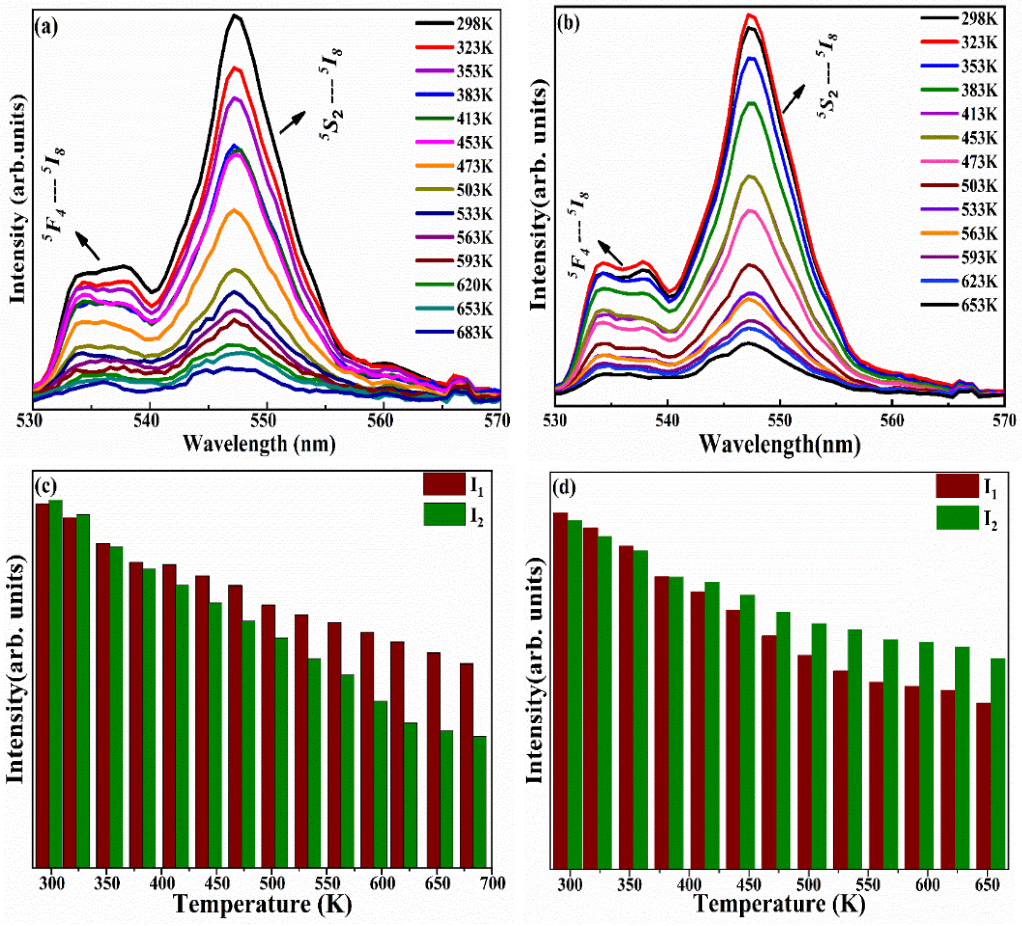

Fig 6.11: (a) Temperature-based up conversion spectra of H2 sample under excitation wavelength of 980nm; (b) variation of 537 nm and 548nm at different temperatures of H2 sample; (c) Temperature-based up conversion spectra of Y2 sample under excitation of 980 nm; (d) Variation of 537 nm and 548 nm at different temperature from 298 K to 683 K

Here, I_u, I_l is the intensity of upper and lower levels, respectively. B is constant, T is temperature, ΔE is separation between two energy levels, and k is Boltzmann constant. Fig 6.11(a, b) shows that the peak positions for both samples remain unchanged across the temperature from 298 K to 683 K, but quenching in overall green emission occurs with an increase in temperature. As the temperature of the sample increases, the probability of energy transfer and cross-relaxation is

enhanced due to the increase in the charge transfer band which ultimately causes in diminishment of overall intensity (X. Wang et al., 2018).

Here, it can be seen from Fig 6.11(c, d) that the intensity I_2 decreases more intensively than I_1. This may be due to the cross-relaxation between $^5F_4$ and $^5S_2$ levels causing the slower decrement in upper levels as compared to the lower level with increasing temperature. In the case of Y2, where Yb^{3+} concentration is higher than H2, the two distinct stark components are also visible at 535 nm and 537 nm. With the increase in temperature, the intensity remains constant up to 323 K, while a further increase in temperature causes a rapid decrease in the population of $^5S_2$, while the population of $^5F_4$ remains almost the same up to 423 K and then slowly declines afterward. This pattern, resulting from cross-relaxation of population between thermally coupled levels also causes an increase in luminescence intensity ratio which shows the exponential dependence with temperature and is employed for further temperature sensing measurements. The ***ΔE/k and B*** have been calculated by fitted curves shown in Fig 6.12(a, c). For H2, *ΔE/k* was 447 ± 13.2 and for Y2 the value was 380 ± 10.1 which is nearly equal to the theoretical value i.e. 438. 84. These values were used for further senor sensitivity calculation which can be expressed as follows (Y. Guo et al., 2018; Ryszczyńska et al., 2021):

$$S_{Abs}(T) = \frac{\partial(LIR)}{\partial T} = B\,\frac{\Delta E}{kT^2}\exp\left(-\frac{\Delta E}{kT}\right) \qquad \text{Eq, 6.3}$$

$$S_{Rel}(T) = \left(\frac{S_{Abs}}{LIR}\right) = \frac{\Delta E}{kT^2} \qquad \text{Eq. 6.4}$$

From the observed value of *B* and *ΔE/K*, sensing parameters were calculated and variations of sensitivities with temperature were shown in Fig 6.12(b and d). At 298 K the S_{abs} of H2 and Y2 sample were 51.3 x 10^{-4} and 42.74 x 10^{-4}, respectively. At 683 K these values were 9.58 x 10^{-4} and 8.6 x 10^{-4}, respectively. The relative sensitivity (S_{rel}) at 298 K was 22.24 x 10^{-4} and 18. 18 x 10^{-4} for H2 and Y2, respectively, and the S_{rel} decreased up to 6.68 x 10^{-4} and 4.98 x 10^{-4} at 683 K, respectivelyIt is observed that at lower temperatures the sensitivity is better and

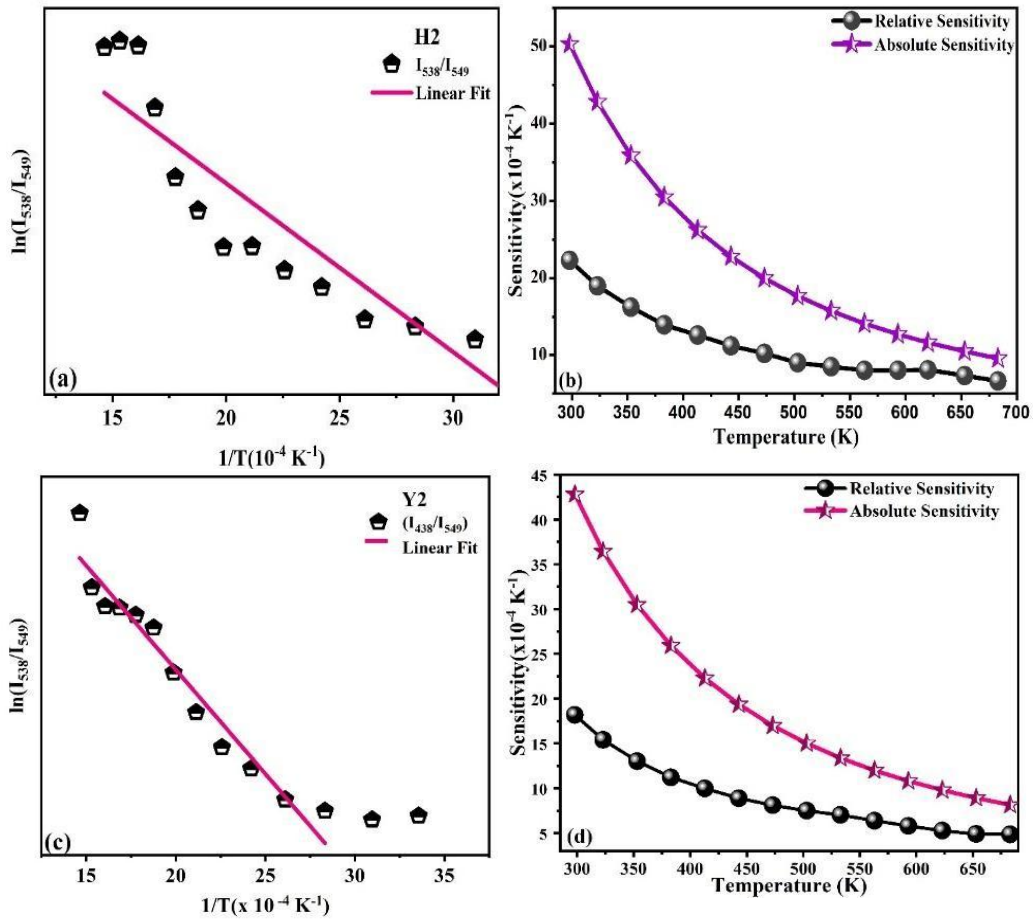

Fig 6.12: (a) Intensity ratio of green emission of H2 with temperature; (b) Sensitivity plot with temperature for H2 sample;(c) Intensity ratio of green emission of Y2 with temperature; (d) Sensitivity plot of Y2 sample with temperature.

also at lower concentrations of Yb^{3+} the sensitivities are higher suggesting that the rate of radiative transitions varies with the rare earth ions doping concentration, specifically with the Yb^{3+} ions. Consequently, the doping concentration of ions must optimized properly for specific applications to attain effective results. Furthermore, to assess the practical stability of prepared phosphors under the input laser exposure, the input laser effect was also measured to check the stability of samples with time up to 60 mins. The input power density may cause the thermal effect, which can increase the temperature of samples and can further affect the

luminescence characteristics. The H2 and Y2 were continuously exposed to an NIR laser with an input power density for 60 mins and the spectra were collected at intervals of 5 minutes. The internal temperature of phosphors has been derived by using Eq, 6.3. Calculated results shown in Fig 6.13 indicate that the temperature remains relatively constant throughout the exposure, suggesting that both samples achieve thermal equilibrium efficiently. However, it has also been observed that the temperature of Y2 is higher than H2 indicating that an increased concentration of Yb leads to an increase in internal temperature and a more pronounced thermal effect from input power.

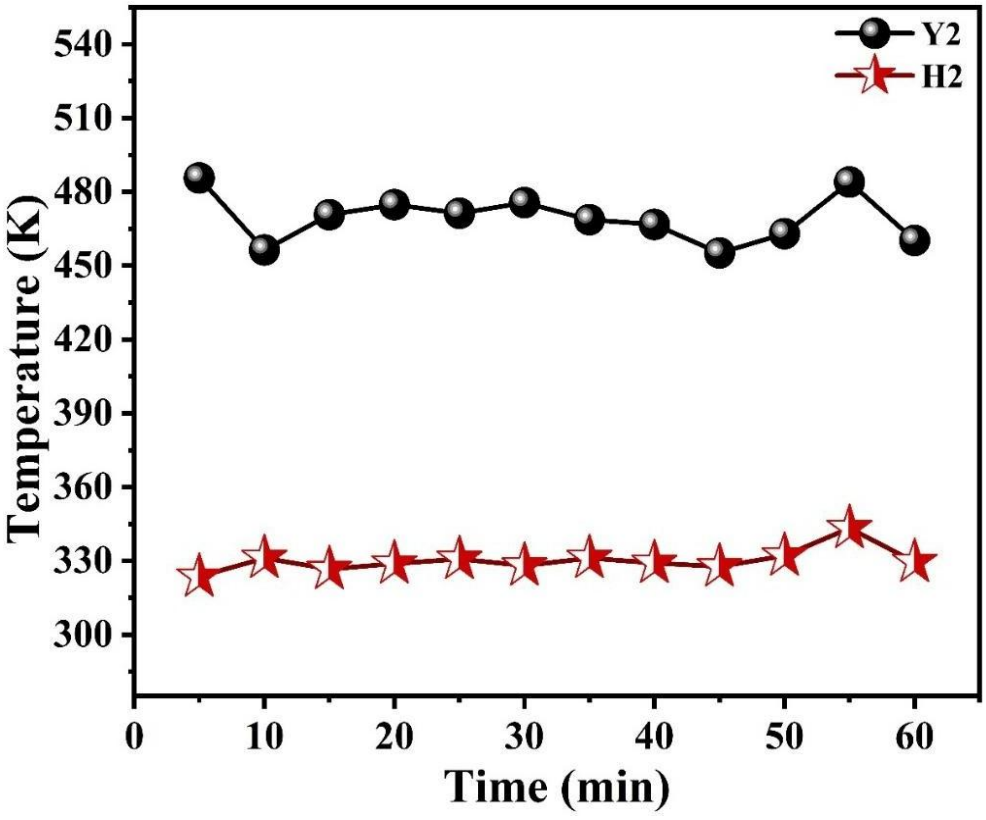

Fig 6.13: Variation of internal temperature of H2 and Y2 nanophosphors on the time under 980 nm exposure

6.3.5 Colorimetric Analysis and Anti-counterfeiting Application

The colorimetric parameters were calculated by using a CIE diagram using OSRAM software and shown in Fig 6.14. The CIE parameters, purity, and CCT are summarized in the Table 6-3. The color purity of all the samples is greater than 96 % and highest in the Y1 and Y2 samples. With the increase in Yb^{3+}, all the colors move towards the yellowish region due to an increase in red contribution with Yb^{3+} enhancement. The correlated color temperature (CCT) is above 5000 K making all the phosphors natural color emitters except for Y5 where the value is below 5000 K. It suggests that with an increase in concentration of Yb^{3+}, the emitted colors shift towards warm light. Another interesting result is obtained by analyzing the colorimetric parameters with the variation of input power of different samples. The parameters for Y1, Y2, and Y5 have been summarized in the Table 6-4. It is observed that at minimum power all the samples emit in the yellow region and with an increase in power it shifts towards a greener region shown in Fig 6.14. Also at the highest concentration of Yb^{3+}, the CCT is 3394 K at low input which is warm light and varies with power to 4929 K. It shows that all the samples move towards natural light with an increase in input power. The stability of these materials suggests that the specific composition of the prepared phosphors has the potential to be employed after collective optimization of concentration and input power for different applications in warm and cool LEDs. Finally, this report presents the novel use of MgO: Y_2O_3 (Ho^{3+}, Yb^{3+}) as the security ink for anti-counterfeiting applications, which was not reported in the literature. The synthesis of the ink has been described in the synthesis section. With the prepared ink some patterns and letters were written on paper, plastic, and card which were not visible in daylight shown in Fig 6.14(e). On the irradiation with 980 nm NIR laser after tuning it to 7 W the patterns and letters INDIA, UPES, and pattern of star illuminated with intense green light. Irradiating the letters again after 1 month no fading was observed confirming the stability of fabricated ink for application purposes. The obtained findings demonstrate that the prepared phosphors will provide a novel

approach to fabricating cost-effective material for advanced security ink applications.

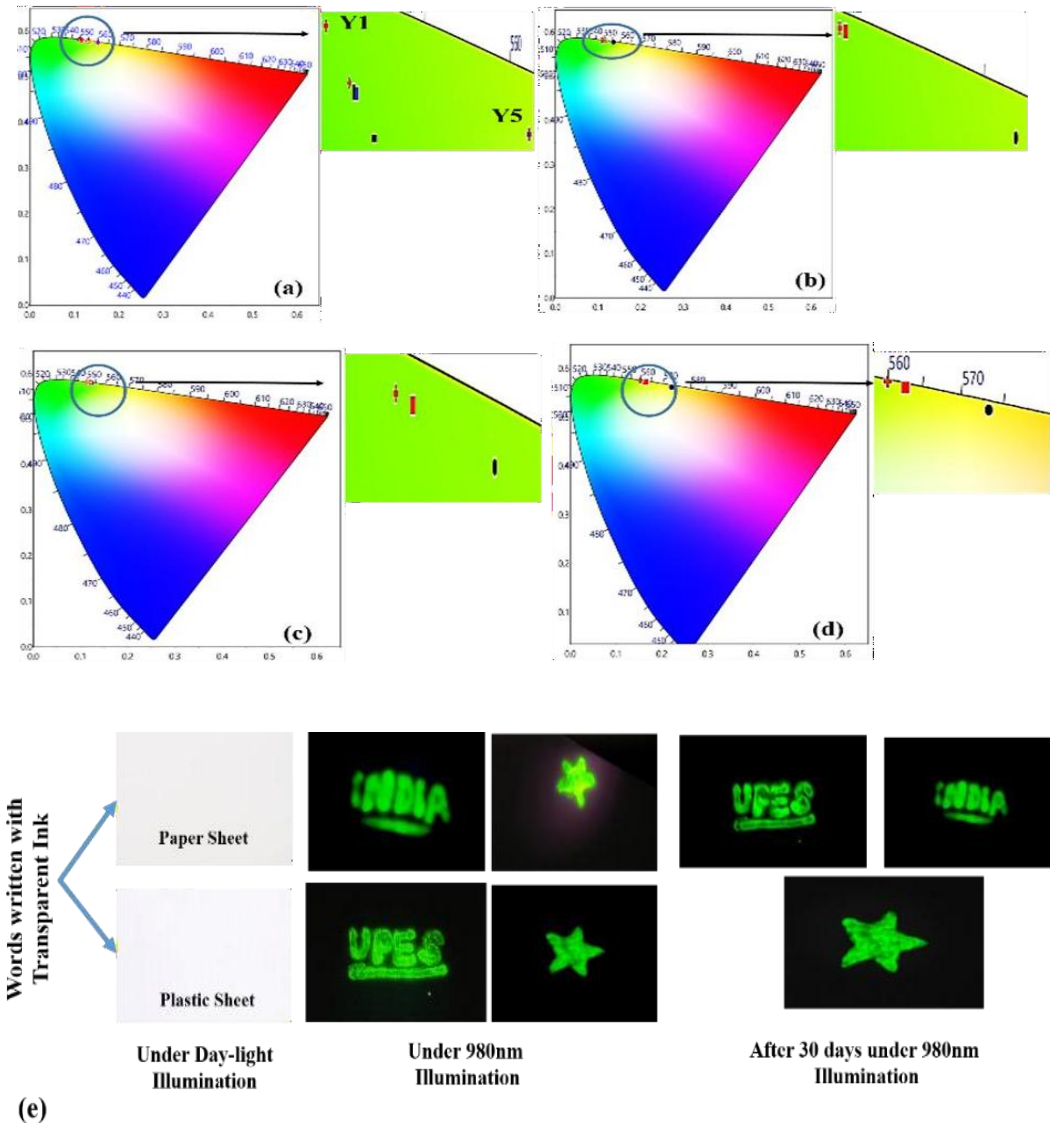

Fig 6.14: (a) CIE parameters of all samples; (b-d) CIE parameter of H2, Y2, and Y5 with power variation (black solid circle represents coordinates for lowest pump power and red solid square is coordinates at highest pump power); (e) Under the irradiation of 7W, 980 nm, the handwritten letters visibility on paper and plastic sheet and stability of Ink after 30 days

Table 6-3: CIE parameters of all phosphors under 980nm variation

Sample	x, y	Purity (%)	CCT(K)
H1	(0.2954, 0.6555)	87.1	6074
H2	(0.3000,0.6897)	98.8	5967
H3	(0.2879,0.6805)	95.6	6158
Y2	(0.3082,0.6819)	98.6	5854
Y3	(0.3346,0.6557)	98.2	5479
Y4	(0.3422,0.6482)	98.1	5367
Y5	(0.3710,0.6195)	97.9	4929

Table 6-4: Colorimetric parameter variation of Y1, Y2, and Y5 with power

Power (mW)	Y1		Y2		Y5	
	Purity (%)	CCT (K)	Purity (%)	CCT (K)	Purity (%)	CCT (K)
0.6	97	5368	98.1	5688	93	3394
1	98.7	5947	98.8	5825	96.5	4643
2	98.8	5967	98.6	5854	97.9	4929

6.4 Conclusion

In the present study, a comprehensive study on MgO-Y_2O_3 nanocomposites co-doped with Er, Yb and Ho, Yb has unveiled the promising results on DC and UC luminescence. It has been investigated that dopants mainly occupy the lattice positions of the Y_2O_3 compound and facilitate structural perturbations. The morphology of doped samples remains invariant under the doping concentration variations. The successful synthesis of dual-phase nanocomposites with controlled morphology, along with the mechanism of UC and DC luminescence demonstrates the composition's versatility in optical applications. In case of Er. Yb co-doping the downconversion observed at excitation of 378 nm and attributed to the Er intra f-f transitions. The green emission is more intense as compare to red emission in case of DC. While in upconversion luminescence the green emission is more intense than red emission. Saturation in green observed at lower concentration Yb ions indicates the red favorable energy transfer between ions.

Additionally, The in-depth analysis of DC and UC luminescence, with optimized concentration at Ho (0.5mol %) Yb (5mol %), conveys that emission in green, red, and NIR regions strongly depends on both the dopant concentrations. The power-dependent luminescence mechanism revealed the involvement of three to four-photon for green emissions and three to four-photon for red and NIR emissions. Additionally, the temperature sensing studies showed that absolute and relative sensitivity for H2 samples were 51.3 x 10^{-4} K^{-1} and 22.24 x 10^{-4} K^{-1} respectively, and the same for Y2 were 42.74 x 10^{-4} K^{-1} and 18. 18 x 10^{--1} at 298 K. Further, both the optimized nanophosphors easily reached thermal equilibrium when irradiated with prolonged 980nm input power showing stability. The tunable colorimetric properties, with adjustable correlated color temperature and color purity > 98%, make them a potential candidate for warm and cool LEDs. The successful demonstration of the fabricated security ink of the MgO-Y_2O_3 nanophosphors and the ability to create invisible patterns obtained from ink that illuminate under NIR excitation, coupled with long-duration stability paves the way for their practical implementation in specific industrial applications.

CHAPTER 7

SUMMARY AND FUTURE SCOPE

SUMMARY AND FUTURE SCOPE

Oxides and nanophosphors are actively investigated for different luminescence applications. Among oxides, the MgO-Y_2O_3 has demonstrated its potential as a phosphor host, exhibiting significant luminescence with the doping of rare-earth and non-rare earth ions. The present study explored the structural and luminescence properties of MgO and MgO-Y_2O_3 nanophosphors. The pure MgO and Bi, Li-doped MgO nanophosphors were synthesized using the combustion method, using urea as a fuel and nitrates as oxidizers. XRD patterns of pure and doped MgO indicate that a single phase of cubic MgO is maintained in both pure as well as in doped samples. However, at higher concentrations of Bi ions, the creation of interstitial defects is observed, while the doping of Li introduces the oxygen vacancies due to the charge difference between dopant and host cations. From XANES spectra of O K-edge indicated the increase in localized states near the conduction band and the creation of F defects in the lattice. Bi L_3-edge revealed the stable oxidation state of the dopant at +3, nullifying any formation of a secondary phase during doping of Bi ions. On the excitation of 275nm, pure MgO emitted strongly in the blue region, along with a weak emission in the red region. The blue emission centered at 428 nm with small shoulders around revealed the presence of several shallow F centers, while the red region is due to the recombination of holes from the valance band with interstitial O ions present within the lattice. Li ion doping did not support the photoluminescence and quenching was observed. In Bi-doped MgO the emission peaks were observed at 362nm and 387 nm attributed to the Bi s→ p transitions. Quenching in emission observed after 0.5 mol% of Bi indicated that doping of Bi ions induced the new defects within the bandgap which leads to emission shift from blue to UV region. The TL glow curves of Bi-doped MgO showed the transfer of charge carriers from shallower to deeper traps with an increase in Bi content. In the case of Li doping characteristics TL peaks of Li defects are observed at low temperatures and the stability of peak with an increase in dose indicated that the stability of traps was higher at lower

temperatures in doped MgO. Furthermore, different concentrations of Sm and Ce doped in MgO and co-doped with Li ions to examine dopant-induced defects and luminescence performance of doped phosphors, examined the strategies for improved luminescence properties. The doped samples were synthesized by using the solution combustion method. XRD patterns confirmed that Sm and Li ions were successfully incorporated without forming a secondary phase. However, the diffraction peaks shifted towards a higher angle with an increased concentration of Sm ions (0.05 – 0.5 mol%) attributed to the interstitial doping along with the substitutional doping at higher concentrations. From TEM images polyhedral shaped nanocrystals of 25-30 nm were observed. From XANES, broadening in features of Mg K edge with increased concentration Sm ions attributed to the creation of unsaturated bonds to anions at edges and surfaces. Without changing the oxidation state Mg cations shifted towards the tetrahedral sites. XANES of O K-edge conveyed the increase in vacancies with doping. The pre-edge features sharpened with increasing Sm concentration confirmed the surface and bulk defect generations. XANES of the Sm L_3-edge confirmed the +3 oxidation state across all doping levels. The Sm^{3+}, Li^{+} doped MgO nanophosphors were excited by using UV excitation 275 nm and blue laser 405 nm. The blue emission was due to the intrinsic F centers of the host suppressed with the addition of Sm while the characteristics 4f transitions of Sm from 550 – 750 nm attributed to the $^4G_{5/2} \rightarrow {}^4H_{5/2}$ enhanced and the highest emission is observed at 0.5 mol%. Adding Li ions strengthened Sm ions' emission and enhanced the red emission due to improved crystallinity and charge compensation. On further excitation at 405 nm, the emission shifted to the red region corresponding to the f-f transition of Sm^{3+} ions. The charge transfer from host to dopant enabled the red emission from Sm^{3+} ions at 405 nm excitation. TL glow curves were recorded after exposing the doped samples to gamma radiation with different doses. Doping of Sm and Li exhibited the new TL peak at 435 K which intensified with the Sm concentration indicating that Sm is the TL activator. Incorporating Li ions further improved the trap efficiency and enhanced the 437 K TL peak. With the dose, the TL intensity increased confirming the stability of TL

peaks. Additionally, MgO is doped with varying concentrations of Ce from 0.01 to 0.3 mol% and a fixed concentration of Li at 0.3 mol% and synthesized by using combustion synthesis. From XRD patterns, the low solubility of Ce ions is observed and the secondary phase of CeO_2 is confirmed at 0.2 mol%. The doping of Ce caused the charge disturbance in the lattice due to the different charges between the host and dopant ion. Li neutralizes the charge disturbance and improves the crystallinity. From XANES of Mg K-edge, it was observed that Ce doping causes the shifting in the edge line towards lower energy due to the tetrahedral site formation. Pre-edge feature of O K -edge intensified and revealed the increase in hybridization of Ce-O orbitals. From XANES of Ce L_3 edge, co-existance of Ce in +3 and +4 oxidation state confirmed. Covalant character of increased with Ce doping. Doping of Ce ions enhanced the red emission centered at 570 nm and 610 nm under 310 nm excitation. TL analysis revealed the generation of new TL peaks at 435 K in singly-doped Ce and at 475 K in double doped MgO. Doping of Ce and Li creates the shallow and stable traps. However, doping in MgO conveyed the low solubility of RE and non RE ions. Rare earth incorporation in MgO-Y_2O_3 yielded interesting outcomes of luminescence properties. The Er, Yb and Ho, Yb codoped in MgO-Y_2O_3 and downconversion and upconversion emission has been studied. The samples were synthesized by solution combustion method. XRD patterns and Rietveld refined parameters confirmed that dopant occupied the Y positions in Y_2O_3 lattice. From Rietveld- refined parameters, it was revealed that Er ions occupy random position of Y ions while Yb ions due to smaller radii prefers C_2 symmetry sites. This site occupation altered the crystal fiel environment which influenced the luminescence properties. At excitation of 378 nm strong green and weak red emission of Er ions observed attributed to the $^2H_{11/2} \rightarrow {}^4I_{15/2}$ and $^4F_{9/2} \rightarrow {}^4I_{15/2}$ transition, respectively. In downconversion, quenching in emission observed due to the dipole-dipole charge transfer from Er to Yb ions. Under excitation of 980 nm, with increase in Yb ion concebtration red emission dominates and highest at 10 mol% of Yb attributed to the efficient energy transfer from sensitizer to activator. Further, the co-doping of Ho and Yb in MgO-Y_2O_3, the luminescence

characteristics studied. In downconversion luminescence, Ho emission in range of 500 to 800 nm under excitation of 448nm but quenching observed after 5 mol,% of Yb ions attributed to the charge transfer from Ho to Yb ions. Under excitation of 980 nm, emission of Ho increased up to 15 mol% Yb ions. The luminescence intensity versus input pump power suggested that three to four photon processes were involved in green emission while two photon process in red emission. Temperature-based upconversion luminescence showed the saturation in intensity at higher temperatures caused the decrease in relative sensitivity with increase in temperature. Apart from analysis of luminescence mechanism, ink was fabricated from the prepared nanophosphors and patterns were created on paper, plastic sheet which was invisible under daylight and illuminated under NIR radiation. No fading of patterns was observed even after two months demonstrated long-term stability for security ink applications. From the insights of structural and luminescence mechanisms of Mgo-Y_2O_3, indicated that this nanophosphor is a potential candidate for security ink and laser applications.

Future Scope

This study of MgO-Y_2O_3 nanophosphors opens promising avenues for future research due to their tunable optical properties, thermal stability, and high sensitivity. These features pose MgO-Y_2O_3 as a potential candidate for variety of advanced applications, such as optial temperature sensing, lighting, security ink, anticounterfeiting. Future investigations must focus on optimizing parameters such as dopant combination, concentration of sensitizer and activator, synthesis, etc. and exploring the site occupation to further enhance the luminescence properties. This nanophosphor is still in infancy for upconversion applications, thus significant opportunity exist in unveiling the downconversion well as upconversion properties. Moreover, the integration of MgO-Y_2O_3 nanophosphors into cutting-edge applications, including optoelectronics, high-resolution displays, thermal sensing devices and counterfeiting could revolutionize these fields. Future research must

focus on the environment stability, synthesis scalable, and integration with other nanomaterials to enhance their practical usability in industrial and commercial domain.

BIBLIOGRAPHY

BIBLIOGRAPHY

Abdelrehman, M. H. M., Kroon, R. E., Yousif, A., Seed Ahmed, H. A. A., & Swart, H. C. (2019). Luminescence properties and cathodoluminescence degradation of Bi doped SrO powder. *Journal of Vacuum Science & Technology B*, *37*(1), 011206. https://doi.org/10.1116/1.5075492

Abdelrehman, M., Kroon, R., Mohmmed, A., Seed Ahmed, H., Swart, H. C., Lyu, T., & Dorenbos, P. (2020). Photoluminescence, thermoluminescence, and cathodoluminescence of optimized cubic Gd 2 O 3 :Bi phosphor powder Photoluminescence, thermoluminescence, and cathodoluminescence of optimized cubic Gd 2 O 3 :Bi phosphor powder. *J. Vac. Sci. Technol.*, *124*(23). https://doi.org/10.1039/C8TC01020J

Abdi-Jalebi, M., Ibrahim Dar, M., Sadhanala, A., Johansson, E. M. J., & Pazoki, M. (2020). Chapter 3 - Optical absorption and photoluminescence spectroscopy. In M. Pazoki, A. Hagfeldt, & T. B. T.-C. T. for P. S. C. M. Edvinsson (Eds.), *Micro and Nano Technologies* (pp. 49–79). Elsevier. https://doi.org/https://doi.org/10.1016/B978-0-12-814727-6.00003-7

Abdurabu Thabit, H., Ismail, A. K., Kabir, N. A., Abu Mhareb, M. H., Al Mutairi, A. M., Bafaqeer, A., Alajerami, Y., & Abualsayyed, M. I. (2024). Photoluminescence and thermoluminescence dosimetry properties of Ag/Y co-doped ZnO nanophosphor for radiation measurements. *Luminescence : The Journal of Biological and Chemical Luminescence*, *39*(2), e4683. https://doi.org/10.1002/bio.4683

Achkar, A. J., Regier, T. Z., Wadati, H., Kim, Y.-J., Zhang, H., & Hawthorn, D. G. (2011). Bulk sensitive x-ray absorption spectroscopy free of self-absorption effects. *Physical Review B*, *83*(8), 81106. https://doi.org/10.1103/PhysRevB.83.081106

Aggarwal, S. (2025). Recent advances in fundamental research on photon avalanches on the nanometre scale. *Nanoscale*.

Akasaki, I. (2015). Nobel Lecture: Fascinated journeys into blue light. *Reviews of*

Modern Physics, *87*(4), 1119–1131.

Amit Sharma, O. P. M. and G. K. G. (2015). Effect of fuel to oxidizer ratio on synthesis of Alumina powder using Solution Combustion Technique-Aluminium Nitrate & Glycine combination. *Acta Zoologica*, *96*(2), 147–153.

An, N., Ye, L., Bao, R., Yue, L., & Wang, L. G. (2019). Up-conversion luminescence characteristics and temperature sensing of Y2O3: Ho3+/Yb3+ single crystal fiber. *Journal of Luminescence*, *215*(July). https://doi.org/10.1016/j.jlumin.2019.116657

Antic, B., Mitric, M., & Rodic, D. (1995). Structure properties and magnetic susceptibility of diluted magnetic semiconductor Y2-xHoxO3. *Journal of Magnetism and Magnetic Materials*, *145*(3), 349–356. https://doi.org/10.1016/0304-8853(94)01625-9

Aoki, T. (2012). Photoluminescence Spectroscopy. In *Characterization of Materials* (pp. 1–12). https://doi.org/https://doi.org/10.1002/0471266965.com058.pub2

Aritani, H., Yamada, H., Nishio, T., Shiono, T., & Imamura, S. (2000). Characterization of Li-Doped MgO Catalysts for Oxidative Coupling of Methane by Means of Mg K-Edge XANES. *The Journal of Physical Chemistry*, 10133–10143. https://doi.org/10.1021/jp000291y

Armaroli, N., & Bolink, H. J. (2016). Luminescence: The Never-Ending Story. *Topics in Current Chemistry*, *374*(4), 44. https://doi.org/10.1007/s41061-016-0044-0

Asakura, H., Hosokawa, S., Teramura, K., & Tanaka, T. (2019). Local Structure Study of Lanthanide Elements by X-Ray Absorption Near Edge Structure Spectroscopy. *Chemical Record*, *19*(7), 1420–1431. https://doi.org/10.1002/tcr.201800164

B., H. (1926). Fishing from the Earliest Times. *Nature*, *118*(2982), 907–908.

https://doi.org/10.1038/118907b0

Bai, Y., Wang, Y., Peng, G., Yang, K., Zhang, X., & Song, Y. (2009). Enhance upconversion photoluminescence intensity by doping Li+ in Ho3+ and Yb3+ codoped Y2O3 nanocrystals. *Journal of Alloys and Compounds*, *478*(1–2), 676–678. https://doi.org/10.1016/j.jallcom.2008.11.114

Balabanov, S., Permin, D., Normani, S., Belyaev, A., Koshkin, V., Andreev, P., Ladenkov, I., Braud, A., Camy, P., Solé, R. M., Mateos, X., & Loiko, P. (2025). Fabrication and luminescent properties of erbium-doped Y2O3–MgO and Gd2O3–MgO nanocomposite ceramics. *Journal of the American Ceramic Society*, *108*(4), e20330. https://doi.org/https://doi.org/10.1111/jace.20330

Balakrishnan, G., Velavan, R., Mujasam Batoo, K., & Raslan, E. H. (2020). Microstructure, optical and photocatalytic properties of MgO nanoparticles. *Results in Physics*, *16*, 103013. https://doi.org/10.1016/J.RINP.2020.103013

Bapat M, S. S. (1985). THERMOLUMINESCENCE OF Li DOPED MgO. *Current Science*, *54*(1), 35–37. http://www.jstor.org/stable/24087239

Bazhukova, I. N., Pustovarov, V. A., Myshkina, A. V, & Ulitko, M. V. (2020). Luminescent nanomaterials doped with rare earth ions and prospects for their biomedical applications (a review). *Optics and Spectroscopy*, *128*, 2050–2068.

Beck, D. D., Capehart, T. W., & Hoffman, R. W. (1989). Determination of Ce valence in Rh-Ce/Al2O3 catalysts by X-ray absorption. *Chemical Physics Letters*, *159*(2–3), 205–213. https://doi.org/10.1016/0009-2614(89)87411-1

Behrens, P. (1992). X-ray absorption spectroscopy in chemistry: II. X-ray absorption near edge structure. *TrAC Trends in Analytical Chemistry*, *11*(7), 237–244. https://doi.org/https://doi.org/10.1016/0165-9936(92)87056-P

Bhattacharya, S., & Acharya, A. (2020). Experimental tools for characterizations of glass nanocomposites containing metal oxides. *Metal Oxide Glass Nanocomposites*, 51–75. https://doi.org/10.1016/B978-0-12-817458-6.00004-4

Bishnoi, P., Brajpuriya, R., Sharma, A., Chae, K. H., Won, S. O., & Vij, A. (2024). Defect modulation and color tuning of MgO: Probing the influence of Sm and Li dopants through x-ray absorption, photoluminescence, and thermoluminescence spectroscopy. *Journal of Alloys and Compounds*, *1002*(March), 175270. https://doi.org/10.1016/j.jallcom.2024.175270

Bishnoi, P., Dhiman, G., Brajpuriya, R., Hwa Chae, K., Won, S. O., & Vij, A. (2024). Structural and luminescence properties of MgO: Li nanocrystals. *Nuclear Instruments and Methods in Physics Research Section B: Beam Interactions with Materials and Atoms*, *552*, 165357. https://doi.org/10.1016/J.NIMB.2024.165357

Bishnoi, P., Kumar, A., Brajpuriya, R., Parmar, K. P. S., Sharma, A., Chae, K. H., & Vij, A. (2024). Electronic structure and luminescence studies of Bi doped MgO nanophosphors. *Ceramics International*. https://doi.org/10.1016/j.ceramint.2024.02.046

Blair, V. L., Fleischman, Z. D., Merkle, L. D., Ku, N., & Moorehead, C. A. (2017). Co-precipitation of rare-earth-doped Y2O3 and MgO nanocomposites for mid-infrared solid-state lasers. *Appl. Opt.*, *56*(3), B154--B158. https://doi.org/10.1364/AO.56.00B154

Blasse, G. (1968). Energy transfer in oxidic phosphors. *Physics Letters A*, *28*(6), 444–445. https://doi.org/10.1016/0375-9601(68)90486-6

Boldu, J. L., Abraham, M. M., & Chen, Y. (1979). Valence compensation of thermally generated [Li]0 defects in MgO. *Physical Review B*, *19*(9), 4421–4426. https://doi.org/10.1103/PhysRevB.19.4421

Bos, A. J. J. (2001). High sensitivity thermoluminescence. *Nuclear Instruments and Methods in Physics Research Section B: Beam Interactions with Materials and Atoms*, *184*, 3–28. https://doi.org/10.1016/S0168-583X(01)00717-0

Bos, A. J. J. (2017). Thermoluminescence as a Research Tool to Investigate Luminescence Mechanisms. *Materials*, *10*, 1357. https://doi.org/10.3390/ma10121357

Bos, A. J. J., Prokić, M., & Brouwer, J. C. (2006). Optically and thermally stimulated luminescence characteristics of MgO:Tb3+. *Radiation Protection Dosimetry*, *119*(1–4), 130–133. https://doi.org/10.1093/rpd/nci641

Bragg, L. (1968). X-RAY CRYSTALLOGRAPHY. *Scientific American*, *219*(1), 58–74. http://www.jstor.org/stable/24927456

Bragg, W. L. (1926). Crystallography. *Annual Reports on the Progress of Chemistry*, *23*(0), 257–279. https://doi.org/10.1039/AR9262300257

Brow, R. K., Tallant, D. R., & Turner, G. L. (1996). Raman and 11B nuclear magnetic resonance spectroscopic studies of alkaline-earth lanthanoborate glasses. In *Journal of the American Ceramic Society* (Vol. 79, Issue 9, pp. 2410–2416). https://doi.org/10.1111/j.1151-2916.1996.tb08990.x

Brumfiel, G. (2003). Nanotechnology: A little knowledge... *Nature*, *424*, 246+. https://link.gale.com/apps/doc/A187747809/AONE?u=anon~39d44fb1&sid=googleScholar&xid=46de3b8f

Buissette, V., Giaume, D., Gacoin, T., & Boilot, J.-P. (2006). Aqueous routes to lanthanide-doped oxide nanophosphors. *Journal of Materials Chemistry*, *16*(6), 529–539.

Busker, G., van Huis, M. A., Grimes, R. W., & van Veen, A. (2000). Predicted vacancy cluster structures in MgO and their interaction with helium. *Nuclear Instruments and Methods in Physics Research Section B: Beam Interactions with Materials and Atoms*, *171*(4), 528–536. https://doi.org/https://doi.org/10.1016/S0168-583X(00)00324-4

Cao, M., Hu, Z., Ivanov, M., Dai, J., Li, C., Kou, H., Shi, Y., Chen, H., Xu, J., Pan, Y., & Li, J. (2018). Effect of Gd substitution on structure and spectroscopic properties of (Lu,Gd)2O3:Eu ceramic scintillator. *Optical Materials*, *76*, 323–328. https://doi.org/10.1016/J.OPTMAT.2017.12.053

Cesaria, M., & Di Bartolo, B. (2019). Nanophosphors-based white light sources.

Nanomaterials, *9*(7), 1048.

Chamarro, M. A., & Cases, R. (1990). Infrared to visible upconversion of Er3+ ions in Yb3+ doped fluorohafnate glasses. *Journal of Luminescence*, *46*(1), 59–65.

Chander, H. (2005). Development of nanophosphors—A review. *Materials Science and Engineering: R: Reports*, *49*(5), 113–155.

Chen, J., & Zhao, J. X. (2012). Upconversion nanomaterials: Synthesis, mechanism, and applications in sensing. *Sensors*, *12*(3), 2414–2435. https://doi.org/10.3390/s120302414

Chen, L., Zheng, H., Cheng, J., Song, P., Yang, G., Zhang, G., & Wu, C. (2008). Site-selective luminescence of Bi3+ in the YBO3 host under vacuum ultraviolet excitation at low temperature. *Journal of Luminescence*, *128*(12), 2027–2030. https://doi.org/10.1016/j.jlumin.2008.07.007

Chen, R., Lawless, J. L., & Pagonis, V. (2018). Thermoluminescence associated with two-hole recombination centers. *Radiation Measurements*, *115*, 1–6. https://doi.org/https://doi.org/10.1016/j.radmeas.2018.05.004

Chen, S., Yang, S., Chen, L., Ma, Z., Chen, J., & Guo, W. (2023a). MgO-Y2O3:Eu composite ceramics with high quantum yield and excellent thermal performance. *Journal of the European Ceramic Society*, *43*(8), 3553–3562. https://doi.org/10.1016/J.JEURCERAMSOC.2023.01.054

Chen, S., Yang, S., Chen, L., Ma, Z., Chen, J., & Guo, W. (2023b). MgO-Y2O3:Eu composite ceramics with high quantum yield and excellent thermal performance. *Journal of the European Ceramic Society*, *43*(8), 3553–3562. https://doi.org/10.1016/J.JEURCERAMSOC.2023.01.054

Chen, Y. (1979). Valence compensation of thermally generated [Li] defects in MgO. *PHYSICAL REVIEW B*, *19*(9).

Chen, Y., Chen, J., Liang, J., He, J., Liu, Z. Q., & Yin, Y. (2020). Localized charge accumulation driven by li+incorporation for efficient LED phosphors with tunable

photoluminescence. *Chemistry of Materials*, *32*(22), 9551–9559. https://doi.org/10.1021/acs.chemmater.0c02547

Chen, Y., Kolopus, J. L., & Sibley, W. A. (1969). Luminescence of the F and F+ Center in MgO. *Physical Review*, *186*(3), 865–870. https://doi.org/10.1103/PhysRev.186.865

Chen, Y., Liu, Y., Zhai, W., Liu, H., Sakthivel, T., Guo, S., & Dai, Z. (2024). Metastabilizing the Ruthenium Clusters by Interfacial Oxygen Vacancies for Boosted Water Splitting Electrocatalysis. *Advanced Energy Materials*, *n/a*(n/a), 2400059. https://doi.org/https://doi.org/10.1002/aenm.202400059

Chen, Y., Williams, R. T., & Sibley, W. A. (1969). Defect Cluster Centers in MgO. *Physical Review*, *182*(3), 960–964. https://doi.org/10.1103/PhysRev.182.960

Cheng, Z., Meng, M., Wang, J., Li, Z., He, J., Liang, H., Qiao, X., Liu, Y., & Ou, J. (2023). High-sensitivity NaYF4:Yb3+/Ho3+/Tm3+ phosphors for optical temperature sensing based on thermally coupled and non-thermally coupled energy levels. *Nanoscale*, *15*(26), 11179–11189. https://doi.org/10.1039/D3NR00893B

Chinthala, M., Balakrishnan, A., Venkataraman, P., Manaswini Gowtham, V., & Polagani, R. K. (2021). Synthesis and applications of nano-MgO and composites for medicine, energy, and environmental remediation: a review. *Environmental Chemistry Letters*, *19*(6), 4415–4454. https://doi.org/10.1007/s10311-021-01299-4

Chopra, V., Kadam, A. R., Swart, H. C., & Dhoble, S. J. (2022). Chapter 1 - Introduction to luminescence and radiation dosimetry techniques. In S. Dhoble, V. Chopra, V. Nayar, G. Kitis, D. Poelman, & H. B. T.-R. D. P. Swart (Eds.), *Woodhead Publishing Series in Electronic and Optical Materials* (pp. 1–27). Woodhead Publishing. https://doi.org/https://doi.org/10.1016/B978-0-323-85471-9.00010-5

Choudhury, B., Basyach, P., & Choudhury, A. (2014). Monitoring F, F+ and F22+ related intense defect emissions from nanocrystalline MgO. *Journal of Luminescence*, *149*, 280–286. https://doi.org/10.1016/j.jlumin.2014.01.041

Choudhury, B., & Choudhury, A. (2014). Microstructural, optical and magnetic properties study of nanocrystalline MgO. *Materials Research Express*, *1*(2), 25026. https://doi.org/10.1088/2053-1591/1/2/025026

Christy, R. W., & Mayhugh, M. R. (1972). Thermoluminescence Mechanism in Dosimetry LiF. *Journal of Applied Physics*, *43*(7), 3216–3217. https://doi.org/10.1063/1.1661690

Collins, L. T. (n.d.). *Notes on Upconversion Nanoparticles*.

Concas, G., Spano, G., Bettinellia, M., & Speghinia, A. (2003). *Investigation of Eu3+ Site Occupancy in Cubic Y2O3 and Lu2O3 Nanocrystals*. *58*(9–10), 551–557. https://doi.org/doi:10.1515/zna-2003-9-1013

Coudray, C., Blaise, G., & Malliavin, M. J. (2000). Simulation of small positively charged MgO clusters and study of their electronic densities. *The European Physical Journal D - Atomic, Molecular, Optical and Plasma Physics*, *11*(1), 127–136. https://doi.org/10.1007/s100530070113

Craggs, T. D. (2009). Green fluorescent protein: structure, folding and chromophore maturation. *Chemical Society Reviews*, *38*(10), 2865–2875.

Cui, X., Feng, Z., Jin, Y., Cao, Y., Deng, D., Chu, H., Cao, S., Dong, C., & Zhang, J. (2015). AutoFP: a GUI for highly automated Rietveld refinement using an expert system algorithm based on FullProf. *Journal of Applied Crystallography*, *48*(5), 1581–1586. https://doi.org/10.1107/S1600576715015125

Daksh, D., & Agrawal, Y. K. (2016). Rare earth-doped zinc oxide nanostructures: a review. *Reviews in Nanoscience and Nanotechnology*, *5*(1), 1–27.

de Groot, F. (2001). High-Resolution X-ray Emission and X-ray Absorption Spectroscopy. *Chemical Reviews*, *101*(6), 1779–1808. https://doi.org/10.1021/cr9900681

Devaraja, P. B., Avadhani, D. N., Nagabhushana, H., Prashantha, S. C., Sharma, S. C., Nagabhushana, B. M., Nagaswarupa, H. P., & Prasad, B. D. (2015a).

Luminescence properties of MgO: Fe3+ nanopowders for WLEDs under NUV excitation prepared via propellant combustion route. *Journal of Radiation Research and Applied Sciences*, *8*(3), 362–373. https://doi.org/10.1016/J.JRRAS.2015.02.001

Devaraja, P. B., Avadhani, D. N., Nagabhushana, H., Prashantha, S. C., Sharma, S. C., Nagabhushana, B. M., Nagaswarupa, H. P., & Prasad, B. D. (2015b). Luminescence properties of MgO: Fe3+ nanopowders for WLEDs under NUV excitation prepared via propellant combustion route. *Journal of Radiation Research and Applied Sciences*, *8*(3), 362–373. https://doi.org/10.1016/J.JRRAS.2015.02.001

Devaraja, P. B., Avadhani, D. N., Prashantha, S. C., Nagabhushana, H., Sharma, S. C., Nagabhushana, B. M., & Nagaswarupa, H. P. (2014). Synthesis, structural and luminescence studies of magnesium oxide nanopowder. *Spectrochimica Acta Part A: Molecular and Biomolecular Spectroscopy*, *118*, 847–851. https://doi.org/10.1016/J.SAA.2013.08.050

Devaraja, P. B., Avadhani, D. N., Prashantha, S. C., Nagabhushana, H., Sharma, S. C., Nagabhushana, B. M., Nagaswarupa, H. P., & Premkumar, H. B. (2014). MgO:Eu3+ red nanophosphor: Low temperature synthesis and photoluminescence properties. *Spectrochimica Acta Part A: Molecular and Biomolecular Spectroscopy*, *121*, 46–52. https://doi.org/10.1016/J.SAA.2013.10.060

Devaraja, P. B., Nagabhushana, H., Sharma, S. C., Naik, R., Prashantha, S. C., Nagaswarupa, H. P., Anantharaju, K. S., Premkumar, H. B., & Jnaneshwara, D. M. (2016a). Spectroscopic and photoluminescence properties of MgO:Cr3+ nanosheets for WLEDs. *Displays*, *41*, 16–24. https://doi.org/10.1016/j.displa.2015.10.006

Devaraja, P. B., Nagabhushana, H., Sharma, S. C., Naik, R., Prashantha, S. C., Nagaswarupa, H. P., Anantharaju, K. S., Premkumar, H. B., & Jnaneshwara, D. M. (2016b). Spectroscopic and photoluminescence properties of MgO:Cr3+

nanosheets for WLEDs. *Displays*, *41*, 16–24. https://doi.org/10.1016/J.DISPLA.2015.10.006

Dexter, D. L. (1953). A theory of sensitized luminescence in solids. *The Journal of Chemical Physics*, *21*(5), 836–850. https://doi.org/10.1063/1.1699044

Dillip, G. R., Mohan Kumar, P., Deva Prasad Raju, B., & Dhoble, S. J. (2013). Synthesis and luminescence properties of a novel Na6CaP 2O9:Sm3+ phosphor. *Journal of Luminescence*, *134*, 333–338. https://doi.org/10.1016/j.jlumin.2012.08.025

Du, K., Feng, J., Gao, X., & Zhang, H. (2022). Nanocomposites based on lanthanide-doped upconversion nanoparticles: diverse designs and applications. *Light: Science & Applications*, *11*(1), 222.

Dubey, N., & Chandra, S. (2022). Upconversion nanoparticles: Recent strategies and mechanism based applications. *Journal of Rare Earths*, *40*(9), 1343–1359. https://doi.org/https://doi.org/10.1016/j.jre.2022.04.015

Egerton, R. F. (2016). *The Transmission Electron Microscope BT - Physical Principles of Electron Microscopy: An Introduction to TEM, SEM, and AEM* (R. F. Egerton (Ed.); pp. 55–88). Springer International Publishing. https://doi.org/10.1007/978-3-319-39877-8_3

Ellervee, A. F. (1977). Luminescence of Ph2+ and Bi3+ Centres in Alkali-Earth Sulphides and Oxides. *Physica Status Solidi (B)*, *82*(1), 91–98. https://doi.org/https://doi.org/10.1002/pssb.2220820107

Ermolaev, V. L. (2018). The Effect of Ligands and Solvents on Nonradiative Transitions in Semiconductor Quantum Dots (A Review). *Optics and Spectroscopy*, *125*(2), 256–274. https://doi.org/10.1134/S0030400X18080052

Ermrich, M., & Opper, D. (2011). X-ray Powder Diffraction for the Analyst. In *PANalytical*.

Etafo, N. O. (2024). Advancements of Lanthanide-doped Phosphors in Solid-state

Lighting Applications. *Current Physics*, *1*(1), E220124225904.

Etchart, I., & Cheetham, A. K. (2007). *Metal Oxides for Efficient Infrared to Visible Upconversion under the supervision of Prof*.

Farangis, B., Nachimuthu, P., Richardson, T. J., Slack, J. L., Perera, R. C. C., Gullikson, E. M., Lindle, D. W., & Rubin, M. (2003). In situ x-ray-absorption spectroscopy study of hydrogen absorption by nickel-magnesium thin films. *Physical Review B - Condensed Matter and Materials Physics*, *67*(8), 1–7. https://doi.org/10.1103/PhysRevB.67.085106

Fox, M. (1997). OpticaI Properties of Solids. *Transport.*

Frati, F., Hunault, M. O. J. Y., & De Groot, F. M. F. (2020). Oxygen K-edge X-ray Absorption Spectra. *Chemical Reviews*, *120*(9), 4056–4110. https://doi.org/10.1021/acs.chemrev.9b00439

Fronzoni, G., De Francesco, R., & Stener, M. (2005). Time dependent density functional theory of X-ray absorption spectroscopy of alkaline-earth oxides. *Journal of Physical Chemistry B*, *109*(20), 10332–10340. https://doi.org/10.1021/jp050755y

Fujita, S., Umayahara, Y., & Tanabe, S. (2010). Influence of light scattering on luminous efficacy in Ce: YAG glass-ceramic phosphor. *Journal of the Ceramic Society of Japan*, *118*(1374), 128–131.

Fultz, B., & Howe, J. (2023). *Transmission Electron Microscopy and Diffractometry of Materials (Fourth Edition)*. Springer. https://doi.org/10.1007/978-3-642-29761-8

Gan, Y. X., Jayatissa, A. H., Yu, Z., Chen, X., & Li, M. (2020). Hydrothermal Synthesis of Nanomaterials. *Journal of Nanomaterials*, *2020*(1), 8917013. https://doi.org/https://doi.org/10.1155/2020/8917013

Garlick, G. F. J. (1958). *Luminescence BT - Light and Matter II / Licht und Materie II* (S. Flügge (Ed.); pp. 1–128). Springer Berlin Heidelberg.

https://doi.org/10.1007/978-3-662-35393-6_1

Gautam, S., Asokan, K., Pal Singh, J., Chang, F. H., Lin, H. J., & Hwa Chae, K. (2014). Electronic structure of Fe/MgO/Fe multilayer stack by X-ray magnetic circular dichroism. *Journal of Applied Physics*, *115*(17), 88–91. https://doi.org/10.1063/1.4862380

Gholam, T., Zheng, L. R., Wang, J. O., Qian, H. J., Wu, R., & Wang, H.-Q. (2019). Synchrotron X-ray Absorption Spectroscopy Study of Local Structure in Al-Doped BiFeO3 Powders. *Nanoscale Research Letters*, *14*(1), 137. https://doi.org/10.1186/s11671-019-2965-3

Gibson, A., Haydock, R., & LaFemina, J. P. (1994). Stability of vacancy defects in MgO: The role of charge neutrality. *Physical Review B*, *50*(4), 2582–2592. https://doi.org/10.1103/PhysRevB.50.2582

Gilliland, G. D. (1997). Photoluminescence spectroscopy of crystalline semiconductors. *Materials Science and Engineering: R: Reports*, *18*(3), 99–399. https://doi.org/https://doi.org/10.1016/S0927-796X(97)80003-4

Gu, F., Li, C., Cao, H., Shao, W., Hu, Y., Chen, J., & Chen, A. (2008). Crystallinity of Li-doped MgO:Dy3+ nanocrystals via combustion process and their photoluminescence properties. *Journal of Alloys and Compounds*, *453*(1–2), 361–365. https://doi.org/10.1016/j.jallcom.2006.11.098

Guckan, V., Altunal, V., Ozdemir, A., & Yegingil, Z. (2020). Optically stimulated luminescence of MgO:Na,Li phosphor prepared using solution combustion method. *Journal of Alloys and Compounds*, *835*, 155253. https://doi.org/10.1016/j.jallcom.2020.155253

Guckan, V., Bokhari, S. W., Altunal, V., Ozdemir, A., Gao, W., & Yegingil, Z. (2021a). Luminescence of Ce3+ and Li+ co-doped MgO synthesized using solid-state reaction method. *Nuclear Instruments and Methods in Physics Research Section B: Beam Interactions with Materials and Atoms*, *503*, 53–61. https://doi.org/10.1016/J.NIMB.2021.07.012

Guckan, V., Bokhari, S. W., Altunal, V., Ozdemir, A., Gao, W., & Yegingil, Z. (2021b). Luminescence of Ce3+ and Li+ co-doped MgO synthesized using solid-state reaction method. *Nuclear Instruments and Methods in Physics Research Section B: Beam Interactions with Materials and Atoms*, *503*, 53–61. https://doi.org/10.1016/J.NIMB.2021.07.012

Guo, L., Wang, Y., Zhang, J., Wang, Y., & Dong, P. (2012). Near-infrared quantum cutting in Ho3+, Yb3+-codoped BaGdF5 nanoparticles via first- and second-order energy transfers. *Nanoscale Research Letters*, *7*(1), 636. https://doi.org/10.1186/1556-276X-7-636

Guo, Y., Wang, D., & He, Y. (2018). Fabrication of highly porous Y2O3:Ho,Yb ceramic and its thermometric applications. *Journal of Alloys and Compounds*, *741*, 1158–1162. https://doi.org/10.1016/j.jallcom.2018.01.229

Gupta, S. K., Sudarshan, K., & Kadam, R. M. (2021). Optical nanomaterials with focus on rare earth doped oxide: A Review. *Materials Today Communications*, *27*, 102277.

Halder, R., & Bandyopadhyay, S. (2017). Synthesis and optical properties of anion deficient nano MgO. *Journal of Alloys and Compounds*, *693*, 534–542. https://doi.org/10.1016/j.jallcom.2016.09.164

Hao, Y. J., Liu, B., Tian, L. G., Li, F. T., Ren, J., Liu, S. J., Liu, Y., Zhao, J., & Wang, X. J. (2017). Synthesis of {111} Facet-Exposed MgO with Surface Oxygen Vacancies for Reactive Oxygen Species Generation in the Dark. *ACS Applied Materials and Interfaces*, *9*(14), 12687–12693. https://doi.org/10.1021/acsami.6b16856

Hatanaka, M., & Yabushita, S. (2009). Theoretical Study on the f−f Transition Intensities of Lanthanide Trihalide Systems. *The Journal of Physical Chemistry A*, *113*(45), 12615–12625. https://doi.org/10.1021/jp9049507

Henderson, G. S., de Groot, F. M. F., & Moulton, B. J. A. (2014). X-ray Absorption Near-Edge Structure (XANES) Spectroscopy. *Reviews in Mineralogy and*

Geochemistry, *78*(1), 75–138. https://doi.org/10.2138/rmg.2014.78.3

Hou, J., Wang, Z., Xu, X., Zhao, X., & Zhang, T. (2024). NaYF4:Yb3+/Ho3+ up-conversion luminescence and its low temperature sensing characteristics. *Modern Physics Letters B*, *38*(20), 2450155. https://doi.org/10.1142/S0217984924501550

Hsiang, E.-L., Yang, Z., Yang, Q., Lan, Y.-F., & Wu, S.-T. (2021). Prospects and challenges of mini-LED, OLED, and micro-LED displays. *Journal of the Society for Information Display*, *29*(6), 446–465. https://doi.org/https://doi.org/10.1002/jsid.1058

Hulla, JE, Sahu, SC, & Hayes, AW. (2015). Nanotechnology: History and future. *Human & Experimental Toxicology*, *34*(12), 1318–1321. https://doi.org/10.1177/0960327115603588

Iglesias-Juez, A., Chiarello, G. L., Patience, G. S., & Guerrero-Pérez, M. O. (2022). Experimental methods in chemical engineering: X-ray absorption spectroscopy—XAS, XANES, EXAFS. *Canadian Journal of Chemical Engineering*, *100*(1), 3–22. https://doi.org/10.1002/cjce.24291

Ildefonse, P., Calas, G., Flank, A. M., & Lagarde, P. (1995). Low Z elements (Mg, Al, and Si) K-edge X-ray absorption spectroscopy in minerals and disordered systems. *Nuclear Inst. and Methods in Physics Research, B*, *97*(1–4), 172–175. https://doi.org/10.1016/0168-583X(94)00710-1

Illas, F., & Pacchioni, G. (1998). Optical properties of surface and bulk F centers in MgO from ab initio cluster model calculations. *Journal of Chemical Physics*, *108*(18), 7835–7841. https://doi.org/10.1063/1.476220

Jablonski, A. (1933). Efficiency of Anti-Stokes Fluorescence in Dyes. *Nature*, *131*(3319), 839–840. https://doi.org/10.1038/131839b0

Jain, M., Bhatia, M., Kumar, M., Lee, H., Won, S. O., Chae, K., Gupta, G., Vij, A., & Thakur, A. (2021). Thermally induced cation ordering in ZnAl2O4:Mg2+, Fe3+ for sensing thermal history through photoluminescence. *Journal of Materials*

Science, *56*, 1–10. https://doi.org/10.1007/s10853-021-06036-4

Jain, M., Manju, Kumar, R., Won, S. O., Chae, K. H., Vij, A., & Thakur, A. (2020). Defect states and kinetic parameter analysis of ZnAl2O4 nanocrystals by X-ray photoelectron spectroscopy and thermoluminescence. *Scientific Reports*, *10*(1), 1–14. https://doi.org/10.1038/s41598-019-57227-8

Jain, M., & Singh, P. (2024). Luminescence: types and mechanism. *Mechanoluminescence in Organic and Inorganic Compounds: Basic Concepts, Instrumentation, and Applications*, 1–18. https://doi.org/10.1016/B978-0-323-95301-6.00011-1

Jaque, D., & Vetrone, F. (2012). Luminescence nanothermometry. *Nanoscale*, *4*(15), 4301–4326.

Jia, Y., Miglio, A., Mikami, M., & Gonze, X. (2018). Ab initio study of luminescence in Ce-doped Lu 2 SiO 5 : The role of oxygen vacancies on emission color and thermal quenching behavior. *Physical Review Materials*, *2*(12), 1–11. https://doi.org/10.1103/PhysRevMaterials.2.125202

Jiang, M., Wang, L., Maimaiti, M., Feng, X., & Zhang, Y. (2024). Upconversion luminescence and temperature sensing properties of Ho3+,Yb3+-codoped Bi2WO6. *Dalton Transactions*, *53*(6), 2591–2601. https://doi.org/10.1039/D3DT03537A

Kadari, A., & Kadri, D. (2010). Numerical model for thermoluminescence of MgO. *Physica B: Condensed Matter*, *405*(23), 4713–4717. https://doi.org/10.1016/j.physb.2010.08.062

Kannan, M. (2018). *Transmission Electron Microscope -Principle, Components and Applications Illumination system (Electron gun and condenser lenses) Electron gun* (pp. 93–101).

Kappers, L. A., Kroes, R. L., & Hensley, E. B. (1970). F+ and F′ centers in magnesium oxide. *Physical Review B*, *1*(10), 4151–4157.

https://doi.org/10.1103/PhysRevB.1.4151

Kaur, P., Kaur, A., Singh, S., & Singh, L. (2021). MgO:Li+ phosphor: In depth analysis of its structural, optical and thermoluminescent behavior after gamma irradiation. *Optical Materials*, *120*, 111435. https://doi.org/10.1016/J.OPTMAT.2021.111435

Kawaguchi, Y. (2000). Luminescence spectra at bending fracture of single crystal MgO. *Solid State Communications*, *117*(1), 17–20. https://doi.org/10.1016/S0038-1098(00)00413-0

Khalid, K., Ishak, R., & Chowdhury, Z. Z. (2024). UV–Vis spectroscopy in non-destructive testing. *Non-Destructive Material Characterization Methods*, 391–416. https://doi.org/10.1016/B978-0-323-91150-4.00021-5

Khaliullin, S. M., Zhuravlev, V. D., & Bamburov, V. G. (2016). Solution-combustion synthesis of oxide nanoparticles from nitrate solutions containing glycine and urea: Thermodynamic aspects. *International Journal of Self-Propagating High-Temperature Synthesis*, *25*(3), 139–148. https://doi.org/10.3103/S1061386216030031

Khamkongkaeo, A., Klysubun, W., Boonchuduang, T., Sailuam, W., Sriwattana, P., Phetrattanarangsi, T., Srimongkon, K., Sakkomolsri, B., Pimsawat, A., Daengsakul, S., Kidkhunthod, P., Bootchanont, A., & Lohwongwatana, B. (2018). X-ray absorption spectroscopy investigation of relationship between Mg vacancy and magnetic properties of MgO powder. *Journal of Magnetism and Magnetic Materials*, *460*, 327–333. https://doi.org/10.1016/j.jmmm.2018.01.074

Kiminami, R. H. G. A. (2001). Combustion synthesis of nanopowder ceramic powders. *KONA Powder and Particle Journal*, *19*(May), 156–165. https://doi.org/10.14356/kona.2001019

Kitis, G., Chen, R., & Pagonis, V. (2008). Thermoluminescence glow-peak shape methods based on mixed order Kinetics. *Physica Status Solidi (A)*, *205*, 1181–1189. https://doi.org/10.1002/pssa.200723470

Kitis, G., Furetta, C., Azorin, J., & Universidad Autonoma Metropolitana Unidad Iztapalapa, M. D. F. (Mexico). (2025). *Observations on the properties of second and general-order kinetics equations describing the thermoluminescence processes*.

Kitis, G., Gomez-Ros, J. M., & Tuyn, J. W. N. (1998). Thermoluminescence glow-curve deconvolution functions for first, second and general orders of kinetics. *Journal of Physics D: Applied Physics*, *31*(19), 2636–2641. https://doi.org/10.1088/0022-3727/31/19/037

Kohale, R. L., Pawade, V. B., Dhoble, S. J., & Deshmukh, A. H. (2021). Introduction to phosphate phosphors. *Optical Properties of Phosphate and Pyrophosphate Compounds*, 1–53. https://doi.org/10.1016/B978-0-12-823044-2.00003-6

Kori, S. P., Rohatgi, R., & Lahariya, V. (2021). Nanophosphors: Emerging Materials for Forensic Applications. *Also of Interest*, 131.

Kricka, L. J., & Thorpe, G. H. G. (1983). Chemiluminescent and bioluminescent methods in Analytical Chemistry. A review. *Analyst*, *108*(1292), 1274–1296. https://doi.org/10.1039/AN9830801274

Kubrin, R. (2014). Nanophosphor coatings: Technology and applications, opportunities and challenges. *KONA Powder and Particle Journal*, *31*, 22–52.

Kumar, A., Dutta, S., Kim, S., Kwon, T., Patil, S. S., Kumari, N., Jeevanandham, S., & Lee, I. S. (2022). Solid-State Reaction Synthesis of Nanoscale Materials: Strategies and Applications. *Chemical Reviews*, *122*(15), 12748–12863. https://doi.org/10.1021/acs.chemrev.1c00637

Kumar, A., & Kumar, J. (2008). On the synthesis and optical absorption studies of nano-size magnesium oxide powder. *Journal of Physics and Chemistry of Solids*, *69*(11), 2764–2772. https://doi.org/10.1016/J.JPCS.2008.06.143

Kumar, P., Sharma, A., Bishnoi, P., Vij, A., Kumar, S., Shin, H.-J. J., Chae, K. H.,

Lee, B. H., & Won, S. O. (2023). Synthesis and characterization of ZnGa2O4:Cr3+Ge3+ compounds with tunable photoluminescence properties. *Journal of the Korean Physical Society*, *83*(6), 463–470. https://doi.org/10.1007/s40042-023-00888-6

Kumawat, A., Chattopadhyay, S., & Misra, K. P. (2023). Significant impact of co-doping Eu-doped ZnO nanoparticles with Li on structural–optical properties relationship. *Materials Technology*, *38*(1). https://doi.org/10.1080/10667857.2023.2253646

Lakowicz, J. R. (1999). *Instrumentation for Fluorescence Spectroscopy BT - Principles of Fluorescence Spectroscopy* (J. R. Lakowicz (Ed.); pp. 25–61). Springer US. https://doi.org/10.1007/978-1-4757-3061-6_2

Lakowicz, J. R. (Ed.). (2006). *Instrumentation for Fluorescence Spectroscopy BT - Principles of Fluorescence Spectroscopy* (pp. 27–61). Springer US. https://doi.org/10.1007/978-0-387-46312-4_2

Lee, K. H., & Crawford, J. H. (1979). X-ray stimulated luminescence in MgO. *Journal of Luminescence*, *20*(1), 9–15. https://doi.org/10.1016/0022-2313(79)90018-8

Lehmann, W. (1973). Calcium oxide phosphors. *Journal of Luminescence*, *6*(5), 455–470. https://doi.org/10.1016/0022-2313(73)90014-8

Lei, B., Lu, L., & Sun, H. (2024). Modulation of phosphor luminescence performance by high concentration self-sensitization of Er and Ho–Yb ion co-doping under 1550 nm excitation. *Journal of Materials Chemistry C*, *12*(26), 9784–9794.

Leng, Y. (2013). *Materials Characterization: Introduction to Microscopic and Spectroscopic Methods*. Wiley. https://books.google.co.in/books?id=URdwAAAAQBAJ

Li, G., Jiang, S., Liu, A., Ye, L., Ke, J., Liu, C., Chen, L., Liu, Y., & Hong, M.

(2023). Proof of crystal-field-perturbation-enhanced luminescence of lanthanide-doped nanocrystals through interstitial H+ doping. *Nature Communications*, *14*(1), 5870. https://doi.org/10.1038/s41467-023-41411-6

Li, H., Li, M., Wang, X., Wu, X., Liu, F., & Yang, B. (2013). Synthesis and optical properties of single-crystal MgO nanobelts. *Materials Letters*, *102–103*, 80–82. https://doi.org/10.1016/J.MATLET.2013.03.118

Li, H., Wang, X., Huang, D., & Chen, G. (2019). Recent advances of lanthanide-doped upconversion nanoparticles for biological applications. *Nanotechnology*, *31*(7), 72001.

Li, M., Yuan, M., Cui, W., Liu, H., Huang, H., Xing, Z., Guo, C., & Han, K. (2024). Impact of high sensitizer doping on the transient multiband upconversion luminescence in β-NaYF4:Yb/Ho microcrystals. *Optical Materials*, *156*, 115993. https://doi.org/https://doi.org/10.1016/j.optmat.2024.115993

Li, X., Liu, X., & Liu, X. (2021). Self-assembly of colloidal inorganic nanocrystals: nanoscale forces, emergent properties and applications. *Chemical Society Reviews*, *50*(3), 2074–2101.

Li, Y., Gecevicius, M., & Qiu, J. (2016). Long persistent phosphors—from fundamentals to applications. *Chemical Society Reviews*, *45*(8), 2090–2136.

Liang, L., Chen, J., Shao, K., Qin, X., Pan, Z., & Liu, X. (2023). Controlling persistent luminescence in nanocrystalline phosphors. *Nature Materials*, *22*(3), 289–304.

Lin, H., Liang, H., Han, B., Zhong, J., Su, Q., Dorenbos, P., Birowosuto, M. D., Zhang, G., Fu, Y., & Wu, W. (2007). Luminescence and site occupancy of Ce3+ in Ba2 Ca (B O3) 2. *Physical Review B - Condensed Matter and Materials Physics*, *76*(3), 1–8. https://doi.org/10.1103/PhysRevB.76.035117

Liu, L., Morita, K., Suzuki, T. S., & Kim, B. N. (2020). Evolution of microstructure, mechanical, and optical properties of Y2O3-MgO nanocomposites fabricated by

high pressure spark plasma sintering. *Journal of the European Ceramic Society*, *40*(13), 4547–4555. https://doi.org/10.1016/J.JEURCERAMSOC.2020.05.046

Liu, X., Chen, S., & Wang, X. (2007). Synthesis and photoluminescence of CeO2:Eu3+ phosphor powders. *Journal of Luminescence*, *127*(2), 650–654. https://doi.org/10.1016/j.jlumin.2007.03.014

Liu, Y., Tu, D., Zhu, H., & Chen, X. (2013). Lanthanide-doped luminescent nanoprobes: controlled synthesis, optical spectroscopy, and bioapplications. *Chemical Society Reviews*, *42*(16), 6924–6958.

Liu, Z., Ikesue, A., & Li, J. (2021). Research progress and prospects of rare-earth doped sesquioxide laser ceramics. *Journal of the European Ceramic Society*, *41*(7), 3895–3910. https://doi.org/10.1016/J.JEURCERAMSOC.2021.02.026

Livage, J., Beteille, F., Roux, C., Chatry, M., & Davidson, P. (1998). Sol–gel synthesis of oxide materials. *Acta Materialia*, *46*(3), 743–750. https://doi.org/10.1016/S1359-6454(97)00255-3

Löble, M. W., Keith, J. M., Altman, A. B., Stieber, S. C. E., Batista, E. R., Boland, K. S., Conradson, S. D., Clark, D. L., Lezama Pacheco, J., Kozimor, S. A., Martin, R. L., Minasian, S. G., Olson, A. C., Scott, B. L., Shuh, D. K., Tyliszczak, T., Wilkerson, M. P., & Zehnder, R. A. (2015). Covalency in lanthanides. An X-ray absorption spectroscopy and density functional theory study of LnCl6x- (x = 3, 2). *Journal of the American Chemical Society*, *137*(7), 2506–2523. https://doi.org/10.1021/ja510067v

Luthra, J. M., Sathyamoorthy, A., & Gupta, N. M. (1977). A thermoluminescence study of defect centres in MgO. *Journal of Luminescence*, *15*(4), 395–404. https://doi.org/10.1016/0022-2313(77)90038-2

Lyu, T., & Dorenbos, P. (2018). Bi3+ acting both as an electron and as a hole trap in La-, Y-, and LuPO4. *Journal of Materials Chemistry C*, *6*(23), 6240–6249. https://doi.org/10.1039/c8tc01020j

M., R. (1980). Xenon lamps. *IEE Proceedings A (Physical Science, Measurement and Instrumentation, Management and Education, Reviews)*, *127*(3), 190–195. https://doi.org/10.1049/ip-a-1.1980.0030

Ma, H. J., Jung, W. K., Park, Y., & Kim, D. K. (2018a). A novel approach of an infrared transparent Er:Y2O3-MgO nanocomposite for eye-safe laser ceramics. *Journal of Materials Chemistry C*, *6*(41), 11096–11103. https://doi.org/10.1039/c7tc05991d

Ma, H. J., Jung, W. K., Park, Y., & Kim, D. K. (2018b). A novel approach of an infrared transparent Er:Y2O3–MgO nanocomposite for eye-safe laser ceramics. *Journal of Materials Chemistry C*, *6*(41), 11096–11103. https://doi.org/10.1039/C7TC05991D

Mahata, M. K., Koppe, T., Kumar, K., Hofsäss, H., & Vetter, U. (2020). Upconversion photoluminescence of Ho3+-Yb3+ doped barium titanate nanocrystallites: Optical tools for structural phase detection and temperature probing. *Scientific Reports*, *10*(1), 8775. https://doi.org/10.1038/s41598-020-65149-z

Malleshappa, J., Nagabhushana, H., Sharma, S. C., Sunitha, D. V., Dhananjaya, N., Shivakumara, C., & Nagabhushana, B. M. (2014). Self propagating combustion synthesis and luminescent properties of nanocrystalline CeO2:Tb3+ (1-10 mol%) phosphors. *Journal of Alloys and Compounds*, *590*, 131–139. https://doi.org/10.1016/j.jallcom.2013.11.213

Mäntele, W., & Deniz, E. (2017). UV–VIS absorption spectroscopy: Lambert-Beer reloaded. *Spectrochimica Acta Part A: Molecular and Biomolecular Spectroscopy*, *173*, 965–968. https://doi.org/10.1016/J.SAA.2016.09.037

Marczewska, B., Gieszczyk, W., Kłosowski, M., Książek, M., Bilski, P., & Borón, Ł. (2021). Uniformity of thermoluminescence and optically stimulated luminescence signals over the length of doped LiMgpO4 crystal rods grown by micro-pulling-down method. *Materials*, *14*(1), 1–13.

https://doi.org/10.3390/ma14010132

Martínez-Boubeta, C., Martínez, A., Hernández, S., Pellegrino, P., Antony, A., Bertomeu, J., Balcells, L., Konstantinović, Z., & Martnez, B. (2011). Blue luminescence at room temperature in defective MgO films. *Solid State Communications*, *151*(10), 751–753. https://doi.org/10.1016/J.SSC.2011.03.007

Marzouk, S. Y., Hammad, A. H., Sun, X. Y., GU, M., ZHANG, M., HUANG, S., Fu, Z., Xu, P., Yang, Y., Li, C. C., Lin, H. H. H., Chen, Q., Yao, G., Zhou, Y., Zeng, F., Eraiah, B., Bhat, S. G., Kaur, P. P., Singh, D. D. P., … Salvo, M. (2020). Luminescence properties of Sm3+ doped Na2B4O7 glasses for lighting application. *Journal of Luminescence*, *222*(1), 1–8. https://doi.org/10.1016/j.jnucmat.2018.11.002%0Ahttp://dx.doi.org/10.1016/j.jallcom.2016.04.274%0Ahttp://dx.doi.org/10.1016/j.matlet.2014.04.104%0Ahttps://doi.org/10.1016/j.matpr.2020.05.073%0Ahttps://doi.org/10.1016/j.pmatsci.2018.05.002%0Ahttps://doi.or

Masenelli, B., Mollet, O., Boisron, O., Canut, B., Ledoux, G., Bluet, J.-M., Mélinon, P., Dujardin, C., & Huant, S. (2013). YAG: Ce nanoparticle lightsources. *Nanotechnology*, *24*(16), 165703.

Mason, S. F. (1984). Mechanisms for f-f transition probabilities in lanthanide coordination compounds. *Inorganica Chimica Acta*, *94*(1), 88. https://doi.org/https://doi.org/10.1016/S0020-1693(00)94556-0

Meno, S., KUMAR, M., & Chougaonkar, M. P. (2012). *Study On Trap Parameters From Thermoluminescence Glow Curves Of Different Tl Materials*.

Mitric, M., Antic, B., Balanda, M., Rodic, D., & Napijalo, M. L. (1997). An x-ray diffraction and magnetic susceptibility study of Yb x Y 2-x O 3. *Journal of Physics Condensed Matter*, *9*(20), 4103–4111. https://doi.org/10.1088/0953-8984/9/20/009

Mizoguchi, T., & Tanaka, I. (2000). Core-hole effects on theoretical electron-energy-loss near-edge structure and near-edge x-ray absorption fine structure of MgO. *Physical Review B - Condensed Matter and Materials Physics*, *61*(3), 2180–

2187. https://doi.org/10.1103/PhysRevB.61.2180

Mondal, M., & Rai, V. K. (2018). Ho3+-Yb3+:YMoO4 core@shell nanoparticles for enhanced visible upconversion and security applications. *Journal of Alloys and Compounds*, *750*, 304–311. https://doi.org/10.1016/j.jallcom.2018.03.148

Monika, Yadav, R. S., Rai, A., & Rai, S. B. (2021). NIR light guided enhanced photoluminescence and temperature sensing in Ho3+/Yb3+/Bi3+ co-doped ZnGa2O4 phosphor. *Scientific Reports*, *11*(1), 4148. https://doi.org/10.1038/s41598-021-83644-9

Morebodi, B. K. (2021). *Synthesis and Luminescence Investigations of Europium (Eu3+) And Samarium (Sm3+) Doped Sodium Alkaline-earth Sulphate Phosphors (Na6Mg (SO4) 4 and Na2Ca (SO4) 2) Via Combustion Method*. University of Johannesburg (South Africa).

Moshtaghioun, B. M., Peña, J. I., & Merino, R. I. (2021). Can Y2O3-MgO eutectics be new promising structural and optical ceramics? *Acta Materialia*, *216*, 117139. https://doi.org/10.1016/J.ACTAMAT.2021.117139

Mourdikoudis, S., Pallares, R. M., & Thanh, N. T. K. (2018). Characterization techniques for nanoparticles: comparison and complementarity upon studying nanoparticle properties. *Nanoscale*, *10*(27), 12871–12934. https://doi.org/10.1039/C8NR02278J

Murthy, K. V. R., & Virk, H. S. (2014). Luminescence Phenomena: An Introduction. *Defect and Diffusion Forum*, *347*, 1–34. https://doi.org/10.4028/WWW.SCIENTIFIC.NET/DDF.347.1

Nadort, A., Zhao, J., & Goldys, E. M. (2016). Lanthanide upconversion luminescence at the nanoscale: fundamentals and optical properties. *Nanoscale*, *8*(27), 13099–13130. https://doi.org/10.1039/C5NR08477F

Nakai, S., Mitsuishi, T., Sugawara, H., Maezawa, H., Matsukawa, T., Mitani, S., Yamasaki, K., & Fujikawa, T. (1987). Oxygen x-ray-absorption. *Phys. Rev. B,*

36(17), 9241.

Nakamura, S. (2015). Nobel Lecture: Background story of the invention of efficient blue InGaN light emitting diodes. *Reviews of Modern Physics*, *87*(4), 1139–1151.

Nantharak, W., Wattanathana, W., Klysubun, W., Rimpongpisarn, T., Veranitisagul, C., Koonsaeng, N., & Laobuthee, A. (2017). Effect of local structure of Sm3+in MgAl2O4:Sm3+phosphors prepared by thermal decomposition of triethanolamine complexes on their luminescence property. *Journal of Alloys and Compounds*, *701*, 1019–1026. https://doi.org/10.1016/j.jallcom.2017.01.090

Natoli, C. R., Benfatto, M., Della Longa, S., & Hatada, K. (2003). X-ray absorption spectroscopy: state-of-the-art analysis. *Journal of Synchrotron Radiation*, *10*(1), 26–42. https://doi.org/10.1107/S0909049502017247

Nieto, J. A. (2018). Thermoluminescence of metallic oxides. Development and applications in Mexico: An overview. *Applied Radiation and Isotopes*, *138*, 35–39. https://doi.org/https://doi.org/10.1016/j.apradiso.2017.07.044

Nishiura, S., Tanabe, S., Fujioka, K., & Fujimoto, Y. (2011). Properties of transparent Ce: YAG ceramic phosphors for white LED. *Optical Materials*, *33*(5), 688–691.

Oliveira, L. C., Milliken, E. D., & Yukihara, E. G. (2013). Development and characterization of MgO:Nd,Li synthesized by solution combustion synthesis for 2D optically stimulated luminescence dosimetry. *Journal of Luminescence*, *133*, 211–216. https://doi.org/10.1016/j.jlumin.2011.10.032

Oliveira, L. C., Yukihara, E. G., & Baffa, O. (2016). MgO:Li,Ce,Sm as a high-sensitivity material for Optically Stimulated Luminescence dosimetry. *Scientific Reports*, *6*(1), 24348. https://doi.org/10.1038/srep24348

Oliveira, L. C., Yukihara, E. G., & Baffa, O. (2019a). Lanthanide-doped MgO: A case study on how to design new phosphors for dosimetry with tailored luminescent properties. *Journal of Luminescence*, *209*, 21–30.

https://doi.org/10.1016/J.JLUMIN.2019.01.015

Oliveira, L. C., Yukihara, E. G., & Baffa, O. (2019b). Lanthanide-doped MgO: A case study on how to design new phosphors for dosimetry with tailored luminescent properties. *Journal of Luminescence*, *209*, 21–30. https://doi.org/https://doi.org/10.1016/j.jlumin.2019.01.015

Orante-Barrón, V., Oliveira, L., Kelly, J. B., Milliken, E., Denis, G., Jacobsohn, L. G., Puckette, J., & Yukihara, E. (2011). Luminescence properties of MgO produced by solution combustion synthesis and doped with lanthanides and Li. *Journal of Luminescence*, *131*, 1058–1065. https://doi.org/10.1016/j.jlumin.2011.01.022

Pan, Y., Lin, H., Liu, J., Xu, X., Hong, R., Tao, C., Han, Z., & Zhang, D. (2021). Fabrication and spectral properties of Yb,Ho:Y2O3 transparent ceramics. *Optical Materials*, *112*, 110479. https://doi.org/https://doi.org/10.1016/j.optmat.2020.110479

Pandey, A., Rai, V. K., Dey, R., & Kumar, K. (2013). Enriched green upconversion emission in combustion synthesized Y 2O3:Ho3+-Yb3+ phosphor. *Materials Chemistry and Physics*, *139*(2–3), 483–488. https://doi.org/10.1016/j.matchemphys.2013.01.043

Park, S., & Lee, J. C. (n.d.). Nanopowders synthesized by solution combustion method and their applications. *Science and Applications of Tailored Nanostructures*, 170–195.

Parsons, J. G., M. V., A., & and Gardea-Torresdey, J. L. (2002). ENVIRONMENTAL AND BIOLOGICAL APPLICATIONS OF EXTENDED X-RAY ABSORPTION FINE STRUCTURE (EXAFS) AND X-RAY ABSORPTION NEAR EDGE STRUCTURE (XANES) SPECTROSCOPIES. *Applied Spectroscopy Reviews*, *37*(2), 187–222. https://doi.org/10.1081/ASR-120006044

Patel, M., Meenu, M., Pandey, J. K., Kumar, P., & Patel, R. (2022). Recent development in upconversion nanoparticles and their application in optogenetics:

A review. *Journal of Rare Earths*, *40*(6), 847–861. https://doi.org/https://doi.org/10.1016/j.jre.2021.10.003

Pathak, N., Ghosh, P. S., Gupta, S. K., Kadam, R. M., & Arya, A. (2016a). Defects induced changes in the electronic structures of MgO and their correlation with the optical properties: A special case of electron-hole recombination from the conduction band. In *RSC Advances* (Vol. 6, Issue 98). https://doi.org/10.1039/c6ra21065a

Pathak, N., Ghosh, P. S., Gupta, S. K., Kadam, R. M., & Arya, A. (2016b). Defects induced changes in the electronic structures of MgO and their correlation with the optical properties: a special case of electron–hole recombination from the conduction band. *RSC Advances*, *6*(98), 96398–96415. https://doi.org/10.1039/C6RA21065A

Patterson, A. L. (1939). The Scherrer Formula for X-Ray Particle Size Determination. *Physical Review*, *56*(10), 978–982. https://doi.org/10.1103/PhysRev.56.978

Penner-Hahn, J. E. (1999). X-ray absorption spectroscopy in coordination chemistry. *Coordination Chemistry Reviews*, *190–192*, 1101–1123. https://doi.org/10.1016/S0010-8545(99)00160-5

Permin, D. A., Belyaev, A. V, Balabanov, S. S., Koshkin, V. A., Boldin, M. S., Novikova, A. V, Timofeev, O. V, Gashpar, Z. K., & Ladenkov, I. V. (2022). Effect of Composition on the Structure and Properties of MgO/Y2O3 Composite Ceramics. *Inorganic Materials*, *58*(6), 643–650. https://doi.org/10.1134/S0020168522060085

Perrella, R. V., Debasu, M. L., K. L. Rezende, T., Carneiro, J. A., Barbosa, H. P., A. S. Ferreirab, R., Carlos, L. D., & Ferrari, J. L. (2023). Temperature sensing based on upconversion properties of Yb3+/Ho3+/Tm3+ tri-doped Y2O3 micro particles phosphors obtained by conventional precipitation method. *Materials Science and Engineering: B*, *297*(July), 116780. https://doi.org/10.1016/j.mseb.2023.116780

Pikhitsa, P. V, Kim, C., Chae, S., Shin, S., Jung, S., Kitaura, M., Kimura, S., Fukui, K., & Choi, M. (2015). Two-band luminescence from an intrinsic defect in spherical and terraced MgO nanoparticles. *Applied Physics Letters*, *106*(18), 183106. https://doi.org/10.1063/1.4918804

Pires, A. M., Heer, S., Güdel, H. U., & Serra, O. A. (2006). Er, Yb doped yttrium based nanosized phosphors: particle size,“host lattice” and doping ion concentration effects on upconversion efficiency. *Journal of Fluorescence*, *16*, 461–468.

Poles, E., Selmarten, D. C., Mićić, O. I., & Nozik, A. J. (1999). Anti-Stokes photoluminescence in colloidal semiconductor quantum dots. *Applied Physics Letters*, *75*(7), 971–973.

Prakash, J. (1993). Thermoluminescence glow curve with second order kinetics. *Solid State Communications*, *85*(7), 647–650. https://doi.org/https://doi.org/10.1016/0038-1098(93)90326-I

Rahate, G., Panse, V. R., Dhoble, S. J., Kokode, N. S., & Sharma, K. (2021). Photoluminescence studies and synthesis of KSrPO4: Ce3+, Eu3+ blue and orange-red emitting phosphor. *IOP Conference Series: Materials Science and Engineering*, *1120*(1), 12005.

Rai, M., Mishra, K., Singh, S. K., Verma, R. K., & Rai, S. B. (2012). Infrared to visible upconversion in Ho3+/Yb3+ co-doped Y2O3 phosphor: Effect of laser input power and external temperature. *Spectrochimica Acta - Part A: Molecular and Biomolecular Spectroscopy*, *97*, 825–829. https://doi.org/10.1016/j.saa.2012.07.071

Ramasamy, P., Chandra, P., Rhee, S. W., & Kim, J. (2013). Enhanced upconversion luminescence in NaGdF 4: Yb, Er nanocrystals by Fe 3+ doping and their application in bioimaging. *Nanoscale*, *5*(18), 8711–8717.

Ramteke, S. K., Yerpude, A. N., Dhoble, S. J., & Kokode, N. S. (2020). Luminescence characterization of KBaPO4: RE (RE= Sm3+, Eu3+, Dy3+)

phosphors. *Luminescence*, *35*(6), 969–973.

Readey, M. J., Lee, R.-R., Halloran, J. W., & Heuer, A. H. (1990). Processing and Sintering of Ultrafine MgO-ZrO2 and (MgO, Y2O3)-ZrO2 Powders. *Journal of the American Ceramic Society*, *73*(6), 1499–1503. https://doi.org/https://doi.org/10.1111/j.1151-2916.1990.tb09786.x

Ricciardi, P. (2021). UV-visible-near IR reflectance spectrophotometry in a museum environment. *Spectroscopy, Diffraction and Tomography in Art and Heritage Science*, 103–131. https://doi.org/10.1016/B978-0-12-818860-6.00003-9

Richter, N. A., Sicolo, S., Levchenko, S. V, Sauer, J., & Scheffler, M. (2013). Concentration of Vacancies at Metal-Oxide Surfaces: Case Study of MgO(100). *Phys. Rev. Lett.*, *111*(4), 45502. https://doi.org/10.1103/PhysRevLett.111.045502

Rinke, P., Schleife, A., Kioupakis, E., Janotti, A., Rödl, C., Bechstedt, F., Scheffler, M., & Van de Walle, C. G. (2012). First-Principles Optical Spectra for F Centers in MgO. *Physical Review Letters*, *108*(12), 126404. https://doi.org/10.1103/PhysRevLett.108.126404

Rizvi, M., Gerengi, H., & Gupta, P. (2022). Functionalization of Nanomaterials: Synthesis and Characterization. In *Functionalized Nanomaterials for Corrosion Mitigation: Synthesis, Characterization, and Applications* (Vol. 1418, p. 1). American Chemical Society. https://doi.org/doi:10.1021/bk-2022-1418.ch001

Robertson, I. M., Schuh, C. A., Vetrano, J. S., Browning, N. D., Field, D. P., Jensen, D. J., Miller, M. K., Baker, I., Dunand, D. C., Dunin-Borkowski, R., Kabius, B., Kelly, T., Lozano-Perez, S., Misra, A., Rohrer, G. S., Rollett, A. D., Taheri, M. L., Thompson, G. B., Uchic, M., … Was, G. (2011). Towards an integrated materials characterization toolbox. *Journal of Materials Research*, *26*(11), 1341–1383. https://doi.org/DOI: 10.1557/jmr.2011.41

Rosenblatt, G. H., Rowe, M. W., Williams, G. P., Williams, R. T., & Chen, Y. (n.d.). Luminescence of F and F+ centers in magnesium oxide. In *PHYSICAL REVIEW B* (Vol. 39).

Ryszczyńska, S., Trejgis, K., Marciniak, Ł., & Grzyb, T. (2021). Upconverting SrF2:Er3+Nanoparticles for Optical Temperature Sensors. *ACS Applied Nano Materials*, *4*(10), 10438–10448. https://doi.org/10.1021/acsanm.1c01964

Safronova, N. A., Yavetskiy, R. P., Kryzhanovska, O. S., Dobrotvorska, M. V., Balabanov, A. E., Vorona, I. O., Tolmachev, V., Baumer, V. N., Matolínová, I., Kosyanov, D. Y., Shichalin, O. O., Papynov, E. K., Hau, S., & Gheorghe, C. (2021a). A novel IR-transparent Ho3+:Y2O3–MgO nanocomposite ceramics for potential laser applications. *Ceramics International*, *47*(1), 1399–1406. https://doi.org/10.1016/J.CERAMINT.2020.08.263

Safronova, N. A., Yavetskiy, R. P., Kryzhanovska, O. S., Dobrotvorska, M. V., Balabanov, A. E., Vorona, I. O., Tolmachev, V., Baumer, V. N., Matolínová, I., Kosyanov, D. Y., Shichalin, O. O., Papynov, E. K., Hau, S., & Gheorghe, C. (2021b). A novel IR-transparent Ho3+:Y2O3–MgO nanocomposite ceramics for potential laser applications. *Ceramics International*, *47*(1), 1399–1406. https://doi.org/10.1016/J.CERAMINT.2020.08.263

Salah, A., El-Faramawy, N., Ahmed, M., & Farouk, S. (2023). Synthesis and thermoluminescence studies of beta particle irradiated CaAl2O4. *Journal of Luminescence*, *253*, 119461. https://doi.org/https://doi.org/10.1016/j.jlumin.2022.119461

Sathyamoorthy, A., & Luthra, J. M. (1978). Mechanism of thermoluminescence in magnesium oxide. *Journal of Materials Science*, *13*(12), 2637–2644. https://doi.org/10.1007/bf00552693

Scarangella, A., Fabbri, F., Reitano, R., Rossi, F., Priolo, F., & Miritello, M. (2017). Visible emission from bismuth-doped yttrium oxide thin films for lighting and display applications. *Scientific Reports*, *7*(1), 17325. https://doi.org/10.1038/s41598-017-17567-9

Schmidt, T., Lischka, K., & Zulehner, W. (1992). Excitation-power dependence of the near-band-edge photoluminescence of semiconductors. *Phys. Rev. B*, *45*(16),

8989–8994. https://doi.org/10.1103/PhysRevB.45.8989

Seth, P., Jain, A., Goswami, L., Gupta, G., & Aggarwal, S. (2023). Defect Induced MgO:Li,Sm nanophosphor as a new highly sensitive material for thermoluminescence dosimetry. *Journal of Alloys and Compounds*, 171329. https://doi.org/https://doi.org/10.1016/j.jallcom.2023.171329

Shahab, S., Sheikhi, M., Filippovich, L., Kumar, R., Dikusar, E., Yahyaei, H., & Khaleghian, M. (2017). Synthesis, geometry optimization, spectroscopic investigations (UV/Vis, excited states, FT-IR) and application of new azomethine dyes. *Journal of Molecular Structure*, *1148*, 134–149. https://doi.org/10.1016/J.MOLSTRUC.2017.07.036

Sharma, R. K., & Ghosh, P. (2021). Lanthanide-doped luminescent nanophosphors via ionic liquids. *Frontiers in Chemistry*, *9*, 715531.

Shi, Q., Wang, C., Li, S., Wang, Q., Zhang, B., Wang, W., Zhang, J., & Zhu, H. (2014). Enhancing blue luminescence from Ce-doped ZnO nanophosphor by Li doping. *Nanoscale Research Letters*, *9*, 480. https://api.semanticscholar.org/CorpusID:9334972

Shi, X., Zhao, S., Wang, F., Jiang, Q., Zhan, C., Li, R., & Zhang, R. (2021). Optical visualization and imaging of nanomaterials. *Nanoscale Advances*, *3*(4), 889–903.

Shirbhate, S. C., Yadav, A. K., & Acharya, S. A. (2016). Extended x-ray absorption fine structure spectroscopy and x-ray absorption near edge spectroscopy study of aliovalent doped ceria to correlate local structural changes with oxygen vacancies clustering. *Applied Physics Letters*, *108*(14). https://doi.org/10.1063/1.4945098

Shvets, V. A., Kuznetsov, A. V, Fenin, V. A., & Kazansky, V. B. (1985). On the nature of the luminescence centres on MgO surface. *Journal of the Chemical Society, Faraday Transactions 1: Physical Chemistry in Condensed Phases*, *81*(12), 2913–2919. https://doi.org/10.1039/F19858102913

Singh, J. P., Chen, C. L., Dong, C. L., Prakash, J., Kabiraj, D., Kanjilal, D., Pong,

W. F., & Asokan, K. (2015a). Role of surface and subsurface defects in MgO thin film: XANES and magnetic investigations. *Superlattices and Microstructures*, *77*, 313–324. https://doi.org/10.1016/j.spmi.2014.10.035

Singh, J. P., Chen, C. L., Dong, C. L., Prakash, J., Kabiraj, D., Kanjilal, D., Pong, W. F., & Asokan, K. (2015b). Role of surface and subsurface defects in MgO thin film: XANES and magnetic investigations. *Superlattices and Microstructures*, *77*, 313–324. https://doi.org/10.1016/j.spmi.2014.10.035

Singh, J. P., Kaur, B., Gautam, S., Lim, W. C., Asokan, K., & Chae, K. H. (2016). Chemical effects at interfaces of Fe/MgO/Fe magnetic tunnel junction. *Superlattices and Microstructures*, *100*, 560–586. https://doi.org/10.1016/j.spmi.2016.10.015

Singh, J. P., Kim, S. H., Won, S. O., Lee, I. J., & Chae, K. H. (2018). Atomic-scale investigation of MgO growth on fused quartz using angle-dependent NEXAFS measurements. *RSC Advances*, *8*(55), 31275–31286. https://doi.org/10.1039/c8ra02873g

Singh, J. P., Lim, W. C., & Chae, K. H. (2019). An interplay among the Mg2+ ion coordination, structural order, oxygen vacancies and magnetism of MgO thin films. *Journal of Alloys and Compounds*, *806*, 1348–1356. https://doi.org/10.1016/j.jallcom.2019.07.293

Singh, J. P., Lim, W. C., Lee, J., Song, J., Lee, I. J., & Chae, K. H. (2018). Surface and local electronic structure modification of MgO film using Zn and Fe ion implantation. *Applied Surface Science*, *432*, 132–139. https://doi.org/10.1016/j.apsusc.2017.05.034

Singh, J. P., Lim, W. C., Song, J., Lee, S., & Chae, K. H. (2021). Fe+ and Zn+ ion implantation in MgO single crystals. *Materials Letters*, *301*(April), 130232. https://doi.org/10.1016/j.matlet.2021.130232

Singh, J. P., Won, S. O., Lim, W. C., Shim, C. H., & Chae, K. H. (2017). Optical behavior of MgO nanoparticles investigated using diffuse reflectance and near edge

X-ray absorption spectroscopy. *Materials Letters*, *198*, 34–37. https://doi.org/10.1016/J.MATLET.2017.03.168

Singh, R. P., Sharma, K., & Mausam, K. (2020). Dispersion and stability of metal oxide nanoparticles in aqueous suspension: A review. *Materials Today: Proceedings*, *26*, 2021–2025. https://doi.org/https://doi.org/10.1016/j.matpr.2020.02.439

Soliman, C. (2009). Thermoluminescence behavior of magnesium oxide exposed to gamma and ultraviolet radiations. *Radiation Effects and Defects in Solids*, *164*(4), 257–265. https://doi.org/10.1080/10420150802349518

Soma, H., & Uchino, T. (2017). Blue and orange photoluminescence and surface band-gap narrowing in lithium-doped MgO microcrystals. *Journal of Physical Chemistry C*, *121*(3), 1884–1892. https://doi.org/10.1021/acs.jpcc.6b12177

Srisuvetha, V. T., Rayar, S. L., & Shanthi, G. (2020). Role of cerium (Ce) dopant on structural, optical and photocatalytic properties of MgO nanoparticles by wet chemical route. *Journal of Materials Science: Materials in Electronics*, *31*(4), 2799–2808. https://doi.org/10.1007/s10854-019-02823-7

Stanjek, H., & Häusler, W. (2004). Basics of X-ray Diffraction. *Hyperfine Interactions*, *154*(1), 107–119. https://doi.org/10.1023/B:HYPE.0000032028.60546.38

Sun, H. T., Zhou, J., & Qiu, J. (2014). Recent advances in bismuth activated photonic materials. *Progress in Materials Science*, *64*(March), 1–72. https://doi.org/10.1016/j.pmatsci.2014.02.002

Sun, H., Zhang, Y., Gong, H., Li, T., & Li, Q. (2014). Microwave sintering and kinetic analysis of Y2O3–MgO composites. *Ceramics International*, *40*(7), 10211–10215. https://doi.org/10.1016/J.CERAMINT.2014.02.106

Sunta, C. M., Ayta, W. E. F., Kulkarni, R. N., Piters, T. M., & Watanabe, S. (1997). General-order kinetics of thermoluminescence and its physical meaning. *Journal*

of Physics D: Applied Physics, *30*(8), 1234. https://doi.org/10.1088/0022-3727/30/8/013

Tamrakar, R., Bisen, D. P., Sahu, I., & Brahme, N. (2014). UV and gamma ray induced thermoluminescence properties of cubic Gd2O3:Er3+ phosphor. *Journal of Radiation Research and Applied Sciences*, *7*. https://doi.org/10.1016/j.jrras.2014.07.003

Tarasov, I. S. (1999). Peculiarities of photoluminescence and electroluminescence properties of spontaneously formed periodical InGaAsP/GaAs structures. *NANOSTRUCTURES*, 154.

Th. Lindner, H. Sauer, W. Engel, and K. K. (1986). Near-edge structure in electron-energy-loss spectra ofMgo. *PHYSICAL REVIEW B*, *34*(7), 22–24.

Thust, A. (2009). High-Resolution Transmission Electron Microscopy on an Absolute Contrast Scale. *Physical Review Letters*, *102*(22), 220801. https://doi.org/10.1103/PhysRevLett.102.220801

Tiwari, S. P., Mahata, M. K., Kumar, K., & Rai, V. K. (2015). Enhanced temperature sensing response of upconversion luminescence in ZnO–CaTiO3: Er3+/Yb3+ nano-composite phosphor. *Spectrochimica Acta Part A: Molecular and Biomolecular Spectroscopy*, *150*, 623–630. https://doi.org/https://doi.org/10.1016/j.saa.2015.05.081

Tyagi, A. K. (2007). Combustion Synthesis : a Soft-Chemical Route for Functional Nano-Ceramics. *Barc Nwesletter*, *285*, 39–48.

Tyagi, M., Singh, A., Banerjee, D., Sugilal, G., & Kaushik, C. P. (2021). Radiation-resistant beta-photovoltaic battery using Ce-doped Gd3Ga3Al2O12 single-crystal scintillator. *Applied Physics Letters*, *118*(17). https://doi.org/10.1063/5.0048090

Uchino, T., & Okutsu, D. (2008). Broadband Laser Emission from Color Centers Inside MgO Microcrystals. *Physical Review Letters*, *101*(11), 117401. https://doi.org/10.1103/PhysRevLett.101.117401

Uchino, T., Okutsu, D., Katayama, R., & Sawai, S. (2009). Mechanism of stimulated optical emission from MgO microcrystals with color centers. *Physical Review B*, *79*(16), 165107. https://doi.org/10.1103/PhysRevB.79.165107

Uenaka, Y., & Uchino, T. (2011). Photoexcitation, trapping, and recombination processes of the F+-type centers in lasing MgO microcrystals. *Physical Review B*, *83*(19), 195108. https://doi.org/10.1103/PhysRevB.83.195108

Upadhyay, M. M., & Kumar, K. (2023). Gd3+ ion induced UV upconversion emission and temperature sensing in Tm3+/Yb3+:Y2O3 phosphor. *Journal of Rare Earths*, *41*(9), 1295–1301. https://doi.org/10.1016/J.JRE.2022.07.005

Uzun, E. (2021). Numerical solutions of the randall-wilkins and one trap one recombination models for first order kinetic. *Cumhuriyet Science Journal*, *42*, 372–379. https://doi.org/10.17776/csj.796263

Valeur, B., & Berberan-Santos, M. N. (2011). A brief history of fluorescence and phosphorescence before the emergence of quantum theory. *Journal of Chemical Education*, *88*(6), 731–738. https://doi.org/10.1021/ed100182h

van Uitert, L. G. (1984). An empirical relation fitting the position in energy of the lower d-band edge for Eu2+ or Ce3+ in various compounds. *Journal of Luminescence*, *29*(1), 1–9. https://doi.org/10.1016/0022-2313(84)90036-X

Van Uitert, L. G. (1967). Characterization of Energy Transfer Interactions between Rare Earth Ions. *Journal of The Electrochemical Society*, *114*(10), 1048. https://doi.org/10.1149/1.2424184

Vedda, A., Fasoli, M., Nikl, M., Laguta, V. V, Mihokova, E., Pejchal, J., Yoshikawa, A., & Zhuravleva, M. (2009). Trap-center recombination processes by rare earth activators in ${\text{YAlO}}_{3}$ single crystal host. *Phys. Rev. B*, *80*(4), 45113. https://doi.org/10.1103/PhysRevB.80.045113

Vejnović, Z., Pavlović, M. B., Ristić, D., & Davidović, M. (1998). On the general-order kinetics of the thermoluminescence glow peak and the calculation of

parameters from glow curves. *Journal of Luminescence*, *78*(4), 279–287. https://doi.org/https://doi.org/10.1016/S0022-2313(98)00006-4

Vij, A., Lochab, S. P., Singh, S., kumar, R., & Singh, N. (2009). Thermoluminescence study of UV irradiated Ce doped SrS nanostructures. *Journal of Alloys and Compounds*, *486*(1), 554–558. https://doi.org/10.1016/J.JALLCOM.2009.07.003

Virk, H. (2015). History of Luminescence from Ancient to Modern Times. *Defect and Diffusion Forum*, *361*, 1–13. https://doi.org/10.4028/www.scientific.net/DDF.361.1

Wang, F., & Liu, X. (2014). Multicolor tuning of lanthanide-doped nanoparticles by single wavelength excitation. *Accounts of Chemical Research*, *47*(4), 1378–1385.

Wang, H., Yang, Q., Sun, Y., Jiang, X., & Huang, D. (2017). Optical spectroscopy studies of Ho/Yb co-doped yttrium lanthanum oxide transparent ceramics. *Journal of Luminescence*, *192*, 752–756. https://doi.org/https://doi.org/10.1016/j.jlumin.2017.07.067

Wang, J., Chen, D., Jordan, E. H., & Gell, M. (2010). Infrared-Transparent Y2O3–MgO Nanocomposites Using Sol–Gel Combustion Synthesized Powder. *Journal of the American Ceramic Society*, *93*(11), 3535–3538. https://doi.org/https://doi.org/10.1111/j.1551-2916.2010.04071.x

Wang, W., Qiao, X., Chen, J., Tan, F., & Li, H. (2009). Influence of titanium doping on the structure and morphology of MgO prepared by coprecipitation method. *Materials Characterization*, *60*(8), 858–862. https://doi.org/10.1016/J.MATCHAR.2009.02.002

Wang, X., Li, X., Zhong, H., Xu, S., Cheng, L., Sun, J., Zhang, J., Li, L., & Chen, B. (2018). Up-conversion luminescence, temperature sensing properties and laser-induced heating effect of Er3+/Yb3+ co-doped YNbO4 phosphors under 1550 nm excitation. *Scientific Reports*, *8*(1), 5736. https://doi.org/10.1038/s41598-018-

23981-4

Wang, Y., Mu, H., Wu, N., Zhang, M., Zhu, Q., Sun, X., & Li, X. (2023). Effects of Ho3+ concentration on the fabrication and properties of Ho: Y2O3-MgO nanocomposite for Mid-infrared laser applications. *Ceramics International*, *49*(7), 10625–10633. https://doi.org/10.1016/J.CERAMINT.2022.11.250

Wang, Z., Li, P., Yang, Z., & Guo, Q. (2012). A novel red phosphor BaZn 2(PO 4) 2:Sm 3+, R + (R=Li, Na, K). *Journal of Luminescence*, *132*(8), 1944–1948. https://doi.org/10.1016/j.jlumin.2012.03.022

Wang, Z., Lou, S., & Li, P. (2014). Luminescent properties and energy transfer of Sr3La(PO 4)3:Sm3+, Eu3+ for white LEDs. *Journal of Alloys and Compounds*, *586*, 536–541. https://doi.org/10.1016/j.jallcom.2013.10.023

Wei, X., Li, Y., Cheng, X., Chen, Y., & Yin, M. (2011). Strong dependence of upconversion luminescence on doping concentration in holmium and ytterbium co-doped Y2O3 phosphor. *Journal of Rare Earths*, *29*(6), 536–539. https://doi.org/10.1016/S1002-0721(10)60493-0

Williamson, G. K., & Hall, W. H. (1953). X-ray line broadening from filed aluminium and wolfram. *Acta Metallurgica*, *1*(1), 22–31.

Wu, Y., Meng, F., Li, Q., Koschan, M., & Melcher, C. L. (2014). Role of Ce4+ in the scintillation mechanism of codoped Gd3Ga3Al2 O12:Ce. *Physical Review Applied*, *2*(4), 1–13. https://doi.org/10.1103/PhysRevApplied.2.044009

X-Ray Diffraction - an overview | ScienceDirect Topics. (n.d.). Retrieved May 1, 2025, from https://www.sciencedirect.com/topics/materials-science/x-ray-diffraction

Xiang, G., Ma, Y., Zhou, X., Jiang, S., Li, L., Luo, X., Hao, Z., Zhang, X., Pan, G.-H., Luo, Y., & Zhang, J. (2017). Investigation of the Energy-Transfer Mechanism in Ho3+- and Yb3+-Codoped Lu2O3 Phosphor with Efficient Near-Infrared Downconversion. *Inorganic Chemistry*, *56*(3), 1498–1503.

https://doi.org/10.1021/acs.inorgchem.6b02600

Xiao-Jing, L., Hui, Y., Fu-Ping, Z., Hou-Long, X., Zi-Yuan, S., Meng-Jia, W., Jie, Y., Chen, L., Wen-Yao, L., Tong-Xiang, L., & Hong-Hui, J. (2025). Facile fabrication of Y_2O_3-MgO nanocomposite transparent ceramics with enhanced optical properties. *Ceramics International*. https://doi.org/10.1016/J.CERAMINT.2025.01.514

Xu, Y.-N., Gu, Z., & Ching, W. Y. (1997). Electronic, structural, and optical properties of crystalline yttria. *Phys. Rev. B*, *56*(23), 14993–15000. https://doi.org/10.1103/PhysRevB.56.14993

Yamashita, N., Ikeda, S. ichi, & Asano, S. (1987). Photoluminescence and excitation spectra of the SrO:Bi3+ phosphor. *Physics Letters A*, *121*(2), 94–96. https://doi.org/10.1016/0375-9601(87)90272-6

Yan, B. (2022). Chapter 5 - Luminescence responsive sensing mechanism in rare earth metal-organic framework hybrid materials. In B. B. T.-R. E. M.-O. F. H. M. for L. R. C. S. Yan (Ed.), *Woodhead Publishing Series in Electronic and Optical Materials* (pp. 145–175). Woodhead Publishing. https://doi.org/https://doi.org/10.1016/B978-0-323-91236-5.00006-2

Yano, J., & Yachandra, V. K. (2009). X-ray absorption spectroscopy. *Photosynthesis Research*, *102*(2), 241–254. https://doi.org/10.1007/s11120-009-9473-8

Yantake, R., Kaiheriman, M., Yusufu, T., & Sidike, A. (2021). Effect of Li+ doping on the luminescence performance of a novel KAlSiO4:Tb3+ green-emitting phosphor. *Scientific Reports*, *11*(1), 5123. https://doi.org/10.1038/s41598-021-84220-x

Yoshida, T., Tanaka, T., Yoshida, H., Funabiki, T., Yoshida, S., & Murata, T. (1995). Study of dehydration of magnesium hydroxide. *Journal of Physical Chemistry*, *99*(27), 10890–10896. https://doi.org/10.1021/j100027a033

Yousif, A., Abas, B. H., Som, S., Shivaramu, N. J., & Swart, H. C. (2020). Structural and luminescence properties of Y2O3:Eu3+red phosphor by incorporation of Ga3+ and Bi3+ions. *Materials Research Bulletin*, *124*, 110752. https://doi.org/https://doi.org/10.1016/j.materresbull.2019.110752

Yu, D. C., Rabouw, F. T., Boon, W. Q., Kieboom, T., Ye, S., Zhang, Q. Y., & Meijerink, A. (2014). Insights into the energy transfer mechanism in Ce3+-Yb3+ codoped YAG phosphors. *Physical Review B - Condensed Matter and Materials Physics*, *90*(16), 1–7. https://doi.org/10.1103/PhysRevB.90.165126

Yu, J., Luo, M., Lv, Z., Huang, S., Hsu, H.-H., Kuo, C.-C., Han, S.-T., & Zhou, Y. (2020). Recent advances in optical and optoelectronic data storage based on luminescent nanomaterials. *Nanoscale*, *12*(46), 23391–23423.

Yu, Y., Zheng, Y., Qin, F., Liu, L., Zheng, C., Chen, G., Zhang, Z., & Cao, W. (2011). Influence of Yb3+ concentration on upconversion luminescence of Ho3+. *Optics Communications*, *284*(4), 1053–1056. https://doi.org/10.1016/j.optcom.2010.10.042

Yukihara, E. G., Milliken, E. D., Oliveira, L. C., Orante-Barrón, V. R., Jacobsohn, L. G., & Blair, M. W. (2013). Systematic development of new thermoluminescence and optically stimulated luminescence materials. *Journal of Luminescence*, *133*, 203–210. https://doi.org/10.1016/j.jlumin.2011.12.018

Zhai, W., Chen, Y., Liu, Y., Ma, Y., Vijayakumar, P., Qin, Y., Qu, Y., & Dai, Z. (2024). Covalently Bonded Ni Sites in Black Phosphorene with Electron Redistribution for Efficient Metal-Lightweighted Water Electrolysis. *Nano-Micro Letters*, *16*(1), 115. https://doi.org/10.1007/s40820-024-01331-6

Zhang, F., Wang, P., Koberstein, J., Khalid, S., & Chan, S. W. (2004). Cerium oxidation state in ceria nanoparticles studied with X-ray photoelectron spectroscopy and absorption near edge spectroscopy. *Surface Science*, *563*(1–3), 74–82. https://doi.org/10.1016/J.SUSC.2004.05.138

Zhang, Y., Duan, W., Yang, Y., Zhao, Z., Ren, G., Zhang, N., Zheng, L., Chen, J.,

Wang, J., & Sun, T. (2024). Are 4f-Orbitals Engaged in Covalent Bonding Between Lanthanides and Triphenylphosphine Oxide? An Oxygen K-Edge X-ray Absorption Spectroscopy and Density Functional Theory Study. *Inorganic Chemistry*, *63*(5), 2597–2605. https://doi.org/10.1021/acs.inorgchem.3c03834

Zheng, B., Fan, J., Chen, B., Qin, X., Wang, J., Wang, F., Deng, R., & Liu, X. (2022). Rare-earth doping in nanostructured inorganic materials. *Chemical Reviews*, *122*(6), 5519–5603.

Zhou, J., Liu, Q., Feng, W., Sun, Y., & Li, F. (2015). Upconversion Luminescent Materials: Advances and Applications. *Chemical Reviews*, *115*(1), 395–465. https://doi.org/10.1021/cr400478f

Zimmer, M. (2009). GFP: from jellyfish to the Nobel prize and beyond. *Chemical Society Reviews*, *38*(10), 2823–2832. https://doi.org/10.1039/B904023D

Ziniker, W. M., Merrow, J. K., & Meuller, J. I. (1972). Thermally stimulated luminescence in MgO. *Journal of Physics and Chemistry of Solids*, *33*(7–9), 1619–1630. https://doi.org/10.1016/S0022-3697(72)80456-6

LIST OF PUBLICATIONS

LIST OF PUBLICATIONS

Name: Priyanka Bishnoi

ORCID ID: 0009-0007-1347-2049

Included in Thesis

1. **Priyanka Bishnoi**, Ashish Kumar, Ranjeet Brajpuriya, KPS Parmar, Aditya Sharma, Keun Hwa Chae, Ankush Vij, 'Electronic structure and luminescence studies of Bi-doped MgO nanophosphors', *Ceramics International (SCI)*, vol 50, no. 9, pp. 15657-15667, 2024, doi.org/10.1016/j.ceramint.2024.02.046
2. **Priyanka Bishnoi**, Gargi Dhiman, Ranjeet Brajpuriya, Keun Hwa Chae, SO Won, Ankush Vij, 'Structural and luminescence properties of MgO: Li nanocrystals', *Nuclear Instruments and Methods in Physics Research Section B: Beam Interactions with Materials and Atoms (NIMB)(SCI IF 1.4)*, vol 552, pp. 165357, 2024, doi.org/10.1016/j.nimb.2024.165357
3. **Priyanka Bishnoi,** Ranjeet Brajpuriya, Aditya Sharma, Keun Hwa Chae, SO Won, Ankush Vij, 'Defect modulation and color tuning of MgO: Probing the influence of Sm and Li dopants through X-ray absorption, Photoluminescence, and Thermoluminescence spectroscopy', *Journal of Alloys and Compounds (SCI IF 5.8)*, vol 1002, pp. 175270, 2024, doi.org/10.1016/j.jallcom.2024.175270
4. **Priyanka Bishnoi,** Aditya Sharma, Ranjeet Brajpuriya, Keun Hwa Chae, SO Won, Ankush Vij, 'Probing structural and luminescence properties of Ce^{3+} and Li-doped MgO nanocrystals via XAS, PL, and TL studies', *Journal of Photochemistry & Photobiology,A: Chemistry(SCI)*, vol 463, pp. 116281, 2025, doi.org/10.1016/j.jphotochem.2025.116281
5. **Priyanka Bishnoi**, Vaishali Rathi, Madaan M. Upadhyay, Aditya Sharma, Kaushal Kumar, Ranjeet Barajpuriya, Ankush Vij, 'Investigating NIR Radiated Luminescence, Temperature Sensing and Laser Induced Thermal

Effect of Ho^{3+}, Yb^{3+} doped MgO: Y_2O_3 nanocomposites for Security Ink Applications' *Journal of Photochemistry & Photobiology,A: Chemistry(SCI)*, vol 471, doi.org/10.1016/j.photochem.2025.116673

Priyanka Bishnoi, Vaishali Rathi, Madaan M. Upadhyay, Aditya Sharma, Kaushal Kumar, Ranjeet Barajpuriya, Ankush Vij, 'Tuning Upconversion emission in MgO-Y_2O_3 Nanocomposites with Er^{3+}-Yb^{3+} Doping' (*manuscript to be communicated*)

Other Collaborative Publications

1. Priya Jasrotia, Bhanu Priya, Raj Kumar, **Priyanka Bishnoi**, Ankush Vij, Tanuj Kumar, 'A correlation between fractal growth, water contact angle, and SERS intensity of R6G on ion beam nanostructured ultra-thin gold (Au) films', *Frontiers in Physics*, vol 11, pp. 1125004, 2023.
2. Priya Jasrotia, Bhanu Priya, Raj Kumar, **Priyanka Bishnoi**, Tanuj Kumar, 'SERS detection of rhodamine-6G on ion beam nanostructured ultra-thin gold (Au) films: A correlation between fractal growth, water contact-angle and Raman Intensity', *ECS Journal of Solid State Science and Technology*, vol 12, pp. 027005, 2023.
3. Pankaj Kumar, Aditya Sharma, **Priyanka Bishnoi,** Ankush Vij, Sandeep Kumar, Hyun-Joon Shin, KH Chae, BH Lee, SO Won, 'Synthesis and characterization of $ZnGa_2O_4$:$Cr^{3+}Ge^{3+}$ compounds with tunable photoluminescence properties', *Journal of the Korean Physical Society*, vol 83, 6, pp. 463-470, 2023.
4. Gargi Dhiman, **Priyanka Bishnoi,** Ashish Kumar, Manjeet Singh Goyat, Shalendra Kumar, Ranjeet Brajpuriya, 'Oxygen ion irradiation: Insights into the structural modifications of CVD-grown graphene', *Nuclear Instruments and Methods in Physics Research Section B: Beam Interactions with Materials and Atoms*, vol 552, pp. 165359, 2024.
5. Savita, Madan Murari Upadhyay, **Priyanka Bishnoi**, Sanjay Kumar, Kaushal Kumar, Ankush Vij, Anup Thakur, 'Up-converted white light emission in Er^{3+} doped $MgAl_2O_4$ nanocrystals, *Journal of Applied Physics*, vol 135,12, 2024.

6. Pankaj Kumar, Aditya Sharma, **Priyanka Bishnoi**, Ankush Vij, Sandeep Kumar, Ashima Juyal, Ranjeet Brajpuriya, 'Structural and optical properties of $ZnGa_{2-x}(Yb_XCrGe)_xO_4$ (X= Ho and Er) up-conversion photoluminescence materials', *Chemical Physics Letters*, vol 842, pp. 141204, 2024.

APPENDICES

APPENDIX A: CONFERENCES/ WORKSHOPS ATTENDED

1. International Conference of Futuristic Materials (ICFM-2022) held at Manav Rachna International Institute of Research and Studies, Faridabad, Haryana.
2. International /Young Researcher Conclave 2023, UPES, Dehradun.
3. International Conference on Nanostructuring by Ion Beams(ICNIB, IUAC), UPES Dehradun.
4. 28th International Conference on Nuclear Track and Radiation Measurements, Gurugram University, Gurugram.
5. International Conference on Energy Materials & Rechargeable Batteries, MRU, Faridabad.
6. 1st International Conference on Recent Advancements in Applied Sciences and Technology, UPES, Dehradun.
7. International Young Researcher Conclave 2024, UPES, Dehradun.
8. International Conference on Physics for Sustainable Development, CUJ, Jammu.
9. Workshop "Awareness program on Advance materials and their application 1.0" held at UPES.
10. Online Workshop on "Online Hands on Training on Rietveld Refinement" organized by SIAS research Forum.
11. Online Workshop on "Hands-on training on Elemental analysis" organized by SIAS Research Forum.
12. Workshop "Awareness program on Advance materials and their application 2.0" held at UPES.

APPENDIX B: PAPER PRESENTED IN CONFERENCES

1. Poster entitled “Structural and photoluminescence studies of Bi-doped MgO nanocrystals” presented at *International Conference of Futuristic Materials (ICFM-2022)* held at Manav Rachna International Institute of Research and Studies, Faridabad, Haryana.

2. Poster entitle “Effect of Co-doping doping of Bi, Li ions on structural and Luminescence properties of MgO nanocrystals” presented *International /Young Researcher Conclave 2023*, UPES, Dehradun.

3. Poster entitled “Structural and luminescence properties of MgO: Li Nanocrystals” presented at *International Conference on Nanostructuring by Ion Beams*(ICNIB, IUAC), UPES Dehradun.

4. Oral talk on paper entitled “Investigation of Doping of Ce, Li ions on the Structural and Luminescence Behavior of MgO Nanoparticles by XAS, PL, and TL Studies” at *28th International Conference on Nuclear Track and Radiation Measurements*, Gurugram University, Gurugram.

5. Oral talk on paper entitled “Green emitting Ho 3+ -Yb 3+ activated MgO-Y_2O_3 upconverting nanocomposites” *International Conference on Energy Materials & Rechargeable Batteries*, MRU, Faridabad.

6. Oral talk on paper entitled “Tuning Upconversion emission in MgO-Y_2O_3 Nanocomposites with Er^{3+}-Yb^{3+} Doping” *1st International Conference on Recent Advancements in Applied Sciences and Technology*, UPES, Dehradun.

7. Poster entitled “Investigation structural and luminescence properties of Sm, Li doped in MgO nanocrystals” presented at International *Young Researcher Conclave 2024*, UPES, Dehradun.

8. Oral talk on paper entitled “Influence of co-doping Er^{3+}-Yb^{3+} on enhanced upconversion red luminescence in doped MgO-Y_2O_3 Nanocomposites” in *International Conference on Physics for Sustainable Development*, CUJ, Jammu.

Priyanka_Thesis

ORIGINALITY REPORT

2%	1%	1%	0%
SIMILARITY INDEX	INTERNET SOURCES	PUBLICATIONS	STUDENT PAPERS

PRIMARY SOURCES

1	"Handbook of Sol-Gel Science and Technology", Springer Science and Business Media LLC, 2018 Publication	1%
2	"Upconverting Nanoparticles", Wiley, 2022 Publication	1%
3	scholar.ufs.ac.za Internet Source	1%

Exclude quotes	Off	Exclude matches	< 1%
Exclude bibliography	On		